

Synthesis Of Inorganic-Organic Hybrid Nanocomposites For Environmental Application

Thesis submitted for the degree of

Doctor of Philosophy (Science)

in

Chemistry (Inorganic)

by

Sankar Das

Department of Chemistry

University of Calcutta

July, 2018

***DEDICATED TO MY PARENTS AND
SUPERVISOR...***

With deep regards and profound respect, I take this opportunity to convey my deepest gratitude to my supervisor Dr. Subhra Jana for introducing me to such an interesting and advanced field of research. Her invaluable guidance, advice, technical discussion, constructive criticism, extensive support, constant encouragement and valuable suggestions kept me inspired throughout this research work. She continuously motivated me to think and execute my plans independently. She has an excellence sense of humour and it was always a pleasure to talk to her. I am really fortunate to have such an enthusiastic supervisor. I found joy and enthusiasm for her research and dedication towards work. Her involvement in research has triggered and nourished my intellectual maturity. I am especially grateful for her constant availability and helpful discussions for my research work.

I am also very much grateful to my associate supervisor Prof. Gautam Gangopadhyay for his extensive support, encouragement and spending his valuable time towards the academic discussions during my research work.

I would like to express my profound gratitude to Prof. Chittaranjan Sinha, Department of Chemistry, Jadavpur University for his moral support, affection, encouragement and suggestions throughout my academic carrier.

I am also thankful to all the thesis committee members, faculty members and staffs of S. N. Bose National Centre for Basic Sciences for their sincere cooperation and help.

I would like to thank my lab mate Arnab Samanta for his generous assistance in every moment. I would like to express my sincere thanks to my all SNB friends for providing a wonderful and friendly environment in campus. My life in S. N. Bose Centre was enjoyable as I have many good friends, seniors and juniors.

I gratefully acknowledge Ramakrishna Mission Residential College (Autonomous), Narendrapur for giving me perfect ambience and educational support during bachelor and master courses.

Words are not enough to convey my gratitude to all my teachers from primary school till my master's degree for their inspirational teaching in ethics and discipline in life. I convey my sincere gratitude to my loving teacher (Jethu) Asit Dasmahapatra.

I express my sincere gratitude to my Jethu (Bishnupada Payra) and his family for their love, moral support and encouragement.

I am especially grateful to Sutapa, kaku and kakima for their mental support, affection and encouragement during this journey. It is impossible to express my feelings in word about those moments which I have shared with my sister (Sandita).

I am thankful to my college friends particularly Rajkumar, Kartik, Rajorshi, krishnendu, Kaushik, Shubhrangshu, Arghya, Soumen, Sumanta and Snehashis for their memorable, pleasant and perpetual refreshment and support in my difficult time during this journey.

I gratefully acknowledge S. N. National Centre for Basic Sciences for providing me fellowship and research facilities.

I would like to thank everybody who was important for the successful realization of the thesis and express my sincere apology to anyone if I have inadvertently missed him/her.

Last but not the least, I express my deep sense of gratitude to my parents and my brother (Paltu) for their love, dream, encouragement and moral support over the years of my study. Without their sacrifices, moral supports and blessings, the thesis would not have taken its shape.

Dated:

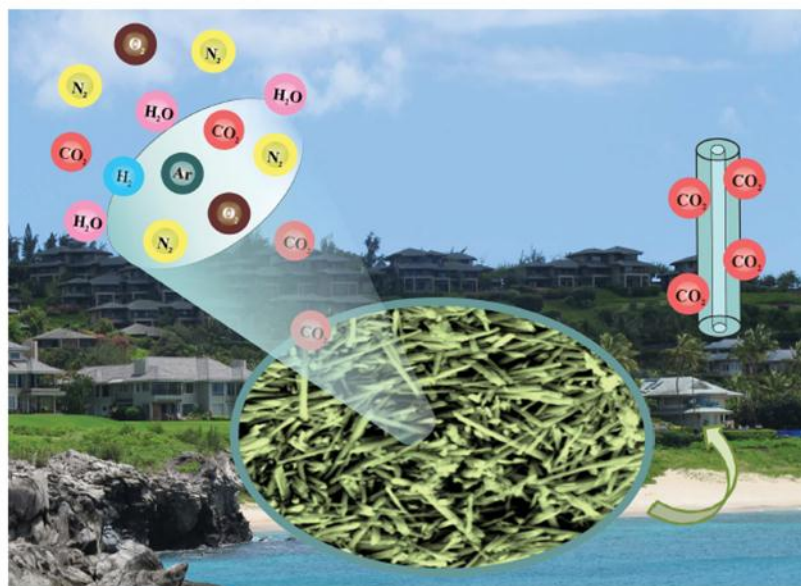
(Sankar Das)

*Department of Chemical, Biological and Macro-Molecular Sciences,
S. N. Bose National Centre for Basic Sciences,
Salt lake, Kolkata-700106, India*

List of Publications

- ❖ 1. **S. Das**, A. Samanta and S. Jana, *Fabrication of Large Surface Area Dandelion-Like Silica Nanoflowers for CO₂ Capture*. 2018 (Communicated).
- ❖ 2. **S. Das**, A. Samanta, G. Gangopadhyay and S. Jana, *Clay-Based Nanocomposites as Recyclable Adsorbent toward Hg(II) Capture: Experimental and Theoretical Understanding*. **ACS Omega**, 2018, 3, 6283.
- 3. A. Samanta, **S. Das** and S. Jana, *Exploring β -FeOOH Nanorods as an Efficient Adsorbent for Arsenic and Organic Dyes*. **ChemistrySelect**, 2018, 3, 2467.
- ❖ 4. **S. Das**, A. Samanta and S. Jana, *Light-Assisted Synthesis of Hierarchical Flower-Like MnO₂ Nanocomposites with Solar Light Induced Enhanced Photocatalytic Activity*. **ACS Sustainable Chemistry & Engineering**, 2017, 5, 9086.
- ❖ 5. **S. Das** and S. Jana, *A Tubular Nanoreactor Directing the Formation of In-situ Iron Oxide Nanorods with Superior Photocatalytic Activity*. **Environmental Science: Nano**, 2017, 4, 596.
- ❖ 6. **S. Das**, C. Ghosh and S. Jana, *Moisture Induced Isotopic Carbon Dioxide Trapping from Ambient Air*. **Journal of Materials Chemistry A**, 2016, 4, 7632 (**Back Cover**).
- ❖ 7. **S. Das**, A. Maity, M. Pradhan and S. Jana, *Assessing Atmospheric CO₂ Entrapped in Clay Nanotubes Using Residual Gas Analyzer*. **Analytical Chemistry**, 2016, 88, 2205.
- ❖ 8. **S. Das** and S. Jana, *A Facile Approach to Fabricate Halloysite/Metal Nanocomposite with Preformed and In-situ Synthesized Metal Nanoparticles: A Comparative Study of their Enhanced Catalytic Activity*. **Dalton Transactions**, 2015, 44, 8906.
- ❖ 9. S. Jana, **S. Das**, C. Ghosh, A. Maity and M. Pradhan, *Halloysite Nanotubes Capturing Isotope Selective Atmospheric CO₂*. **Scientific Reports**, 2015, 5, 8711.
- ❖ 10. S. Jana and **S. Das**, *Development of Novel Inorganic–Organic Hybrid Nanocomposites as a Recyclable Adsorbent and Catalyst*. **RSC Advances**, 2014, 4, 34435.

❖ (Incorporated in the Thesis)



Demonstrating a study on the trapping of isotopic carbon dioxide from seasonal ambient air in clay nanotubes by Dr Subhra Jana at the S. N. Bose National Centre for Basic Sciences.

Moisture induced isotopic carbon dioxide trapping from ambient air

Novel clay-based nanocomposites have been fabricated to capture isotopic CO_2 ($^{13}\text{C}^{18}\text{O}_2$, $^{14}\text{C}^{16}\text{O}_2$, and $^{13}\text{C}^{16}\text{O}^{18}\text{O}$) from seasonal ambient air as well as to explore the underlying adsorption mechanism, keeping an eye on the relative humidity-induced CO_2 adsorption efficacy of these nanotubes in an oxidative environment.

As featured in:



See Subhra Jana et al.,
J. Mater. Chem. A, 2016, 4, 7632.



www.rsc.org/MaterialsA

Registered charity number: 207890

List of Patents

1. **S. Das** and S. Jana, *A Clay Based Nano Confined Reactor*, 2017 (Indian Patent Applied). File No.: 201731043481
2. **S. Das**, A. Samanta and S. Jana, *An Improved Method for the Synthesis of δ -MnO₂ Nanocomposites with Enhanced Photocatalytic Activity*, 2017 (Indian Patent Applied). File No.: 201731040027

In the present thesis, synthetic strategies, characteristic properties and potential applications of nanocomposites have been discussed. Several inorganic-organic hybrid nanocomposites were synthesized for environmental remediation and their catalytic activity has also been explored. Based on a simple and facile route, high surface area mesoporous dandelion-like silica nanoflowers with adequate accessible adsorption sites were produced through the light-assisted hydrolysis route to capture toxic gases from the atmosphere. In a step-wise fashion, novel solid-phase adsorbents were synthesized via selective modification of a clay nanotube using aminosilanes which contain primary and/or secondary amine groups for CO₂ adsorption under standard temperature and pressure. Moisture dependent CO₂ adsorption and stability of these novel adsorbents in oxidative environment have been demonstrated in detail. Another major finding is the development of inexpensive solid adsorbents to remove heavy metal ions, since their contamination in ground water has become a serious ecological and health issues. The adsorption properties and kinetics of these solid adsorbents have been studied in details for Hg(II) ions and effect of solution pH during adsorption has also been presented. Environmentally benign and low-cost heterogeneous catalysts have been fabricated through the immobilization of metal precursors followed by reduction or direct loading of preformed metal nanoparticles over the surface of organosilane modified nanoclays to be explored them as catalysts for the reduction of nitroaromatics. Then, their catalytic activity was evaluated and compared with the reported heterogeneous catalysts. Afterwards, hierarchical MnO₂ nanoflowers comprising of assemblies of intersected nanosheets were produced over the outer surfaces of nanoclays and their photocatalytic activity was investigated under natural sunlight irradiation for the degradation of several toxic organic dyes. Finally, a general method was established to achieve tubular nanoreactor for the degradation of refractory pollutants under renewable and never-ending solar light.

Keywords: Hybrid nanocomposites, Solid adsorbents, Heterogeneous catalysts, Dandelion-like silica nanoflowers, Hierarchical MnO₂ nanoflowers, Nanoreactor, CO₂ working capacity, Catalysis.

Title Page	i
Acknowledgement	iii
List of Publications	v
List of Patents	vii
Abstract	viii
Contents	
Chapter 1	Introduction
1.1 Nanoscience and Nanotechnology	1
1.2 Nanomaterials	1
1.3 Classification of Nanomaterials	3
1.3.1 Zero Dimensional (0-D)	3
1.3.2 One Dimensional (1-D)	3
1.3.3 Two Dimensional (2-D)	4
1.3.4 Three Dimensional (3-D)	4
1.4 Important Usage of Metal and Metal Oxide Nanoparticles	4
1.5 Quantum Dots	8
1.6 Nanoparticle Synthetic Strategies	11
1.6.1 Top-Down Approaches	12
1.6.2 Bottom-Up Approaches	13
1.7 Stabilization of Nanoparticles	14
1.7.1 Electrostatic Stabilization	15
1.7.2 Steric Stabilization	16
1.7.3 Electrosteric Stabilization	17
1.7.4 Stabilization by Ligand	18
1.7.5 Stabilization by Dendrimers	18
1.8 Important Properties of Nanoparticles	19

1.8.1 Surface Properties	19
1.8.2 Optical Properties	20
1.8.2.1 Origin of Surface Plasmon Resonance	23
1.8.3 Electronic Properties	24
1.8.4 Mechanical Properties	26
1.8.5 Magnetic Properties	28
1.9 Nanocomposites	29
1.10 Applications of Nanoparticles	31
1.10.1 Catalysis Involving Nanoparticles	32
1.11 Objectives and Outline of Thesis	34
1.12 References	37
Chapter 2	Materials, Instrument and Characterization Techniques
2.1 Materials	53
2.2 Instrument and Characterization Techniques	53
2.2.1 Fourier Transform Infrared Spectroscopy	54
2.2.2 UV-Vis Absorption Spectroscopy	56
2.2.3 Nuclear Magnetic Resonance Spectroscopy	57
2.2.4 CHNS Elemental Analyzer	59
2.2.5 X-ray Diffraction Spectroscopy	60
2.2.6 Scanning Electron Microscopy	62
2.2.7 Transmission Electron Microscopy	63
2.2.8 Brunauer-Emmett-Teller (BET) Method for Surface Area Measurement	65
2.2.9 Thermogravimetric Analysis	66
2.2.10 Zeta-potential	67
2.2.11 Vibrating-Sample Magnetometer	68

	2.2.12 Inductively Coupled Plasma Optical Emission Spectrometry	69
	2.3 References	69
Chapter 3	Moisture Induced Carbon Dioxide Trapping from Ambient Air	
	3.1 Introduction	71
	3.2 Experimental Section	73
	3.2.1 Preparation of Adsorbents	73
	3.2.2 Residual Gas Analyzer-Mass Spectrometry (RGA-MS) Technique	75
	3.2.3 Integrated Cavity Output Spectroscopy	76
	3.2.4 CO ₂ Adsorption Measurements	76
	3.3 Results and Discussion	77
	3.3.1 Characterization of Clay Based Adsorbents	78
	3.3.1.1 TEM and FESEM Analysis	78
	3.3.1.2 XRD Analysis	80
	3.3.1.3 FTIR Study	80
	3.3.1.4 NMR Study	81
	3.3.1.5 CHN Elemental Analysis	82
	3.3.2 CO ₂ Adsorption from Ambient Air	83
	3.3.2.1 CO ₂ Adsorption Study	83
	3.3.2.2 Adsorption of CO ₂ Isotopes	90
	3.3.2.3 Impact of Moisture during CO ₂ Uptake	92
	3.3.2.4 Reusability of the Adsorbents	96
	3.3.2.5 CO ₂ Adsorption Mechanism	99
	3.4 Conclusions	102
	3.5 References	103

Chapter 4	Synthesis of Mesoporous Silica Nanoflowers for CO₂ Capture	
	4.1 Introduction	107
	4.2 Experimental Section	108
	4.2.1 Synthesis of Silica Nanomaterials	108
	4.2.2 Functionalization of Silica Nanoflowers	109
	4.2.3 CO ₂ Adsorption Study	109
	4.3 Results and Discussion	110
	4.3.1 Characterization of Silica Nanoflowers	110
	4.3.1.1 FESEM and TEM Analysis	110
	4.3.1.2 STEM-EDS Analysis	111
	4.3.1.3 Growth Mechanism of the SiO ₂ Nanoflowers	112
	4.3.1.4 NMR Analysis	113
	4.3.1.5 FTIR Analysis	114
	4.3.1.6 Surface Area Measurement	114
	4.3.1.7 XRD Analysis	115
	4.3.1.8 TGA Study	116
	4.3.2 Characterization of Amine-Loaded SiO ₂ Nanoflowers	117
	4.3.2.1 Solid State NMR Analysis	118
	4.3.2.2 FTIR Analysis	119
	4.3.2.3 CHN Elemental Analysis	120
	4.3.3 CO ₂ Adsorption by Amine-Loaded SiO ₂ Nanoflowers	121
	4.3.3.1 CO ₂ Adsorption Study	121
	4.3.3.2 CO ₂ Adsorption Mechanism	122
	4.3.3.3 Recyclability Study of these Adsorbents	123
	4.3.3.4. Comparison of Amine Efficiency	124

	4.4 Conclusions	125
	4.5 References	126
Chapter 5	Development of Hybrid Nanocomposites for Hg(II) Removal from Aqueous Solution	
	5.1 Introduction	129
	5.2 Experimental Section	131
	5.2.1 Synthesis of Inorganic-Organic Hybrid Nanocomposites	131
	5.2.2 Batch Adsorption Study	132
	5.3 Results and Discussion	133
	5.3.1 Hg (II) Removal from Aqueous Solution	
	Using SH-HNTs NCs	133
	5.3.1.1 Characterization of the SH-HNTs	133
	5.3.1.1.1 TGA Study	133
	5.3.1.1.2 FTIR Study	134
	5.3.1.1.3 XRD Analysis	135
	5.3.1.1.4 FESEM and TEM Study	136
	5.3.1.1.5 EDS Study	137
	5.3.1.1.6 Analysis of Sulphur (S) Content	138
	5.3.1.2 Mercury Adsorption Study by SH-HNTs	138
	5.3.1.3 Chemical Stability and Regenerability of SH-HNTs	141
	5.3.1.4 Adsorption of Different Toxic Metals by SH-HNTs	142
	5.3.2 Hg (II) Removal from Aqueous Solution Using	
	Amine Functionalized HNTs	143
	5.3.2.1 Characterization of M-HNTs and S-HNTs	143
	5.3.2.1.1 FTIR Study	143
	5.3.2.1.2 NMR Study	144

	5.3.2.1.3 FESEM Study	145
	5.3.2.1.4 XRD Study	146
	5.3.2.1.5 CHN Elemental Analysis	146
	5.3.2.1.6 Surface Area Analysis	147
	5.3.2.2 Mercury Adsorption Study using M-HNTs and S-HNTs	147
	5.3.2.3 Temperature Dependence of Adsorption Capacity	152
	5.3.2.4 Relation between Kinetics and Thermodynamics	155
	5.3.2.5 Adsorption of Different Toxic Metals	157
	5.3.2.6 Effect of Solution pH	158
	5.4 Conclusions	161
	5.5 References	161
Chapter 6	Fabrication of Halloysite/Metal Nanocomposites with Preformed and <i>In-Situ</i> Synthesized Metal Nanoparticles: A Comparative Study of Their Enhanced Catalytic Activity	
	6.1 Introduction	165
	6.2 Experimental Section	167
	6.2.1 Synthesis of Aminosilane Modified Halloysite Nanotubes	167
	6.2.2 Fabrication of HNTs/Metal NCs with Preformed Metal Nanoparticles	168
	6.2.3 Fabrication of HNTs/Metal NCs with <i>In-Situ</i> Synthesized Metal Nanoparticles	168
	6.2.4 Catalytic Reaction	170
	6.3 Results and Discussion	170
	6.3.1 Characterization of HNTs-NH ₂	170
	6.3.1.1 FESEM and TEM Study	170

6.3.1.2 EDX Study	171
6.3.1.3 CHN Elemental Analysis	172
6.3.1.4 FTIR Study	172
6.3.1.5 XRD Study	173
6.3.2 Characterization of the HNTs/Metal NCs	174
6.3.2.1 FTIR Study	174
6.3.2.2 XRD Analysis	175
6.3.2.3 UV-Visible and TEM Analyses	175
6.3.3 Catalytic Activity of the HNTs/Metal Nanocomposites	179
6.3.3.1 Catalytic Activity Study	179
6.3.3.2 Catalytic Efficiency of Preformed and <i>In-situ</i> Synthesized Catalysts	181
6.3.3.3 Activation Energy of the Reaction	182
6.3.3.4 Recyclability Study of the Catalyst	184
6.3.3.5 Mechanism of the Reduction Reaction	185
6.3.3.6 Comparison of Catalytic Activity	186
6.4 Conclusions	188
6.5 References	189
Chapter 7	
Light-Assisted Synthesis of Hierarchical Flower-Like MnO₂ Nanocomposites with Solar Light Induced Enhanced Photocatalytic Activity	
7.1 Introduction	194
7.2 Experimental Section	196
7.2.1 Surface Functionalization of Halloysite Nanotubes	196

7.2.2 Fabrication of HNTs/MnO ₂ Nanocomposites	197
7.2.3 Photocatalytic Reaction	197
7.3 Results and Discussion	199
7.3.1 Characterization of the Surface Modified HNTs	199
7.3.1.1 FTIR Analysis	199
7.3.1.2 FESEM Study	200
7.3.1.3 CHN Elemental Analysis	201
7.3.1.4 Zeta-potential Measurement	201
7.3.2 Characterization of HNTs/MnO ₂ NCs	201
7.3.2.1 FESEM Analysis	201
7.3.2.2 TEM and HRTEM Analyses	202
7.3.2.3 EDS Analysis	204
7.3.2.4 STEM-EDS Elemental Mapping Analysis	205
7.3.2.5 XRD Study	206
7.3.2.6 Phase Transition of MnO ₂ /HNTs NCs	207
7.3.2.7 Determination of Zeta-potential of δ -MnO ₂ /HNTs NCs	208
7.3.2.8 Growth Mechanism Study	208
7.3.2.9 BET Surface Area Measurement	211
7.3.2.10 UV-visible Diffuse Reflectance Study	212
7.3.2.11 ICP-OES Analysis	213
7.3.3 Photocatalytic Activity of HNTs/MnO ₂ NCs	213
7.3.3.1 Degradation of Organic Pollutants	213
7.3.3.2 Kinetics of the Degradation Reaction	215
7.3.3.3 Recyclability Study	218
7.3.3.4 Comparison of Catalytic Efficiency	218
7.3.3.5 Photocatalytic Degradation Mechanism	220

	7.4 Conclusions	223
	7.5 References	224
Chapter 8	Clay Nanotubes as Nanoreactor for the Synthesis of Iron Oxides with Enhanced Photocatalytic Activity	
	8.1 Introduction	229
	8.2 Experimental Section	230
	8.2.1 Lumen Modification of Halloysite Nanotubes	230
	8.2.2 Synthesis of α -Fe ₂ O ₃ within the Lumen of Modified Halloysite Nanotubes	231
	8.2.3 Photocatalytic Reaction	232
	8.3 Results and Discussion	233
	8.3.1 Characterization of the Lumen Modification of HNTs	233
	8.3.1.1 TEM Study	233
	8.3.1.2 FTIR Analysis	234
	8.3.1.3 NMR Study	236
	8.3.1.4 XRD Study	237
	8.3.1.5 CHN Elemental Analysis	238
	8.3.2 Characterization of Iron Oxide Nanorods inside Halloysite Lumen	238
	8.3.2.1 TEM and EDS Analysis	239
	8.3.2.2 STEM-EDS Elemental Mapping Analysis	240
	8.3.2.3 XRD Study	242
	8.3.2.4 Zeta-potential Measurement	242
	8.3.2.5 BET Study	243
	8.3.2.6 UV-Visible Diffuse Reflectance Analysis	244

8.3.2.7 VSM Study	244
8.3.2.8 ICP-OES Study	246
8.3.3 Photocatalytic Activity of α -Fe ₂ O ₃ /HNTs NCs	246
8.3.3.1 Degradation of Organic Pollutants	246
8.3.3.2 Kinetics of the Degradation Reaction	248
8.3.3.3 Recyclability of α -Fe ₂ O ₃ /HNTs NCs	249
8.3.3.4 Degradation Mechanism	250
8.4. Conclusions	252
8.5 References	253
Chapter 9	Conclusions and Future Scope of the Study
9.1 Conclusions	256
9.2 Future Scope of the Study	258

Introduction

1.1 Nanoscience and Nanotechnology

Nanoscience can be defined as the science of objects and phenomena taking place at the level of few nanometers. Nanotechnology is the ability to work at atomic, molecular and supramolecular level with possible applications. Science and technology research in nanotechnology explore innovation of materials in the areas of manufacturing, nanoelectronics, medicines, health care, energy sector, biotechnology, national security, information technology etc. Nanotechnology is an interesting but emerging field of the scientific research and expected to open new avenues in science and technology, which are under constant evolution and hence offering a wide scope of research activity.

During the last few years, nanotechnology being an emerging and advanced field of research, has drawn a considerable interest in the multidisciplinary research areas including chemistry, biochemistry, medicine and material science. The term “Nanotechnology” is increasingly employed to illustrate the process technologies and analytical techniques for materials in the ultrafine range of the order of a millionth of a millimeter. Analysts claim that it has a prospective impact across an entire range of industries and great implications on human health, environment, sustainability and national security.¹

1.2 Nanomaterials

Generally, if the size of the particles is in 1-100 nm range, they are called nanoparticles (NPs) or nanomaterials.²⁻⁴ The term nano means “*dwarf*” and has been derived from the Greek word “*nanos*”. Nanometer (nm) is equal to one billionth (10^{-9}) of a metre. Schematic presentation of size comparison of several objects from

macroscale to nanoscale is shown in Figure 1.1. Nanoparticles are of great interest as they are effectively a bridge between bulk materials and atomic structures. Physical properties of the bulk materials should be constant regardless of its size but at the nanoscale they have different properties as compared to their bulk form. The novel materials that are in nanoscale range offer unique and different properties. These special and unique properties could be attributed to their small sizes and large surface area to volume ratio. Due to their small particle sizes and high reactivity, the nanoscale metal particles may be valuable in a wide range of applications. Nanomaterials demonstrate several fascinating properties in the field of electronics,^{5,6} spectroscopy,⁷⁻⁹ catalysis,¹⁰⁻¹² photography,^{13,14} information storage^{15,16} and bio-sensing.¹⁷⁻¹⁹ New applications for nanomaterial in the areas of photonics,^{20,21} imaging^{22,23} and medicine²⁴⁻²⁶ have also been developed. However, their activity and properties can be affected and extremely reduced once they start agglomerating, which results in the formation of bulk like materials. To prevent agglomeration and achieve well dispersed particles, these NPs can be either immobilized on solid supports or fabricated them directly over the supports.²⁷⁻²⁹ Nanomaterials exist with enormous chemical diversity in the form of nanoparticles, nanotubes, nanowires, nanoporous solids, quantum dots etc.

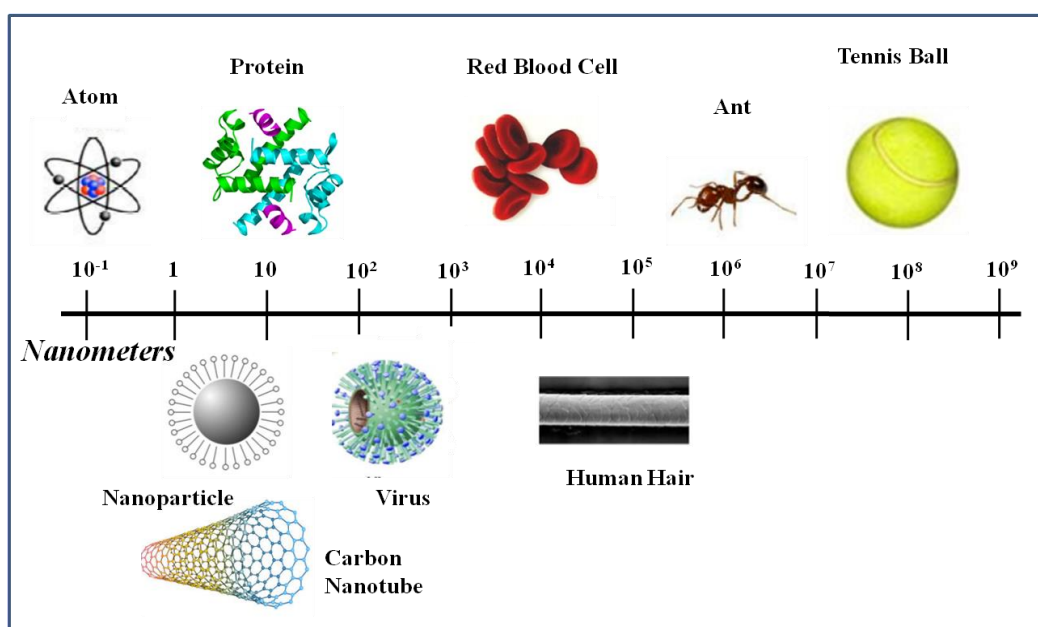


Figure 1.1: Schematic presentation of size comparison of several objects from macroscale to nanoscale.

1.3 Classification of Nanomaterials

Nanoparticles can exist as nanostructure or as composites material. According to the dimension, the nanomaterials can be classified as zero dimensional (0-D), one dimensional (1-D), two dimensional (2-D) and three dimensional (3-D) nanostructures, as shown in Figure 1.2.

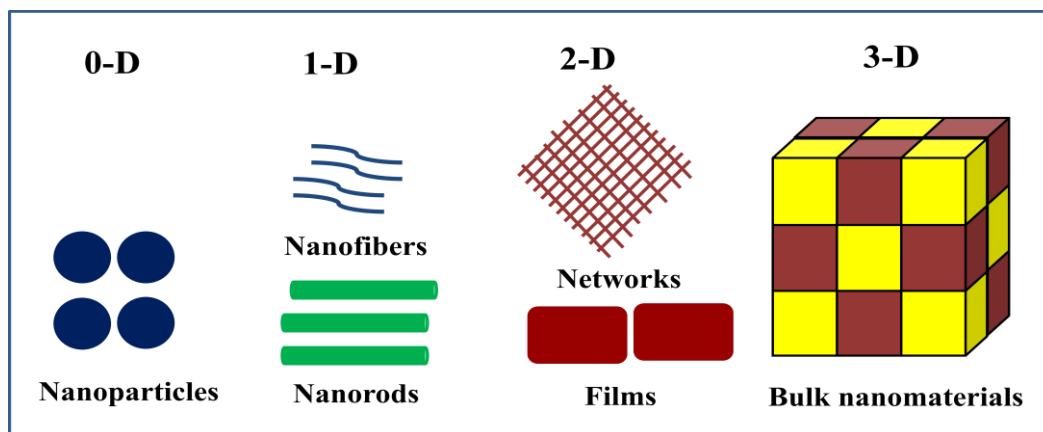


Figure1.2: Schematic presentation of different dimensional nanomaterials according to their dimension.

1.3.1 Zero Dimensional (0-D)

The zero dimensional nanostructures and nanomaterials are defined as those in which all the three dimensions are less than 100 nm. Basically, these nanomaterials have nano-dimensions in all the three directions. Nanoparticles are the common representations of zero-dimensional nanomaterials. Metallic nanoparticles and semiconductor such as quantum dots are the ideal example of this kind of nanomaterials.

1.3.2 One Dimensional (1-D)

In these nanomaterials, one of the dimensions of the nanostructured materials will be more than the nanometer range. One dimensional nanomaterials include nanowire, nanorod and nanotube. These materials are of several micrometers in length, but

having diameter of only a few nanometers. Nanowires and nanotubes of metals, metal oxides and other materials are few examples of this class of materials.

1.3.3 Two Dimensional (2-D)

In case of 2-D nanomaterials, two dimensions are outside the nanometer range. 2-D nanomaterials exhibit plate-like shape. This type of nanomaterials includes nanofilms, nanoplatelets, nanolayers and nanocoatings. The area of the nanofilms can be large (micrometer range), but the thickness is always at the nanoscale level.

1.3.4 Three Dimensional (3-D)

All the dimensions of three dimensional materials are beyond the nanometer range. In this type of nanomaterials, it includes bulk materials composed of the individual building block that lies in the nanometer range.

1.4 Important Usage of Metal and Metal Oxide Nanoparticles

The earliest confirmation of the use and application of nanomaterials can be ascertained by the use carbon nanotubes or cementite nanowires found in the microstructure of wootz steel manufactured in ancient India from the time period of 600 BC and exported globally.³⁰ The extraction of gold started in the 5th millennium B.C. in Bulgaria, but the applications of this material were considered in the 5th century B.C. in Egypt and China.³¹ The word ‘Nano’ for common people is just a very tiny little object. Although the word nanotechnology was introduced relatively recently, mankind has known and used the properties of such materials few years back without actually knowing the origin of their fascinating properties. Luster caused by a metallic film was used to the transparent surface of a glazing, which contains silver and copper NPs dispersed homogeneously in the glassy matrix of the ceramic glaze. The artisans fashioned these NPs by incorporating copper and silver salts and oxides together with vinegar, ochre and clay on the surface of previously-glazed pottery.³²⁻³³

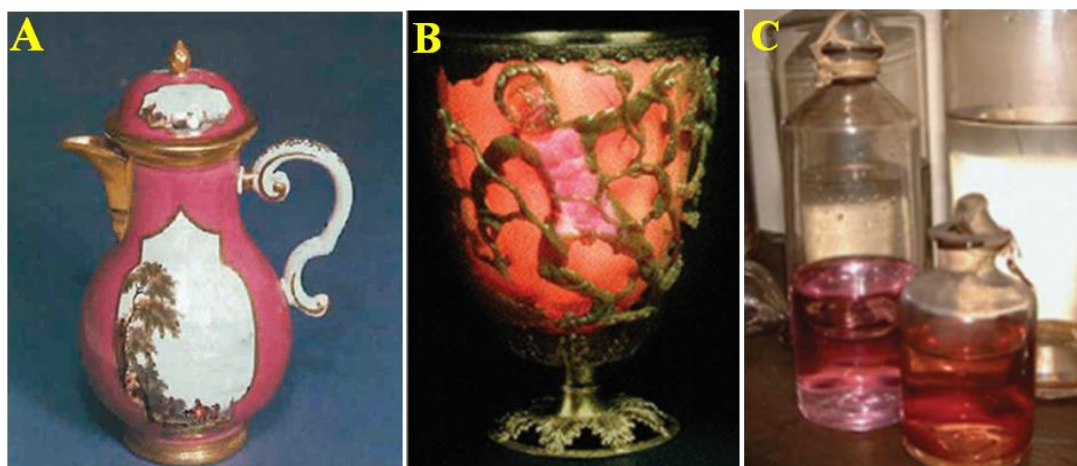


Figure 1.3: (A) Porcelain jug made at Meissen, Germany in about 1740. The Red colour of the decoration is due to the presence of gold NPs in the glaze. The same colour is seen every day by the users of diagnostic tests in which gold NPs render trace amounts of target molecules visible to the naked eye. Picture courtesy of the Victoria and Albert Museum, London. (B) Lycurgus cup and (C) a display of colloidal solutions of gold made by M. Faraday at the Royal Institution (Picture taken from Google).

Until the middle ages, the soluble gold was used to reveal fabulous curative powers for different diseases, such as heart and venereal problems, dysentery, epilepsy, tumors and for diagnosis of syphilis. The optical properties of gold sols have attracted interest ever since the Romans began to utilize them as colorants in glasses, which were called as ‘Purple of Cassius’. By the beginning of the 18th century, gold NPs were also used as a pigment in the decoration of porcelain (Figure 1.3A) and metalwork. Their use spread from Europe to China where they were applied in the characteristic pink glaze of Family-Rose porcelain during the Qing dynasty. Again, gold has also been withdrawn attention of many alchemists. An attractive ancient bowl (Lycurgus bowl (Figure 1.3B), created on 4th century AD) set aside in the British museum that shows some remarkable optical properties.³⁴ It changes colour with a change of source of the light. The green of bowl appears in normal light and becomes red in illuminated light. It is realized nowadays that this unusual property of colour change of the bowl is due to colloidal gold particles present in the bowl. The famous chemist and physicist Michael Faraday had prepared such gold NPs to study their interactions with light and had named them as “divided states of the metals”.³⁵⁻³⁶ In

1857, he reported the formation of deep red solution of colloidal gold by reduction of aqueous solution of chloroaurate (AuCl_4^-) using phosphorus in CS_2 (a two-phase system). Figure 1.3C displays of colloidal solution of gold made by M. Faraday at the Royal Institution. He also examined the optical properties of thin films prepared from dried colloidal solutions and observed reversible colour change of the films from bluish-purple to green upon mechanical compression. In 1861, the term ‘colloid’ (from the French, colle) was introduced shortly thereafter by Graham. In 1908, G. Mie first introduced his legendary theory to explain the red colour of the gold nanoparticles in solution.³⁷ The colour variation of colloidal gold with reference to its size motivated Mie to apply the general theory of light extinction for tiny particles. Mie’s idea about the study of the optical properties of gold clusters with sizes below the resolution limit of light microscopes took about 50 years for its realization. This idea has guided to the advancement of a new field of cluster science and has grown the subject of immense investigation as the time progresses.

Prof. Richard Feynman, a Nobel laureate in physics and Professor of Californian Institute of Technology, inaugurate (1959) the field of nano in his lecture called “There is plenty of room at the bottom” wherein he explained first insight into the possibility of creating nanosized materials by using atoms as building blocks.³⁸ However, the term “nanotechnology” was first defined by Norio Taniguchi in 1974 at the international conference on industrial production in Tokyo.³⁹⁻⁴¹

Since the days of Michael Faraday, metal NPs have been fabricated by chemical reduction of corresponding metal salts by appropriate reducing agents such as sodium citrates, borohydride, aldehydes, alcohols, di-ketones, sugars etc.⁴²⁻⁴⁶ Later, Turkevich and Nord had performed extensive studies and synthesized Pd NPs and used them efficient catalysts.^{48,49} To obtain Au NPs of prechosen size (between 16 and 147 nm) via their controlled formation, a technique was proposed by Frens in 1973, where the ratio between the reducing/stabilizing agents and metal (the trisodium citrate-to-gold ratio) was varied.⁴⁹ Toshima *et al.* invented the alcohol reduction process to prepare metal colloids in presence of protective polymers.^{50,51} Murphy *et al.* also prepared Au nanorods by a seeding growth approach in the presence of an aqueous miceller template.⁵²

Transition metal oxides are significantly important for developing new materials with functionality and smartness.⁵³⁻⁵⁸ In particular, transition metal oxide NPs and their assemblies have been widely used in a variety of fundamental research and technological applications because of their unique material properties and potential for desired nanostructures.⁵⁹⁻⁶² The unique properties of these materials are associated to the presence of elements with mixed valences of transition elements. As a result, it is not astonishing that long-term endeavours have determined on the synthesis of monodisperse metal oxide NPs and their exploitation as convenient nanobuilding blocks in constructing ordered superlattice assemblies with advanced functions.⁶³⁻⁶⁵ Manganese is the 11th most abundant element in the Earth's crust, and it has considerable significance in natural aquatic systems. Manganese oxide minerals have been utilized for thousands of years by the ancients for pigments and to clarify glass, and today as ores of Mn metal. During the last few decades, nanoscale manganese oxide particles are gaining increasing potential applications in diverse areas, including rechargeable lithium ion batteries, catalysis, molecular adsorption, gas sensors, energy storage, and magnetics. They gain considerable concern in many technological applications, such as electrochemical reaction and batteries, due to their outstanding structural flexibility combined with novel chemical and physical properties.⁶⁶⁻⁶⁹ Their performance is highly dependent on their morphology as well as crystallographic forms. Manganese oxide NPs are expected to demonstrate better properties compared to their bulk counterparts owing to a larger surface-to-volume ratio that would lead to an improved capacity in absorbing oxygen for oxidation of carbon monoxide and nitrogen.⁷⁰⁻⁷² Several routes have been developed for the fabrication of manganese dioxide (MnO₂) NPs, nanorods and nanowires of α -, β -, γ -, and δ -MnO₂.⁷³ In recent time, α -MnO₂ core-shell structure with spherically aligned nanorods was synthesized by Xie and co-workers.⁷⁴ Sun *et al.* have also reported the preparation of MnOOH and β -MnO₂ whiskers using cationic surfactant cetyltrimethylammonium bromide and so on.⁷⁵

Iron is the fourth most abundant element and the second most abundant metal, after aluminium, in the Earth's crust. Therefore, it stands as the backbone of current infrastructure. Over half of the total iron content in the body is found within erythrocytes as a constituent of heme, which acts as the fundamental porphyrin

prosthetic group of haemoglobin that helps O₂ transport.⁷⁶ However, in comparison to the transition elements, such as cobalt, nickel, gold and platinum, iron oxides are to some extent neglected.⁷⁷ Iron (III) oxide exists in the form of rust in nature.⁷⁸ Usually, iron oxides are widely used as they are inexpensive and play a very important role in many biological and geological processes. They are also extensively used by humans, e.g.; as iron ores in thermite, catalysts and durable pigments. Three most general forms of iron oxides in nature are magnetite (Fe₃O₄), maghemite (γ -Fe₂O₃) and hematite (α -Fe₂O₃). Due to their low toxicity, superparamagnetic properties and simple separation methodology, iron oxide nanomaterials have received much attention and are particularly interesting in biomedical applications for protein immobilization, such as diagnostic magnetic resonance imaging (MRI), thermal therapy and drug delivery.⁷⁹ Liu *et al.* have reported the synthesis of ultrathin γ -Fe₂O₃ nanostructures (NSs) with merits of large surface area and quick magnetic response at external low magnetic field as well as abundant surface hydroxyl groups.⁸⁰ In addition, Fe₂O₃ NSs such as nanorods, nanowires, nanobelts, and nanotubes have also been prepared and utilized for investigating their peculiar properties.⁸¹⁻⁸⁴ Zhang *et al.* managed to produce α -Fe₂O₃ nanowires out of the oxidized surface of iron substrates.⁸⁵ Woo *et al.* fabricated α -Fe₂O₃ nanorods by a sol-gel mediated reaction of ubiquitous Fe³⁺ ions in reverse micelles.⁸⁶ Recently, Fe₂O₃ hollow nanowires with outer diameters of 50 nm have been prepared through a vacuum-pyrolysis route from α -FeOOH nanowires.⁸⁷ Nevertheless, it still remains a challenge to develop simple and versatile approaches to synthesize nanostructures of metal or metal oxide, which will facilitate their shape and size-dependent properties.

1.5 Quantum Dots

The nanomaterials in which the carriers (electrons and holes) are confined within the nanometer sized region in all three dimensions are called quantum dot. All material systems including metal, insulators and semiconductors show size dependent optical or electronic properties in the quantum size regime. The term quantum dot is more commonly used for the semiconductor nanostructures and has been most attracted to the researcher for the last few years due to their novel electronic, optical, magnetic

and catalytic properties.^{88,89} The number of atoms in a quantum dot, ranging from 1000 to 100000, assemble in it neither as an extended solid structure nor a single molecular entity. When dimension of a material is reduced from macroscopic size to nanometer size, the physical and chemical properties of the material drastically change. The electrons in quantum dots have an energy range. Excitons have an average physical separation between the electron and hole, known as the Exciton Bohr Radius, this physical distance is different for each material. The dimensions of the semiconductor bulk materials are much larger than the Exciton Bohr Radius, permitting the exciton to extend to its natural limit. If the size of a semiconductor material becomes too small that it approaches to the size of the material's Exciton Bohr Radius, then the electron energy levels can no longer be treated as continuous, they must be treated as discrete, i.e., there is a small and finite separation between energy levels. This phenomenon of discrete energy levels is called quantum confinement and under this situation, the semiconductor material is known as quantum dot.^{90,91} Generally the physical sizes range of this class of materials range from 1 to 10 nm.

The presence of a widely tunable energy band gap causes a semiconductor to emit light when excited by a radiation of enough energy. Quantum dots with tunable energy band gap are considered to be the materials for next generation photovoltaic, optoelectronic devices, laser, photonic band gap devices and sensors. As a result of quantum size effects, the band gap of the semiconductor materials increases and at the edges of the valence and conduction band discrete energy levels occur. Since to the electron energy levels in quantum dots are discrete rather than continuous, the addition or subtraction of just a few atoms to the quantum dot has enough impact of altering the boundaries of the band gap. The change in geometry of the surface of the quantum dot also tunes the band gap energy owing again to the small size of the dot and the effect of quantum confinement. The size of the band gap can be regulated simply by adjusting the size of the quantum dot as shown in Figure 1.4. Their ability to absorb a broad range of wavelengths produces them useful for solar cell applications.⁹² The larger the band gap of a solar cell semiconductor, helps the more energetic the photons to be absorbed, and causes the larger the output voltage.

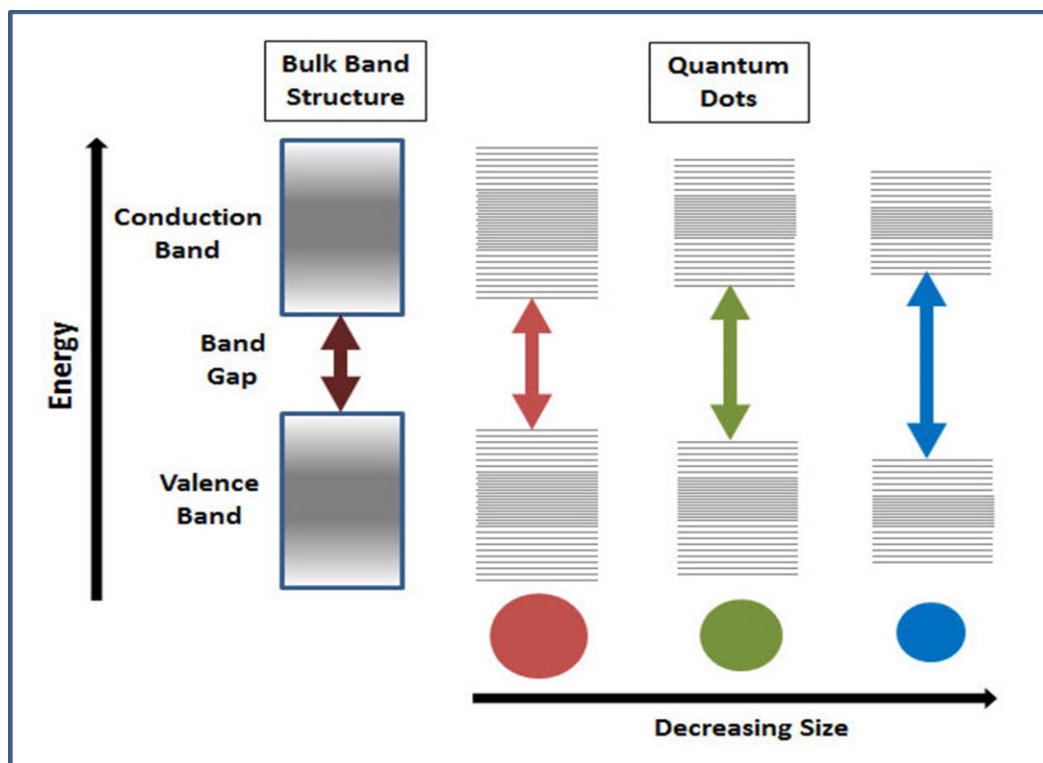


Figure 1.4: Splitting of energy levels in quantum dots due to the quantum confinement effect. Band gap in semiconductor increases with decrease in size of the nanocrystal. [Source: www.sigmaaldrich.com/technical-documents/articles/materials-science/nanomaterials/quantum-dots.html]

Conversely, a low band gap results in the capture of more photons including those in the red end of the solar spectrum, resulting in a greater output of current but at a lesser output voltage. Therefore, there is a need of an optimum band gap to achieve maximum possible solar-electric energy conversion. This can be obtained by using a combination of quantum dots of different sizes for harvesting the greatest proportion of the incident light. The change in the band gap energy of the quantum dot with size alters in their light absorption spectra. When quantum dots are excited by a radiation of sufficient energy, fluorescence spectra would shift to the lower wavelengths as the size of the quantum dot decreases which in turn causes an increase in the band gap of the quantum dot. This shift of wavelength to lower region is known as blue shift. Due to the blue shift in the absorption spectrum with decrease in size, the colour of quantum dots shifts from red to green.⁹³ Thus the different coloured emission can be observed from the same material. These quantum dots of same material can be applied

for the fabrication of LEDs having emission over the whole visible spectrum. Semiconductors receive their great importance from the fact that their electrical conductivity can be significantly changed by an external stimulus (voltage, photon flux, etc), producing semiconductors critical parts of different kinds of electrical circuits and optical applications.⁹⁴ Optical properties of the quantum dots can be simply tuned with the particle size.⁹⁰ These size dependent optical properties have lots of prospective applications in the areas of chemical, biological, solar energy conversion, light emitting devices, photocatalysis and sensors.⁹⁵

1.6 Nanoparticle Synthetic Strategies

Producing nanoparticles is an enormous technological challenge to the researcher since controlled synthesis of NPs is their not only significant for diverse applications but also properties of these materials depend on their size, shape, morphology and stoichiometry.⁹⁶ The commonly used approach for the synthesis of nanostructure materials is divided into two categories; top-down (physical method: size reduction from bulk materials) and bottom-up (chemical method: material synthesis from atomic level) methods.⁹⁷ A schematic presentation of the ‘top-down’ and ‘bottom-up’ approaches is shown in Figure 1.5. Top down approach mainly starts with a bulk material and then it breaks into smaller pieces using mechanical, chemical or other form of energy. In contrast, bottom-up approach begins to synthesize the material from atomic or molecular species via chemical reactions, allowing the precursor particles to grow in size, in some cases through smart use of self-organization. At the present time, the research interest has been focused towards the development of a reproducible synthetic strategy for the transition metal colloids. The synthesis parameters must fulfil the following conditions: (a) formation of identical NPs every time, i.e.; same size and shape; (b) NPs should have similar morphology; (c) the same crystal and chemical bonding take place on the surface or inside the NPs and (d) the fabrication process must be reproducible. If any synthesis procedure meets all these four criteria, it is then considered a reliable technique for the synthesis of nanostructure materials. In this regard, top-down method produced NPs having wide size distribution with comparatively larger size with inconsistent catalytic activity.⁹⁸

Alternatively, bottom-up methods are the most suitable ways to control the size of the particles. There are a number of methods that in the future might improve the quality of the nanostructures. A promising approach is the combination of top-down and bottom-up methods, where the smallest NPs achieved by bottom-up methods can be controlled and interconnected by lithographical technique to make it a very interesting route.⁹⁹

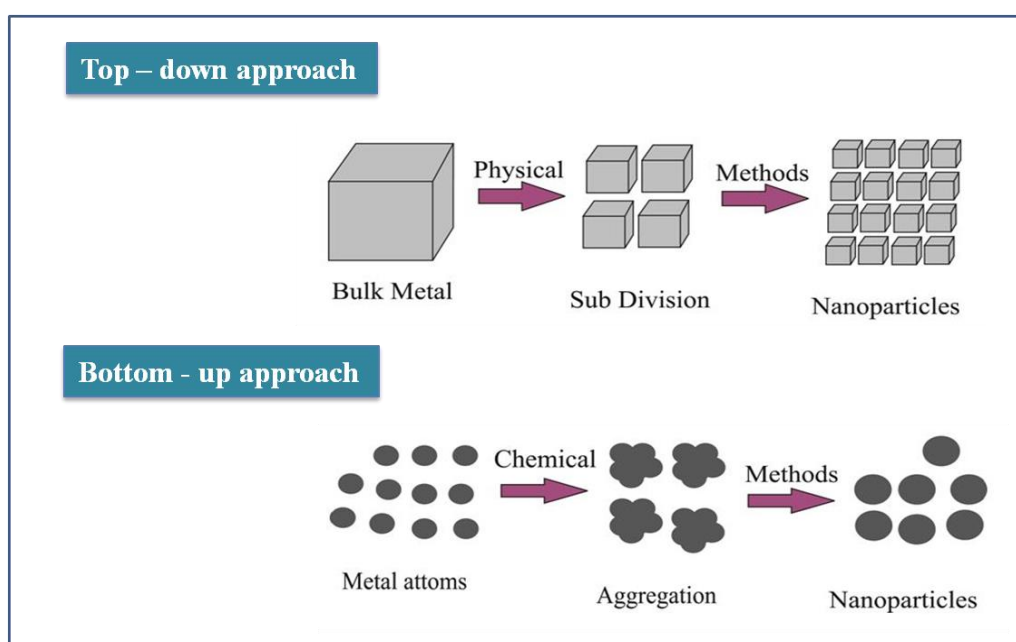


Figure 1.5: Schematic representation of the top-down and bottom-up approaches.

1.6.1 Top-Down Approaches

Top-down approach being an engineering of fabrication technique can produce a variety of materials with numerous of shapes and sizes.¹⁰⁰ This technique includes in the typical solid-state processing of the materials. This method is based on the breaking up larger particles to form smaller ones by the use of physical processes. One popular top down method is milling, where larger size materials are steadily milled down until NPs are formed. This method is simple as well as straightforward and can synthesize NPs ranging from several micrometers to few nanometers. However, the biggest drawback of this method is the formation of a wide range of particle sizes and shapes. In addition, there can be considerable levels of impurities

produced as a result of the milling medium. Therefore, NPs produced by this method can only be used in those applications which do not need a specific particle size or shape. Several well established top down methods, such as near-IR laser irradiation,^{101,102} thermolysis,¹⁰³ photolithography,¹⁰⁴ sonolysis,^{105,106} radiolysis^{107,108} have been adopted for the fruitful preparation of metal NPs in a variety of environments. In recent time, lithographic methods (such as laser-beam lithography, electron-beam lithography etc.) are being applied for the manufacture of well-defined size and non-spherical nanoparticles.¹⁰⁹⁻¹¹¹ Nanosphere lithography is the second generation innovation technique, generally known as natural lithography, which is an inexpensive nanofabrication technique and is now being used in laboratories around the world. It is well known to all that the conventional top-down method can cause significant crystallographic damage to the processed materials.

1.6.2 Bottom-Up Approaches

The bottom-up methods are widely been utilised than top down methods for the fabrication of nanoscale materials. In bottom-up methods, the atoms and molecules are assembled into the smallest nanostructures by cautiously controlled the chemical reactions. This method is very common for the synthesis of metal NPs through the chemical reduction of metal salts. This method is often utilised for preparing most of the nano-scale materials as it has the ability to produce a uniform size, shape and distribution. This route often resembles a "seed" model, where the beginnings are small but finally grow in complexity and completeness. It successfully covers chemical synthesis and precisely controls the reaction to inhibit further particle growth. This has been divided into two major types, one is photochemical and another is wet chemical reduction. Photochemical method usually involves production of metal NPs from specific metal precursor by means of photo-irradiation techniques.¹¹²⁻¹¹⁵ The photo-generated radicals is the efficient reducing agent for the transformation of metal ions to the corresponding atoms. Hydrated electrons and radicals generated in-situ by photolysis, radiolysis or electrolytic process can also reduce solute ionic moieties to produce nanoparticles.¹¹⁶ Conversely, An aqueous solution of ionic metal salt is reduced to its corresponding atom in wet chemical method by an appropriate

medium in the presence of surfactant using reducing agents like sodium borohydride,¹¹⁷ hydrazine hydrate,¹¹⁸ sodium citrate,¹¹⁹ alcohols,¹²⁰ di-ketones,¹²¹ aldehydes,¹²² sugars^{123,124} etc. Here, a capping agent or stabilising agent is also used to stabilise the NPs. The advantages of this method are the following; it can be performed at ambient condition, NPs can be synthesized using general laboratory equipment and can be easily scaled up the quantities. Hence, bottom up method promises a better chance to acquire NPs with fewer defects and more homogeneous chemical composition together with it plays an important role in fabricating and processing of nanomaterials.

1.7 Stabilization of Nanoparticles

Transition metal NPs have been utilised as catalysts for a variety of organic reactions because of their outstanding catalytic activity. Size, shape and surface morphology play pivotal roles in controlling the physical, chemical, optical and electronic properties in case of metal and metal oxide NPs. Fabrication of NPs usually involves reduction of metal ions in solution or in high temperature gaseous environment. The large surface energy of these particles makes them enormously reactive and most of the systems undergo aggregation without protection or passivation of their surfaces.¹²⁵⁻¹²⁹ The commonly applied methods for surface passivation include protection by self-assembled monolayers, thiol-functionalized organics,¹²⁶ encapsulation in H₂O pools of reverse microemulsions¹³⁰ and dispersion in polymeric matrixes.¹³¹ Moreover, NPs tend to aggregate or coagulate which leads to the significant decrease in their catalytic activity. Therefore, in order to prevent the aggregation of particles, they need to be stabilized using some stabilizers. The stabilization of metallic colloids to conserve their finely dispersed state is an essential feature, which must be considered during their synthesis.¹³²⁻¹³⁴ At a short interparticle distance, the van der Waals forces attract two colloidal metal particles to each other. In the absence of repulsive forces opposed to the van der Waals forces, the aggregation of colloidal metal particles occurs. The choice of stabilizer is vital while synthesizing metal NPs. Consequently, the use of a stabilizing agent that can induce a repulsive force opposed to the van der Waals force is required to give stable NPs in

solution.¹²⁹ In general, the stabilizers' roles are (i) prevention of uncontrollable growth of particles, (ii) prevention of particle aggregation, (iii) control of growth rate, (iv) control of particle size and (v) allowing particle solubility in various solvents.¹³⁵ Based on the nature of protective agents used, stabilization procedures can be classified as: (i) electrostatic stabilization, (ii) steric stabilization, (iii) the combination of these two kinds of stabilization, electrosteric stabilization, (iv) stabilization by a ligand and (v) stabilization by dendrimers.

1.7.1 Electrostatic Stabilization

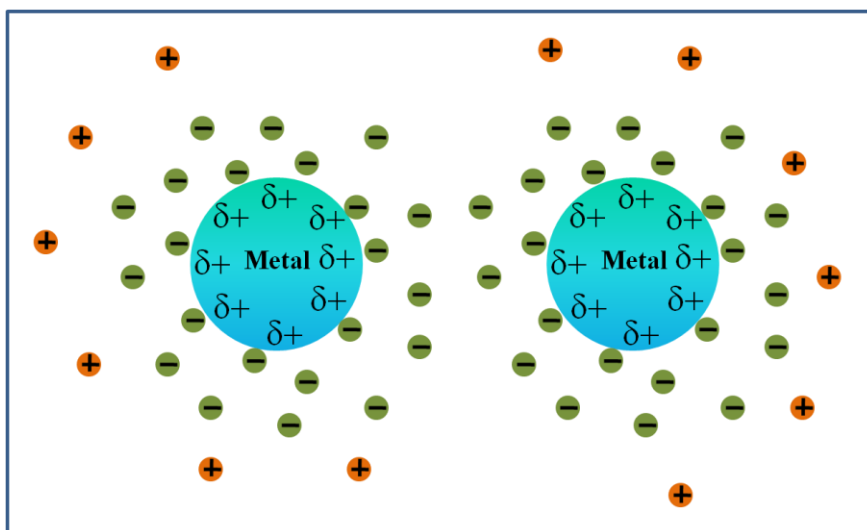


Figure 1.6: Schematic representation of the electrostatic stabilization in metal nanoparticles.

The stabilization of metal NPs can be achieved by means of electrostatic stabilization. The source of electrostatic stabilization is the repulsive electrostatic force. Electrostatic stabilization involves the generation of an electrical double layer arising from ions adsorbed onto the particle surface and associated counter ions that surround the particle in the dispersing media. Therefore, if the electric potential associated with the double layer is adequately high, coulombic repulsion between the particles will protect their agglomeration. Ionic compounds, such as halides, carboxylates, or

polyoxoanions, dissolved in aqueous solution can produce the electrostatic stabilization. The adsorption of these molecules and their related counter ions on the metallic surface creates an electrical double-layer around the particles (Figure 1.6), resulting in a Coulombic repulsion between the particles that prevents the aggregation of the particles.^{136-138.}

1.7.2 Steric Stabilization

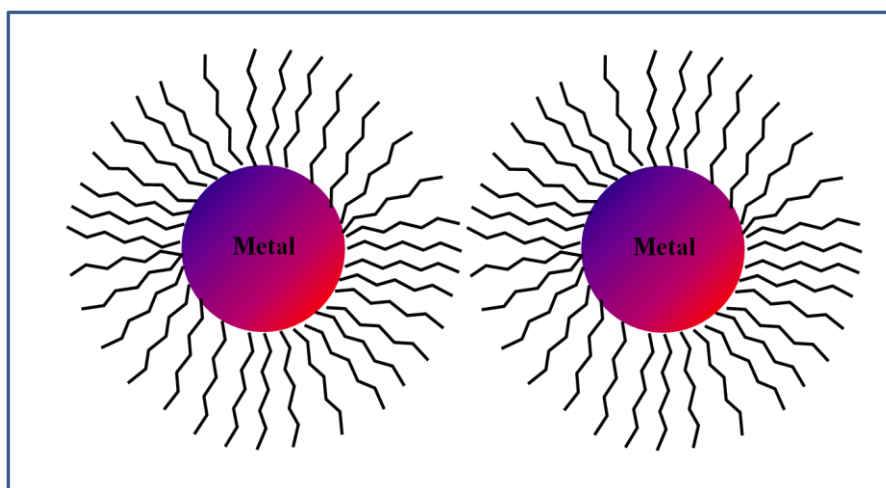


Figure 1.7: Schematic representation of the steric stabilization in metal nanoparticles.

Another stabilization process is based on the steric repulsion between molecules or ions adsorbed on adjacent particles. Basically, steric stabilization of colloidal particles occurs due to the adsorption of macromolecules to the surfaces of the particles (Figure 1.7). Metal colloid particles can be prevented from aggregation by steric stabilization, using macromolecules, such as polymers, oligomers etc.¹³⁹ Chemical nature and size of these molecules decide the degree of stabilization of the particles. Due to geometric constraints around NPs, large or bulky molecules generally give an effective stabilization. At interparticle space, adsorbed molecules get restricted in motion, resulting in decrease in entropy and an increase in free energy. In contrast to the electrostatic stabilization, which is mainly used in aqueous media, the steric

stabilization can be utilised both in organic and aqueous phase. Strongly adsorbing large molecules are prime candidates for stabilization of particles. Most commonly used polymers include PVP,¹⁴⁰⁻¹⁴⁴ polyacrylate,¹⁴⁵⁻¹⁴⁷ polystyrene^{148,149} etc. The bulky groups of these molecules will produce a protective layer around the surface of NPs thereby preventing the aggregation of the particles. The concept of steric stabilization plays a significant role in the successful synthesis of metal NPs.

1.7.3 Electrosteric Stabilization

Electrostatic repulsion is sensitive to the added electrolyte, whereas steric repulsion is sensitive to the change in the solvency and molar mass of the adsorbed polymer layer. In most of the time, both electrostatic and steric effects impart stability to the dispersion, which in turn forms stable metallic NPs in solution.¹⁵⁰ This kind of stabilization can be provided by the use of ionic surfactants, such as polyoxoanions.^{151,152} These compounds have a polar head group that creates electrical double layer and the lyphophilic side chain give steric repulsion as shown in Figure 1.8. Surfactant like ammonium (Bu_4N^+)/polyoxoanion has bulky ammonium counter ions with a highly charged polyoxoanions that provide efficient electrosteric stability and thus prevent agglomeration of the resultant NPs in solutions.¹⁵⁰⁻¹⁵²

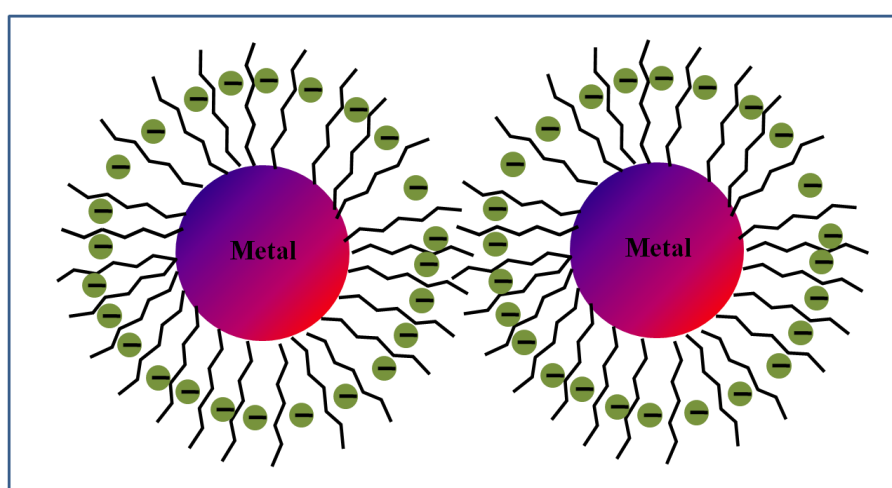


Figure 1.8: Schematic representation of the electrosteric stabilization in metal nanoparticles.

1.7.4 Stabilization by Ligand

One of the most frequently employed stabilizers for metal NPs is the ligand, as shown in Figure 1.9. This type of stabilization for the protection of various metal NPs can be achieved by the use of ligands, such as phosphines,¹⁵³⁻¹⁵⁵ thiols¹⁵⁶⁻¹⁵⁸ or amines¹⁵⁹ etc. This type of stabilization occurs by the coordination of ligand molecules to the metal NPs. It has recently been reported that solvent molecules can also stabilize the NPs more efficiently.¹⁶⁰ Several NPs were prepared in tetrahydrofuran or thioethers without adding steric or electrostatic stabilizers.^{161,162}

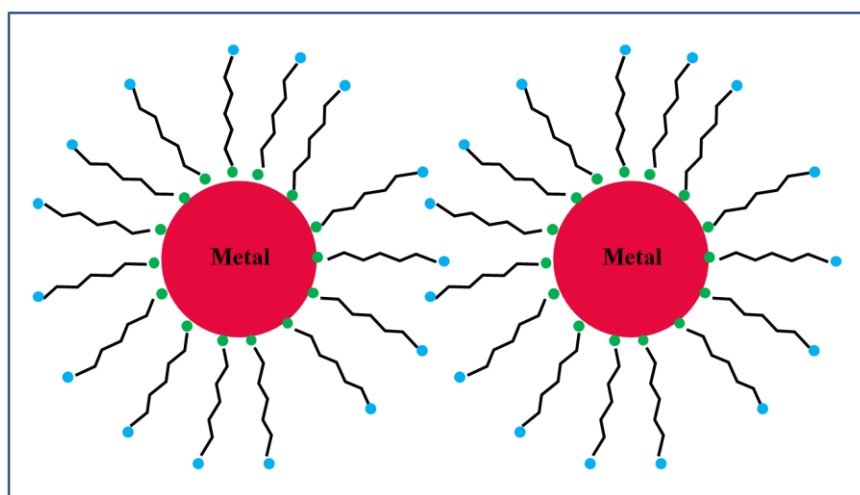


Figure 1.9: Schematic representation of the stabilization by ligand in metal nanoparticles.

1.7.5 Stabilization by Dendrimers

Dendrimers are a type of polymeric materials that are extremely branched monodispersed macromolecules. Dendrimers become densely packed as the chain grows and produce a closed membrane-like structure shown in Figure 1.10. It is also used as stabilizer to synthesize metal NPs.¹⁶³⁻¹⁶⁹ Most commonly used dendrimers contain PAMAM poly(amido amine)¹⁶⁸ and PPI poly(propylene imine) dendrimers.¹⁶⁷ The NPs prepared in presence of dendrimers do not agglomerate and are stabilized by encapsulation within the dendrimers. Dendrimers demonstrate a significant role in the stability and catalytic activity exhibited by the encapsulated NPs.

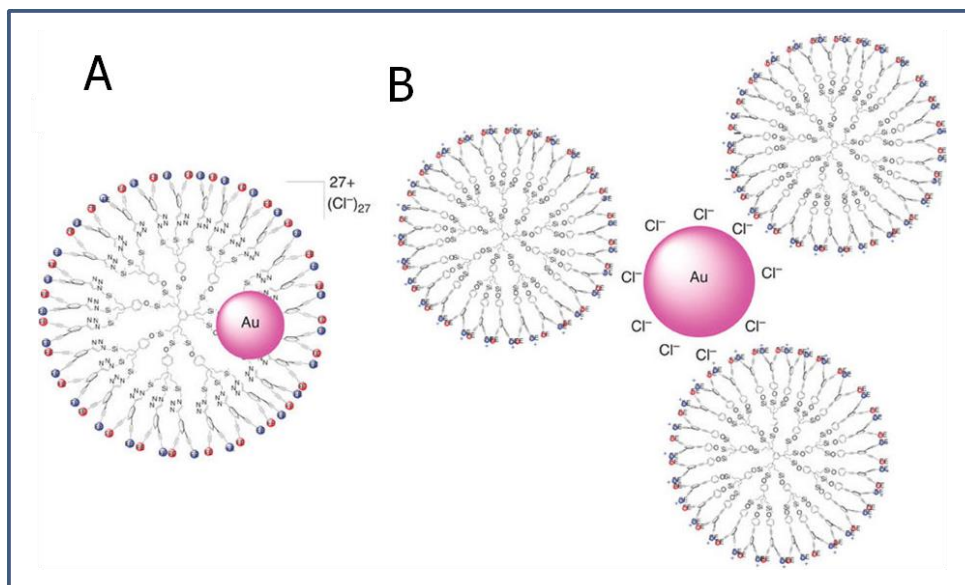


Figure 1.10: Schematic representation of the stabilization of Au NP by dendrimers. (A) Intradendritic Au NP stabilization by a ‘click’ dendrimer $6B^{27+}$ involving Au NP-triazole interactions. (B) Interdendritic stabilization by many ‘Sonogashira’ dendrimers $6A^{27+}$. Chloride anions surround the Au NPs in both cases.¹⁶⁹

1.8 Important Properties of Nanoparticles

Nanoparticles are made up of clusters of atoms, hence they have an intermediate size between a single atom and the bulk material. They also have the structural features in between of those atoms and the bulk materials. On contrary, microstructured materials have analogous properties to the corresponding bulk materials. The properties of materials with nanometer dimensions are drastically different from those of atoms and bulk materials. This is mainly due to the typical nanometer size of the materials which provide them: (a) large fraction of surface atoms, (b) high surface energy, (c) spatial confinement and (d) reduced imperfections. This type of special feature does not exist in the corresponding bulk materials.

1.8.1 Surface Properties

The most technologically relevant property of NPs is their large surface to volume ratio. If a bulk material is divided into individual NPs, the reduction in particle size

from the bulk to nano is accompanied with the increase in surface area without any change in volume, as shown in Figure 1.11 and Table 1.1. Therefore, there is a considerable increase in the surface to volume ratio (S/V). Increased S/V ratio is mainly significant for applications where the surface of the material is a functional and essential entity to acquire a good performance. For surface chemistry, the chemical groups which are present at the surface of a material and its environment are the key factors in determining the properties such as chemical reactivity, decrease of melting temperature, adhesion, gas storage, catalytic activity etc. In case of NPs, due to the exposure of large number of atoms, the surface is extremely reactive than their bulk counterparts. Now consider radius of a spherical particle is r , then surface area (S) of the particle will be $4\pi r^2$ and volume (V) of the particle becomes $(4/3) \pi r^3$. Thus, the surface to volume (S/V) ratio is $(3/r)$. Basically, the surface to volume ratio is inversely proportional to radius of the particles (r). With the decrease in the particle size of the materials, the surface effects of the materials turn into more prominent. Because of the high surface to volume ratio of the NPs, they are usually unstable and the tendency of small NPs is to agglomerate and finally produces larger particles in order to diminish their surface energies. As a result, diverse methods are adapted to minimize their energy to attain a low energy state. The most widespread example of improved surface activity of NPs is nano-catalyst because of its high reactive nature.^{170,171}

1.8.2 Optical Properties

In addition to the surface chemical properties, another most attractive and valuable aspect of NPs is their optical properties. Application of nanomaterials based on their optical properties includes optical detector, laser, sensor, imaging, solar cell, photocatalysis, photoelectrochemistry and biomedicine. The optical properties depend on the size, shape, surface characteristics and other variables including doping and interaction with the surrounding environment of nanomaterials.

Size and shape have extraordinary influence on the optical properties of metal nanostructures. If the size of a material is reduced to nanoscale level, the material may

act differently with completely new properties. We know the eminent golden colour of gold ornaments. The change in the colour of gold NPs with the particle size is shown in Figure 1.12A. A lot of shapes of noble metal NPs have been prepared,¹⁷²⁻¹⁷⁷ like nanospheres, nanorods, nanocubes, nanowires, nanooctahedra etc. Nanorods

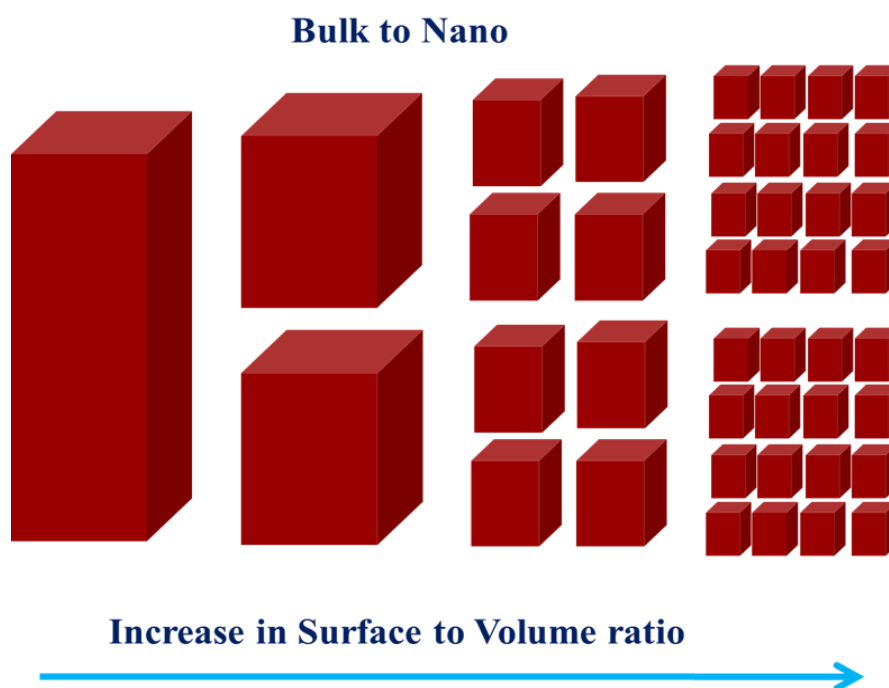


Figure 1.11: Schematic representation of bulk to nano, demonstrating high surface to volume ratio with decrease in size of the materials.

Table 1.1: Increase in the surface area with decrease in size of the cubes.

Size of the cube side	Number of cubes	Collective surface area
1 m	1	6 m ²
0.1 m	1000	60 m ²
0.01 m = 1 cm	10 ⁶	600 m ²
0.001 m = 1 mm	10 ⁹	6000 m ²
10 ⁻⁶ m = 1 μm	10 ¹⁸	6×10 ⁶ m ² = 6 km ²
10 ⁻⁹ m = 1 nm	10 ²⁷	6×10 ⁹ m ² =6000 km ²

have attracted the most attention, because of the ease of preparation, availability of the large number of synthetic methods, high monodispersity and the easy control over the aspect ratio, which is mainly responsible for the alteration of their optical properties.¹⁷⁷⁻¹⁸⁰ Nanorods demonstrate two plasmon resonances,¹⁸¹ one due to the transverse oscillation of the electrons around 520 nm for gold and the other due to the longitudinal plasmon resonance at longer wavelength. Figure 1.12B represents absorption spectra of gold nanorods having varied aspect ratios. The transverse surface plasmon resonance does not depend on the aspect ratio of nanorods and is observed at the same wavelength as the plasmon resonance of spheres. On the other hand, longitudinal surface plasmon resonance depends on the aspect ratio of nanorods and increases as the aspect ratio increases. The anisotropy has been shown to have large control over the optical absorbance for all shapes.¹⁸² Thus, the plasmon resonance can be tuned across the visible region by altering the aspect ratio of the materials. The increase in the intensity of the surface plasmon resonance absorption leads to an enhancement of the electric field, which can be exploited in many applications in diverse field.

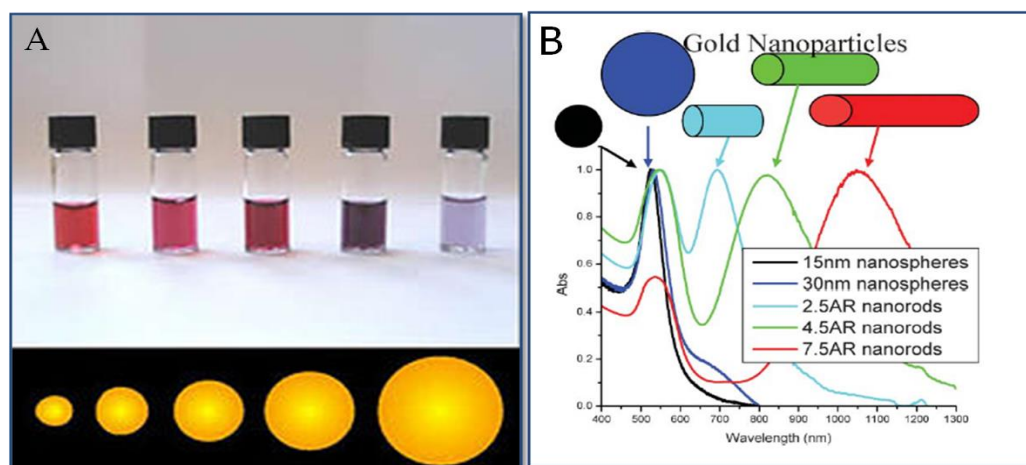


Figure 1.12: (A) Gold colloidal solutions with different colours corresponding to the different sizes of particles. (Source: https://en.wikipedia.org/wiki/Colloidal_gold) (B) Absorption spectra of various sizes and shapes of gold nanoparticles.¹⁸³

1.8.2.1 Origin of Surface Plasmon Resonance

Metal NPs display a strong absorption band in UV-visible region, which can be assigned to the surface plasmon resonance of the metal clusters. While a small spherical metallic NP is irradiated by light, the oscillating electric field makes the conduction electrons to oscillate coherently. This is schematically shown in Figure 1.13. If the electron cloud is displaced relative to the nuclei, a restoring force comes from Coulomb attraction between electrons and nuclei that results in oscillation of the electron cloud relative to the nuclear framework. The collective oscillation of the electrons is known the dipole plasmon resonance of the materials. The oscillation frequency is generally measured by the following factors: the density of electrons, the effective electron mass and the size and shape of the charge distribution. Higher modes of plasmon excitation can take place, such as the quadrupole mode where half of the electron cloud moves parallel to the applied field and other half moves anti-parallel. For a metal, like silver, the plasmon frequency is also influenced by the electrons present in d-orbital. This effect stops the plasmon frequency from being easily calculated by electronic structure calculations. On the other hand, it is not hard to relate the plasmon frequency to the metal dielectric constant, which is a property that can be determined as a function of wavelength for bulk metal.¹⁸² Basically, surface plasmon resonance is caused by the coherent motion of the conduction band electrons, which interact with an electromagnetic field. Thus, all the interactions are expected to be with the surface electrons of the materials. The frequency and width of the surface plasmon absorption depend on the size and shape of metal NPs, dielectric constant of the metal itself and the surrounding medium of the metal.¹⁸⁴⁻¹⁸⁶ With the change in shape or size of the nanoparticle, the surface geometry of the particles changes causing a shift in the electric field density on the surface. This induces a change in the oscillation frequency of the electrons, producing different cross-sections for the optical properties, including absorption and scattering. Changing the dielectric constant of the surrounding material also have an effect on the oscillation frequency due to the changing ability of the surface to accommodate electron charge density from the NPs. Changing the solvent will alter the dielectric constant, but the capping material is most significant in determining the shift of the plasmon resonance due to the local nature of its effect on the surface of the NPs. Chemically bonded molecules

can be detected by the change in the electron density on the surface of the materials, which results in a shift in the surface plasmon absorption maximum. This is the basis for the exploitation of noble metal NPs as sensitive sensors. Noble metals, such as copper, silver and gold have a strong visible light plasmon resonance, whereas most of the other transition metals show only a broad and weakly resolved absorption band in the ultraviolet region.^{187,188}

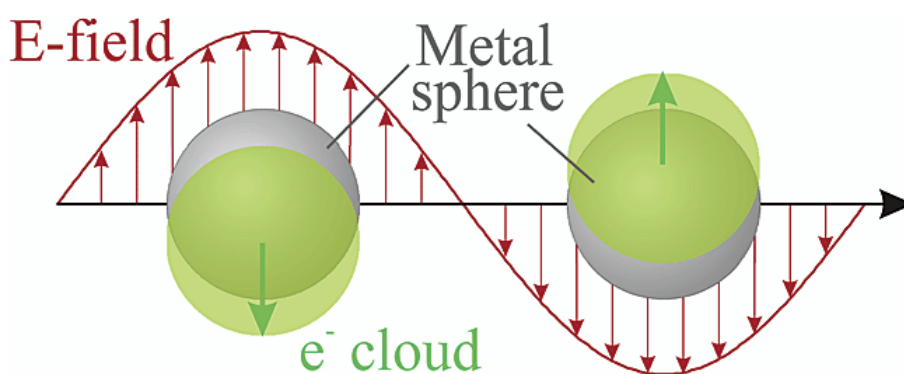


Figure 1.13: Schematic presentation of plasmon oscillation for a metal sphere, showing the displacement of the conduction electron charge cloud relative to the nuclei as a result of electromagnetic field.¹⁸²

1.8.3 Electronic Properties

The electronic properties of nanoscale metals, insulators and semiconductors have been extensively investigated as they originate interesting transport and optical phenomena. Nanomaterials exhibit some special electrical properties as well. At extremely small dimensions the energy levels are quantized and the band overlapping present in the bulk materials vanishes and a band gap is created or enhanced. Therefore, a few metals can behave as semiconductor. Semiconductor can behave insulators when their size is reduced. At a specific temperature, size dependant properties change significantly in semiconductors than that of metals, insulators, Van-der-Waal's crystals or molecular crystals. In every case, the density of the states is discrete at the band edges. With increasing size, the center of a band develops first and the edges arise last. In Van-der-Waals or molecular crystals, the nearest-

neighbour interactions are much weak and the bands in the solid are extremely narrow. As a result, size variation in optical or electrical properties is not expected that much nano regime. This kind of change in their properties occurs due to the systematic transformations in the density of electronic energy levels with respect to the size of the interior, which is called quantum size effects. Nanocrystals are in between the atomic and molecular limit of discrete density of electronic states and the extended crystalline boundary of continuous bands. Figure 1.14A represents the band structure of metals in bulk form, nano form and as atoms. Figure 1.14B demonstrates the density of states in semiconductor type materials.¹⁸⁹ The band gap is zero (valence and conduction bands overlap) and Fermi level coincides with the top of the filled band in case of metals.

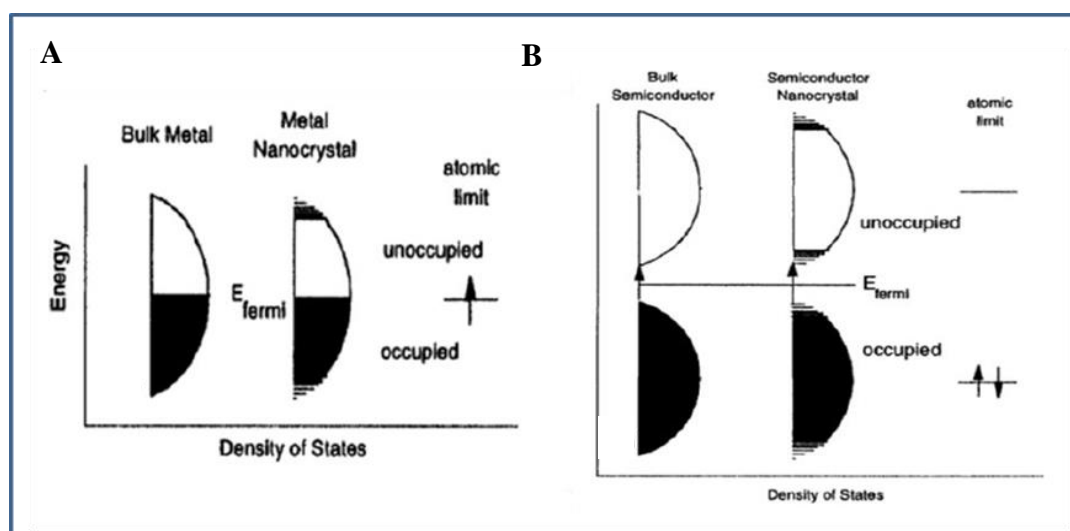


Figure 1.14: Density of states in (A) bulk metal, metal nanocrystals and atom; (B) in semiconductor.¹⁸⁹

In case of semiconductors, as the Fermi level lies between two bands, the edges of the bands dominate the low energy optical and electrical behaviour. The band gap of semiconductors increases with decreasing size, because of the reduction in the band width in the nano-regime, along with decrease in number of atoms and weakening of the adjacent neighbour interactions. This is the major effect observed in the semiconductor nanocrystal that causes an important change in their optical properties which are sensitive to the size of the materials.¹⁹⁰⁻¹⁹³ As the size of metal

nanocrystal decreases, they can demonstrate insulating behaviour owing to the alteration in their electronic structure. This transition is known as size-induced metal–insulator transition.

It is also possible to visualize simple geometric objects of differing dimensionality (2, 1, and 0), each case is associated with the homogeneous semiconductor material with ideal surface termination.¹⁸⁹ The schematic presentation of density of states for 3D, 2D, 1D and 0D was presented in Figure 1.15. Such type of structures should show the idealized variations in density of electronic states predicted by simple particle in a box model of elementary quantum mechanics, with the continuous levels of the 3D case evolving into the discrete states of the 0-D case.

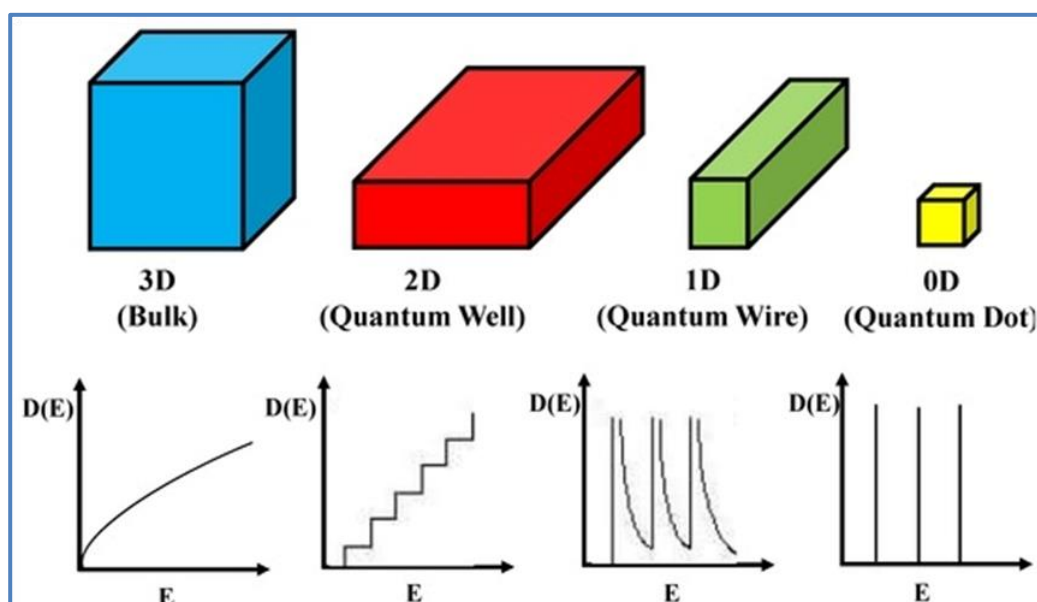


Figure 1.15: Schematic presentation of the density of states for 3D, 2D, 1D and 0D materials.¹⁹⁴

1.8.4 Mechanical Properties

Sometimes nanomaterials show typical mechanical properties, e.g.; tremendously high strength. It is known that mechanical properties usually depend on the density of dislocations, surface-to-volume ratio, chemical composition and grain size of a solid material. A decrease in grain size drastically changes the strength and hardness. One

of the most key applications of nanomaterials is their use in superplasticity, the capacity of a polycrystalline material to undergo extensive tensile deformation without necking or fracture. Grain boundary diffusion and sliding are the two essential criteria for superplasticity.¹⁹⁵ For example, single wall and multiwall carbon nanotubes are enormously stronger than steel due to their small size and lighter weight. These carbon nanotubes have honeycomb-like lattice structure of graphite. Usually the presence of defects or imperfections decreases the strength of the materials. Therefore, nanomaterials, like nanorods, nanowires etc. demonstrate high mechanical strength because of small cross section and less numbers of imperfections.¹⁹⁶ Since imperfections are thermodynamically energy intensive, nanomaterials try to eliminate the imperfections to obtain higher mechanical strength.

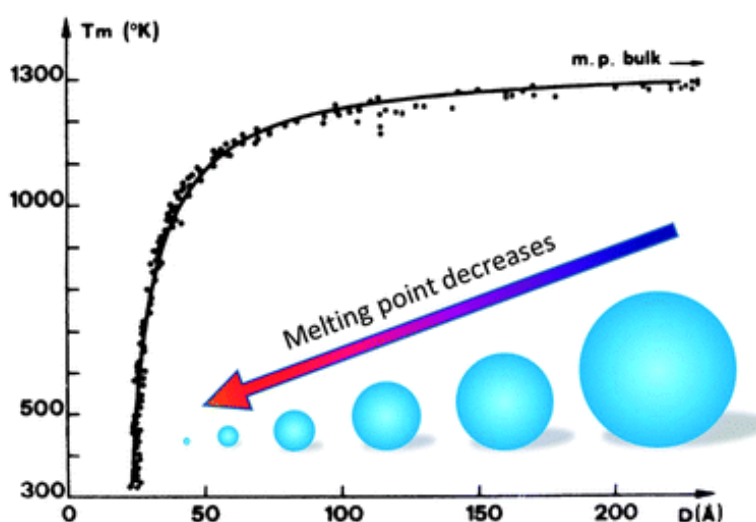


Figure 1.16: Schematic presentation of the melting point vs. particle diameter of gold NPs,¹⁹⁸ decreasing as the size of NPs decreases.

Apart from strength, melting point also decreases with reduction of the size of materials. Normally, melting point can be defined as the temperature at which lattice vibrations tend to partly conquer fraction of the intermolecular force strength that holds them in a permanent position in a solid. This phenomenon is exceptionally important in nanoscale materials, which melt at temperatures hundreds of degrees lower than the same bulk materials. This phenomenon is observed as the atoms in a material present at the surface are surrounded by less number of atoms, while atoms

present inside the bulk are surrounded by a large numbers of atoms.¹⁹⁷ Thus as the size of the materials decreases, more atoms will be present at the surface. Since, surface atoms have higher energy rather more reactive than that of bulk atoms, resulting in lowering of melting point as the size reduces. Figure 1.16 demonstrates the depression of melting point with the decrease in particle size of gold.¹⁹⁸ The melting point of gold NPs decreases was found to be below 200 °C when the size of the particle is around 5 nm.¹⁹⁹ This indicates that smaller size of the NPs causes decrease in the melting point.²⁰⁰

1.8.5 Magnetic Properties

Magnetic materials are those materials that demonstrate some response to an applied magnetic field. Nanomaterials exhibit size-dependent magnetic properties that range from ferromagnetic to paramagnetic to superparamagnetic.²⁰¹⁻²⁰³ As the size decreased from bulk to nano, below a critical size, the magnetic particle can exist as a single magnetic domain with all the spins coupled in the similar directions. Under this circumstance, the nanomaterials behave as a single magnetic dipole. Basically, the magnetic properties of nanomaterials change from their bulk counterpart mostly in these points. The large surface-to-volume ratio of the nanomaterials results in a diverse local environment for the surface atoms in their magnetic coupling with the nearby atoms, leading to the mixed volume and surface magnetic characteristics. The superparamagnetism occurs in nanoparticles which are single-domain, i.e.; composed of a single magnetic domain. In this case, the magnetization of the particles is randomly distributed. However, under an applied magnetic field, they are aligned and the alignment disappears once the external field is removed.

It should be noted that the coercivity is extremely sensitive to the size of the nanomaterials. Coercivity of a particle progressively increases to a highest value at a particular size and then rapidly decreases to zero as the particle size further decreases.²⁰⁴ Figure 1.17 display coercivity as a function of particle sizes. It should be note that when the particle diameter (D) decreases, a magnetic multi-domain (MD) state changes to a single-domain (SD) state. D_S is the diameter at which MD state transform to SD state. For an SD particle, the coercivity value is typically high. The

decrease in coercivity below D_S is owing to an increased thermal contribution, which randomizes the magnetization. With further decrease in the particle size, the coercivity becomes zero in case of superparamagnetic state and diameter at the zero-coercivity is referred to as D_P .

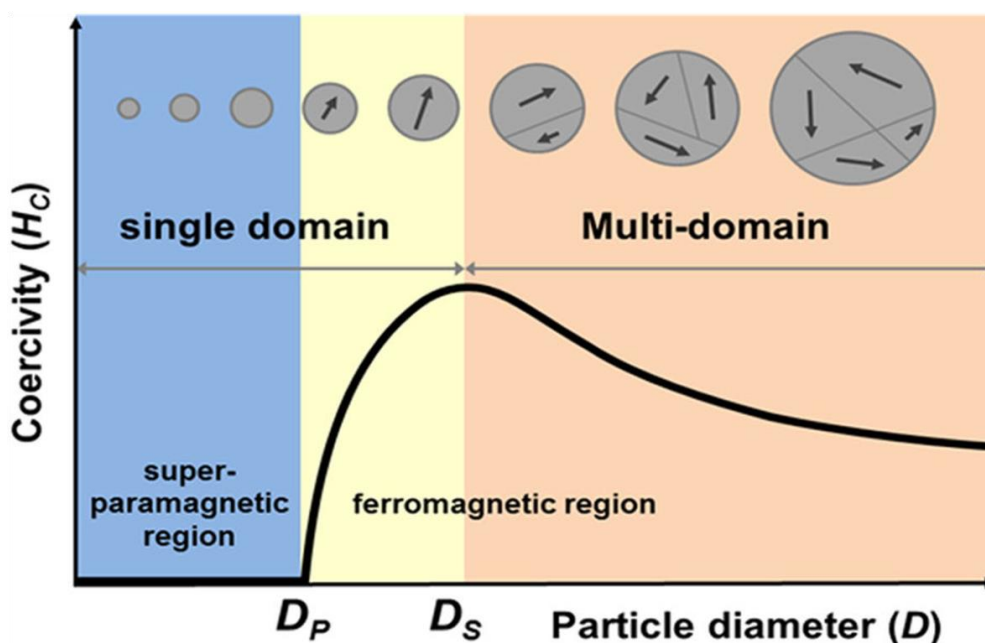


Figure 1.17: A schematic presentation of the coercivity (H_c) behaviour of a magnetic particle as a function of its diameter (D). As a particle size decreases, the domain wall disappears, resulting in an increase in H_c until the particle size reaches to D_S . As the particle size further decreases, thermal agitation energy overcomes magnetic anisotropy energy and as a consequence, the particle enters into the superparamagnetic regime, D_P .²⁰⁵

1.9 Nanocomposites

Nanocomposites (NCs) are a type of multiphase solid material in which at least one of the phases has dimensions in the nanometre range. Inorganic-organic hybrid NCs are not just physical mixtures, rather they are intimately mixed.²⁰⁶⁻²¹⁴ In fact, hybrids NCs are either homogeneous systems derived from monomers and miscible inorganic and organic components or heterogeneous systems consisting of at least one of phase dimension in the nanometre range. Inorganic-organic hybrid NCs do not represent only an innovative substitute to propose novel materials or compounds for academic

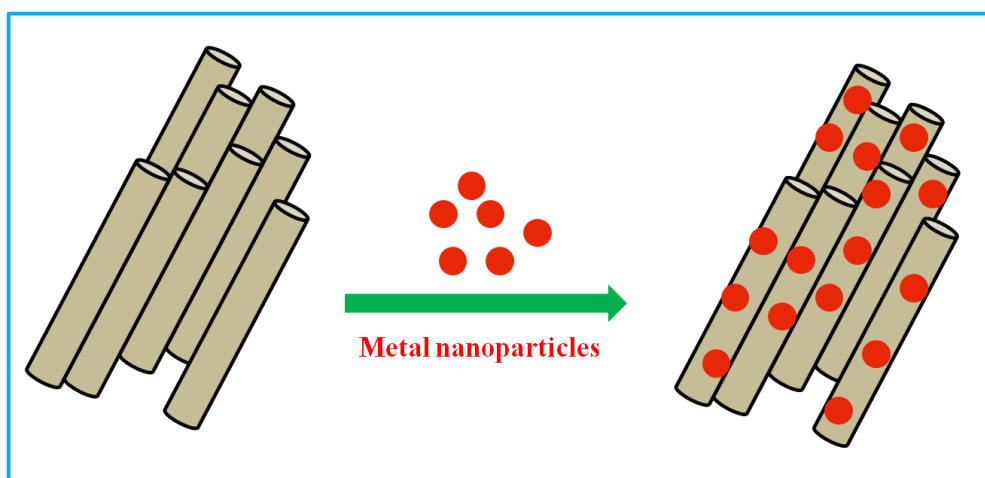


Figure 1.18: Schematic representation of synthesis of nanocomposites, where metal nanoparticles are immobilised over the surface of clay nanotubes.

research, but their extraordinary properties allow to use them for several applications. It is clear that their property is not only the summation of the individual assistance of both phases, but also the function of the inner interfaces is predominant. The addition of NPs imparts an enhancement in their properties, including mechanical strength, toughness and electrical or thermal conductivity. Generally, hybrid NCs are synthesised using the conventional soft chemistry based routes. These synthetic processes are classified into two groups; one route involves the copolymerisation of functional organosilanes, macromonomers and metal alkoxides and other route is the organic functionalization of nanofillers, nanoclays or other compounds with lamellar structures etc. The chemical strategies developed by the academic researchers in present time, allow an intelligent tuned coding, development of a new chemistry, ability to direct the assembling of a large variety of structurally well-defined nano-objects into inorganic-organic hybrid NCs in terms of structure and functions. The key in producing such novel materials needs to manipulate the guest-host chemistry occurring between the polymer and the layered compounds or the nanoparticles. Figure 1.18 demonstrates schematic representation of the synthesis of nanocomposite. At present, two different strategies can be applied to acquire metal-polymer NCs: *ex situ* and *in situ* synthesis methods. In the *in-situ* strategy, metal NPs are formed inside

the polymer matrix by decomposition or reduction of metal precursors, whereas *ex situ* strategy involves first formation of metal NPs by chemical methods and then distribution of the synthesized NPs into a polymer solution or monomer solution to polymerize.

Various NCs have been synthesized from several inorganic materials, such as layered metal phosphates, metal oxides, zeolites and mesoporous silica, but clays are the most important host because of their significant ability to hold guest molecules. Recently, there are a variety of clays exploited as inert support for the polymerization reactions, recovery of enzymes, delivery of molecules and remediation purposes. The montmorillonite (MMT) clay was extensively used in polymerization studies of aniline or its derivate with the aim to produce nanocomposites with controlled structure.²¹⁵⁻²¹⁸ These supported nanomaterials have joined immense interest as they allow well dispersion and stabilization of metallic NPs, which in turn facilitate to access a much larger number of catalytically active atoms.^{219,220} These advanced hybrid NCs will play a major role in the development of advanced functional materials for promising applications in the field of optics, electronics, energy, environment, biology, medicine, functional smart coatings, fuel, solar cells, catalysts, sensors etc.

1.10 Applications of Nanoparticles

During the last few decades, materials at nanoscale have received enormous importance due to their fundamental scientific significance and many technological applications. Nanoparticles have exceptional catalytic, optical, magnetic and electrical properties owing to their nano-scale dimensions.²²¹ Metal oxide nanoparticles, such as oxides of tin, iron, zinc and titanium are unprecedented and play an important role in the fabrication of devices.^{222,223} The lack of enough stability of several NPs has become the major concern during the development of real world applications of nanomaterials. It has also probably been the reason behind the important role of gold in the pioneering experiments performed mainly by Schmid and co-workers. Over the past 20 years they have been able to demonstrate that nano-electronic devices are achievable using ligand-stabilized Au₅₅ clusters.^{153,224,225} Gold

NPs are the most widely studied metal due to their unique tunable optical properties, which has been utilised in diverse applications, ranging from sensing to detection of biological molecules at low concentrations or imaging.²²⁶⁻²²⁸ Additionally, Au NPs are attractive in photothermal therapeutic, diagnostic and drug delivery applications.^{229,230}

They can also be used to improve both Rayleigh and Raman signals for obtaining chemical information on several biological species, of interest, which were earlier almost impossible to achieve using simple spectroscopies techniques.²³¹⁻²³³ Thus, the tuning in the size or shape of the Au NPs represents an attractive strategy for biosensing applications as well as for other future applications. In recent times, gold NPs are used for medicinal applications, like treatment of cancer therapy²³⁴ and silver NPs have been used for the sensing application of Alzheimer's disease.²³⁵

The researchers have also put forward their effort towards the study of optical properties of noble metal NPs.²³⁶⁻²³⁹ Magnetic NPs are also applied to deliver drugs to some specific areas of body and help in magnetic resonance imaging (MRI) technique. Now a days, in data storage industries, these NPs found enormous applications in ultra-fast optical data storage.^{225,240} Catalysis is also another very important application of metal NPs. Apart from the above mentioned applications, they also utilized in the field of photochemistry, nanoelectronics or optics.²⁴¹⁻²⁴³ Other valuable application of NPs includes ultra-fine wiring, efficient solar cell, doping for metal, ceramic, fiber and coating for surfaces of glass, lens, film, electrode etc. The applications of the NPs are ranging from environmental development to consumer products and even therapeutic usage.

1.10.1 Catalysis Involving Nanoparticles

Catalysis is one of the most important areas in which nanomaterials have been widely used. In the past several years, enormous research has been performed using nanomaterials as catalysts as well as catalyst supports.²⁴⁴⁻²⁴⁶ Transition metal colloids are extensively used as a catalyst for numerous organic reactions.²⁴⁷⁻²⁴⁹ It is evident that all the aspects connected to the synthesis of extremely small NPs of narrow size distribution, their stabilization and unique property compared to the larger particles

have fascinated to the researchers from materials science, computational chemistry and also to the catalysis community. Advances in materials science demonstrate the possibility to design, synthesize and tune the properties of nanomaterials. Smart catalysts can be composed using NPs compared to bulk materials due to their large surface-to-volume ratio. Hence, the exceptionally small size of NPs has increased surface area and more exposed active sites for the reactants to be adsorbed, leading to an increase in reaction rate. Thus, catalysis by gold is a typical example where, high activity was observed in the case of small nanoparticles, but reduced above 10 nm of particle size and disappeared completely as the particle size grows into the micrometer length scale.

Two different processes have been developed in catalysis; homogeneous catalysis and heterogeneous catalysis. Although homogeneous catalysis is associated with high activity and selectivity, but a major drawback of this process is the separation and recyclability of the catalyst together with agglomeration during the reaction. This can be overcome using heterogeneous catalysts where NPs are loaded over solid support or synthesized over the support. Basically, heterogeneous catalysts demonstrate not only high activity and selectivity but also it is easier to recover them through simple process. In materials science, nanocatalyst plays like a bridge between homogeneous and heterogeneous catalysts and imparts unique solutions to the challenging problems. The catalytic property has already been examined for metals, metal oxides, carbon materials and their composites. The properties of nanocatalyst can be tuned by changing the morphologies, sizes and facets of the nanomaterials and metal oxides, including MnO₂, TiO₂, CuO, Fe₂O₃, Fe₃O₄, zeolites and several metals such as Au, Ag, Pt, Pd, Fe, Cu, Co etc. have been extensively utilized as nanocatalyst in diverse applications.²⁵⁰⁻²⁵⁶ Further, the surface areas of metal or metal oxides NPs can be tuned by immobilised them in high surface area support material. A number of immobilization methods and support materials have been reported in the literature for this purpose.²⁵⁷⁻²⁵⁹ The immobilization of such nanomaterials on solid supports seems to be an attractive strategy as the nanocatalyst can be now recycled by simple filtration and further provide large surface area and high mechanical strength to the catalysts. Such, supported metal NPs show an enormous improvement in their activity and stability during catalysis.

1.11 Objectives and Outline of Thesis

Naturally occurring clay minerals offer an immense potential, in various technological applications due to their adsorptive and ionic exchange properties as a result of their specific structure. Immense research has been conducted to use the clay materials for the synthesis of several inorganic-organic hybrid NCs. Halloysite nanotubes (HNTs) are naturally occurring clay mineral with nanotubular structure, composed of aluminium, silicon, hydrogen and oxygen via surface weathering of aluminosilicate minerals. The chemical composition of HNTs can be represented as $\text{Al}_2\text{SiO}_2\text{O}_5(\text{OH})_4.n\text{H}_2\text{O}$, where n becomes 2 for hydrated and 0 for dehydrated form of HNTs respectively.^{260,261} In 1826, P. Berthier *et al.* reported that HNTs are a dioctahedral 1:1 clay mineral of the kaolin group and found broadly deposited in soils worldwide.²⁶²⁻²⁶⁴ HNTs are abundant materials and used to be mined from naturally deposits in several countries like China, France, Belgium and New Zealand. They are hollow tubes with outer diameter smaller than 100 nm and inner diameter of 10-15 nm. HNTs are rather polydisperse in size with lengths typically ranging from 500 nm to 1.2 micron. HNTs consist of silica on the outer surfaces and alumina in the innermost surfaces.^{265,266} Therefore, they have different inner and outer compositions and demonstrate different chemical properties in their internal and external surfaces. As a result of their surface chemistry and biocompatibility, they have the capability of immobilization of enzymes and controlled release of drug molecules.^{267,268} Owing to their low-cost and availability in nature, much attention has turned towards HNTs for the development of new inorganic-organic hybrid NCs to explore them in catalysis, as an adsorbent and a nanoreactor to host reactants for nanosynthesis.

Based on the above discussions of nanomaterials and nanocomposites, it is obvious that intense research is still required to further expand the properties of various metal, metal oxides and their nanocomposites to fulfil the desired property or application. The objective of my thesis is to synthesize noble metal and transition metal oxides NPs as well as development of clay based nanocomposites by employing novel routes for environmental applications. Outline of my thesis includes the following chapters;

In the **Chapter 1**, the important concept in nanoscience and nanotechnology along with a brief overview and a literature survey on the properties and applications of nanomaterials and nanocomposites have been discussed.

In the **Chapter 2**, general outline of the instruments and methods used for the characterization of these nanomaterials and nanocomposites have been demonstrated.

In the **Chapter 3**, the naturally occurring halloysite clay nanotubes (HNTs) have been introduced as a solid adsorbent due to their chemical tunability, high length-to-diameter ratio and high temperature resistant property. Several solid-phase adsorbents have been synthesized through the selective modification of the outer surfaces of the HNTs using aminosilanes which contain primary and/or secondary amine groups. CO₂ adsorption as a function of time by these amine functionalised clay nanotubes containing several viable amines with varied amine densities and adsorption sites has been examined at standard temperature and ambient pressure using a residual gas analyzer mass spectrometry system coupled with a high vacuum chamber. Then, adsorption kinetics of three major abundant isotopes of CO₂ (¹²C¹⁶O₂, ¹³C¹⁶O₂, and ¹²C¹⁶O¹⁸O) present in the ambient air have been demonstrated using a spectroscopic technique. The effect of relative humidity during CO₂ adsorption using these adsorbents has also been studied and the underlying adsorption mechanism has been ascribed under dry and humid conditions. Further the efficiency together with durability of these adsorbents has been evaluated.

In the **Chapter 4**, a facile strategy was developed to synthesize novel porous silica materials through the light-assisted hydrolysis of a silica precursor using an organic template. This method has the capability of large scale production of flower like silica materials with high surface area. Functionalization of nanosilica surfaces was carried out via simple covalent attachment of various organosilanes having amine groups. The CO₂ adsorption performance of these amine-functionalized nanosilica sorbents was studied. The efficiency of these adsorbents for CO₂ capture was evaluated and recyclability was examined by their repetitive usage.

In the **Chapter 5**, the development of an adsorbent was demonstrated to remove heavy metal ions, since contamination of ground water by heavy metal ions

has become a serious ecological and health issues due to their toxic effects even they present at very low concentration. To address these issues, novel solid-phase adsorbents were synthesized using the selective modification of the outer surface of the HNTs with organosilanes to extract heavy metal ions from the aqueous solutions. After the synthesis and characterization, the adsorption properties and adsorption kinetics of these solid adsorbents have been studied in details towards Hg(II) adsorption. Effect of solution pH during adsorption has also been discussed.

In the **Chapter 6**, environmentally benign and low-cost heterogeneous catalysts have been fabricated through the immobilization of metal precursors followed by reduction or direct loading of preformed metal nanoparticles over the surface of organosilane modified HNTs. Then, their catalytic activity was evaluated and compared for the reduction of nitroaromatics. Activation energy, pre-exponential factor, and entropy of activation have been estimated for this reduction reaction. A comparison study of their catalytic activity was carried out with the reported heterogeneous catalysts, indicating the higher activity of these catalysts for the reduction of nitroaromatics.

In the **Chapter 7**, hierarchical MnO₂ nanoflowers have been synthesized over the surface of HNTs using a novel green chemistry route based on the decomposition of a manganese precursor. Flower-like δ -MnO₂ nanostructures comprising of assemblies of intersected nanosheets were grown over the outer surfaces of HNTs. The photocatalytic activity of HNTs/MnO₂ NCs has been investigated under natural sunlight irradiation for the degradation of several organic dyes. The degradation mechanism demonstrates the formation of reactive oxygen species, which in turn facilitate the degradation of dyes. This study also substantiates that there is no need of any supplementary oxygen sources during photodegradation.

In the **Chapter 8**, exploiting the inner lumen of halloysite clays as nanoconfined reactor, the synthesis of rod shaped nanoscale inorganic materials within the lumen of the nanoclays have been reported. Selective modification of the clay lumen using a chelating ligand produces an inorganic micelle-like architecture, facilitating the formation of rod shaped nanoscale iron oxide inside the lumen of the clay nanotubes and finally giving rise to a nanocomposite having α -Fe₂O₃ core with

halloysite shell. The as-prepared α -Fe₂O₃/HNTs NCs exhibit enhanced photocatalytic activity toward the degradation of organic dyes in presence of sunlight.

In the **Chapter 9**, all the research works described in this thesis have been summarized and pointed out the probable avenues for future investigations.

1.12 References

1. Roco, M. C.; Bainbridge, W. S. *Societal Implications of Nanoscience and Nanotechnology*. NSET workshop report, **2001**.
2. Fahlman, B. D. *Materials Chemistry*. Springer, Mount Pleasant, **2007**, *1*, 282 – 283.
3. Jana, S. Advances in Nanoscale Alloys and Intermetallics: Low Temperature Solution Chemistry Synthesis and Application in Catalysis. *Dalton Trans.* **2015**, *44*, 18692–18717.
4. Jana, S.; Chang, J. W.; Rioux, R. M. Synthesis and Modeling of Hollow Intermetallic Ni–Zn Nanoparticles Formed by the Kirkendall Effect. *Nano Lett.* **2013**, *13*, 3618–3625.
5. Davey, N. M.; Seymour, R. J. The Platinum Metals in Electronics. *Platinum Met. Rev.* 1985, **29**, 2–11.
6. Jeong, S.; Woo, K.; Kim, D.; Lim, S.; Kim, J. S.; Shin, H.; Xia, Y.; Moon, J. Controlling the Thickness of the Surface Oxide Layer on Cu Nanoparticles for the Fabrication of Conductive Structures by Ink-Jet Printing. *Adv. Funct. Mater.* **2008**, *18*, 679–686.
7. Bartelmess, J.; Quinn, S. J.; Giordani, S. Carbon Nanomaterials: Multi-Functional Agents for Biomedical Fluorescence and Raman Imaging. *Chem. Soc. Rev.* **2015**, *44*, 4672-4698.
8. Lane, L.A.; Qian, X.; Nie, S. SERS Nanoparticles in Medicine: From Label-Free Detection to Spectroscopic Tagging. *Chem. Rev.* **2015**, *115*, 10489-10529.
9. Jana, S.; Basu, S.; Pande, S.; Ghosh, S. K.; Pal, T. Shape-Selective Synthesis, Magnetic Properties, and Catalytic Activity of Single Crystalline β -MnO₂ Nanoparticles. *J. Phys. Chem. C* **2007**, *111*, 16272–16277.
10. Somorjai, G. A. Modern Surface Science and Surface Technologies: An Introduction. *Chem. Rev.* **1996**, *96*, 1223–1236.
11. Jana, S.; Pande, S.; Sinha, A. K.; Pal, T. Synthesis of Superparamagnetic β -MnO₂ Organosol: a Photocatalyst for the Oxidative Phenol Coupling Reaction. *Inorg. Chem.* **2008**, *47*, 5558–5560.
12. Jana, S.; Pande, S.; Sinha, A. K.; Sarkar, S.; Pradhan, M.; Basu, M.; Saha, S.; Pal, T. A Green Chemistry Approach for the Synthesis of Flower-like Ag-Doped MnO₂ Nanostructures Probed by Surface-Enhanced Raman Spectroscopy. *J. Phys. Chem. C* **2009**, *113*, 1386–1392.
13. Hamilton, J. F. The Silver Halide Photographic Process. *Adv. Phys.* **1988**, *37*, 359-441.

14. Tani, T. Physics of the Photographic Latent Image. *Phys. Today* **1989**, *42*, 36–41.
15. Sun, S.; Murray, C. B.; Weller, D.; Folks, L.; Moser, A. Monodisperse FePt Nanoparticles and Ferromagnetic FePt Nanocrystal Superlattices. *Science* **2000**, *287*, 1989–1992.
16. Maier, S. A.; Brongersma, M. L.; Kik, P. G.; Meltzer, S.; Requicha, A. A. G.; Atwater, H. A. Plasmonics-A Route to Nanoscale Optical Devices. *Adv.Mater.* **2001**, *13*, 1501–1505.
17. Mirkin, C. A.; Letsinger, R. L.; Mucic, R. C.; Storhoff, J. J. A DNA-Based Method for Rationally Assembling Nanoparticles into Macroscopic Materials. *Nature* **1996**, *382*, 607–609.
18. Taton, T. A.; Mirkin, C. A.; Letsinger, R. L. Scanometric DNA Array Detection with Nanoparticle Probes. *Science* **2000**, *289*, 1757–1760.
19. Han, M.; Gao, X.; Su, J. Z.; Nie, S. Quantum-Dot-Tagged Microbeads for multiplexed Optical Coding of Biomolecules. *Nat. Biotechnol.* **2001**, *19*, 631–635.
20. Baffou, G. Gold Nanoparticles as Nanosources of Heat. *Photoniques* **2018**, 42–47.
21. Sanders, A. W.; Routenberg, D. A.; Wiley, B. J.; Xia, Y.; Dufresne, E. R.; Reed, M. A.; Observation of Plasmon Propagation, Redirection, and Fan-Out in Silver Nanowires. *Nano Lett.* **2006**, *6*, 1822–1826.
22. Cang, H.; Sun, T.; Li, Z.-Y.; Chen, J.; Wiley, B. J.; Xia, Y.; Li, X. Gold Nanocages as Contrast Agents for Spectroscopic Optical Coherence Tomography. *Opt. Lett.* **2005**, *30*, 3048–3050.
23. Yang, X.; Skrabalak, S. E.; Li, Z. Y.; Xia, Y.; Wang, L. V. Photoacoustic Tomography of a Rat Cerebral Cortex in vivo with Au Nanocages as an Optical Contrast Agent. *Nano Lett.* **2007**, *7*, 3798–3802.
24. Jain, P. K.; El-Sayed, I. H.; El-Sayed, M. A. Au Nanoparticles Target Cancer. *NanoToday* **2007**, *2*, 18–29.
25. Skrabalak, S. E.; Au, L.; Lu, X.; Li, X.; Xia, Y. Gold Nanocages for Cancer Detection and Treatment. *Nanomedicine* **2007**, *2*, 657–668.
26. Au, L.; Zheng, D.; Zhou, F.; Li, Z.-Y.; Li, X.; Xia, Y. A Quantitative Study on the Photothermal Effect of Immuno Gold Nanocages Targeted to Breast Cancer Cells. *ACS Nano* **2008**, *2*, 1645–1652.
27. Jana, S.; Praharaj, S.; Panigrahi, S.; Basu, S.; Pande, S.; Chang, C. -H.; Pal, T. Light-Induced Hydrolysis of Nitriles by Photoproduced α -MnO₂ Nanorods on Polystyrene Beads. *Org. Lett.* **2007**, *9*, 2191–2193.
28. Ivanova, S.; Pitchon, V.; Zimmermann, Y.; Petit, C. Preparation of Alumina Supported Gold Catalysts: Influence of Washing Procedures, Mechanism of Particles Size Growth. *Appl.Catal. A* **2006**, *298*, 57–64.
29. Garcia-Martinez, J. C.; Lezutekong R.; and Crooks, R. M. Dendrimer-Encapsulated Pd Nanoparticles as Aqueous, Room-Temperature Catalysts for the Stille Reaction. *J. Am. Chem. Soc.* **2005**, *127*, 5097–5103.
30. Sanderson, K. Sharpest cut from nanotube sword. *Nature News.* **2006**.
31. Daniel, M. -C.; Astruc, D. Gold Nanoparticles: Assembly, Supramolecular Chemistry, Quantum-Size-Related Properties, and Applications toward Biology, Catalysis, and Nanotechnology. *Chem. Rev.* **2004**, *104*, 293–346.
32. Khan, F. A. *Biotechnology Fundamentals*, CRC Press, **2011**.

33. Rawson, P. S. *Ceramics*, University of Pennsylvania Press, **1984**.
34. Thompson, D. Michael Faraday's Recognition of Ruby Gold: the Birth of Modern Nanotechnology. *Gold Bulletin* **2007**, 40, 267-269.
35. Faraday, M. Experimental Relations of Gold (and other Metals) to Light. *Philos. Trans. R. Soc. London Ser. A* **1857**, 147, 145-181.
36. Freestone, I.; Meeks, N.; Sax, M.; Higgitt, C. *Gold Bulletin* **2007**, 40, 270-277.
37. Mie, G. Beiträge zur Optik trüber Medien, Speziell Kolloidaler Metallösungen. *Ann. Phys.* **1908**, 25, 377-445.
38. Feynman, R. P. *Engineering and Science magazine* **1960**.
39. Sundeeep, H.; Yo, H.; Huang, J. Tem-Based Investigations on CVD-Assisted Growth of ZnO Nanowires Inside Nanochannels of Anodized Aluminum Oxide Template. *Int. J. Nanoscience* **2010**, 9, 225-235.
40. Ravikrishna, A. *Engineering Chemistry*, Sri Krishna Hi-Tech Publishing Company, Chennai, **2009**.
41. Arivalagan, K.; Karthikeyan, R.; *Engineering Chemistry*, Shiv Publications, Chennai, **2007**.
42. Caswell, K. K.; Bender, C. M.; Murphy, C. J.; Seedless, Surfactantless Wet Chemical Synthesis of Silver Nanowires. *Nano Lett.* **2003**, 3, 667-669.
43. Nath, S.; Ghosh, S. K.; Kundu, S.; Praharaj, S.; Panigrahi, S. ; Pal, T. Is Gold Really Softer than Silver? HSAB Principle Revisited. *J. Nanoparticle Res.* **2006**, 8, 111-116.
44. Henglein, A. Physicochemical Properties of Small Metal Particles in Solution: "Microelectrode" Reactions, Chemisorption, Composite Metal Particles, and the Atom-to-Metal Transition. *J. Phys. Chem.* **1993**, 97, 5457-5471.
45. Kundu, S.; Pal, A.; Ghosh, S. K.; Nath, S.; Panigrahi, S.; Praharaj, S.; Pal, T. A New Route to Obtain Shape-Controlled Gold Nanoparticles from Au(III)- β -diketonates. *Inorg. Chem.* **2004**, 43, 5489-5491.
46. Panigrahi, S.; Kundu, S.; Ghosh, S. K.; Nath, S.; Pal, T. General Method of Synthesis for Metal Nanoparticles. *J. Nanoparticle Res.* **2004**, 6, 411-414.
47. Turkevich, J.; Kim, G. Palladium: Preparation and Catalytic Properties of Particles of Uniform Size. *Science* **1970**, 169, 873-879.
48. Rampino, D. ; Nord, F. F. Applicability of Palladium Synthetic High Polymer Catalysts. *J. Am. Chem. Soc.* **1941**, 63, 3268-3268.
49. Frens, G. Controlled Nucleation for the Regulation of the Particle Size in Monodisperse Gold Suspensions. *Nature: Phys. Sci.* **1973**, 241, 20-22.
50. Hirai, H.; Nakao, Y.; Toshima, N.; Adachi, K. Colloidal Rhodium in Polyvinyl Alcohol as Hydrogenation Catalyst of Olefins. *Chem. Lett.* **1976**, 5, 905-910.
51. Hirai, H.; Nakao, Y.; Toshima, N. Colloidal Rhodium in Poly(vinylpyrrolidone) as Hydrogenation Catalyst for Internal Olefins. *Chem. Lett.* **1978**, 545-548.
52. Jana, N.R.; Gearheart, L.; Murphy, C.J. Wet Chemical Synthesis of High Aspect Ratio Cylindrical Gold Nanorods. *J. Phys. Chem. B* **2001**, 105, 4065-4067.
53. Zarur, A. J.; Ying, J. Y. Reverse microemulsion synthesis of nanostructured complex oxides for catalytic combustion. *Nature* **2000**, 403, 65-67.

54. Zhang, W.; Yang, Z.; Liu, Y.; Tang, S.; Han, X.; Chen, M. Controlled Synthesis of Mn_3O_4 Nanocrystallites and MnOOH Nanorods by a Solvothermal Method. *J. Cryst. Growth* **2004**, *263*, 394-399.
55. Ramesh, K.; Chen, L.; Chen, F.; Zhong, Z.; Chin, J.; Mook, H.; Han, Y. F. Preparation and Characterization of Coral-Like Nanostructured $\alpha\text{-Mn}_2\text{O}_3$ Catalyst for Catalytic Combustion of Methane. *Catal. Commun.* **2007**, *8*, 1421-1426.
56. Marbán, G.; Valdés-Solís, T.; Fuertes, A. B. Mechanism of Low-Temperature Selective Catalytic Reduction of NO with NH_3 Over Carbon-Supported Mn_3O_4 : Role of Surface NH_3 Species: SCR Mechanism. *J. Catal.* **2004**, *226*, 138-155.
57. Folch, B.; Larionova, J.; Guari, Y.; Guérin, C.; Reibel, C. Synthesis of MnOOH Nanorods by Cluster Growth Route from $[\text{Mn}_{12}\text{O}_{12}(\text{RCOO})_{16}(\text{H}_2\text{O})_n]$ ($\text{R}=\text{CH}_3, \text{C}_2\text{H}_5$). Rational Conversion of MnOOH into Mn_3O_4 or MnO_2 Nanorods. *J. Solid State Chem.* **2005**, *178*, 2368-2375.
58. Tang, X.; Li, J.; Sun, L.; Hao, J. Origination of N_2O from NO reduction by NH_3 over $\beta\text{-MnO}_2$ and $\alpha\text{-Mn}_2\text{O}_3$. *Appl. Catal. B: Environ.* **2010**, *99*, 156-162.
59. Sun, S.; Zeng, H. Size-Controlled Synthesis of Magnetite Nanoparticles. *J. Am. Chem. Soc.* **2002**, *124*, 8204-8205.
60. Chen, Z. W.; Lai, J. K. L.; Shek, C. H. Influence of Grain Size on the Vibrational Properties in Mn_2O_3 Nanocrystals. *J. Non-Cryst. Solids* **2006**, *352*, 3285-3289.
61. Ren, T. Z.; Yuan, Z. Y.; Hu, W.; Zou, X. Single Crystal Manganese Oxide Hexagonal Plates with Regulated Mesoporous Structures. *Microporous Mesoporous Mater.* **2008**, *112*, 467-473.
62. Shao, C.; Guan, H.; Liu, Y.; Li, X.; Yang, X. Preparation of Mn_2O_3 and Mn_3O_4 Nanofibers via an Electrospinning Technique. *J. Solid State Chem.* **2004**, *177*, 2628-2631.
63. Ge, J.; Hu, Y.; Biasini, M.; Beyermann, W. P.; Yin, Y. Superparamagnetic Magnetite Colloidal Nanocrystal Clusters. *Angew. Chem. Int. Ed.* **2007**, *46*, 4342-4345.
64. Chen, Z. W.; Lai, J. K. L.; Shek, C. H. Shape-Controlled Synthesis and Nanostructure Evolution of Single-Crystal Mn_3O_4 Nanocrystals. *Scr. Mater.* **2006**, *55*, 735-738.
65. Yuan, Z. Y.; Ren, T. Z.; Du, G.; Su, B. L. A Facile Preparation of Single-Crystalline $\alpha\text{-Mn}_2\text{O}_3$ Nanorods by Ammonia-Hydrothermal Treatment of MnO_2 . *Chem. Phys. Lett.* **2004**, *389*, 83-86.
66. Kim, D. K.; Muralidharan, P.; Lee, H. W.; Ruffo, R.; Yang, Y.; Chan, C. K.; Peng, H.; Huggins, R. A.; Cui, Y. Spinel LiMn_2O_4 Nanorods as Lithium Ion Battery Cathodes. *Nano Lett.* **2008**, *8*, 3948-3952.
67. Shen, Y. F.; Zenger, R. P.; Deguzman, R. N.; Suib, S. L.; Mccurdy, L.; Potter, D. I.; O'Young, C. L. Manganese Oxide Octahedral Molecular Sieves: Preparation, Characterization, and Applications. *Science* **1993**, *260*, 511-515.
68. Chen, Z. W.; Lai, J. K. L.; Shek, C. H. Evolution of Electronic Structure and Spectral Evaluation in Single-Crystal Mn_3O_4 Nanorods. *J. Chem. Phys.* **2006**, *124*, 184707-184711.
69. Han, Y. F.; Chen, F.; Zhong, Z. Y.; Ramesh, K.; Widjaja, E.; Chen, L. W. Synthesis and Characterization of Mn_3O_4 and Mn_2O_3 Nanocrystals on SBA-15:

- Novel Combustion Catalysts at Low Reaction Temperatures. *Catal. Commun.* **2006**, *7*, 739-744.
70. Chen, Z. W.; Shek, C. H.; Lai, J. K. L. An Analysis of the Grain Growth Kinetics in Mn₂O₃ Nanocrystals. *Appl. Phys. A: Mater. Sci. Process.* **2005**, *80*, 703.
71. Hosono, E.; Kudo, T.; Honma, I.; Matsuda, H.; Zhou, H. Synthesis of Single Crystalline Spinel LiMn₂O₄ Nanowires for a Lithium Ion Battery with High Power Density. *Nano Lett.* **2009**, *9*, 1045-1051.
72. Isber, S.; Majdalani, E.; Tabbal, M.; Christidis, T.; Zahraman, K.; Nsouli, B. Study of Manganese Oxide Thin Films Grown by Pulsed Laser Deposition. *Thin Solid Films* **2009**, *517*, 1592-1595.
73. Wang, X.; Li, Y. Selected-Control Hydrothermal Synthesis of α - and β -MnO₂ Single Crystal Nanowires. *J. Am. Chem. Soc.* **2002**, *124*, 2880-2881.
74. Li, Z. Q.; Ding, Y.; Xiong, Y. J.; Yang, Q.; Xie, Y. One-step Solution-based Catalytic Route to Fabricate Novel α -MnO₂ Hierarchical Structures on a Large. *Chem. Commun.* **2005**, *7*, 918-920.
75. Sun, X.; Ma, C.; Wang, Y.; Li, H. Preparation and Characterization of MnOOH and β -MnO₂ Whiskers. *Inorg. Chem. Commun.* **2002**, *5*, 747-750.
76. Laurent, S.; Forge, D.; Port, M.; Roch, A.; Robic, C.; Vander Elst, L.; Muller, R. N. Magnetic Iron Oxide Nanoparticles: Synthesis, Stabilization, Vectorization, Physicochemical Characterizations, and Biological Applications. *Chem. Rev.* **2008**, *108*, 2064-2110.
77. Huber, D. L. Synthesis, Properties, and Applications of Iron Nanoparticles. *Small* **2005**, *1*, 482-501.
78. Cornell, R. M.; Schwertmann, U. *The Iron Oxides: Structure, Properties, Reactions, Occurrences and Uses*. 2nd ed. John Wiley & Sons, **2006**.
79. Hasany, S.; Ahmed, I.; Rajan, J.; Rehman, A. Systematic Review of the Preparation Techniques of Iron Oxide Magnetic Nanoparticles. *Nanosci. Nanotechnol.* **2012**, *2*, 148-158.
80. Liu, R.; Liu, J. F.; Zhang, L. Q.; Sun, J. F.; Jiang, G. B. Low temperature synthesized ultrathin γ -Fe₂O₃ nanosheets show similar adsorption behaviour for As (III) and As (V). *J. Mater. Chem. A* **2016**, *4*, 7606-7614.
81. Vayssieres, L.; Beermann, N.; Lindquist, S.-E.; Hagfeldt, A. Controlled Aqueous Chemical Growth of Oriented Three-Dimensional Crystalline Nanorod Arrays: Application to Iron(III) Oxides. *Chem. Mater.* **2001**, *13*, 233-235.
82. Wang, R.; Chen, Y.; Fu, Y.; Zhang, H.; Kisielowski, C. Bicrystalline Hematite Nanowires. *J. Phys. Chem. B* **2005**, *109*, 12245-12249.
83. Wen, X.; Wang, S.; Ding, Y.; Wang, Z. L.; Yang, S. Controlled Growth of Large-Area, Uniform, Vertically Aligned Arrays of α -Fe₂O₃ Nanobelts and Nanowires. *J. Phys. Chem. B* **2005**, *109*, 215-220.
84. Jia, C. J.; Sun, L. D.; Yan, Z. G.; You, L. P.; Luo, F.; Han, X. D.; Pang, Y. C.; Zhang, Z.; Yan, C. H. Single-Crystalline Iron Oxide Nanotubes. *Angew. Chem., Int. Ed.* **2005**, *117*, 4402-4407.
85. Fu, Y. Y.; Wang, R. M.; Xu, J.; Chen, J.; Yan, Y.; Narlikar, A. V.; Zhang, H. Synthesis of Large Arrays of Aligned α -Fe₂O₃ Nanowires. *Chem. Phys. Lett.* **2003**, *379*, 373-379.

86. Woo, K.; Lee, H. J.; Ahn, J. P.; Park, Y. S. Sol-Gel Mediated Synthesis of Fe₂O₃ Nanorods. *Adv. Mater.* **2003**, *15*, 1761-1764.
87. Xiong, Y.; Li, Z.; Li, X.; Hu, B.; Xie, Y. Thermally Stable Hematite Hollow Nanowires. *Inorg. Chem.* **2004**, *43*, 6540-6542.
88. Wang, L. -W. Calculating the Influence of External Charges on the Photoluminescence of a CdSe Quantum Dot. *J. Phys. Chem. B* **2001**, *105*, 2360-2364.
89. Rossetti, R.; Ellison, J. L.; Gibson, J.M.; Brus, L.E. Size Effects in the Excited Electronic States of Small Colloidal CdS Crystallites. *J. Chem. Phys.* **1984**, *80*, 4464-4469.
90. Alivisatos, A. P. Semiconductor Clusters, Nanocrystals, and Quantum Dots. *Science* **1996**, *271*, 933-937.
91. Zheng, N.; Bu, X.; Lu, H.; Zhang, Q.; Feng, P. Crystalline Superlattices from Single-Sized Quantum Dots. *J. Am. Chem. Soc.* **2005**, *127*, 11963-11965.
92. Khitun, A.; Balandin, A.; Liu J. L.; Wang, K. L. The Effect of the Long-range Order in a Quantum Dot Array on the In-plane Lattice Thermal Conductivity. *Superlattices Microstruct.* **2001**, *30*, 1-8.
93. Bruchez, M.; Moronne, M.; Gin, P.; Weiss, S.; Alivisatos, A. P. Semiconductor Nanocrystals as Fluorescent Biological Labels. *Science* **1998**, *281*, 2013-2016.
94. Sang, W.; Qian, Y.; Min, J.; Li, D.; Wang, L.; Shi, W.; Yinfeng, L. Microstructural and Optical Properties of ZnS:Cu Nanocrystals Prepared by an Ion Complex Transformation Method. *Solid State Commun.* **2002**, *121*, 475-478.
95. Colvin, V. L.; Schlamp, M. C.; Alivisatos, A. P. Light-Emitting Diodes Made from Cadmium Selenide Nanocrystals and a Semiconducting Polymer. *Nature*, **1994**, *370*, 354-357.
96. Willner, I.; Mandler, D. Characterization of Palladium-.Beta.-Cyclodextrin Colloids as Catalysts in the Photosensitized Reduction of Bicarbonate to Formate. *J. Am. Chem. Soc.* **1989**, *111*, 1330-1336.
97. Whitesides, G. M.; Love, J. C. The Art of Building Small. *Sci. Am.* **2001**, *285*, 38-47.
98. Finke, R. G. *In metal nanoparticles: Synthesis, Characterisation and applications*. Jr., Eds., Marcel Dekker: New York, **2002**, Chapter 2, 17-54.
99. Bae, E. J.; Choi, W. B.; Jeong, K. S.; Chu, J. U.; Park, G. S.; Song, S.; Yoo, I. K. Selective Growth of Carbon Nanotubes on Pre-patterned Porous Anodic Aluminum Oxide. *Adv. Matter.* **2002**, *14*, 277-279.
100. Jansen, H. V.; Tas, N. R.; Berenschot, J. W. Encyclopedia of Nanoscience and Nanotechnology, Nalwa, **2004**, *5*, 163.
101. Zhou, Y.; Wang, C. Y.; Zhu, Y. R.; Chen, Z. Y. A Novel Ultraviolet Irradiation Technique for Shape-Controlled Synthesis of Gold Nanoparticles at Room Temperature. *Chem. Mater.* **1999**, *11*, 2310-2312.
102. Niidome, Y.; Hori, A.; Sato, T.; Yamada, S. Enormous Size Growth of Thiol-Passivated Gold Nanoparticles Induced by Near-IR Laser Light. *Chem. Lett.* **2000**, *29*, 310-311.
103. Nakamoto, M.; Yamamoto, M.; Fukusumi, M. Thermolysis of Gold(I) Thiolate Complexes Producing Novel Gold Nanoparticles Passivated by Alkyl Groups. *Chem. Commun.* **2002**, *15*, 1622-1623.

104. Sun, S.; Mendes, P.; Critchley, K.; Diegoli, S.; Hanwell, M.; Evans, S. D.; Leggett, G. J.; Preece, J. A.; Richardson, T. H.. Fabrication of Gold Micro-and Nanostructures by Photolithographic Exposure of Thiol-Stabilized Gold Nanoparticles. *Nano Lett.* **2006**, *6*, 345-350.
105. Chen, W.; Cai, W. P.; Liang, C. H.; Zhang, L. D. Synthesis of Gold Nanoparticles Dispersed within Pores of Mesoporous Silica Induced by Ultrasonic Irradiation and Its Characterization. *Mater. Res. Bull.* **2001**, *36*, 335-342.
106. Chen, W.; Cai, W.; Zhang, L.; Wang, G.; Zhang, L. Sonochemical Processes and Formation of Gold Nanoparticles within Pores of Mesoporous Silica. *J. Colloid Interface Sci.* **2001**, *238*, 291-295.
107. Henglein, A.; Meisel, D. Radiolytic Control of the Size of Colloidal Gold Nanoparticles. *Langmuir* **1998**, *14*, 7392-7396.
108. Dawson, A.; Kamat, P. V. Complexation of Gold Nanoparticles with Radiolytically Generated Thiocyanate Radicals ((SCN)₂^{•-}). *J. Phys. Chem. B* **2000**, *104*, 11842-11846.
109. Balaji, K.; Kulkarni, R. P.; Majumdar, A. DNA-Based Programmed Assembly of Gold Nanoparticles on Lithographic Patterns with Extraordinary Specificity. *Nano Lett.* **2004**, *4*, 1521-1524.
110. Haes, A. J.; Zou, S.; Schatz, G. C.; Van Duyne, R. P. Nanoscale Optical Biosensor: Short Range Distance Dependence of the Localized Surface Plasmon Resonance of Noble Metal Nanoparticles. *J. Phys. Chem. B* **2004**, *108*, 6961-6968.
111. Mendes, P. M.; Jacke, S.; Critchley, K.; Plaza, J.; Chen, Y.; Nikitin, K.; Palmer, R. E.; Preece, J. A.; Evans, S. D.; Fitzmaurice, D. Gold Nanoparticle Patterning of Silicon Wafers Using Chemical e-Beam Lithography. *Langmuir* **2004**, *20*, 3766-3768.
112. Huang, Z.; Mills, G.; Hajek, B. Spontaneous Formation of Silver Particles in Basic 2-propanol. *J. Phys. Chem.* **1993**, *97*, 11542-11550.
113. Mössmer, S.; Spatz, J. P.; Möller, M.; Aberle, T.; Schmidt, J.; Burchard, W. Solution Behavior of Poly(styrene)-*block*-poly(2-vinylpyridine) Micelles Containing Gold Nanoparticles. *Macromolecules* **2000**, *33*, 4791-4798.
114. Meltzer, S.; Resch, R.; Koel, B. E.; Thompson, M. E.; Madhukar, A.; Requicha, A. A. G.; Will, P. Fabrication of Nanostructures by Hydroxylamine Seeding of Gold Nanoparticle Templates. *Langmuir* **2001**, *17*, 1713-1718.
115. Mallick, K.; Wang, Z. L.; Pal, T. Seed-Mediated Successive Growth of Gold Particles Accomplished by UV Irradiation: A Photochemical Approach for Size-Controlled Synthesis. *J. Photochem. Photobiol.* **2001**, *140*, 75-80.
116. Henglein, A. The Reactivity of Silver Atoms in Aqueous Solutions (A γ -Radiolysis Study). *Ber. Bunsenges. Phys. Chem.* **1977**, *81*, 556-561.
117. Mulfinger, L.; Solomon, S.D.; Bahadory, M.; Jeyarajasingam, A.V.; Rutkowsky, S.A.; Boritz, C. Synthesis and Study of Silver Nanoparticles. *J. Chem. Educ.* **2007**, *84*, 322.
118. Guzmán, M. G.; Dille, J.; Godet, S. Synthesis of Silver Nanoparticles by Chemical Reduction Method and Their Antibacterial Activity. *Int. J. Chem. Biomol. Eng.* **2009**, *2*, 104-111.

119. Bastús, N. G.; Comenge, J.; Puentes, V. Kinetically Controlled Seeded Growth Synthesis of Citrate-Stabilized Gold Nanoparticles of Up to 200 nm: Size Focusing Versus Ostwald Ripening. *Langmuir* **2011**, *27*, 11098-11105.
120. Henglein, A. Physicochemical Properties of Small Metal Particles in Solution: "Microelectrode" Reactions, Chemisorption, Composite Metal Particles, and the Atom-to-Metal Transition. *J. Phys. Chem.* **1993**, *97*, 5457-5471.
121. Kundu, S.; Pal, A.; Ghosh, S. K.; Nath, S.; Panigrahi, S.; Praharaj, S.; Pal, T. A New Route to Obtain Shape-Controlled Gold Nanoparticles from Au(III)- β -diketonates. *Inorg. Chem.* **2004**, *43*, 5489-5491.
122. Garnweitner, G.; Antonietti, M.; Niederberger, M. Nonaqueous Synthesis of Crystalline Anatase Nanoparticles in Simple Ketones and Aldehydes as Oxygen-Supplying Agents. *Chem. Commun.* **2005**, 397-399.
123. Darroudi, M.; Ahmad, M.B.; Abdullah, A. H.; Ibrahim, N. A. Green Synthesis and Characterization of Gelatin-based and Sugar-reduced silver Nanoparticles. *Int. J Nanomedicine* **2011**, *6*, 569.
124. Pande, S.; Ghosh, S. K.; Praharaj, S.; Panigrahi, S.; Basu, S.; Jana, S.; Pal, A.; Tsukuda, T.; Pal, T. Synthesis of Normal and Inverted Gold-Silver Core-Shell Architectures in β -Cyclodextrin and Their Applications in SERS. *J. Phys. Chem. C* **2007**, *111*, 10806-10813.
125. Freeman, R. G.; Grabar, K. C.; Allison, K. J.; Bright, R. M.; Davis, J. A.; Guthrie, A. P.; Hommer, M. B.; Jackson, M. A.; Smith, P. C. Self-Assembled Metal Colloid Monolayers: An Approach to SERS Substrates. *Science* **1995**, *267*, 1629-1632.
126. Ullman, A. Formation and Structure of Self-Assembled Monolayers. *Chem. Rev.* **1996**, *96*, 1533-1554.
127. Zhao, M.; Sun, L.; Crooks, R. M. Preparation of Cu Nanoclusters within Dendrimer Templates. *J. Am. Chem. Soc.* **1998**, *120*, 4877-4878.
128. Wang, R.; Yang, J.; Zheng, Z.; Carducci, M. D.; Jiao, J.; Seraphin, S. Dendron-Controlled Nucleation and Growth of Gold Nanoparticles. *Angew. Chem. Int. Ed.* **2001**, *40*, 549-552.
129. Zheng, J.; Stevenson, M. S.; Hikida, R. S.; Patten, P. G. V. Influence of pH on Dendrimer-Protected Nanoparticles. *J. Phys. Chem. B* **2002**, *106*, 1252-1255.
130. Petit, C.; Lixon, P.; Pileni, M. In Situ Synthesis of Silver Nanocluster in AOT Reverse Micelles. *J. Phys. Chem. B* **1993**, *97*, 12974-12983.
131. Suslick, K. S.; Fang, M.; Hyeon, T. Sonochemical Synthesis of Iron Colloids. *J. Am. Chem. Soc.* **1996**, *118*, 11960-11961.
132. Goodwin, J. W. *Colloidal Dispersions*, The Royal Society of Chemistry: London, **1982**.
133. Aiken, J. D.; Lin, Y.; Finke, R. G. A Perspective on Nanocluster Catalysis: Polyoxoanion and $(n\text{-C}_4\text{H}_9)_4\text{N}^+$ Stabilized Ir(0)₋₃₀₀ Nanocluster 'Soluble Heterogeneous Catalysts'. *J. Mol. Catal. A: Chem.* **1996**, *114*, 29-51.
134. Hirtzel, C. S.; Rajagopalan, R. *Colloidal Phenomena: Advanced Topics*, New Jersey, **1985**, 27.
135. Yang J.; Deivaraj T. C.; Too H. P.; Lee J. Y. Acetate Stabilization of Metal Nanoparticles and Its Role in the Preparation of Metal Nanoparticles in Ethylene Glycol. *Langmuir* **2004**, *20*, 4241-4245.
136. Hunter, R. J. *Foundations of Colloid Science*, Vol. 1, Oxford University Press, New York, **1986**.

137. Bard, A. J.; Faulkner, L.R. *Electrochemical Methods: Fundamentals and Applications*, Wiley, New York, **1980**.
138. Hunter, R. J. In *Foundations of Colloid Science*, Oxford University Press: New York, **1987**, 1, 316.
139. Duteil, A.; Schmid, G.; Meyer-Zaika, W. Ligand Stabilized Nickel Colloids. *J. Chem. Soc. Chem. Commun.* **1995**, 1, 31-32.
140. Teranishi, T.; Miyake, M. Size Control of Palladium Nanoparticles and Their Crystal Structures. *Chem. Mat.* **1998**, 10, 594-600.
141. Li, Y.; Hong, X. M.; Collard, D. M.; El-Sayed, M. A. Suzuki Cross-Coupling Reactions Catalyzed by Palladium Nanoparticles in Aqueous Solution. *Org. Lett.* **2000**, 2, 2385-2388.
142. Narayanan, R.; El-Sayed, M. A. Effect of Catalytic Activity on the Metallic Nanoparticle Size Distribution: Electron-Transfer Reaction between $\text{Fe}(\text{CN})_6$ and Thiosulfate Ions Catalyzed by PVP-Platinum Nanoparticles. *J. Phys. Chem. B* **2003**, 107, 12416-12424.
143. Hirai, H.; Yakura, N. Protecting Polymers in Suspension of Metal Nanoparticles. *Polym. Adv. Tech.* **2001**, 12, 724-733.
144. Borsla, A.; Wilhelm, A. M.; Delmas, H. Hydrogenation of Olefins in Aqueous Phase, Catalyzed by Polymer-Protected Rhodium Colloids: Kinetic Study. *Catal. Today.* **2001**, 66, 389-395.
145. Narayanan, R.; El-Sayed, M. A. Effect of Nanocatalysis in Colloidal Solution on the Tetrahedral and Cubic Nanoparticle SHAPE: Electron-Transfer Reaction Catalyzed by Platinum Nanoparticles. *J. Phys. Chem. B* **2004**, 108, 5726-5733.
146. Ahmadi, T. S.; Wang, Z. L.; Green, T. C.; Henglein, A.; El-Sayed, M. A. Shape-Controlled Synthesis of Colloidal Platinum Nanoparticles. *Science* **1996**, 272, 1924-1925.
147. Li, Y.; Petroski, J.; El-Sayed, M. A. Activation Energy of the Reaction between Hexacyanoferrate(III) and Thiosulfate Ions Catalyzed by Platinum Nanoparticles. *J. Phys. Chem. B* **2000**, 104, 10956-10359.
148. Lakina, N. V.; Sul'man, E. M.; Matveeva, V. G.; Mikhailov, I. A. Selective Oxidation of L-Sorbose in the Synthesis of L-Ascorbic Acid. *Pharm. Chem. J.* **2000**, 34, 138-140.
149. Sulman, E.; Lakina, N.; Sulman, M.; Ankudinova, T.; Matveeva, V.; Sidorov, A.; Sidorovt, S. Selective oxidation of monosaccharides using Pt-containing catalysts. *Stud. Surf. Sci. Catal.* **2000**, 130, 1787-1792.
150. Dassenoy, F.; Philippot, K.; Ould Ely, T.; Amiens, C.; Lecante, P.; Snoeck, E.; Mosset, A.; Casanove, M. J.; Chaudret, B. Platinum Nanoparticles Stabilized by CO and Octanethiol Ligands or Polymers: FT-IR, NMR, HREM and WAXS Studies. *New J. Chem.* **1998**, 22, 703-712.
151. Aiken III, J. D.; Finke, R. G. A Review of Modern Transition-Metal Nanoclusters: Their Synthesis, Characterization, and Applications in Catalysis. *J. Mol. Catal. A: Chem.* **1999**, 145, 1-44.
152. Lin, Y.; Finke, R. G. Novel Polyoxoanion- and Bu_4N^+ -Stabilized, Isolable, and Redissolvable, 20-30-Å. Ir³⁰⁰⁻⁹⁰⁰ Nanoclusters: The Kinetically Controlled Synthesis, Characterization, and Mechanism of Formation of Organic Solvent-Soluble, Reproducible Size, and Reproducible Catalytic Activity Metal Nanoclusters. *J. Am. Chem. Soc.* **1994**, 116, 8335-8353.

153. Schmid, G.; Pfeil, R.; Boese, R.; Bandermann, F.; Meyers, S.; Calis, G. H.; Van Der Velden, J. W. $[\text{Au}_{55}\{\text{P}(\text{C}_6\text{H}_5)_3\}_{12}\text{C}_6]$ -A Gold Cluster of Unusual Size. *Chem. Ber.* **1981**, *114*, 3634-3642.
154. Weare, W.W.; Reed, S.M.; Warner, M.G.; Hutchison, J.E. Improved Synthesis of Small (d core \approx 1.5 nm) Phosphine-Stabilized Gold Nanoparticles. *J. Am. Chem. Soc.* **2000**, *122*, 12890-12891.
155. Amiens, C.; Decaro, D.; Chaudret, B.; Bradley, J. S.; Mazel, R.; Roucau, C. Selective Synthesis, Characterization, and Spectroscopic Studies on a Novel Class of Reduced Platinum and Palladium Particles Stabilized by Carbonyl and Phosphine Ligands. *J. Am. Chem. Soc.* **1993**, *115*, 11638-11639.
156. Chen, S.; Kimura, K. Synthesis of Thiolate-Stabilized Platinum Nanoparticles in Protolytic Solvents as Isolable Colloids. *J. Phys. Chem. B* **2001**, *105*, 5397-5403.
157. Dasog, M.; Scott, R. W. J. Understanding the Oxidative Stability of Gold Monolayer-Protected Clusters in the Presence of Halide ions under Ambient Conditions. *Langmuir*. **2007**, *23*, 3381-3387.
158. Hou, W. B.; Dasog, M.; Scott, R. W. J. Probing the Relative Stability of Thiolate- and Dithiolate-Protected Au Monolayer-Protected Clusters. *Langmuir*. **2009**, *25*, 12954-12961.
159. Astruc, D.; Lu, F.; Aranzaes, J. R. Nanoparticles as Recyclable Catalysts: the Frontier between Homogeneous and Heterogeneous Catalysis. *Angew. Chem. Int. Ed.* **2005**, *44*, 7852-7872.
160. Zhou, Y. Recent Advances in Ionic Liquids for Synthesis of Inorganic Nano-Materials. *Current Nanoscience* **2005**, *1*, 35-42.
161. Bönnemann, H.; Braun, G.; Brijoux, W.; Brinkmann, R.; Schulze Tilling, A.; Seevogel, K.; Siepen, K. Nanoscale Colloidal Metals and Alloys Stabilized by Solvents and Surfactants Preparation and Use as Catalyst Precursors. *J. Organomet. Chem.* **1996**, *520*, 143-162.
162. Vidoni, O.; Philippot, K.; Amiens, C.; Chaudret, B.; Balmes, O.; Malm, J. O.; Bovin, J. O.; Senocq, F.; Casanove, M. J. Novel, Spongelike Ruthenium Particles of Controllable Size Stabilized Only by Organic Solvents. *Angew. Chem. Int. Ed.* **1999**, *38*, 3736-3738.
163. Guoping, L.; Wenting, L.; Yunjun, L.; Min, X.; Chunpeng, C.; Xiaoqing, W. Synthesis and Characterization of Dendrimer-Encapsulated Bimetallic Core-Shell PdPt Nanoparticles. *Chin. J. Chem.* **2012**, *30*, 541-546.
164. Zhao, M.; Crooks, R. M. Homogeneous Hydrogenation Catalysis with Monodisperse, Dendrimer-Encapsulated Pd And Pt Nanoparticles. *Angew. Chem., Int. Ed.* **1999**, *38*, 364-365.
165. Mingqi, Z.; Sun, L. Dendrimer-encapsulated transition metal nanoclusters: synthesis, characterization, and applications to catalysis. *Polym. Prepr.* **1999**, *40*, 400-401.
166. Chechik, V.; Crooks, R. M. Dendrimer-Encapsulated Pd Nanoparticles as Fluorous Phase-Soluble Catalysts. *J. Am. Chem. Soc.* **2000**, *122*, 1243-1244.
167. Crooks, R. M.; Zhao, M. Q.; Sun, L.; Chechik, V.; Yeung, L. K. Dendrimer-Encapsulated Metal Nanoparticles: Synthesis, Characterization, and Applications to Catalysis. *Acc. Chem. Res.* **2001**, *34*, 181-190.

168. Narayanan, R.; El-Sayed, M. A. Some Aspects of Colloidal Nanoparticle Stability, Catalytic Activity, and Recycling Potential. *Top. Catal.* **2008**, *47*, 15-21.
169. Wang, Y.; Salmon, L.; Ruiz, J.; Astruc, D. Metallodendrimers in Three Oxidation States with Electronically Interacting Metals and Stabilization of Size-Selected Gold Nanoparticles. *Nat. Commun.* **2014**, *5*, 3489-3500.
170. Schmid, G.; Corain, B. Nanoparticulated Gold: Syntheses, Structures, Electronics, and Reactivities. *Eur. J. Inorg. Chem.* **2003**, *17*, 3081-3098.
171. Akamatsu, K.; Hasegawa, J.; Nawafune, H.; Katayama, H.; Ozawa, F. Highly Reactive Intermediate-Functionalized Gold Clusters: Synthesis and Immobilization on Silica Supports through Amide-Forming Coupling. *J. Mater. Chem.* **2002**, *12*, 2862-2865.
172. Hao, E.; Schatz, G. C.; Hupp, J. T. Synthesis and optical properties of anisotropic metal nanoparticles. *J. Fluoresc.* **2004**, *14*, 331-341.
173. Burda, C.; Chen, X.; Narayanan, R.; El-Sayed, M. A. Chemistry and Properties of Nanocrystals of Different Shapes. *Chem. Rev.* **2005**, *105*, 1025-1102.
174. Xia, Y.; Yang, P.; Sun, Y.; Wu, Y.; Mayers, B.; Gates, B.; Yin, Y.; Kim, F.; Yan, H. One-Dimensional Nanostructures: Synthesis, Characterization, and Applications. *Adv. Mater.* **2003**, *15*, 353-389.
175. Pileni, M. P. The Role of Soft Colloidal Templates in Controlling the Size and Shape of Inorganic Nanocrystals. *Nat. Mater.* **2003**, *2*, 145-149.
176. Jin, R. C. Cao, Y. W.; Mirkin, C. A.; Kelly, K. L.; Schatz, G. C.; Zheng, J. G. Photoinduced Conversion of Silver Nanospheres to Nanoprisms. *Science* **2001**, *294*, 1901-1903.
177. Murphy, C. J.; Sau, T. K.; Gole, A. M.; Orendorff, C. J. G.; Gou, J. L.; Hunyadi, S. E.; Li, T. Anisotropic Metal Nanoparticles: Synthesis, Assembly, and Optical Applications. *J. Phys. Chem. B* **2005**, *109*, 13857-13870.
178. Link, S. El-Sayed, M. A. Spectral Properties and Relaxation Dynamics of Surface Plasmon Electronic Oscillations in Gold and Silver Nanodots and Nanorods. *J. Phys. Chem. B* **1999**, *103*, 8410-8426.
179. Link, S.; El-Sayed, M. A. Shape and Size Dependence of Radiative, Non-Radiative and Photothermal Properties of Gold Nanocrystals. *Int. Rev. Phys. Chem.* **2000**, *19*, 409-453.
180. Link, S.; El-Sayed, M. A. Optical Properties and Ultrafast Dynamics of Metallic Nanocrystals. *Annu. Rev. Phys. Chem.* **2003**, *54*, 331-366.
181. El-Sayed, M. A. Some Interesting Properties of Metals Confined in Time and Nanometer Space of Different Shapes. *Acc. Chem. Res.* **2001**, *34*, 257-264.
182. Kelly, K. L.; Coronado, E.; Zhao, L. L.; Schatz, G. C. The Optical Properties of Metal Nanoparticles: The Influence of Size, Shape, and Dielectric Environment. *J. Phys. Chem. B* **2003**, *107*, 668-677.
183. Eustis, S.; El-Sayed, M.A. Why Gold Nanoparticles are More Precious than Pretty Gold: Noble Metal Surface Plasmon Resonance and Its Enhancement of the Radiative and Nonradiative Properties of Nanocrystals of Different Shapes. *Chem. Soc. Rev.* **2006**, *35*, 209-217.
184. Kerker, M. *The Scattering of Light and Other Electromagnetic Radiation*, New York: Academic, **1969**.
185. Bohren, C. F.; Huffman, D. R. *Absorption and Scattering of Light by Small Particles*, New York: Wiley, **1983**.

186. Papavassiliou, G. C. Optical Properties of Small Metal Particles. *Prog. Solid State Chem.* **1979**, *12*, 185-271.
187. Lavrich, D. J.; Wetterer, S. M.; Bernasek, S. L.; Scoles, G. Physisorption and Chemisorption of Alkanethiols and Alkyl Sulfides on Au (111). *J. Phys. Chem. B* **1998**, *102*, 3456-3465.
188. Maier, J. Defect Chemistry and Ionic Conductivity in Thin Films. *Solid State Ionics* **1987**, *23*, 59-67.
189. Alivisatos, A. P. Perspectives on the Physical Chemistry of Semiconductor Nanocrystals. *J. Phys. Chem.* **1996**, *100*, 13226-13239.
190. Ellert, C.; Schmidt, M.; Schmitt, C.; Reiners, T.; Haberland, H. Temperature Dependence of the Optical Response of Small, Open Shell Sodium Clusters. *Phys. Rev. Lett.* **1995**, *75*, 1731-1734.
191. Halperin, W. P. Quantum Size Effects in Metal Particles. *Rev. Mod. Phys.* **1986**, *58*, 533-606.
192. Simon, U. Charge Transport in Nanoparticle Arrangements, *Adv. Mater.* **1998**, *10*, 1487-1492.
193. Alivisatos, A. P. Birth of a Nanoscience Building Block. *ACS Nano* **2008**, *2*, 1514-1516.
194. Kailasa, S. K.; Cheng, K. H.; Wu, H. F.. Semiconductor Nanomaterials-Based Fluorescence Spectroscopic and Matrix-Assisted Laser Desorption/Ionization (MALDI) Mass Spectrometric Approaches to Proteome Analysis. *Materials* **2013**, *6*, 5763-5795.
195. Karch, J.; Birringer, R.; Gleiter, H. Ceramics Ductile at Low Temperature. *Nature* **1987**, *330*, 556-558.
196. Edelstein, A. S.; Cammarata, R. C. *Nanomaterials: Synthesis, Properties, and Applications*, London Institute of Physics. **1996**, Chapter 13, 323.
197. Castro, T.; Reifengerger, R.; Choi, E.; Andres, R. P. Size-Dependent Melting Temperature of Individual Nanometer-sized Metallic Clusters. *Phys. rev. B* **1990**, *13*, 8548.
198. Buffat, P.; Borel, J. P. Size Effect on the Melting Temperature of Gold Particles. *Phys. Rev. A* **1976**, *13*, 2287-2298.
199. Allen, G. L.; Bayles, R. A.; Gile, W. W.; Jesser, W. A. Small Particle Melting of Pure Metals. *Thin Solid Films*, **1986**, *144*, 297-308.
200. Qi, W. H.; Wang, M. P. Size Effect on the Cohesive Energy of Nanoparticle. *J. Mater. Sci. Lett.* **2002**, *21*, 1743-1745.
201. Darling, S. B.; Bader, S. D. A Materials Chemistry Perspective on Nanomagnetism. *J. Mater. Chem.* **2005**, *15*, 4189-4195.
202. Jun, Y. W.; Seo, J. W.; Cheon, A. Nanoscaling Laws of Magnetic Nanoparticles and Their Applicabilities in Biomedical Sciences. *Acc. Chem. Res.* **2008**, *41*, 179-189.
203. Krishnan, K. M.; Pakhomov, A. B.; Bao, Y.; Blomqvist, P.; Chun, Y.; Gonzales, M.; Griffin, K.; Ji, X.; Roberts, B. K. Nanomagnetism and Spin Electronics: Materials, Microstructure and Novel Properties. *J. Mater. Sci.* **2006**, *41*, 793-815.
204. Kneller, E. F.; Luborsky, F. E. Particle Size Dependence of Coercivity and Remanence of Single-Domain Particles. *Appl. Phys.* **1963**, *34*, 656-658.

205. Lee, J. S.; Cha, J. M.; Yoon, H. Y.; Lee, J. K.; Kim, Y. K. Magnetic Multi-Granule Nanoclusters: A Model System That Exhibits Universal Size Effect of Magnetic Coercivity. *Sci. rep.* **2015**, *5*, 12135-12141.
206. Sanchez, C.; Julián, B.; Belleville, P.; Popall, M. Applications of Hybrid Organic-Inorganic Nanocomposites. *J. Mater. Chem.* **2005**, *15*, 3559-3592.
207. Schmidt, H.; Kaiser, A.; Patzelt, H.; Sholze, H. Mechanical and Physical Properties of Amorphous Solids Based on (CH₃)₂SiO-SiO₂ Gels. *J. Phys.* **1982**, *12*, 275-278.
208. Livage, J.; Henry, M.; Sanchez, C. Sol-Gel Chemistry of Transition Metal Oxides. *Prog. Solid State Chem.* **1988**, *18*, 259-341.
209. Avnir, D.; Levy, D.; Reisfeld, R. The Nature of the Silica Cage as Reflected by Spectral Changes and Enhanced Photostability of Trapped Rhodamine 6G. *J. Phys. Chem.* **1984**, *88*, 5956-5959.
210. Brinker, C. J.; Scherrer, G. W. *Sol-Gel Science, The Physics and Chemistry of Sol-Gel Processing*. Academic Press, San Diego, **1990**.
211. Sanchez, C.; Soler-Illia, G. J. de A. A.; Ribot, F.; Lalot, T.; Mayer, C. R.; Cabuil, V. Designed Hybrid Organic-Inorganic Nanocomposites from Functional Nanobuilding Blocks. *Chem. Mater.* **2001**, *13*, 3061-3083.
212. Schubert, U.; Huesing, N.; Lorenz, A. Hybrid Inorganic-Organic Materials by Sol-Gel Processing of Organofunctional Metal Alkoxides. *Chem. Mater.* **1995**, *7*, 2010-2027.
213. Dunn, B.; Zink, J. I. Optical Properties of Sol-Gel Glasses Doped with Organic Molecules. *J. Mater. Chem.* **1991**, *1*, 903-913.
214. Sanchez, C.; Gómez-Romero, P. *Functional Hybrid Materials*, Wiley VCH, Weinheim, **2004**.
215. Kojima, Y.; Usuki, A.; Kawasumi, M.; Okada, A.; Fukushima, Y.; Kurauchi, T.; Kamigaito, O. Mechanical Properties of Nylon 6-Clay Hybrid. *J. Mater. Res.* **1993**, *8*, 1185-1189.
216. Alexandre, M.; Dubois, P. Polymer-Layered Silicate Nanocomposites: Preparation, Properties and Uses of a New Class of Materials. *Mater. Sci. Eng. Rep.* **2000**, *28*, 1-63.
217. Schmidt, D.; Shah, D.; Giannelis, E. P. New Advances in Polymer/Layered Silicate Nanocomposites. *Current Opinion in Solid State and Materials Science*, **2002**, *6*, 205-212.
218. Ray, S. S.; Okamoto, M. Polymer/Layered Silicate Nanocomposite: A Review from Preparation to Processing. *Progress in Polymer Science* **2003**, *28*, 1539-1641.
219. Auer, E.; Freund, A.; Pietsch, J.; Tacke, T. Carbons as Supports for Industrial Precious Metal Catalysts. *Appl. Catal. A* **1998**, *173*, 259-271.
220. Caruso, R. A.; Antonietti, M. Sol-Gel Nanocoating: An Approach to the Preparation of Structured Materials. *Chem. Mater.* **2001**, *13*, 3272-3282.
221. Thamima, M.; Karuppuchamy, S. Biosynthesis of Titanium Dioxide and Zinc Oxide Nanoparticles from Natural Sources: A Review. *Advanced Science, Engineering and Medicine* **2014**, *6*, 1-8.
222. Mbonyirivuze, A.; Omollo, I.; Ngom, B. D.; Mwakikunga, B.; Dhlamini, S. M.; Park, E.; Maaza, M. Natural Dye Sensitizer for Grätzel Cells: Sepia Melanin. *Physics and material chemistry* **2015**, *3*, 1-6.

223. Maurya, A. Chauhan, P. Mishra, A. and Pandey, A. K. Surface Functionalization of TiO₂ with Plant Extracts and their Combined Antimicrobial Activities against E. Faecalis And E. Coli. *J. Res. Updates Polym. Sci.* **2012**, *1*, 43-51.
224. Schmid, G.; Morun, B.; Malm, J. O. Pt₃₀₉Phen₁₃₆*O_{30 ± 10}, a Four-Shell Platinum Cluster. *Angew. Chem. Int. Ed.* **1989**, *28*, 778-780.
225. Schmid, G. *Clusters and Colloids, from Theory to Applications*; VCH, Weinheim, **1994**.
226. Lu, C.; Wu, N.; Jiao, X.; Luo, C.; Cao, W. Micropatterns Constructed from Au Nanoparticles. *Chem. Commun.* **2003**, 1056-1057.
227. Holtz, J. H.; Asher, S. A. Polymerized Colloidal Crystal Hydrogel Films as Intelligent Chemical Sensing Materials. *Nature* **1997**, *389*, 829-832.
228. Wilson, R. The Use of Gold Nanoparticles in Diagnostics and Detection. *Chem. Soc. Rev.* **2008**, *37*, 2028–2045.
229. Chen, H.; Kou, X.; Yang, Z.; Ni, W.; Wang, J. Shape- and Size-Dependent Refractive Index Sensitivity of Gold Nanoparticles. *Langmuir* **2008**, *24*, 5233-5237.
230. Lee, K. S.; El-Sayed, M. A. Gold and Silver Nanoparticles in Sensing and Imaging: Sensitivity of Plasmon Response to Size, Shape, and Metal Composition. *J. Phys. Chem. B* **2006**, *110*, 19220-19225.
231. Nie, S.; Emery, S. R. Probing Single Molecules and Single Nanoparticles by Surface-Enhanced Raman Scattering. *Science* **1997**, *275*, 1102-1106.
232. Krug, J. T.; Wang, G. D.; Emory, S. R.; Nie, S. Efficient Raman Enhancement and Intermittent Light Emission Observed in Single Gold Nanocrystals. *J. Am. Chem. Soc.* **1999**, *121*, 9208-9214.
233. Rodriguez-Lorenzo, L.; Alvarez-Puebla, R. A.; de Abajo, F. J. G.; LizMarzan, L. M. Surface Enhanced Raman Scattering Using Star-Shaped Gold Colloidal Nanoparticles. *J. Phys. Chem. C* **2010**, *114*, 7336-7340.
234. Hirsch, L. R.; Stassord, R. J.; Bankson, J. A.; Sershen, S. R.; Rivera, B.; Price, R. E.; Hazle, J. D.; Halas, N. J.; West, J. L. Nanoshell-mediated Near-infrared Thermal Therapy of Tumors under Magnetic Resonance Guidance. *Proc. Natl. Acad. Sci.* **2003**, *100*, 13549-13554.
235. Haes, A. J.; Hall, W. P.; Chang, L.; Klein, W. L.; Van Duyne, R. P. A Localized Surface Plasmon Resonance Biosensor: First Steps toward an Assay for Alzheimer's Disease. *Nano Lett.* **2004**, *6*, 1029-1034.
236. Tarcha, P. J.; Desaja-Gonzalez, J.; Rodriguez-Llorente, S.; Aroca, R. Surface-Enhanced Fluorescence on SiO₂-Coated Silver Island Films. *Appl. Spectrosc.* **1993**, *53*, 43-48.
237. Elghanian, R.; Storhoff, J. J.; Mucic, R. C.; Letsinger, R. L.; Mirkin, C. A. Selective Colorimetric Detection of Polynucleotides Based on the Distance-Dependent Optical Properties of Gold Nanoparticles. *Science* **1997**, *277*, 1078-1081.
238. Pipino, A. C. R.; Schatz, G. C.; Van Duyne, R. P. Surface-enhanced Second-harmonic Diffraction: Experimental Investigation of Selective Enhancement. *Phys. Rev. B* **1996**, *53*, 4162-4169.
239. Krenn, J. R.; Dereux, A.; Weeber, J. C.; Bourillot, E.; Lacroute, Y.; Coadonnet, J. P. Squeezing the Optical Near-Field Zone by Plasmon Coupling of Metallic Nanoparticles. *Phys. Rev. Lett.* **1999**, *82*, 2590-2593.

240. Kamat, P. V.; Meisel, D. Semiconductor Nanoclusters-Physical, Chemical, and Catalytic Aspects; Studies in Surface Science and Catalysis Amsterdam: Elsevier, **1997**.
241. Kamat, P. V. Photochemistry on Nonreactive and Reactive (Semiconductor) Surfaces. *Chem. Rev.* **1993**, *93*, 267-300.
242. Link, S.; El-Sayed, M. A. Size and Temperature Dependence of the Plasmon Absorption of Colloidal Gold Nanoparticles. *J. Phys. Chem. B* **1999**, *103*, 4212-4217.
243. Rao, C. N. R.; Kulkarni, G. U.; Thomas, P. J.; Edwards, P. P. Metal Nanoparticles and Their Assemblies. *Chem. Soc. Rev.* **2000**, *29*, 27-35.
244. Astruc, D.; Lu, F.; Aranzaes, J. R. Nanoparticles as Recyclable Catalysts: The Frontier between Homogeneous and Heterogeneous Catalysis. *Angew. Chem. Int. Ed.* **2005**, *44*, 7852-7872.
245. De Vries, J. G. A unifying mechanism for all high-temperature Heck reactions. The role of palladium colloids and anionic species. *Dalton Trans.* **2006**, 421-429.
246. Astruc, D. Palladium Nanoparticles as Efficient Green Homogeneous and Heterogeneous Carbon-Carbon Coupling Precatalysts: A Unifying View. *Inorg. Chem.* **2007**, *46*, 1884-1894.
247. Roucoux, A.; Schulz, J.; Patin, H. Reduced Transition Metal Colloids: A Novel Family of Reusable Catalysts. *Chem. Rev.* **2002**, *102*, 3757-3778.
248. Pradhan, N.; Pal, A.; Pal, T. Catalytic Reduction of Aromatic Nitro Compounds by Coinage Metal Nanoparticles. *Langmuir* **2001**, *17*, 1800-1802.
249. Rashid, Md. H.; Bhattacharjee, R. R.; Kotal, A.; Mandal, T. K. Synthesis of Spongy Gold Nanocrystals with Pronounced Catalytic Activities. *Langmuir* **2006**, *22*, 7141-7143.
250. Robinson, D. M.; Go, Y. B.; Greenblatt, M.; Dismukes, G. C. Water Oxidation by λ -MnO₂: Catalysis by the Cubical Mn₄O₄ Subcluster Obtained by Delithiation of Spinel LiMn₂O₄. *J. Am. Chem. Soc.* **2010**, *132*, 11467-11469.
251. Espinal, L.; Suib, S. L.; Rusling, J. F. Electrochemical Catalysis of Styrene Epoxidation with Films of MnO₂ Nanoparticles and H₂O₂. *J. Am. Chem. Soc.* **2004**, *126*, 7676-7682.
252. Liao, M.; Feng, J.; Luo, W.; Wang, Z.; Zhang, J.; Li, Z.; Yu, T.; Zou, Z. Co₃O₄ Nanoparticles as Robust Water Oxidation Catalysts Towards Remarkably Enhanced Photostability of a Ta₃N₅ Photoanode. *Adv. Funct. Mater.* **2012**, *22*, 3066-3074.
253. Yan, Q.; Li, X.; Zhao, Q.; Chen, G. Shape-Controlled Fabrication of the Porous Co₃O₄ Nanoflower Clusters for Efficient Catalytic Oxidation of Gaseous Toluene. *J. Hazard. Mater.* **2012**, *209*, 385-391.
254. Sivula, K.; Formal, F. L.; Grätzel, M. Solar Water Splitting: Progress Using Hematite (α -Fe₂O₃) Photoelectrodes. *ChemSusChem* **2011**, *4*, 432-449.
255. Wang, C.; Daimon, H.; Sun, S. Dumbbell-like Pt-Fe₃O₄ Nanoparticles and Their Enhanced Catalysis for Oxygen Reduction Reaction. *Nano Lett.* **2009**, *9*, 1493-1496.
256. Stratakis, M.; Garcia, H. Catalysis by Supported Gold Nanoparticles: Beyond Aerobic Oxidative Processes. *Chem. Rev.* **2012**, *112*, 4469-4506.
257. Praharaj, S.; Nath, S.; Ghosh, S. K.; Kundu, S.; Pal, T. Immobilization and Recovery of Au Nanoparticles from Anion Exchange Resin: Resin-Bound

- Nanoparticle Matrix as a Catalyst for the Reduction of 4-Nitrophenol. *Langmuir* **2004**, *20*, 9889-9892.
258. Jana, S.; Pande, S.; Panigrahi, S.; Praharaj, S.; Basu, S.; Pal, A.; Pal, T. Exploitation of Electrostatic Field Force for Immobilization and Catalytic Reduction of o-Nitrobenzoic Acid to Anthranilic Acid on Resin-bound Silver Nanocomposites. *Langmuir* **2006**, *22*, 7091-7095.
259. Lu, Y.; Mei, Y.; Ballauff, M.; Drechsler, M. Thermosensitive Core-Shell Particles as Carrier Systems for Metallic Nanoparticles. *J. Phys. Chem. B* **2006**, *110*, 3930-3937.
260. Kautz, C. Q.; Ryan, P. C. The 10 Å to 7 Å Halloysite Transition in a Tropical Soil Sequence, Costa Rica. *Clays Clay Miner.* **2003**, *51*, 252-263.
261. Hillier, S.; Ryan, P. C. Identification of Halloysite (7 Å) by Ethylene Glycol Solvation: the 'MacEwan Effect'. *Clay Miner.* **2002**, *37*, 487-496.
262. P. Berthier, *Annales de Chimie et de Physique*, **1826**, *32*, 332.
263. Prudencio, M. I.; Braga, M. A. S.; Paquet, H.; Waerenborgh, J. C.; Pereira L. C. J.; Gouveia, M. A. Clay Mineral Assemblages in Weathered Basalt Profiles from Central and Southern Portugal: Climatic Significance. *Catena* **2002**, *49*, 77-89.
264. Joussein, E.; Petit, S.; Churchman, J.; Theng, B.; Righi, D.; Delvaux, B. Halloysite Clay Minerals-A Review. *Clay Miner.* **2005**, *40*, 383-426.
265. Nakagaki, S.; Wypych, F. Nanofibrous and Nanotubular Supports for the Immobilization of Metalloporphyrins as Oxidation Catalysts. *J. Colloid Interface Sci.* **2007**, *315*, 142-157.
266. Liu, M.; Guo, B.; Du, M.; Cai, X.; Jia, D. Properties of Halloysite Nanotube-Epoxy Resin Hybrids and the Interfacial Reactions in the Systems. *Nanotechnology* **2007**, *18*, 455703-455711.
267. Yuan, P.; Southern, P. D.; Liu, Z.; Kepter, C. J. Organosilane Functionalization of Halloysite Nanotubes for Enhanced Loading and Controlled Release. *Nanotechnology* **2012**, *23*, 375705-375709.
268. Abdullayev, E.; Lvov, Y. Clay Nanotubes for Corrosion Inhibitor Encapsulation: Release Control with End Stoppers. *J. Matter. Chem.* **2010**, *20*, 6681-6687.

Materials, Instrument and Characterization Techniques

2.1 Materials

All the chemicals were of analytical grade and used without further purification. Milli-Q water was used throughout the experiment. Halloysite nanotubes, gold (III) chloride trihydrate ($\geq 99.9\%$), silver nitrate (99.9999%), sodium borohydride (NaBH_4), iron (III) chloride (FeCl_3), copper(II) chloride, 1-octadecene, and oleylamine (70%), (3-mercaptopropyl) trimethoxysilane (97%), tetraethyl orthosilicate (TEOS), trimethoxy[3-(methylamino)propyl]silane, 1,4-benzoquinone, N-[3-(trimethoxysilyl)propyl]ethylenediamine, N1-(3-trimethoxysilylpropyl) diethylenetriamine were purchased from Sigma-Aldrich. Toluene, ethanol, potassium hexacyanoferrate (II) trihydrate, sodium azide, potassium permanganate (KMnO_4) and hydrogen peroxide were obtained from Merck, India. (3-aminopropyl) triethoxysilane (APTES, 97%) was acquired from Alfa Aesar. Mercury acetate, lead nitrate, 4-nitrophenol (4-NP), cadmium acetate, ethylenediaminetetra acetic acid disodium salt, sodium hydroxide (NaOH), potassium ferricyanide, sodium chloride, cetyltrimethyl ammonium bromide (CTAB), urea, Hydrochloric acid, congo red (CR) eosin yellow (EY) and methylene blue (MB) were received from Sisco Research Laboratory, India. Methyl phenyl ether, triethanolamine (TEA), *tert*-butanol (*t*-BA) and hexanol were procured from Spectrochem, India.

2.2 Instrument and Characterization Techniques

A detailed characterization of the nanocomposites is very essential in order to ensure the quality and composition of the synthesized material. The properties of the nanocomposites are very significant to employ them for any application. If the dimensions of materials are reduced to nanoscale they have different properties from their bulk counterparts. Their structural and optical properties considerably change

when the size is reduced. Such changes in the properties of the material can make the analysis complicated. Therefore it is very significant to select the suitable characterization techniques that will give precise and clear information about the nanocomposites. The following characterization techniques were used for the present doctoral work.

2.2.1 Fourier Transform Infrared Spectroscopy

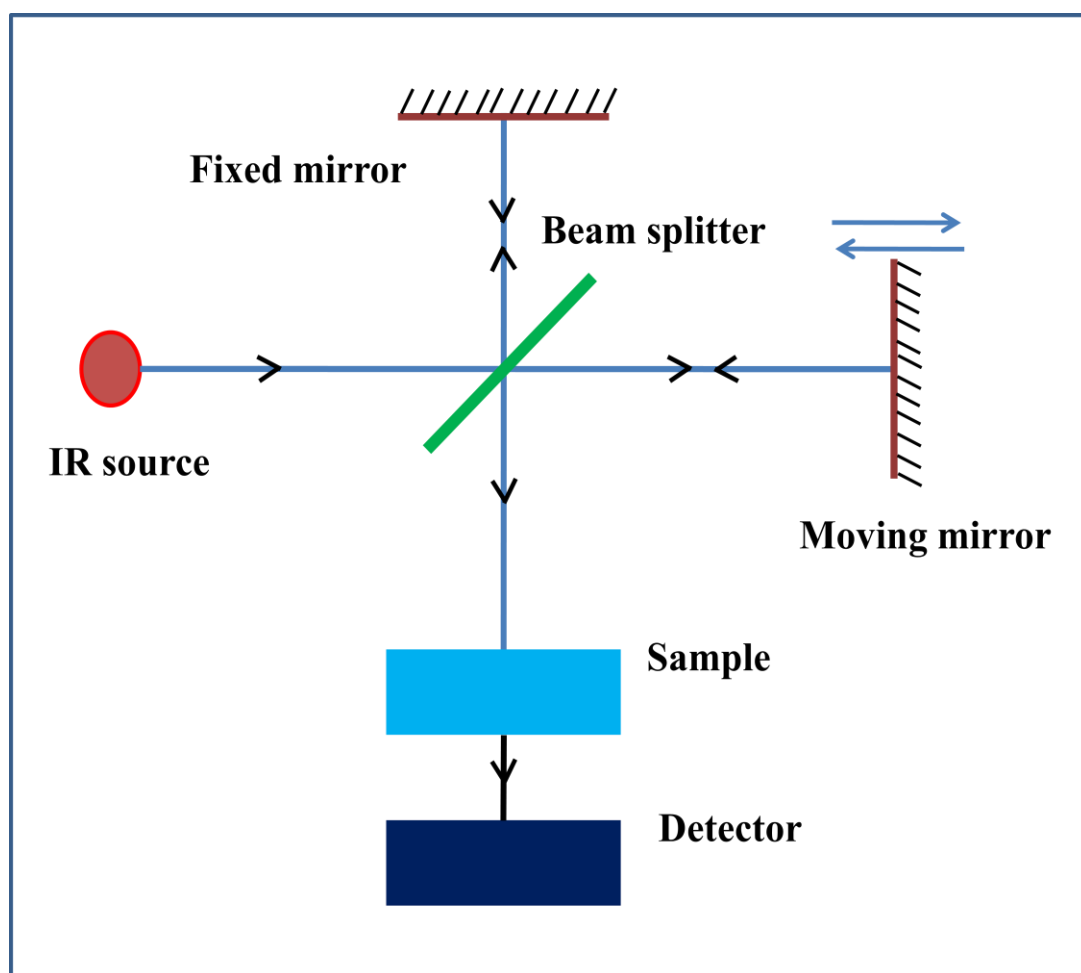


Figure 2.1: Schematic presentations of Fourier transform infrared (FTIR) spectrophotometer.

Fourier transform infrared (FTIR) spectroscopy is the excellent technique that provides structural information about the chemical bonding or molecular structure of the materials. IR spectrophotometer consists of primarily source, monochromator and detector.^{1,2} Figure 2.1 shows the schematic presentations of FTIR spectrophotometer. During this measurement process, the materials are exposed with infrared radiation which excites the characteristic vibrational modes in the chemically bonded functional groups of the molecule. The vibrational spectrum of the materials is considered to be a unique physical property and is characteristic of the molecule.

The infrared spectrum can be utilized as a fingerprint of the material. The infrared regions of the electromagnetic spectrum is divided into three parts; the near-, mid- and far- infrared, named for their relation to the visible spectrum. The lower energy far-infrared, approximately $400\text{-}10\text{ cm}^{-1}$ may be used for rotational spectroscopy. The mid-infrared, approximately $4000\text{-}400\text{ cm}^{-1}$ may be utilized to study the fundamental vibrations and associated rotational-vibational structure, while the higher energy near-IR ($14000\text{-}4000\text{ cm}^{-1}$) can excite overtone or harmonic vibrations. Infrared spectrum appears only when the vibrations amongst bonded atoms produces a change in the permanent electric dipole moment of the material. Those bonds have a permanent electric dipole moment that changes as a function of time, which are capable of absorbing IR radiation. Homonuclear or symmetric diatomic molecules such as H_2 , O_2 , Cl_2 etc., do not absorb IR radiation because they do not have permanent electric dipole moment. Alternatively, heteronuclear diatomic molecules such as CO , HCl , NO etc., do possess permanent electric dipole moment and hence are IR active. It is sensible to suppose that the more polar a bond, the more intense will be IR spectrum appearing from the vibrations of that bond. During this measurement time, powdered samples were well mixed with the standard KBr powder. FTIR spectroscopy measurements of the samples were carried out in the range of $500\text{ to }4000\text{ cm}^{-1}$ using JASCO FT/IR 6300. All the FTIR spectra were analyzed in KBr pellets in the transmission mode. No of scans was fixed to 50 with a resolution of 2 cm^{-1} .

2.2.2 UV-Vis Absorption Spectroscopy

UV-Vis spectroscopy is one of the most common and fundamental technique that records the transmitted or reflected light from the material and presents information about the absorption signals due to the electronic transitions. The spectroscopy is also known as electronic spectroscopy. The electronic spectra of molecules are obtained due to the absorption of UV and visible regions of electromagnetic spectrum. It provides about the information regarding the size, shape and degree of aggregation of nanoparticles.^{3,4} The frequency and width of the surface plasmon depend on the size and shape of the metal nanoparticles and the dielectric constant of the metal itself as well as the medium surrounding it.⁵⁻⁸ It is also an excellent technique to determine the band gap energy of semiconducting material. This UV-Vis spectrometer can operate in two modes (i) transmission and (ii) reflection mode. In transmission mode usually the well-dispersed colloidal NPs in solvent are used.

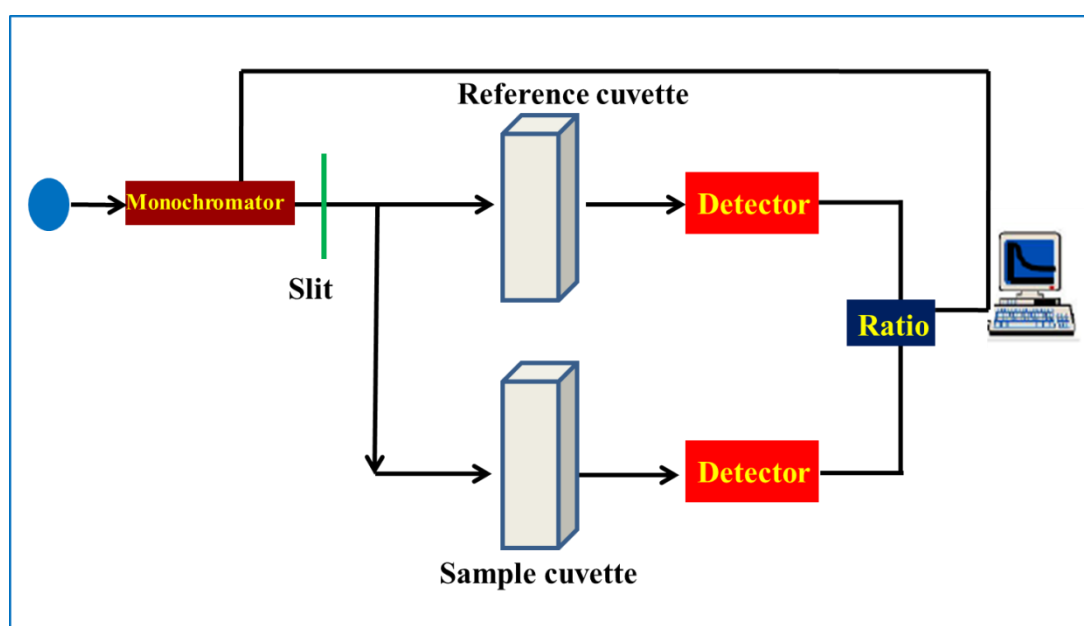


Figure 2.2: Schematic presentations of UV-Vis spectrophotometer in transmission mode.

The optical measurements for opaque thin films and those NPs which are not dispersible in solvents are recorded in the diffuse reflectance (DRS) mode. Intensity of spectral lines depends on three main factors that are transition probability,

population of states and concentration of the material and path length. Transition probability is governed by quantum mechanical selection rules. Population of states is the number of atoms or molecules initially in the state from which the transition occurs. This is usually governed by the equation, $N_{\text{upper}} / N_{\text{lower}} = \exp(-\Delta E/kT)$; Where, $\Delta E = E_{\text{upper}} - E_{\text{lower}}$, T = temperature (K), k = Boltzman's Constant = 1.38×10^{-23} J/K. The concentration of the sample and path length is also very important factor for the energy absorption. Based on this, Beer-Lambert law is often written as,

$$A = \log(I_0/I_t) = \epsilon cl \quad (2.1)$$

where, A is the measured absorbance, I_0 is the intensity of the incident light at a given wavelength, I_t is the transmitted intensity, l is the path length of the sample, and c is the concentration of the absorbing species. For each species and wavelength, ϵ is a constant known as the molar absorptivity or extinction coefficient. This constant is a fundamental molecular property in a given solvent at a particular temperature and pressure. Basically, absorbance is directly proportional to the concentration, where the path length and molar extinction coefficient are supposed to be constant for the particular measurement. The source utilized for the UV and visible light are deuterium and tungsten lamps respectively and the detector used is usually photomultiplier tube. The schematic presentation of UV-Vis Spectrophotometer in transmission mode is shown in Figure 2.2. In the present work, UV-visible absorption spectra were recorded at room temperature using a Shimadzu spectrometer, UV-2600 and taking the solutions in a 1 cm quartz cuvette. The UV-visible diffuse reflectance absorption spectrum of the nanocomposites was obtained using the same spectrophotometer (Shimadzu, Japan) equipped with a diffuse reflectance accessory.

2.2.3 Nuclear Magnetic Resonance Spectroscopy

Nuclear magnetic resonance (NMR) spectroscopy was used to elucidate about the structural information of a molecule and determine the content and purity of a sample, especially in terms of chemical environment. NMR spectroscopy technique is a non-

destructive method that is valuable when recovery of the sample is important. The sensitivity of NMR changes significantly depending on the observed nucleus, its abundance and its chemical environment. NMR spectrum can be broadened due to the paramagnetic components in the sample which do not affect the resolution of Infrared or Raman spectra. NMR spectroscopy was applied to measure the transitions between nuclear spin energy levels in the presence of an external magnetic field. The energies of the transitions between nuclear spin energy levels are sensitive to the local chemical environment of the nuclei. NMR spectroscopy can be employed to any nucleus having a spin $I > 0$ although some nuclei have low abundance or low sensitivities especially in the solid samples.^{9,10} Resolutions in solid state spectrum are weak with broader line width and lower signal-to-noise ratios as compared to liquid samples. In nuclear magnetic resonance, magic-angle spinning (MAS) is a technique usually applied to perform experiments in solid-state NMR spectroscopy. High resolution spectrum of solids is obtained from a combination of magic angle spinning (MAS) and pulse sequences provide compositional and structural information of the sample. By spinning the sample with a frequency of 1-130 kHz with a magic angle ($\theta_m = 54.74^\circ$, $\cos^2\theta_m=1/3$) with respect to the direction of the magnetic field, normally the broader lines become narrower, which increase the resolution for identification and better analysis of the spectrum.

A nuclear spin generally experiences greater number of interactions like dipolar, chemical shift anisotropy, quadrupolar leading to very broad lines. However, these three interactions in solids samples are orientation-dependent and can be averaged by MAS. Nuclear-electron interactions occur in case of chemical shift anisotropy, it averages to a non-zero value. In liquid organic compounds, most of the interaction averages out because of the fast time averaged molecular motions that take place.¹¹ Similar phenomenon is followed in solid samples, resulting into narrower signals giving rise to isotropic value and spinning side bands which happen at multiples of the spinning side bands and can be utilized to determine the chemical shift anisotropy. The solid state ^{29}Si and ^{13}C cross-polarization magic-angle spinning (CPMAS) NMR spectra were obtained using a JEOL JNM-ECX400II spectrometer.

2.2.4 CHNS Elemental Analyzer

CHNS elemental analyzer is an experimental technique that provides the rapid determination of carbon, hydrogen, nitrogen and sulphur in organic matrices and other types of materials. The method is widely used in variety of sample types, including solids, liquids, volatile and viscous samples, in the field of pharmaceuticals, polymers, chemicals, environment, food and energy. The name derives from the four primary elements measured by the device: carbon (C), hydrogen (H), nitrogen (N) and sulphur (S).

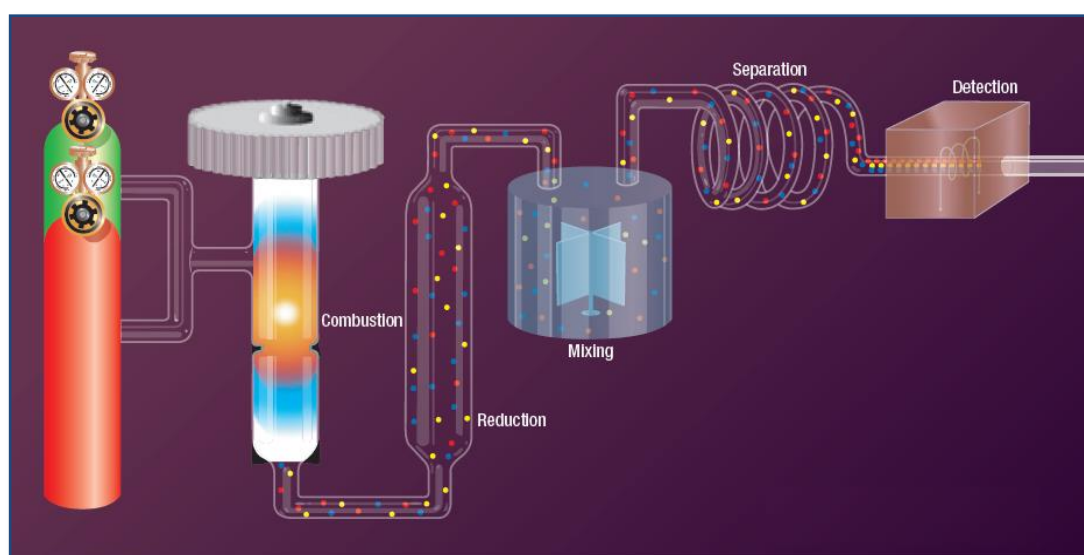


Figure 2.3: Schematic presentation of 2400 Series II CHNS analysis. (Source: www.perkinelmer.com)

In this method, CHNS analysis requires high temperature combustion in the presence of an oxygen-rich environment with combustion reagents and is based on the classical Pregl-Dumas method. The material is placed into a high temperature furnace and combusted in pure oxygen. This combustion can be performed under both static conditions i.e.; introduction of a set volume of oxygen or dynamic conditions i.e.; a constant flow of oxygen for a set period of time. Catalysts have been added usually to the combustion tube in order to assist conversion. In the combustion process (furnace at 1000°C), carbon is converted to carbon dioxide (CO_2), hydrogen to water (H_2O),

nitrogen to nitrogen gas (N₂) or oxides of nitrogen and sulphur to sulphur dioxide (SO₂). The resulting combustion products are then passed to the Gas Control Zone of the elemental analyzers. The schematic of CHNS analysis is shown in Figure 2.3. CHNS analysis was done by PerkinElmer 2400 Series II CHNS Elemental Analyzer.

2.2.5 X-ray Diffraction Spectroscopy

X-ray diffraction (XRD) is a fast and nondestructive technique. It is widely used to realize structural properties of materials and obtain information about crystal structure or phase, lattice parameters, crystallite size and orientation of single crystals.¹²⁻¹⁵ This technique is appropriate for thin films, bulk and nanomaterials. In XRD, a collimated monochromatic beam of X-rays is incident on the material for diffraction to occur. A constructive interference takes place only for certain θ 's correlating to those (hkl) plane, where path difference is an integral multiple (n) of wavelength. Based on this, the Bragg's condition is simply written by,

$$n\lambda = 2d \sin \theta \quad (2.2)$$

Where, λ is the wavelength of the incident X-ray, d is the interplaner distance, θ is the scattering angle and n is an integer-called order of diffraction. These X-ray can penetrate deep into the material and provide information about the structural arrangement of atoms and molecules. X-rays are diffracted by the oriented crystallites at a particular angle to fulfil the Bragg's condition. As the value of θ and λ is known, one can evaluate the interplaner spacing. The XRD can be taken in diverse modes such as θ - 2θ scan mode, θ - 2θ rocking curve and ϕ scan. In the θ - 2θ scan mode, a monochromatic beam of X-ray is incident on the material at an angle of θ with the material surface. The detector motion is coupled with the X-ray source in such a way that detector motion always makes an angle 2θ with the incident direction of the X-ray beam. The resulting spectrum is a plot against the intensity versus 2θ . Schematic view of XRD is shown in Figure 2.4.

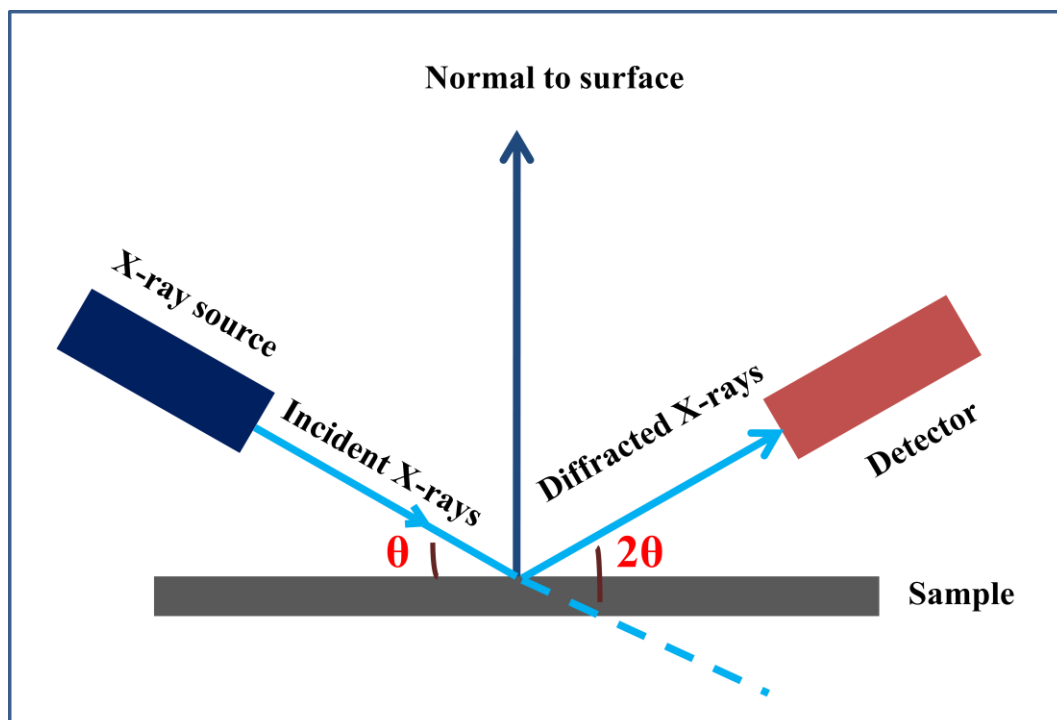


Figure 2.4: Schematic representation of X-ray Diffraction. The θ - 2θ scan maintains these angles with the sample, detector and X-ray source. Only planes of atoms that share this normal will be seen in the θ - 2θ scan.

Nanomaterials have smaller sized crystallites and considerable strains due to surface effects, causing significant peak broadening and shifts in the peak positions with respect to standard data. The crystallinity and particle size of the nanoparticles are often experimentally calculated by X-rays diffraction.¹⁶ The particle size is calculated using the Scherrer formula,¹⁷

$$t = \frac{k\lambda}{\beta \cos \theta} \quad (2.3)$$

where, k is the Scherrer's Constant ≈ 0.9 , β is the intensity at FWHM (Full Width at Half Maximum) in terms of 2θ and t is the thickness (particle size). Powder X-ray diffraction patterns were recorded on a RIGAKU MiniFlex II powder diffractometer using Cu $K\alpha$ radiation with 35 kV beam voltage and 15 mA beam current.

2.2.6 Scanning Electron Microscopy

Scanning electron microscopy (SEM) is a type of electron microscope. SEM is one of the most repeatedly used methods for topography and morphological analysis of materials with high resolution and depth of field than optical microscope. It is very useful for the particles in the micrometer range. Tungsten or lanthanum hexaboride (LaB_6) thermionic emitters are generally used as electron gun.¹⁸ Here a well-focused beam of electrons is incident on a solid surface of the material and scanned back and forth across the surface of the material.

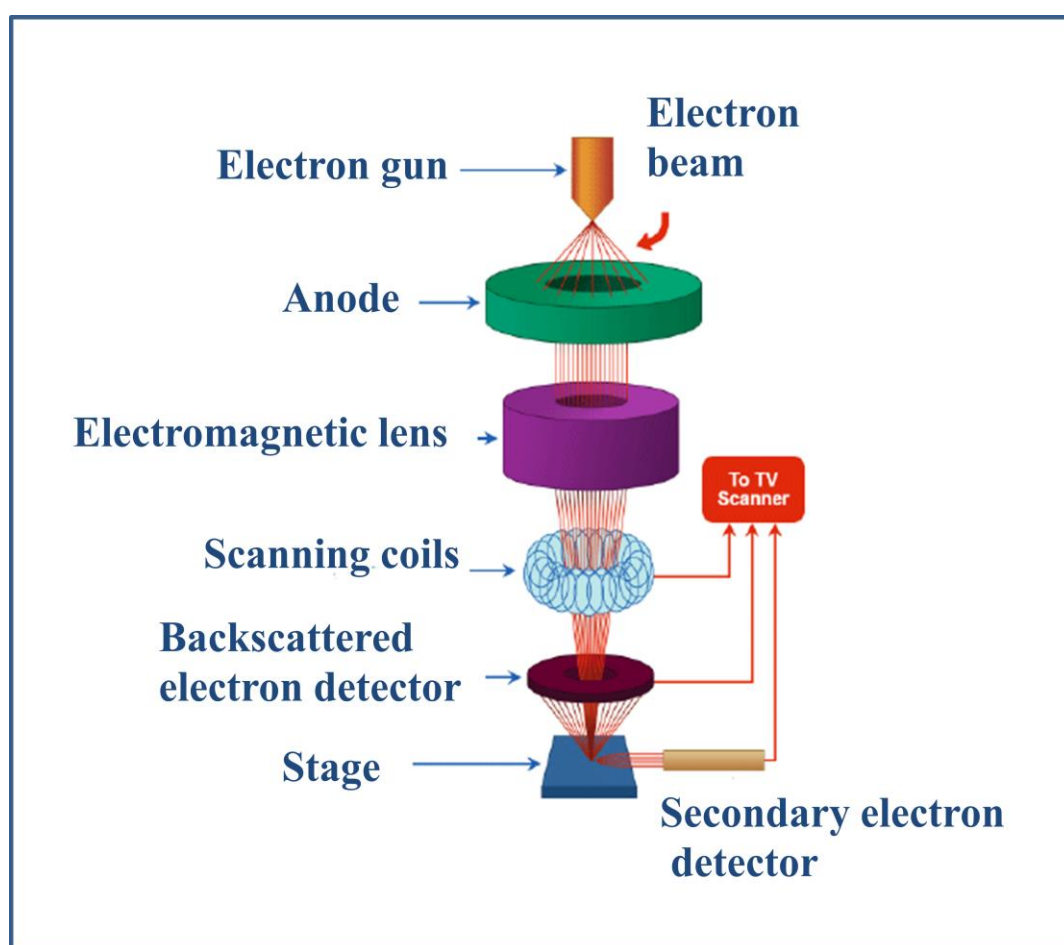


Figure 2.5: Schematic diagram of the scanning electron microscope. [Source: www.google.com]

The electrons which are particularly reflected back from surface of the material after striking it are collected by the detector. When the electron beam scans over the surface of material, the electron can lose the energy in the form of heat, emission of low-energy secondary electrons and high-energy backscattered electrons,

light emission or X-ray emission etc. Those provide different signals which give us the information about the topography and morphology of the material. During energy dispersive analysis of X-rays (EDAX), the electron beam knocks off an inner shell electron, the atom rearranges by dropping an outer shell electron to an inner one. As a result, the difference in energy between the higher-energy shell and the lower energy shell may be released in the form of an X-ray. The unique amounts of energy of the X-rays emitted from a material can be measured, which are characteristic of the material and can be used for analysis by EDAX. EDAX is an analytical technique used for the elemental composition analysis or characterization of a material. Figure 2.5 shows the schematic diagram of scanning electron microscope. The morphology of the material was determined using field emission scanning electron microscopy (FESEM: FEI QUANTA FEG 250).

2.2.7 Transmission Electron Microscopy

Transmission electron microscopy (TEM) is one of the most powerful and versatile techniques in which a beam of electrons is transmitted through a specimen to form an image. It is used to inspect the internal structure of micro- and nanomaterials when the particle size, shape, dispersion and structure are important.¹⁹ There are generally three types of electron guns on today's transmission electron microscopes, the tungsten cathode, the lanthanum hexaboride (LaB₆) cathode and the field emission gun. In TEM, the electron beam is well focused using electromagnetic lenses. The schematic of TEM is shown in Figure 2.6. A thin specimen is illuminated using uniform and high intensity electrons. Electrons interact with a solid as they pass the specimen. The interaction results in a number of elastic or inelastic scattering phenomena (backscattering or reflection, emission of secondary electrons, X-rays or optical photons and transmission of the undeviated beam along with beams deviated as a consequence of elastic single atom scattering, diffraction or inelastic phenomena). The TEM technique is devoted to the analysis of the transmitted beam. The beam is passed through a series of lenses to obtain image which is magnified and focused by an objective lens and onto an imaging device, such as a fluorescent screen or to be detected by a sensor such as a CCD camera. In low resolution TEM, the

objective aperture can be adjusted for selection of the central beam (containing the less-scattered electrons) or of a particular diffracted (or scattered in any form) beam to form the bright-field or dark-field image, respectively.

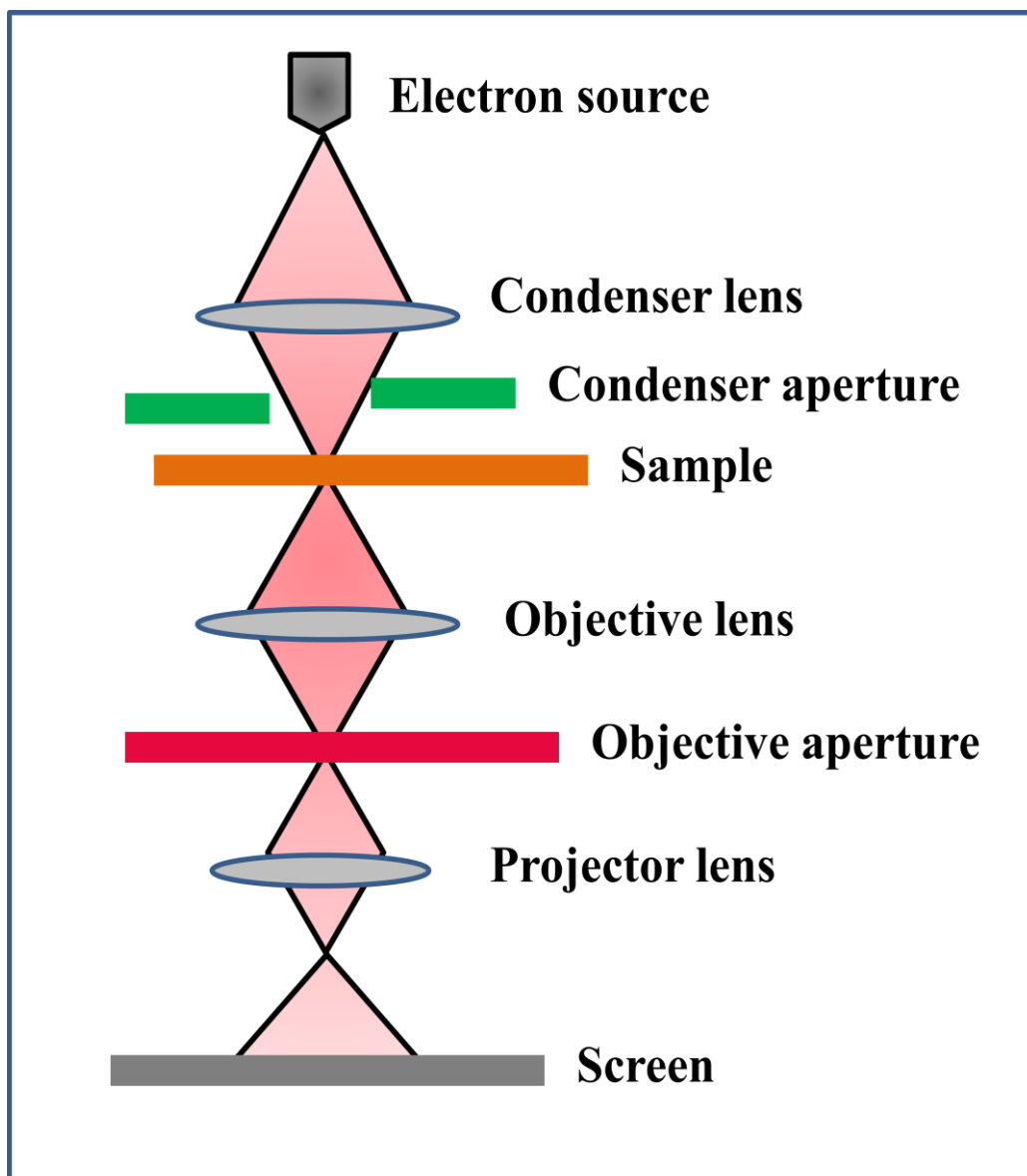


Figure 2.6: A simplified ray diagram of a TEM consists of an electron source, condenser lens with aperture, specimen, objective lens with aperture, projector lens and fluorescent screen.

TEM provide the direct identification of the chemistry of single nanocrystal. The high resolution TEM (HRTEM) analysis is also valuable to investigate the

faceting, crystallinity and ordering of nanocrystal. TEM coupled with selected area electron diffraction (SAED) allow the important information on the crystallographic direction in the structures, useful to understand the growth kinetics and also use in defect analysis.²⁰⁻²² Transmission electron microscopy (TEM: FEI TECNAI G2 F20-ST) operates at 200 kV after drop casting a drop of solution on a silicon wafer and a carbon coated copper grid. High resolution transmission electron microscopy (HRTEM) and Energy dispersive X-ray spectroscopy (EDS) analyses were performed in the above mentioned TEM using an accelerating voltage of 200 kV.

2.2.8 Brunauer-Emmett-Teller (BET) Method for Surface Area Measurement

The specific surface area of a material can be measured by BET surface area analyzer. BET theory directs to explain the physical adsorption of gas molecules on a solid surface of the materials.²³ It serves as the basis for an important analysis technique for the measurement of the specific surface area of a material. In 1938, Stephen Brunauer, Paul Hugh Emmett and Edward Teller published an article about the BET theory in a journal for the first time.²⁴ The word "BET" consists of the first initials of their family names 'Brunauer-Emmett-Teller'. The concept of the theory is an expansion of the Langmuir theory, which is a theory for monolayer molecular adsorption to multilayer adsorption with the following hypotheses: (a) gas molecules physically adsorb on a solid in layers infinitely; (b) there is no interaction between each adsorption layer; and (c) the Langmuir theory can be applied to each layer. The resulting BET equation is expressed by following equation,

$$\frac{1}{v[(\frac{p_0}{p})-1]} = \frac{c-1}{v_m c} \left(\frac{p}{p_0}\right) + \frac{1}{v_m c} \quad (2.4)$$

where p and p_0 are the equilibrium and the saturation pressure of adsorbates at the temperature of adsorption, v is the adsorbed gas quantity (for example, in volume units) and v_m is the monolayer adsorbed gas quantity. c is the BET constant which is expressed by following equation,

$$c = \exp\left(\frac{E_1 - E_L}{RT}\right) \quad (2.5)$$

where, E_1 is the heat of adsorption for the first layer, and E_L is that for the second and higher layers and is equal to the heat of liquefaction. BET Equation is an adsorption isotherm and can be plotted as a straight line with $1/v[(p_0/p) - 1]$ on the y-axis and $\phi = p/p_0$ on the x-axis according to experimental results. This well-known plot is called a BET plot. The linear relationship of BET equation is supported only in the range of $0.05 < p/p_0 < 0.35$. The value of the slope (A) and the y-intercept (I) of the linear plot are used to evaluate the monolayer adsorbed gas quantity v_m and the BET constant c . The following equations can be utilized,

$$v_m = \frac{1}{A+I} \quad (2.6)$$

$$c = 1 + \frac{A}{I} \quad (2.7)$$

The BET method is commonly used in surface science for the calculation of surface areas of solids by physical adsorption of gas molecules. Total surface area S_{total} and a specific surface area (S) are calculated using following equations,

$$S_{total} = \frac{v_m N S}{V} \quad (2.8)$$

$$S = \frac{S_{total}}{a} \quad (2.9)$$

where v_m is in units of volume which are also the units of the molar volume of the adsorbate gas, N is Avogadro's number, S is adsorption cross section of the adsorbing species, V is molar volume of adsorbate gas and a is mass of material or adsorbent (g). Specific surface area was determined by the BET method using nitrogen adsorption/desorption isotherms at 77 K with 3flex Micromeritics analyzer.

2.2.9 Thermogravimetric Analysis

Thermogravimetric analysis (TGA) is an analytical technique used to measure the thermal stability of materials and its fraction of volatile components by monitoring the weight change. Weight change takes place when the material is heated it undergoes certain physical and chemical changes. The weight is recorded as a function of increasing temperature over time. Thermo gravimetric analysis and

differential analysis (DTA) are utilized to study the thermal behaviour of the nanocomposites. A typical thermogravimetric analyzer consists of a precision balance with a sample pan placed inside a furnace with a programmable control temperature. The temperature is usually increased at constant rate. In most cases, TGA analysis is carried out in an oxidative atmosphere (air or oxygen and inert gas mixtures) with a linear temperature ramp. Thermal gravimetric analysis will be interfaced with a mass spectrometer to identify and determine the vapours generated, though there is much greater sensitivity when the mass spectroscopy heating is performed in an ultrahigh vacuum system. Thermogravimetric analysis in the present study was done under nitrogen atmosphere. The heating rate was 5 °C/min. Thermogravimetric analyses were performed on a Perkin Elmer DAIMOND TG/DTA instruments.

2.2.10 Zeta-potential

Zeta (ζ) potential values provide an indirect measurement of the net charge on the surface of materials. The measurement of zeta potential of colloidal dispersions is routinely performed using the technique of micro-electrophoresis. During a zeta potential measurement, a voltage gradient is applied across the samples, inducing the movement of charged particles. The ratio between the particle velocity and the external applied field is known as electrophoretic mobility. Then, the measured electrophoretic mobility (U_E) is converted into ζ - potential using Henry's equation,

$$U_E = \frac{2\varepsilon\zeta f(k\alpha)}{3\eta} \quad (2.10)$$

where ε and η are the dielectric constant and viscosity of the medium respectively. $f(k\alpha)$ is known as “the Henry function”, where α is the hydrodynamic radius and k is known as the Debye parameter, which represent the thickness of the electrical double layer) that depend on the ionic strength of the medium and on the temperature of the sample. Zeta potential was performed by Malvern Nano ZS instrument.

2.2.11 Vibrating-Sample Magnetometer

A vibrating-sample magnetometer (VSM) is a scientific instrument that measures magnetic properties of the materials. In VSM, when a sample material is placed in a direct current (DC) magnetic field (H) and vibrated sinusoidally so that the resulting variation of magnetic flux (B) can induce a voltage in pickup coils based on Faraday's law of Induction. The induced voltage in the pickup coil is proportional to the materials magnetic moment, but does not depend on the strength of the applied magnetic field. The frequency is the same as that of the sinusoidal motion. The schematic diagram of the sample holder and detection mechanism of a VSM is shown in Figure 2.7. Magnetic study of our sample was carried out in a Lake Shore VSM equipped with an electromagnet, capable of generating field of up to 1.6 T. Magnetization measurement of the sample was done with a vibrating sample magnetometer (VSM), Lake Shore 7400 series.

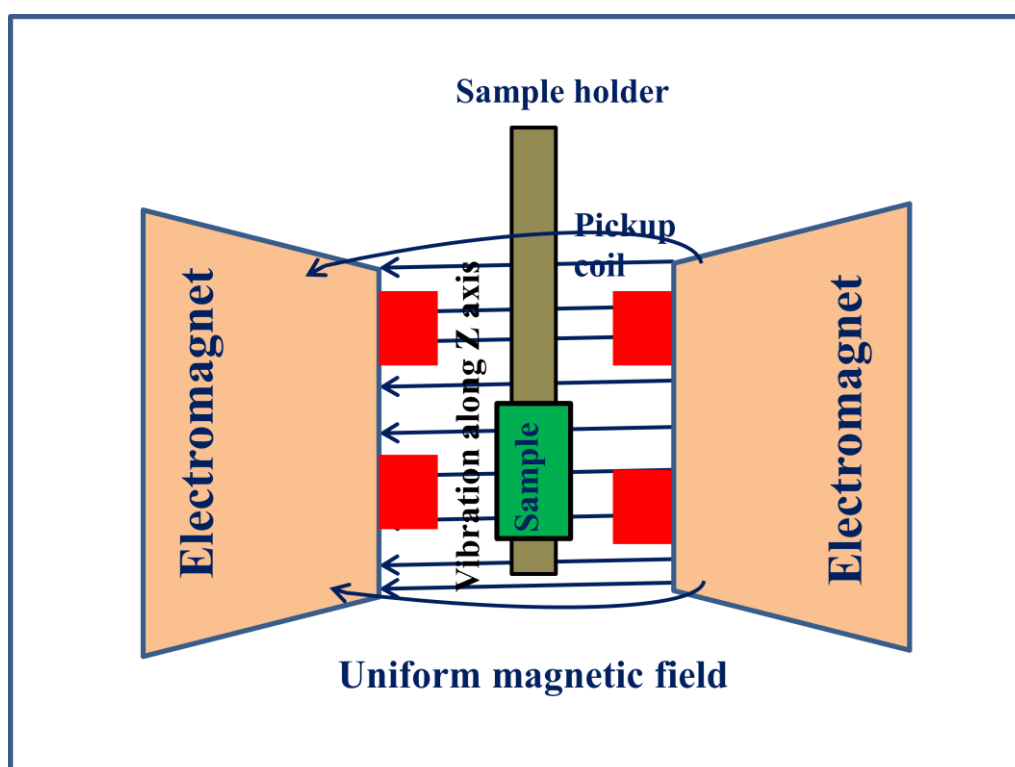


Figure 2.7: Schematic presentation of VSM sample holder and detection mechanism.

2.2.12 Inductively Coupled Plasma Optical Emission Spectrometry

Inductively coupled plasma - optical emission spectrometry (ICP-OES) also referred to as inductively coupled plasma atomic emission spectroscopy (ICP-AES). ICP-OES is an analytical technique used for the detection of chemical elements. The composition of elements in samples (mostly water-dissolved) can be measured using plasma and a spectrometer. It is a type of emission spectroscopy that utilizes the inductively coupled plasma to produce excited atoms and ions that emit electromagnetic radiation at wavelengths characteristic of a particular element. Argon gas is generally used to create the plasma. The intensity of this emission is investigative of the concentration of the element within the sample. ICP-OES analysis was carried out using the PerkinElmer ICP-OES instrument (PerkinElmer, Inc., Shelton, CT, USA). For ICP-OES analysis, nanocomposite was dissolved in dilute HCl and the supernatant was used to estimate the element concentration in the nanocomposite

2.3 References

1. Banwell, C. N.; McCash, E. M. *Fundamentals of Molecular Spectroscopy*. 4th Ed., Tata McGraw Hill Publishing Co. Ltd. **2002**.
2. Coates, J. *Interpretation of Infrared Spectra: A Practical Approach*. Encyclopedia of Analytical Chemistry, John Wiley & Sons Ltd. **2000**.
3. El-Sayed, M. A. Some Interesting Properties of Metals Confined in Time and Nanometer Space of Different Shapes. *Acc. Chem. Res.* **2001**, *34*, 257-264.
4. Burda, C.; Chen, X.; Narayanan, R.; El-Sayed, M. A. Chemistry and Properties of Nanocrystals of Different Shapes. *Chem. Rev.* **2005**, *105*, 1025-1102.
5. Kreibig, U.; Vollmer, M. *Optical Properties of Metal Clusters*. Berlin: Springer, **1995**.
6. Kerker, M. *The Scattering of Light and Other Electromagnetic Radiation*. New York: Academic, **1969**.
7. Bohren, C. F.; Huffman, D. R. *Absorption and Scattering of Light by Small Particles*. New York: Wiley, **1983**.
8. Papavassiliou, G. C. Optical Properties of Small Inorganic and Organic Metal Particles. *Prog. Solid State Chem.* **1979**, *12*, 185-271.
9. Keeler, J. *Understanding NMR Spectroscopy*. John Wiley and Sons Ltd. **2005**.
10. Bovey, A. F. *Nuclear Magnetic Resonance Spectroscopy*. Academic Press, New York, **1969**.
11. Iggo, J. A. *NMR Spectroscopy in Inorganic Chemistry*. Oxford University Press, **1999**.

12. Dijkamp, D.; Venkatesan, T.; Wu, X. D.; Shaheen, S. A.; Jisrawi, N.; Min-Lee, Y. H.; McLean, W. L.; Croft, M. Preparation of Y-Ba-Cu Oxide Superconductor Thin Films using Pulsed Laser Evaporation from High T_c Bulk Material. *Appl. Phys. Lett.* **1987**, *51*, 619-621.
13. Buerger, M. J. *X-ray Crystallography*. Wiley, New York, **1942**.
14. Klug, H. P.; Alexander, L. E. *X-ray Diffraction Procedures*. Wiley, New York, **1954**.
15. Cullity, B. D. *Elements of X-ray Diffraction*, Addison Wesley. Massachusetts, **1956**.
16. Zanchet, D.; Hall, B. D.; Ugarte, D. Structure Population in Thiol-passivated Gold Nanoparticles. *J. Phys. Chem. B* **2000**, *104*, 11013-11018.
17. Taylor, A. *X-ray Metallography*. Wiley, New York, **1942**.
18. Goldstein, J. I.; Newbury, D. E.; Michael, J. R.; Ritchie, N.W.; Scott, J. H. J.; Joy, D. C. *Scanning Electron Microscopy and X-ray Microanalysis*. Kluwer Academic, Plenum Publishers, New York, **2003**.
19. Wang, Z. L. Transmission Electron Microscopy of Shape-Controlled Nanocrystals and Their Assemblies, *J. Phys. Chem. B* **2000**, *104*, 1153-1175.
20. Williams, D. B.; Carter, C. B. *Transmission Electron Microscope*, Vol I-III, Kluwer Academic, Plenum Publishers, **1996**.
21. Duan, J.; Yang, S.; Liu, H.; Gong, J.; Huang, H.; Zhao, X.; Zhang, R.; Du, Y. J. Single Crystal SnO₂ Zigzag Nanobelts. *J. Am. Chem. Soc.* **2005**, *127*, 6180 -6181.
22. Ding, Y.; Wang, Z. L. Structure Analysis of Nanowires and Nanobelts by Transmission Electron Microscopy. *J. Phys. Chem. B.* **2004**, *108*, 12280-12291.
23. Adamson, A.; Gast, A. *Physical Chemistry of Surfaces*. 6th ed. Wiley, **1997**.
24. Brunauer, S.; Emmett, P. H.; Teller, E. Adsorption of Gases in Multimolecular layers. *J. Am. Chem. Soc.* **1938**, *60*, 309-319.

Moisture Induced Carbon Dioxide Trapping from Ambient Air

3.1 Introduction

The growing concentration of anthropogenic carbon dioxide in ambient air due to the large industrial sources of emission arising from fossil fuel power plants, chemical processing, and deforestation caused by usage of land, is a key challenge in the ongoing effort to diminish the effect of greenhouse gases on global climate change by developing more-efficient and improved procedures for CO₂ capture and sequestration.¹⁻³ A probable pathway to deal with these emissions is to capture CO₂ directly from the ambient air. However, CO₂ capture from air followed by its separation and recovery in a large scale is still in its infancy and recently has only drawn adequate interests to the researchers.

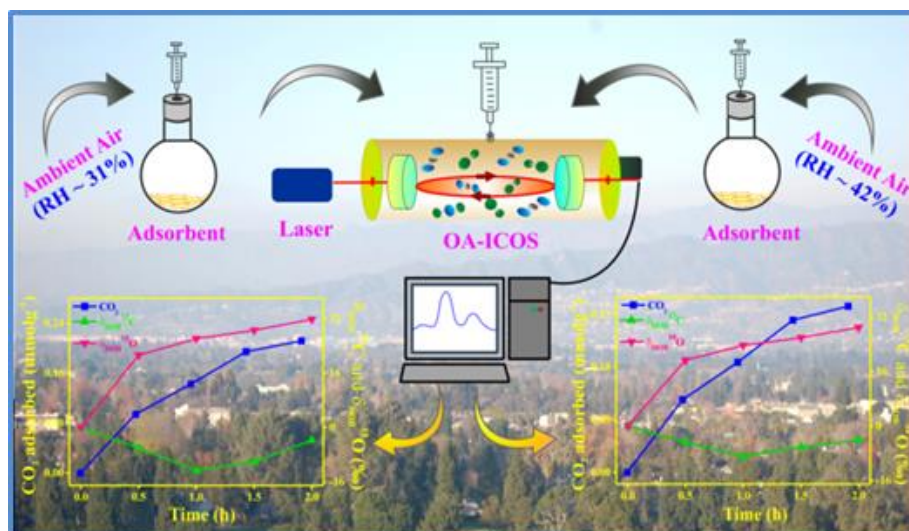
Liquid phase amine scrubbing process which is an industrially established approach to capture CO₂ owing to the ability of the amines to chemisorb acidic CO₂, involves high regeneration cost as high heat capacity of aqueous amine makes the endothermic regeneration step very energy intensive, poor thermal stability associated with contamination of the gas with the solvent vapour, equipment corrosion, and oxidative degradation of amines, resulting in a strong motivation to develop stable and recyclable solid adsorbents with appropriate CO₂ capture capability.³⁻⁷ Up till now, several solid CO₂ adsorbents have widely been explored, such as zeolites, activated carbon, mesoporous silica, metal organic frameworks, metal oxides, alkali hydroxide, polymer based adsorbents etc.⁷⁻¹⁹ However, low tolerance of adsorbents to water vapour in the feed gas, slow adsorption kinetics causes long time to reach saturation, reduced activity in presence of moisture due to unfavourable completion and higher adsorption temperature, low thermal and chemical stability, sometimes restrict the implementation of the most of the procedures and always become a contentious issue about their effectiveness, whereas adsorbents with high adsorption

capacity, fast adsorption and desorption procedure, moisture tolerance capacity, and low energy requirement for recycling are always desirable for CO₂ capture.

A key goal during the design and subsequent synthesis of a solid adsorbent is to increase the available adsorption sites per mass of materials to enhance the efficacy of that adsorbent and at the same time to reduce the effective cost. Development of clay based adsorbents with different viable aminosilanes having varied concentration of amino groups along with thermal and hydrothermal stability will serve the purpose well. Besides all the earlier attributes, amine based solid adsorbents have the ability to tolerate the presence of moisture in the feed gas, which in turn enhances their maximum equilibrium CO₂ uptake ability in moisture. The higher uptake of moist CO₂ is a consequence of a change in the adsorption mechanism, resulting in upsurge in the adsorption proficiency as well as increase in the amine efficiency. Additionally, adsorbent composed of multi-amine molecules will be a superior alternative for this purpose owing to their high amine densities.

The present work demonstrates the development of several clay based solid adsorbents having grafted with diverse aminosilanes containing both primary and secondary amine sites to capture CO₂ from ambient air under standard temperature and pressure. We have investigated the atmospheric CO₂ adsorption efficiency of amine modified clay nanotubes using a simple and easy handling bench-top mass spectrometer, residual gas analyser (RGA-MS). Keeping the sensitivity and accuracy towards the measurement of atmospheric CO₂ in mind, we have validated our findings by comparing with the results acquired from an optical cavity-enhanced integrated cavity output spectrometer (ICOS), indicating the results obtained from RGA-MS and ICOS are in good agreement. We have also studied the preferential adsorption of the three major abundant isotopes of CO₂ like ¹²C¹⁶O₂, ¹³C¹⁶O₂, and ¹²C¹⁶O¹⁸O using integrated cavity output spectroscopy (ICOS) technique. Adsorption kinetics describing CO₂ uptake rate has been investigated to evaluate the efficiency of the adsorbents as well as to explore the fundamental mechanism of adsorption. The influence of moisture on the adsorption kinetics has been explored by carrying out the experiment on the seasonal ambient air having different moisture content (Scheme 3.1). Another major aim of this work is to find out the moisture dependent isotopic

CO₂ adsorption together with the stability of these novel adsorbents towards the repetitive use for CO₂ uptake in oxidative environment.



Scheme 3.1: Schematic presentation of moisture induced isotopic CO₂ adsorption from the seasonal ambient air using solid adsorbents analysed by an off-axis laser based integrated cavity output spectroscopy technique, followed by their adsorption trends.

3.2 Experimental Section

3.2.1 Preparation of Adsorbents

All the clay based adsorbents were synthesized under nitrogen atmosphere using standard air free techniques. 4.0 g of halloysite nanotubes (HNTs) were taken in a 50 mL three-necked round bottom flask containing 20.0 mL of toluene. The reaction flask was fixed with rubber septum, condenser, thermocouple adaptor and a quartz sheath through which a thermocouple was inserted. The reaction mixture was deaerated for 30 min with nitrogen and then heated with a heating mantle. After that aminosilane was injected into the flask at 60 °C under stirring condition, subsequently the reaction mixture was refluxed for 20 h at 120 °C. The as synthesized product was obtained after filtration and washed several times with toluene and ethanol respectively and dried at 100 °C overnight under vacuum. (3-aminopropyl)triethoxysilane (2.5 mL) modified HNTs are abbreviated as M-HNTs.

Based on the analogous synthetic route N-[3-(trimethoxysilyl)propyl]ethylenediamine and N¹-(3-trimethoxysilylpropyl)diethylenetriamine grafted HNTs are synthesized with similar concentration of the aminosilanes and the synthesized products were abbreviated as D-HNTs and T-HNTs respectively, as shown in Figure 3.1. Table 3.1 represents the list of aminosilane and structure of amines site.

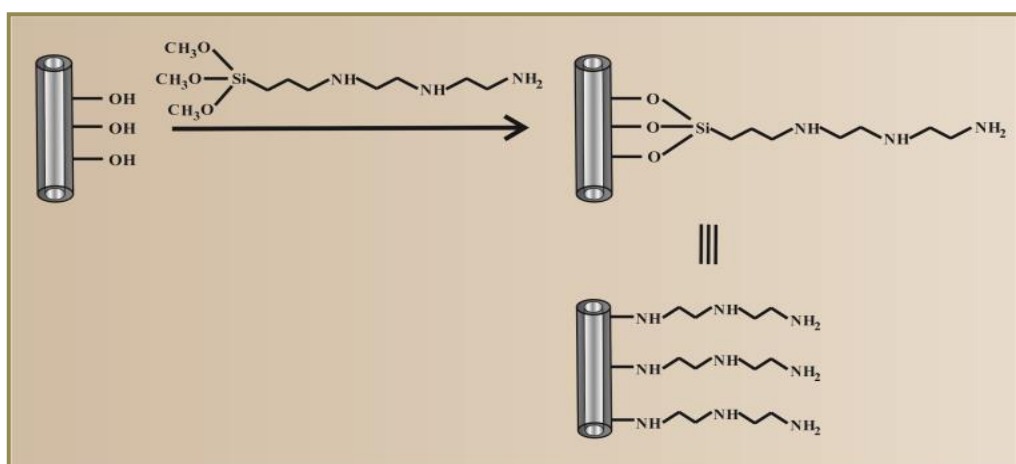


Figure 3.1: Schematic presentation for the synthesis of clay based adsorbents.

Table 3.1: List of aminosilanes and structure of amine for the synthesis of adsorbents.

Aminosilanes	Structure
(3-aminopropyl)triethoxysilane	$\begin{array}{c} \text{C}_2\text{H}_5\text{O} \\ \text{C}_2\text{H}_5\text{O} \\ \text{C}_2\text{H}_5\text{O} \end{array} \text{Si} \text{---} \text{CH}_2\text{CH}_2\text{CH}_2\text{NH}_2$
N-[3-(trimethoxysilyl)propyl]ethylenediamine	$\begin{array}{c} \text{CH}_3\text{O} \\ \text{CH}_3\text{O} \\ \text{CH}_3\text{O} \end{array} \text{Si} \text{---} \text{CH}_2\text{CH}_2\text{CH}_2\text{NHCH}_2\text{CH}_2\text{NH}_2$
N ¹ -(3-trimethoxysilylpropyl)diethylenetriamine	$\begin{array}{c} \text{CH}_3\text{O} \\ \text{CH}_3\text{O} \\ \text{CH}_3\text{O} \end{array} \text{Si} \text{---} \text{CH}_2\text{CH}_2\text{CH}_2\text{NHCH}_2\text{CH}_2\text{NHCH}_2\text{CH}_2\text{NH}_2$

3.2.2 Residual Gas Analyzer-Mass Spectrometry (RGA-MS) Technique

We have demonstrated a residual gas analyzer (RGA) coupled with a high vacuum (HV) chamber to explore its effectiveness in monitoring CO₂ concentration as low as the atmospheric level (~ 400 ppm). A tool comprising of residual gas analyzer (RGA) (Prisma Plus, PT-M05-212-111, Pfeiffer vacuum, 1-200 amu) coupled with a customized HV chamber to measure the atmospheric samples has been discussed. The typical baseline vacuum level inside the HV chamber is ~ 10⁻⁸ Torr which has continually been maintained by combination of a turbo molecular pump (PM-153-915-T, S_p=260 L/s, Pfeiffer) and a turbo-drag-pump (PM-P03-963A, S_p = 10 L/s, Pfeiffer) backed by a diaphragm pump (PK-T01-210, S_p=40 L/s, Pfeiffer). A Pirani gauge (PT-R26-002, Pfeiffer) has been utilized to continuously monitor the vacuum pressure inside the HV chamber. A gas controlled valve termed as all-metal-leak-valve (AMLV) (PFI52031, Pfeiffer) has been employed to regulate the flow of gas samples into the chamber and also to sustain the working condition inside the chamber. For the typical experiments performed in the present study, an atmospheric air sample of volume ~ 5 ml has been used to inject into the HV chamber through the AMLV by an air-tight syringe/stopcock. The experiments were performed under the typical pressure of 2.2-2.3×10⁻⁵ torr inside the HV chamber. The interfacing Quadera software (Prisma Plus, version 4.50) allowed the samples to be analyzed in two different modes, namely Faraday scan mode (FSM) and multiple ions detection (MID). The qualitative analysis for the different molecular species present in the sample has been performed by the FSM whereas MID has been utilized for the quantitative study of the selected mass 44 amu (CO₂). The changes of ion currents for the mass 44 amu due to CO₂ adsorption by three different amine loaded adsorbents with the scanning rate of 1sec/amu have also been illustrated in the results and discussion section. Typically, 25-30 data points have been averaged to obtain the resultant ion current for the concentration of mass 44 amu present in the atmospheric samples.

3.2.3 Integrated Cavity Output Spectroscopy

Using a high precision laser based optical technique based on off-axis integrated cavity output spectroscopy (OA-ICOS) we have evaluated ambient air carbon dioxide and its isotopes trapped in the adsorbents. The advantages for utilization of this technique in comparison to traditional isotope ratio mass spectroscopy (IRMS) have been proved elsewhere.²⁰ The ICOS instrument (CCIA 36-EP, Los Gatos research, USA) is comprised of a high-finesse optical cavity of length 59 cm long. Two high reflectivity mirrors (R~99.98%) have been placed in two ends of the measurement cells of the optical cavity so that laser light can move back and forth to reach the effective optical path-length about 3 km. A continuous wave distributed feedback diode laser operating at ~2.05 μm was coupled into the optical cavity. The frequency of the laser light was tuned to scan over 20 GHz to excite the P(36), R(28) and P(16) ro-vibrational lines for the absorption spectra of $^{12}\text{C}^{18}\text{O}^{16}\text{O}$ (4874.178 cm^{-1}), $^{12}\text{C}^{16}\text{O}^{16}\text{O}$ (4874.448 cm^{-1}) and $^{13}\text{C}^{16}\text{O}^{16}\text{O}$ (4874.086 cm^{-1}).²¹ A photo-detector was utilized to record the transmittance light intensity after passing through the sample cell. A resistive heater with feedback control was employed to maintain the temperature of the cavity about 45°C , whereas the pressure of the cavity was regulated at ~30 Torr by a diaphragm pump. The concentrations of trace gases were determined in accordance with Beer-Lambert law.

3.2.4 CO₂ Adsorption Measurements

To demonstrate the CO₂ adsorption efficiency of adsorbents (M-HNTs, D-HNTs and T-HNTs), ambient air was collected and used as feed gas. At ambient pressure and temperature, CO₂ adsorption experiments were performed taking amine grafted HNTs as an adsorbent in a round bottom flask, which was fitted with a rubber septum and two adapters. To ensure complete desorption of pre-adsorbed CO₂ if any before the adsorption experiment, all the adsorbents was pre-treated with ultra-high pure nitrogen gas at 120°C for a period of 45 min, followed by pull down the vacuum for another 45 min. Keeping all the experimental condition the same, another round bottom flask deprived of any adsorbent was also fitted with a rubber septum and the

adapters. Once the temperature of the flasks cooled down to room temperature, ambient air was injected to the both blank and the sample flasks respectively and kept for equilibration for a desired time. After the equilibration, the amount of unadsorbed CO₂ remain in the ambient air of the flask was measured using RGA-MS technique as well as laser-based ICOS technique. The amount of adsorbed CO₂ was calculated from the absolute change in concentration with respect to the blank flask.

3.3 Results and Discussion

To address these issues regarding the design of adsorbents for CO₂ capture from ambient air, we have synthesized three different adsorbents through the selective grafting of aminosilanes, (3-aminopropyl)triethoxysilane, N-[3-(trimethoxysilyl)propyl] ethylenediamine and N¹-(3-trimethoxysilylpropyl) diethylenetriamine respectively, over the outer surface of a nanoclay, halloysite (Figure 3.2). Halloysite, 1:1 aluminosilicate clay nanotubes (HNTs), represents a perfect tailoring material because of their chemical tunability arising from the positive octahedral array of Al-OH groups at the inner surfaces and negative Si-O-Si groups at the outer surfaces.^{22,23} This rich surface chemistry of HNTs will open up a prospect to alter the structure/properties of the HNTs through selective modification of the outer and/or inner surfaces, together with they are environmentally benign and biocompatible.^{22,24} These clay based adsorbents are therefore, loaded with varied concentration of amino groups as a result of different grafted aminosilanes, some of which contains both primary and secondary amine sites. All the aminosilanes have an amine site associated to a trimethoxysilane or triethoxysilane group through a propyl group embedded over the surface of HNTs to study the structural effects during CO₂ adsorption. The molecular length of attached amine is approximately 0.9, 1.3 and 1.7 nm for M-HNTs, D-HNTs and T-HNTs respectively.^{25,26}

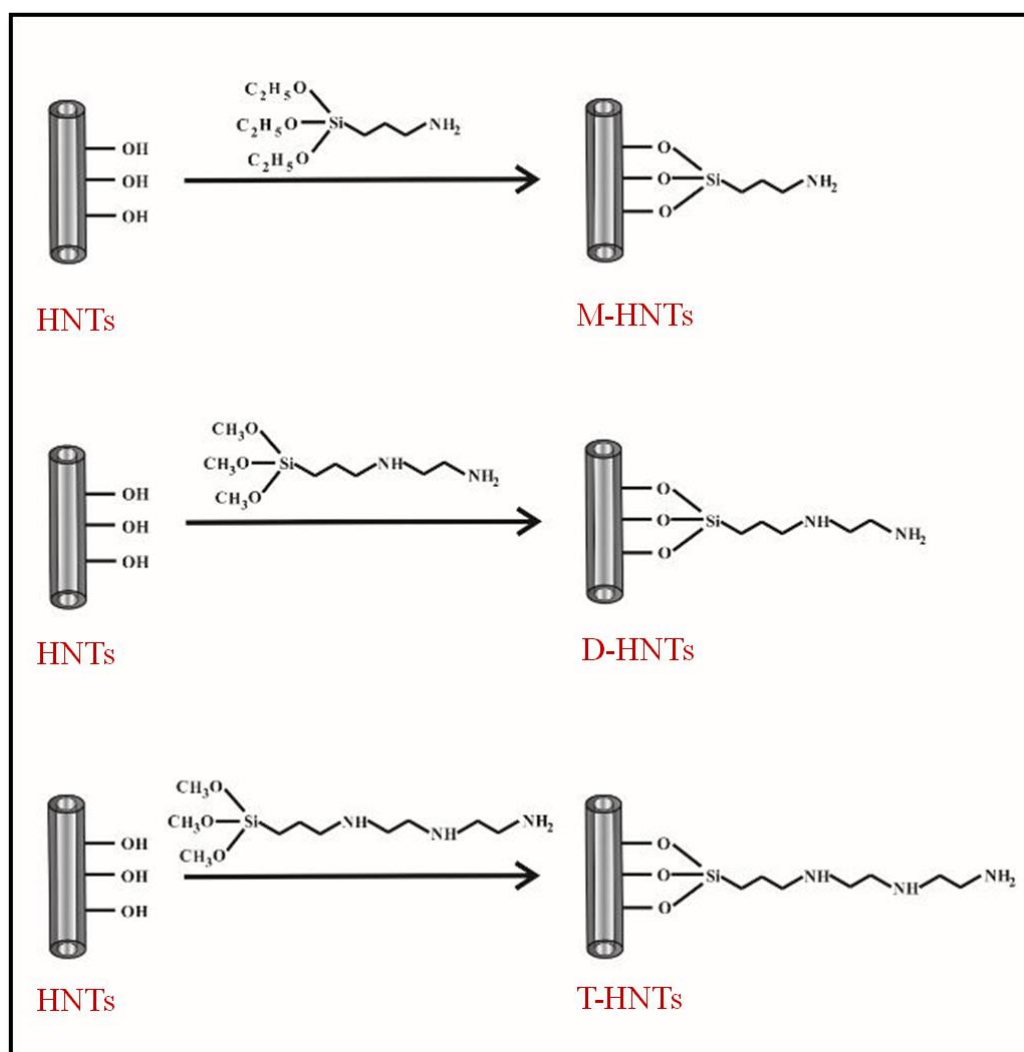


Figure 3.2: Schematic presentation of the synthesis of clay based adsorbents through the immobilization of (3-aminopropyl)triethoxysilane, N-[3-(trimethoxysilyl)propyl] ethylenediamine and N1-(3-trimethoxysilylpropyl)diethylenetriamine respectively over the surface of HNTs based on the grafting reaction to achieve M-HNTs, D-HNTs and T-HNTs.

3.3.1 Characterization of Clay Based Adsorbents

3.3.1.1 TEM and FESEM Analyses

The morphology of all clay based adsorbents characterized by TEM analysis indicated that they comprised of cylindrical shaped tubes with an open-ended lumen having length between 1.0 and 1.5 μm and external and inner diameter of 50-100 nm and 15-20 nm respectively, which is consistent with the corresponding FESEM images

(Figure 3.3). Thus, these adsorbents represent polydispersity in their sizes with comparable morphology to that of bare HNTs and the defects on the surface probably arise from the mechanical damage or crystallographic defects. It should be noted that even after immobilization of the amines, the morphology or size of HNTs remains the same.

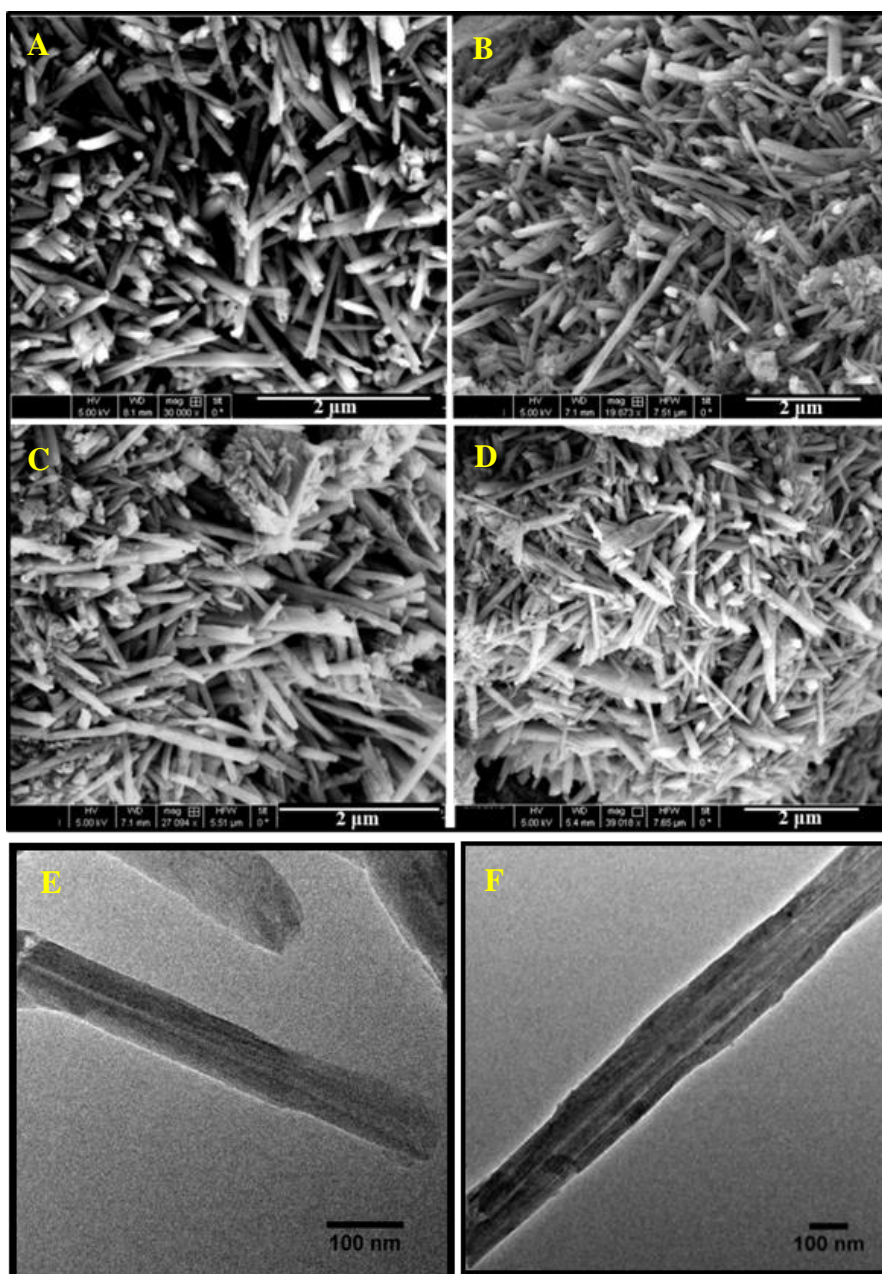


Figure 3.3: FESEM images of (A) HNTs, (B) M-HNTs, (C) D-HNTs and (D) T-HNTs obtained through the grafting of viable aminosilanes. Representative TEM micrographs of (E) HNT and (F) T-HNT.

3.3.1.2 XRD Analysis

The tubular structure of the clay nanotubes has also been established by XRD analysis which demonstrates the presence of (020) reflection (Figure 3.4). The typical (001) reflection does not shift to the lower angles even after grafting, attributing to the absence of any intercalation of aminosilane into the interlayer of HNTs, which in turn point to the inaccessibility of most of the wall interlayer AlOH groups for grafting.^{24,27}

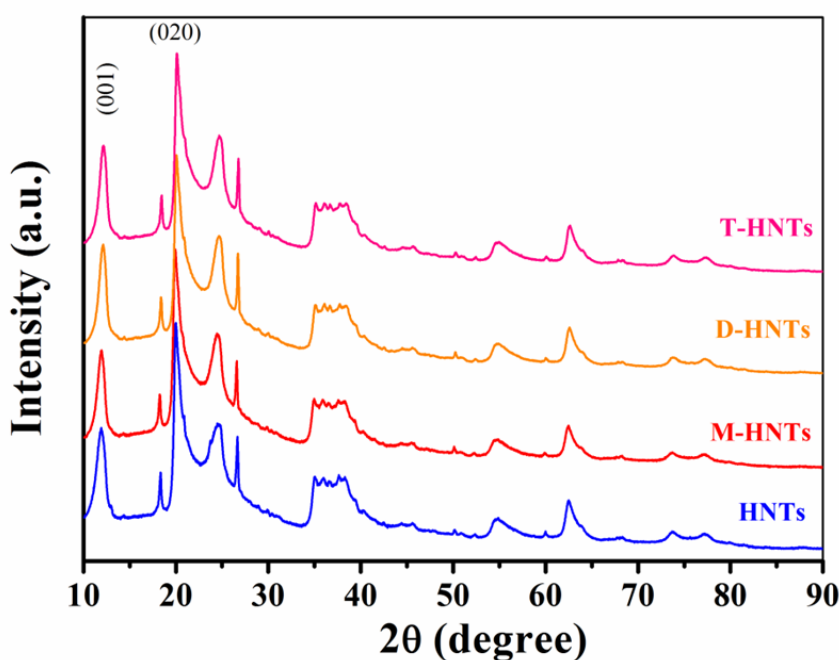


Figure 3.4: XRD patterns of bare HNTs and as-prepared adsorbents, M-HNTs, D-HNTs and T-HNTs obtained through the surface modification of bare HNTs using three viable amines; (3-aminopropyl) triethoxysilane (M-HNTs), N-[3-(trimethoxysilyl)propyl]ethylenediamine (D-HNTs), and N1-(3-trimethoxysilylpropyl)diethylenetriamine (T-HNTs) respectively.

3.3.1.3 FTIR Study

The grafting of aminosilanes over the surface of HNTs to form M-, D- and T-HNTs was verified by FTIR spectroscopy (Figure 3.5). The FTIR spectra demonstrate the presence of three new peaks at 1559, 2937 and 3451 cm^{-1} for N-H deformation and stretching vibration of C-H and N-H respectively, in addition to the two other distinct

bands at 3621 and 3697 cm^{-1} originated due to the stretching vibrations of inner hydroxyl group and inner surface hydroxyl group.^{28,29}

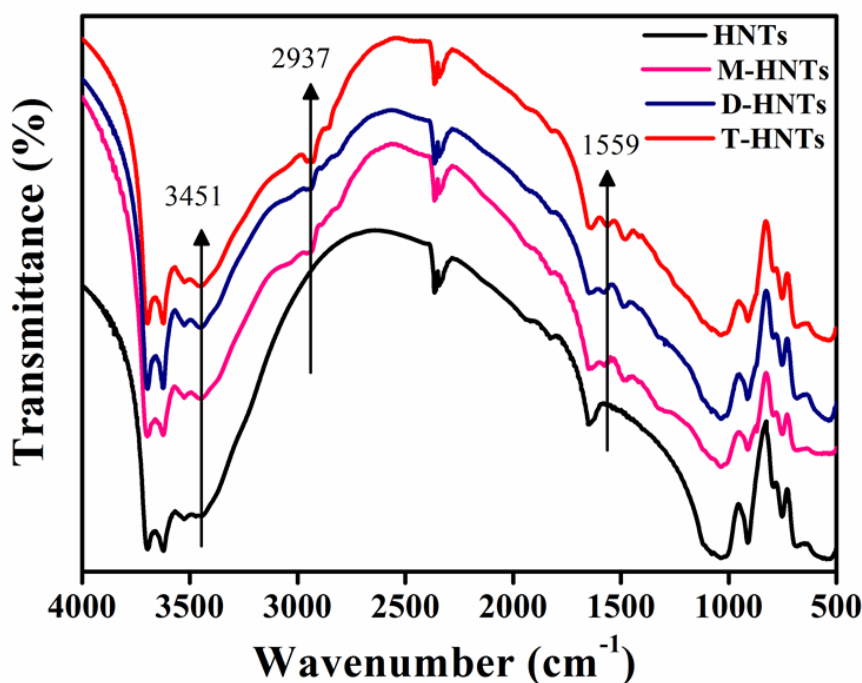


Figure 3.5: FTIR spectra of M-HNTs, D-HNTs and T-HNTs demonstrate the presence of amino group in the adsorbents due to the grafting of aminosilanes onto the surface of HNTs.

3.3.1.4 NMR Study

However, the solid state ^{29}Si and ^{13}C MAS NMR spectroscopy further demonstrates the successful grafting of those aminosilanes over the surface of HNTs (Figure 3.6). The chemical shift at -91 ppm arises due to presence of silicon in both HNTs and M-HNTs. The new peak at -67 ppm in M-HNTs is assigned to the tridentate (T^3) bonded silicon, indicating the hydrolysis of all the three ethoxy groups of (3-aminopropyl)triethoxysilane, which further demonstrates the formation of new chemical bond between the surface hydroxyl groups of HNTs and the organosilane.²⁸ The chemical shifts at 11.8, 24.9 and 44.4 ppm in ^{13}C CP-MAS NMR spectrum of M-HNTs represent the three carbons in the propyl chain of the aforesaid grafted organosilane over the surface of HNTs to form M-HNTs.

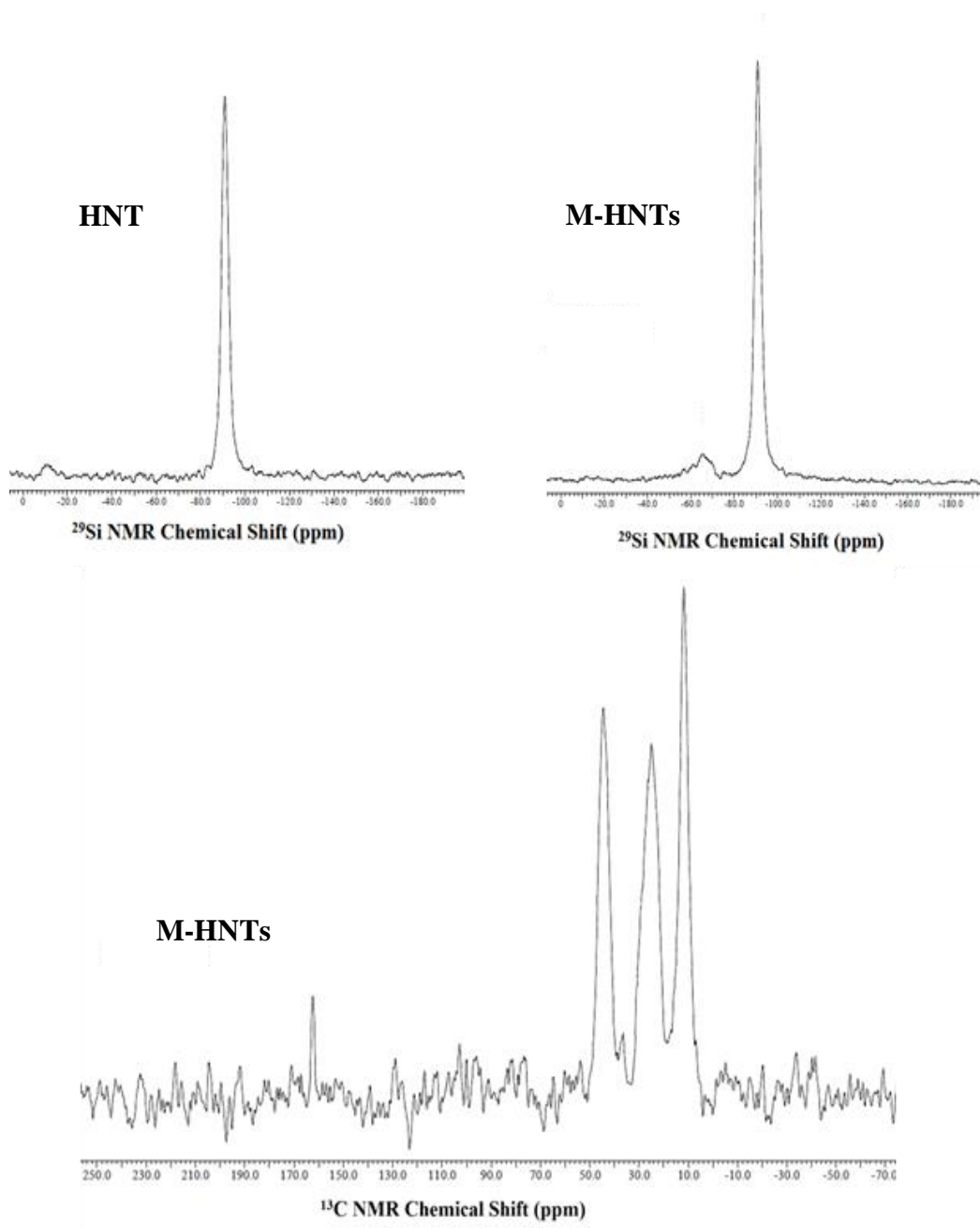


Figure 3.6: ^{29}Si NMR spectra of HNTs and M-HNTs and ^{13}C NMR spectrum of M-HNTs respectively.

3.3.1.5 CHN Elemental Analysis

The actual concentration of grafted amino groups over the surface of HNTs was evaluated using CHN elemental analysis as presented in Table 3.2. The loaded N per gram of M-HNTs, D-HNTs and T-HNTs was estimated to be 0.51, 1.05, and 1.6 wt%

under the present experimental condition. This change in the concentration of the loaded amino group in the adsorbents is owing to the grafting of three different aminosilanes with varied amino groups content. It should be noted that though the concentration of the immobilized amino groups in the solid adsorbents has easily been tuned by changing the aminosilane concentration as well as reaction condition, we have performed all the isotopic CO₂ adsorption study here with the adsorbents having above mentioned amine loading.

Table 3.2: Elemental composition of the adsorbents from CHN elemental analysis.

Adsorbents	C (%)	H (%)	N (%)
M-HNTs	1.81	1.63	0.51
D-HNTs	2.73	1.96	1.05
T-HNTs	3.71	2.25	1.6

3.3.2 CO₂ Adsorption from Ambient Air

3.3.2.1 CO₂ Adsorption Study

In an effort to determine the atmospheric CO₂ adsorption efficiency of these adsorbents, ambient air was used as feed gas and all the adsorption experiments were performed at room temperature (298 K) and pressure (1 atm). For this study, we have inserted the air collected from the atmosphere to the adsorbent bed of a flask and allowed that to reach equilibration for a definite period of time. Exploiting RGA-MS a simple and easy handling bench-top mass spectrometer, the concentration of unadsorbed CO₂ in the ambient air after the adsorption has been assessed and the concentration of adsorbed CO₂ by these adsorbents was measured from the absolute change in concentration in regard to the blank flask. It should be pointed out that in RGA-MS system, the resultant ion current carries the signature of the concentration of the selected mass (represented in terms of m/z ratio). The minimum detection level of

CO₂ by our RGA-MS is ~10 ppm and the precision of the measurements is limited to ± 2.5 ppm, where the potential interference due to neighboring masses remains <5 ppm. The qualitative analysis for the different molecular species present in the sample has been performed by the Faraday scan mode (FSM). The representative RGA mass spectra of ambient air before and after CO₂ adsorption in the scan bar-graph mode have been presented in Figure 3.7A, indicating the presence of CO₂ with the other constituents of air. The ion current for the mass 44 amu (CO₂) was considered to

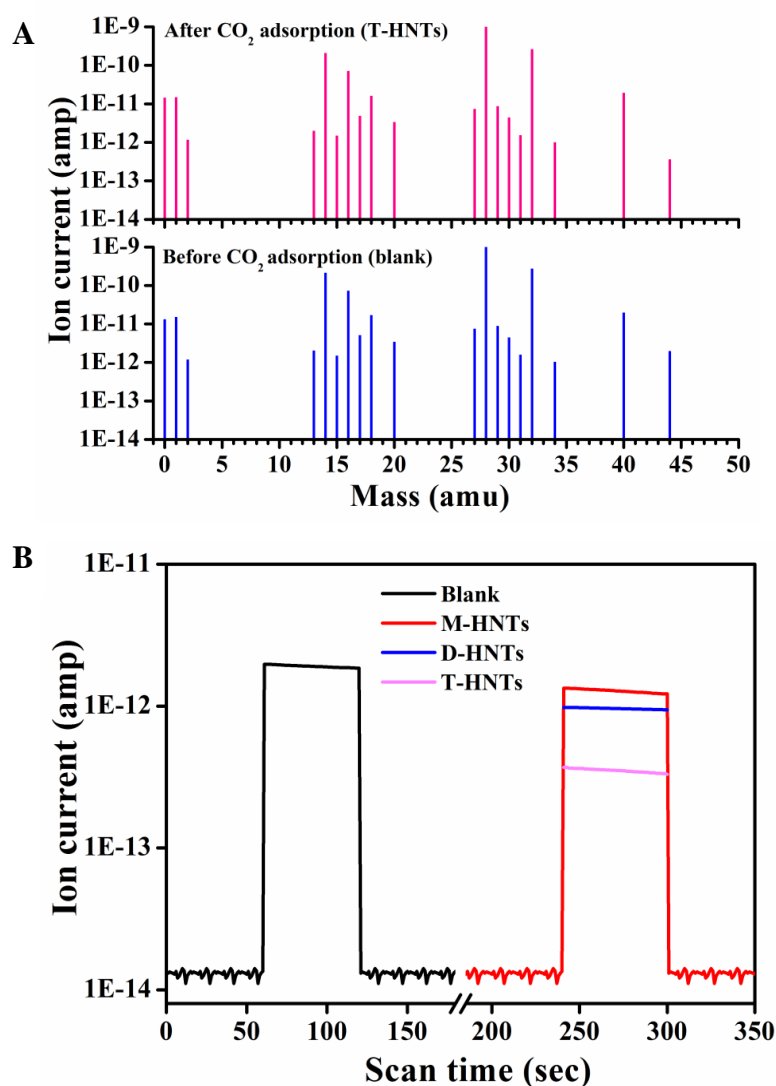


Figure 3.7: (A) Illustration of RGA mass spectra of the feed gas sample before and after CO₂ adsorption by 0.1 g of T-HNTs using Faraday scan mode. (B) Ion current change for the mass 44 amu due to atmospheric CO₂ capture by three different adsorbents after 2 h of adsorption monitored using RGA-MS technique in a multiple ions detection mode.

determine the amount of adsorbed CO_2 by the adsorbents. Figure 3.7B depicts how the ion current changes with the variation of adsorbents from M-HNTs to D-HNTs to T-HNTs after 2 h of adsorption, since they possess varied concentration of amino groups present in three different grafted aminosilanes. It should be noted that D-HNTs and T-HNTs contain both primary and secondary amine binding sites whereas M-HNTs comprises only primary amine binding site. Conversely, pristine HNTs i.e.; without amine loading hardly possess any adsorption capacity under same experimental condition and even when kept for 12 h. To demonstrate the accuracy and sensitivity of RGA-MS for the measurement of such a low concentration of CO_2 present in atmospheric air (~400 ppm), we have further verified the results using an optical cavity-enhanced integrated cavity output spectrometer (ICOS). It is basically a high-finesse optical cavity-enhanced absorption technique to measure the absorption features of CO_2 . The representative linear correlation plot of adsorbed CO_2 by M-HNTs analyzed by RGA-MS and ICOS is presented in Figure 3.8. A close correlation as ascribed by $R^2 = 0.9997$, signifies the validation of RGA-MS technique to precisely analyze CO_2 from the ambient air and even when present at low concentration.

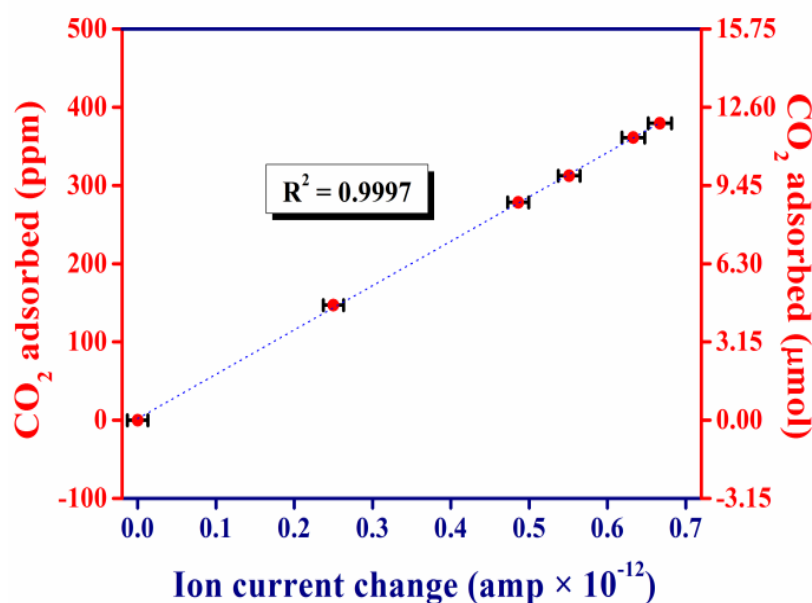


Figure 3.8: Linear correlation plot of adsorbed CO_2 by M-HNTs analyzed by RGA-MS and ICOS, demonstrating the comparable sensitivity and accuracy towards the measurement of atmospheric CO_2 using RGA-MS method to that of ICOS technique. The error bar stands for standard deviation of five successive measurements of a single sample using RGA-MS.

To explore the isotopic CO₂ capture from ambient air using clay based adsorbents, seasonal air has been collected and used as feed gas. Adsorption kinetics of atmospheric CO₂ (~400 ppm) has been elucidated based on laser-based high-precision carbon dioxide isotope analyzer exploiting off-axis integrated cavity output spectroscopy (OA-ICOS) technique. It is essentially an optical cavity-enhanced absorption technique to monitor the absorption features of CO₂.^{20,30} To evaluate the efficiency of the adsorbents, ambient air was administered into the adsorbent bed of the flasks containing M-, D- and T-HNTs respectively and allowed them to reach equilibration at standard room temperature and pressure. After a definite period of time, the amount of unadsorbed CO₂ remained in the ambient air of the sample flasks was assessed from the absolute change in concentration compare to the blank flask via the laser-based spectroscopy technique. We have found that the ambient air contains 12000 ppm of moisture and the corresponding relative humidity has been observed to be 31% during this study. Time dependent atmospheric CO₂ adsorption by M-, D- and T-HNTs demonstrates that 2 h after the injection of ambient air maximum CO₂ uptake was perceived for these adsorbents, subsequently it becomes levelling off as time progresses, shown in Figure 3.9A. The steeper slope at the beginning of the CO₂ adsorption accredited to the fast adsorption rate, which decreases gradually with time until it reaches to equilibrium. The adequate active adsorption sites over the surface of the adsorbents help to enhance the adsorbent-adsorbate interaction which in turn motivates the fast adsorption of atmospheric CO₂, whereas slower adsorption rate may be due to the reduced accessible adsorption sites as well as increased diffusion resistance developed during CO₂ adsorption. Atmospheric CO₂ adsorption capacity under the present experimental condition has been assessed to be 0.09, 0.14, and 0.22 mmol g⁻¹ for M-HNTs, D-HNTs and T-HNTs respectively; since the adsorbents consisted of three different grafted aminosilane with varied amino groups content. It is also important to note that D-HNTs and T-HNTs are composed of both primary and secondary amine binding sites whereas M-HNTs possesses only primary amine binding site. The kinetics of CO₂ adsorption from the ambient air by these solid adsorbents was demonstrated based on the pseudo-first-order,³¹ pseudo-second-order³² and fractional-order kinetic model³³ by fitting the acquired experimental data (Figure 3.9B-D).

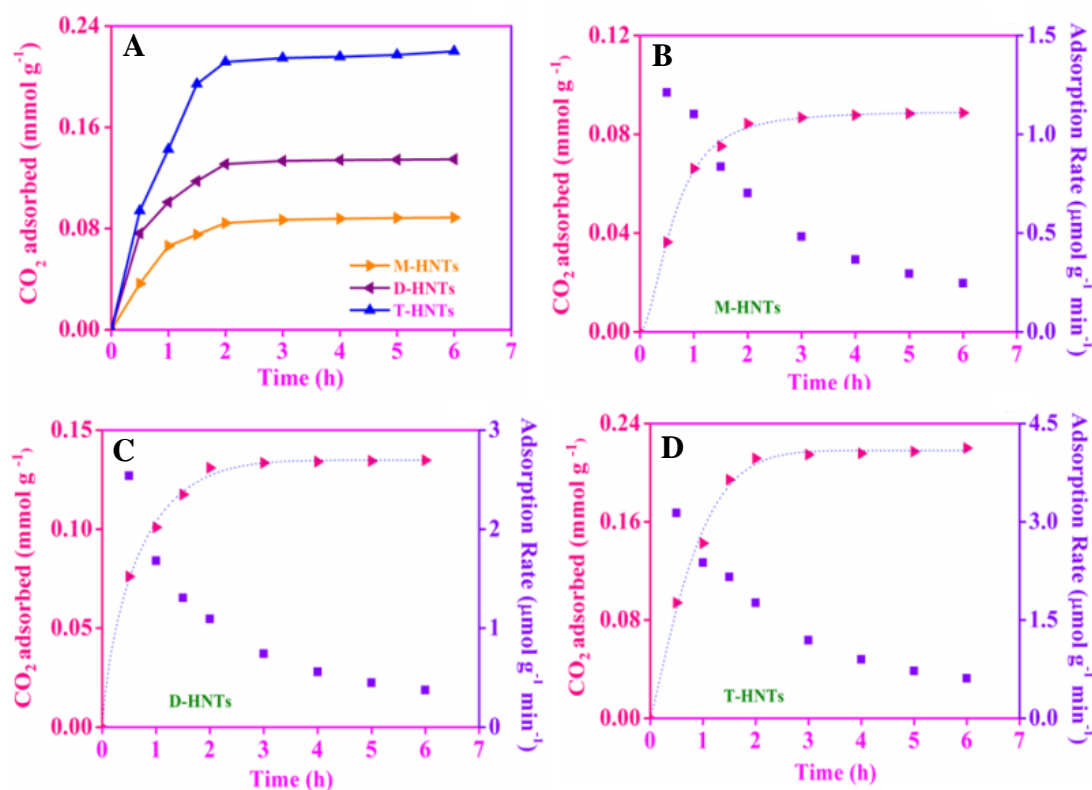


Figure 3.9: (A) Atmospheric CO₂ capture from the ambient air using M-HNTs, D-HNTs and T-HNTs up to 6 h at standard ambient temperature and pressure based on OA-ICOS technique. (B-D) Experimental CO₂ uptake data for all the three adsorbents demonstrate fractional order adsorption kinetics for CO₂.

However, CO₂ adsorption kinetics followed fractional-order kinetic model compared to pseudo-first-order or pseudo-second-order kinetic model for all the adsorbents. Pseudo-first-order, pseudo-second-order and fractional-order rate equations can be expressed as the following:

Pseudo-first-order rate equation:

$$Q_t = Q_e - Q_e e^{-k_1 t}$$

Pseudo-second-order rate equation:

$$Q_t = \frac{k_2 Q_e^2 t}{1 + k_2 Q_e t}$$

Fractional-order rate equation:

$$Q_t = Q_e - \frac{1}{\left[\left((n-1)k_n / m \right) t^m + \left(1/Q_e^{n-1} \right) \right]^{1/n-1}}$$

where, k_1 and k_2 are the rate constants for pseudo-first-order and pseudo-second-order reaction respectively. k_n , m , and n are constants of the fractional-order model. Q_t and Q_e are the adsorption capacity of the adsorbent at time t and at equilibrium. In fractional-order kinetic model, the rate of CO_2 chemisorption onto the active sites of amine is presumed to be directly proportional to the m^{th} power of the demonstrates pseudo-order of the reaction in regard to the adsorption time and n^{th} power of the driving force, where n driving force and k_n is an overall parameter combining several adsorption related factors since the model exhibits the complexity of the reaction mechanism. With higher or lower amine loading, the nature of atmospheric CO_2 adsorption by these adsorbents remains the same and thus, obeyed a general kinetic model based on the fractional-order rate equation. On the contrary, bare HNTs i.e.; without amine loading hardly possess any adsorption efficacy even when kept for 12 h under the same experimental condition (Figure 3.10).

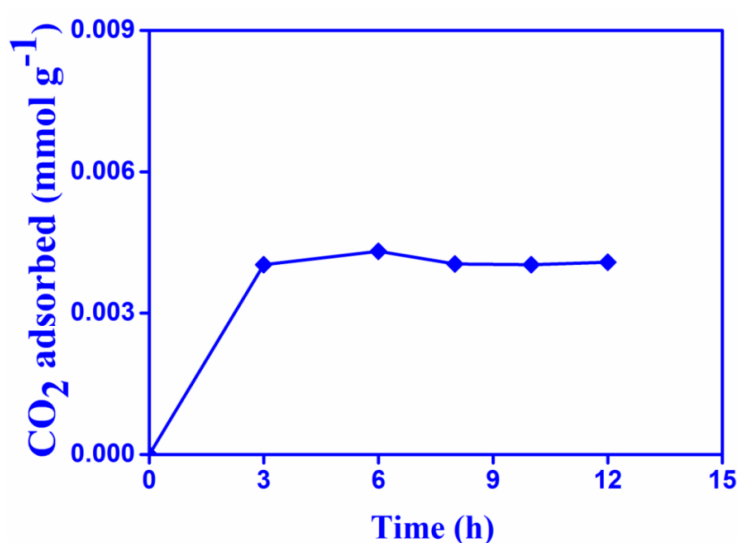


Figure 3.10: Ambient CO_2 adsorption by bare HNTs at standard pressure and temperature measured using OA-ICOS, demonstrating that they hardly possess any adsorption efficiency.

It has also been verified that all the solid adsorbents possess strong dependency on the feed gas concentration, which in turn tune their CO₂ adsorption efficiency. To authenticate this behaviour, we have varied the concentration of CO₂ keeping all other experimental condition unchanged. The concentration dependent CO₂ adsorption by the adsorbents in dry condition has been explicated in Figure 3.11.

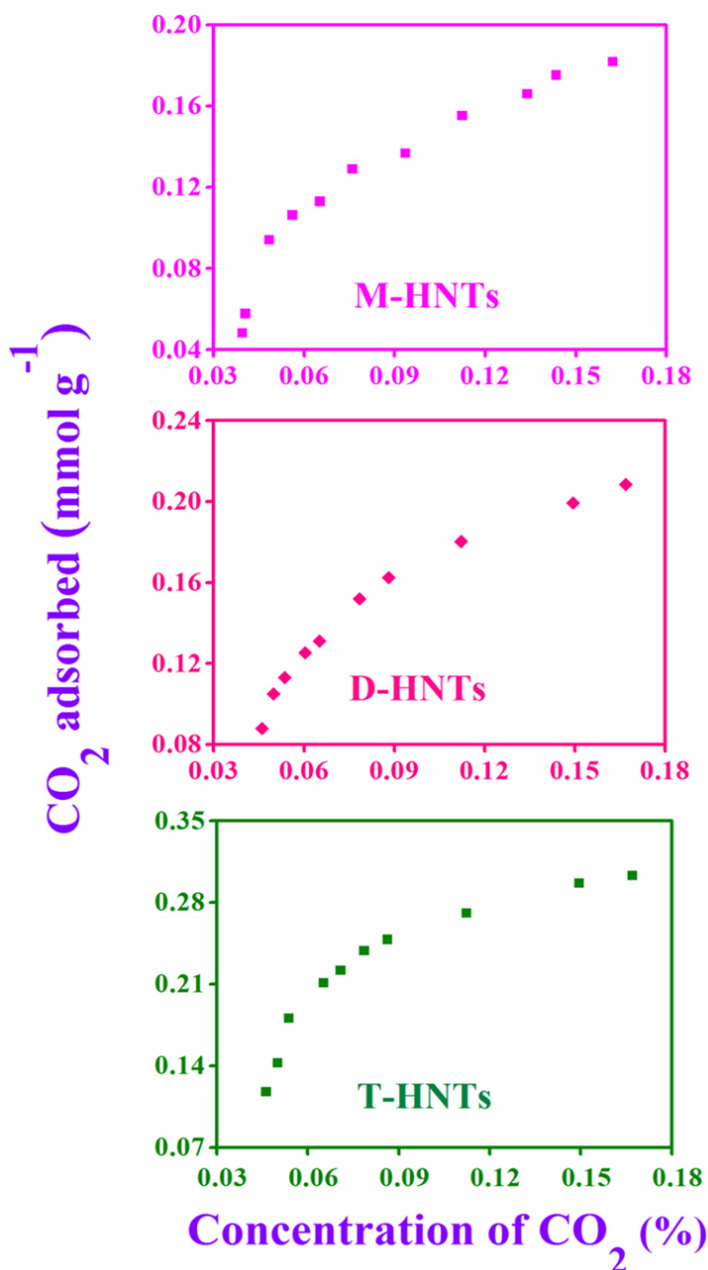


Figure 3.11: CO₂ adsorption capacity of M-HNTs, D-HNTs and T-HNTs at different CO₂ concentration, demonstrating the adsorption efficacy of the adsorbents depends on the feed gas concentration.

3.3.2.2 Adsorption of CO₂ Isotopes

To gain insight into the isotopic CO₂ capture by the clay based adsorbent from the ambient air, we have exclusively studied their adsorption kinetics under the said experimental condition. Since the atmospheric CO₂ comprises of three major stable isotopes ¹²CO₂ (98.42%), ¹³CO₂ (1.1%) and ¹²C¹⁶O¹⁸O (0.394%) therefore, it would be interesting to investigate their adsorption characteristics. ¹³CO₂ and ¹²C¹⁸O¹⁶O isotopic data represented as follows:

$$\delta_{\text{DOB}}^{13}\text{C}\text{‰} = (\delta^{13}\text{C}\text{‰})_{\text{sample}} - (\delta^{13}\text{C}\text{‰})_{\text{blank}}$$

$$\delta_{\text{DOB}}^{18}\text{O}\text{‰} = (\delta^{18}\text{O}\text{‰})_{\text{sample}} - (\delta^{18}\text{O}\text{‰})_{\text{blank}}$$

$$\delta^{13}\text{C}\text{‰} = \left[\frac{\left(\frac{^{13}\text{C}}{^{12}\text{C}}\right)_{\text{sample}}}{\left(\frac{^{13}\text{C}}{^{12}\text{C}}\right)_{\text{standard}}} - 1 \right] \times 1000 \quad \delta^{18}\text{O}\text{‰} = \left[\frac{\left(\frac{^{18}\text{O}}{^{16}\text{O}}\right)_{\text{sample}}}{\left(\frac{^{18}\text{O}}{^{16}\text{O}}\right)_{\text{standard}}} - 1 \right] \times 1000$$

where $\left(\frac{^{13}\text{C}}{^{12}\text{C}}\right)_{\text{standard}}$ and $\left(\frac{^{18}\text{O}}{^{16}\text{O}}\right)_{\text{standard}}$ are the international standard Pee Dee Belemnite (PDB) values of 0.0112372 and 0.0020672 respectively. Figure 3.12 depicts that $\delta^{13}\text{C}$ in ambient air over the adsorbent (M-HNTs) in sample flask were depleted in comparison to blank flask. The maximum decrease in $\delta^{13}\text{C}$ value was observed after 1h of the adsorption; afterwards it gradually increased until it reached to equilibrium at 2 h, after which it remained unchanged. The carbon-13 isotopic adsorption behaviour was found to be identical in D-HNTs and T-HNTs (Figure 3.12). In contrast to carbon-13 isotope, for ¹⁸O of CO₂ we have seen that $\delta^{18}\text{O}$ in sample flask was gradually increasing in comparison to the blank until it reached to equilibrium, subsequently it became levelling off. The above results attribute that though D-HNTs and T-HNTs possess both primary and secondary amine binding sites whereas only primary amine binding site is available in M-HNTs, however, the nature of isotopic adsorption of CO₂ by these clay based solid adsorbents remains the same. This may be due to the fact that a chemical reaction is supposed to be regulated by the electronic

structure of an atom and may not be influenced by the neutron numbers. Since the isotopes of CO₂ having the atoms with same electron number but different neutron number, therefore, they could be assumed to show similar chemical properties during the reactions.

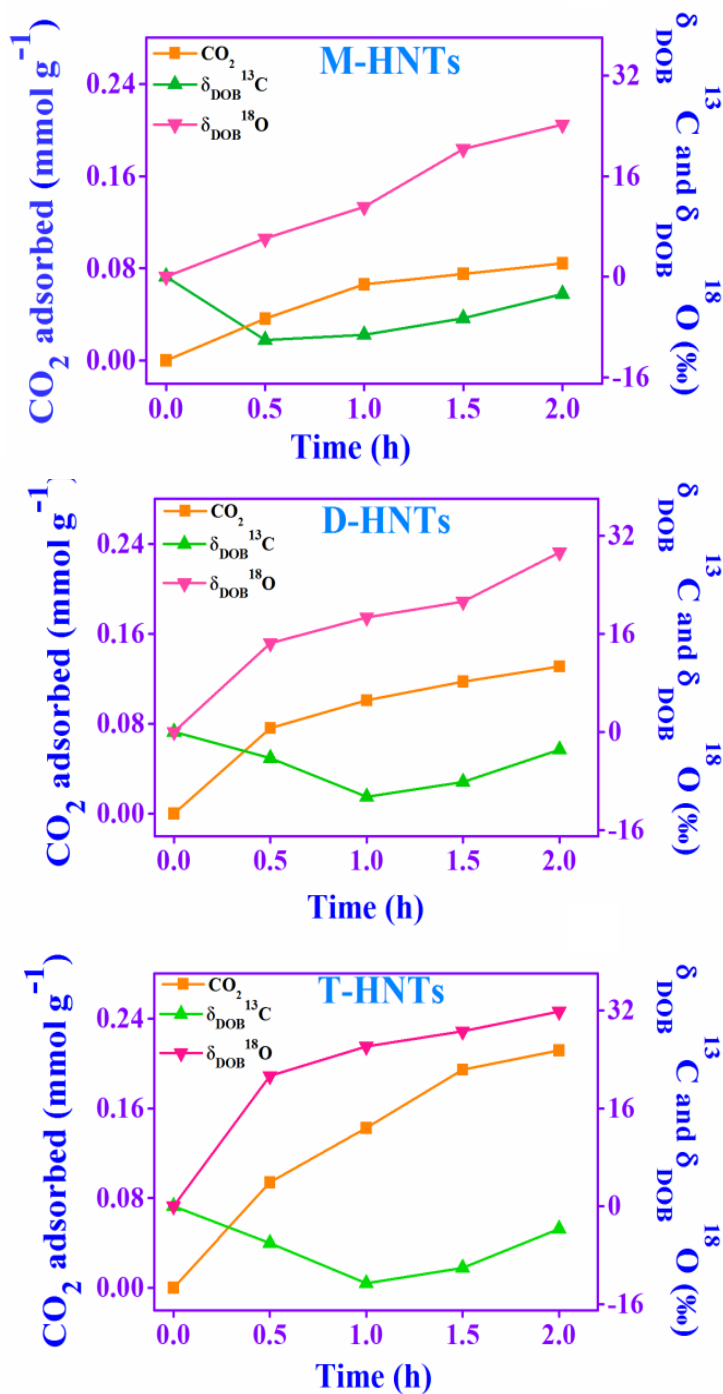


Figure 3.12: Adsorption kinetics of three abundant isotopes of ambient CO₂ (¹²C¹⁶O₂, ¹³C¹⁶O₂, and ¹²C¹⁶O¹⁸O), where adsorption of ¹³CO₂ and ¹⁸O of CO₂ has been expressed in terms of δ_{DOB}¹³C‰ and δ_{DOB}¹⁸O‰.

3.3.2.3 Impact of Moisture during CO₂ Uptake

To explore the impact of moisture during CO₂ uptake, we have carried out the adsorption study using seasonal ambient air as feed gas keeping all other experimental condition the same. We observed that with increasing moisture concentration from 11000 ppm to 15000 ppm in the ambient air, CO₂ uptake efficiency of these adsorbents enhances, as illustrated in Figure 3.13. The observed enhancement of CO₂ adsorption is due to the precise nature of amine - CO₂ interaction, leading to an increase in amine efficiency which in turn points to a higher adsorption capacity.³⁴ However, it should be noted that we have not introduced additional moisture from the outside during this study and we only enable to tune the moisture concentration up to 15000 ppm (corresponding relative humidity has been found to be 42%) in the feed gas as it has been collected in different seasons.

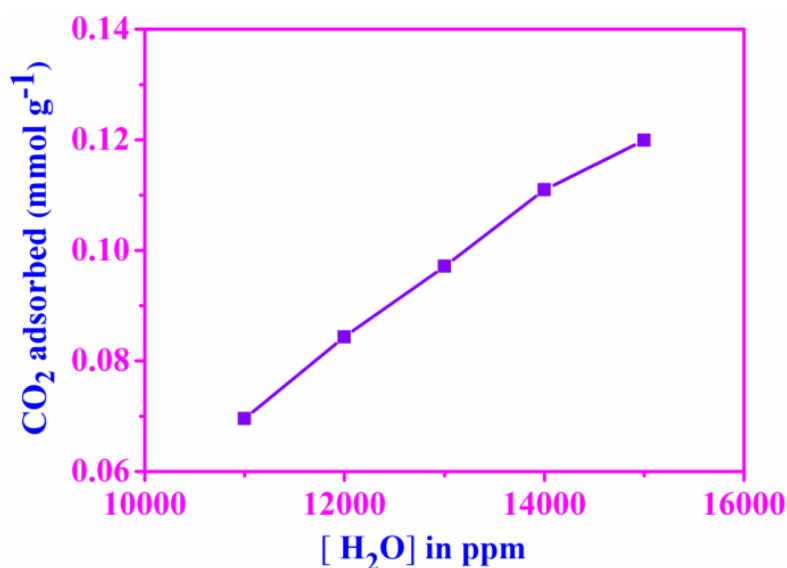


Figure 3.13: Impact of moisture during CO₂ uptake by M-HNTs from the seasonal air having different relative humidity, which has been expressed in terms of moisture content (ppm) measured from ICOS.

Hence, it is interesting to examine the adsorption behaviour of these adsorbents with the atmospheric air having 15000 ppm of moisture content, i.e.; relative humidity (RH) of 42%. Figure 3.14 demonstrates how CO₂ uptake capability of the three solid adsorbents changes once the humidity in the air increases. Under the current experimental condition, atmospheric CO₂ adsorption capacity of M-HNTs, D-

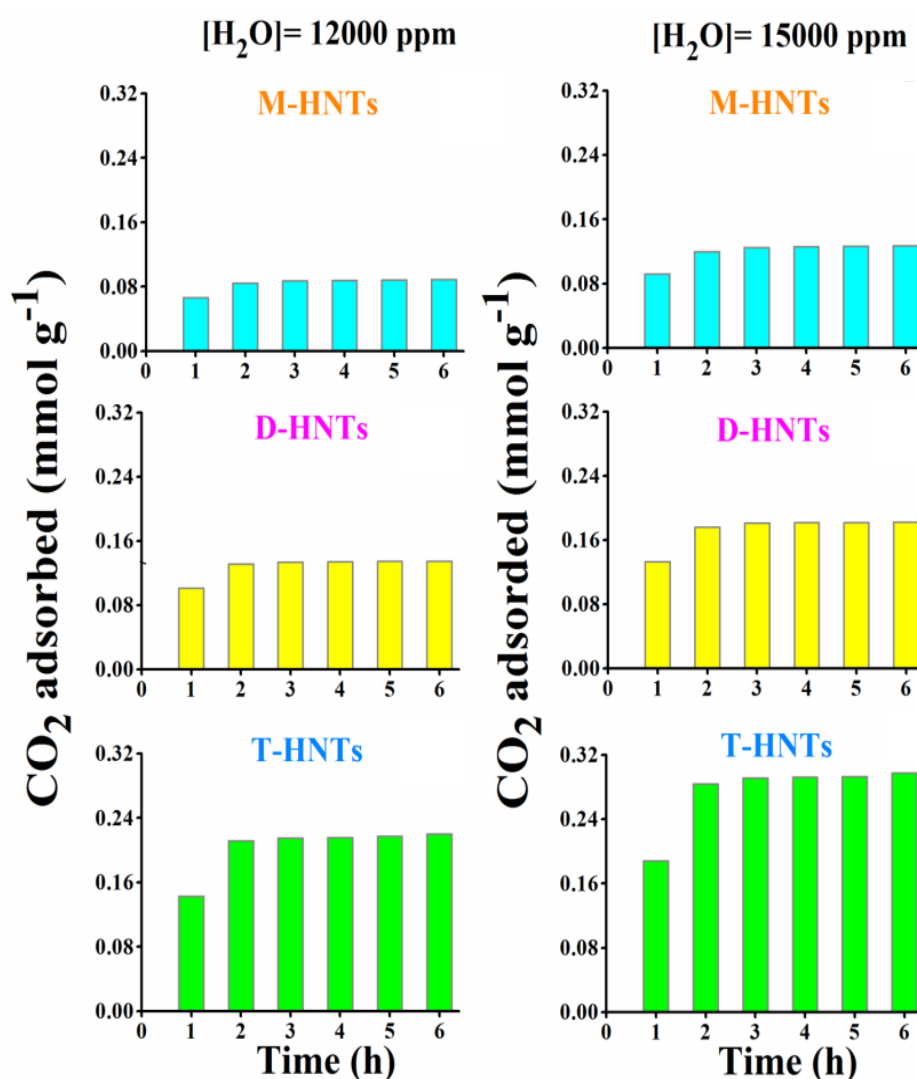


Figure 3.14: CO₂ uptake capacity of the three solid adsorbents changes once the humidity in the air increases from 31 to 42% (12000 and 15000 ppm respectively).

HNTs and T-HNTs has been enhanced from 0.09, 0.14, and 0.22 to 0.13, 0.19 and 0.3 mmol g⁻¹ respectively, attributing to the increase in the amine efficiency of the corresponding adsorbents (Table 3.3). Primary amine grafted adsorbent (M-HNTs) illustrates the highest amine efficiency compared to the other two adsorbents containing both primary and secondary amines i.e.; D-HNTs and T-HNTs. The higher amine efficiency of the adsorbents containing primary amines than the adsorbents having both primary and secondary amines, probably due to the little interaction of the later amines with the CO₂ during the adsorption process as well as ultra-dilute condition further significantly decreases the ability for secondary amines to adsorb

Table 3.3: Amine efficiency of the adsorbents in the seasonal ambient air changes with the change in relative humidity.

Adsorbents	Amine Loading (mmol g ⁻¹)	Moisture in Ambient Air (RH ~ 31 %)		Moisture in Ambient Air (RH ~ 42 %)	
		CO ₂ Adsorption Capacity (mmol g ⁻¹)	Amine Efficiency (mmol _{CO₂} mmol _N ⁻¹)	CO ₂ Adsorption Capacity (mmol g ⁻¹)	Amine Efficiency (mmol _{CO₂} mmol _N ⁻¹)
M-HNTs	0.36	0.09	0.25	0.13	0.36
D-HNTs	0.75	0.14	0.19	0.19	0.25
T-HNTs	1.14	0.22	0.19	0.29	0.25

CO₂.³⁵⁻³⁷ Therefore, the efficacy of an adsorbent depends not only on the surface density of covalently attached amine groups but also on the nature of amine employed as well as the adsorption condition whether it is anhydrous or humid.

To demonstrate the change in isotopic adsorption property of ambient CO₂, we have focused our next study on the isotopic analysis of CO₂ uptake considering the seasonal ambient air having two different moisture concentrations. We observed the similar changes of $\delta_{\text{DOB}}^{13}\text{C}$ and $\delta_{\text{DOB}}^{18}\text{O}$ in M-HNTs, D-HNTs and T-HNTs in both 12000 ppm (RH ~ 31 %) and 15000 ppm (RH ~ 42 %) of moisture as shown in Figure 3.15. In this study, we found that the $\delta_{\text{DOB}}^{13}\text{C}$ was observed to be the maximum after 1h of adsorption, suggesting a preferential adsorption of the ¹³CO₂ isotopes within this particular time by these clay based adsorbents. The preferential adsorption of ¹³CO₂ isotopes possibly attributes to the relatively heavier ¹³CO₂ molecules gradually coming to the vicinity of the absorbent bed with time, which in turn may facilitate the higher rate of adsorption of ¹³CO₂ molecules at the initial stage, finally resulting in the relatively lower ¹³CO₂/¹²CO₂ isotopes ratio in sample flask. As the absorbents are

allowed to keep in contact with the ambient air for more times the availability of $^{13}\text{CO}_2$ molecules decreases into the sample flask, which may be the probable cause for decreasing $\delta^{13}\text{CO}_2$ values in the sample flask.

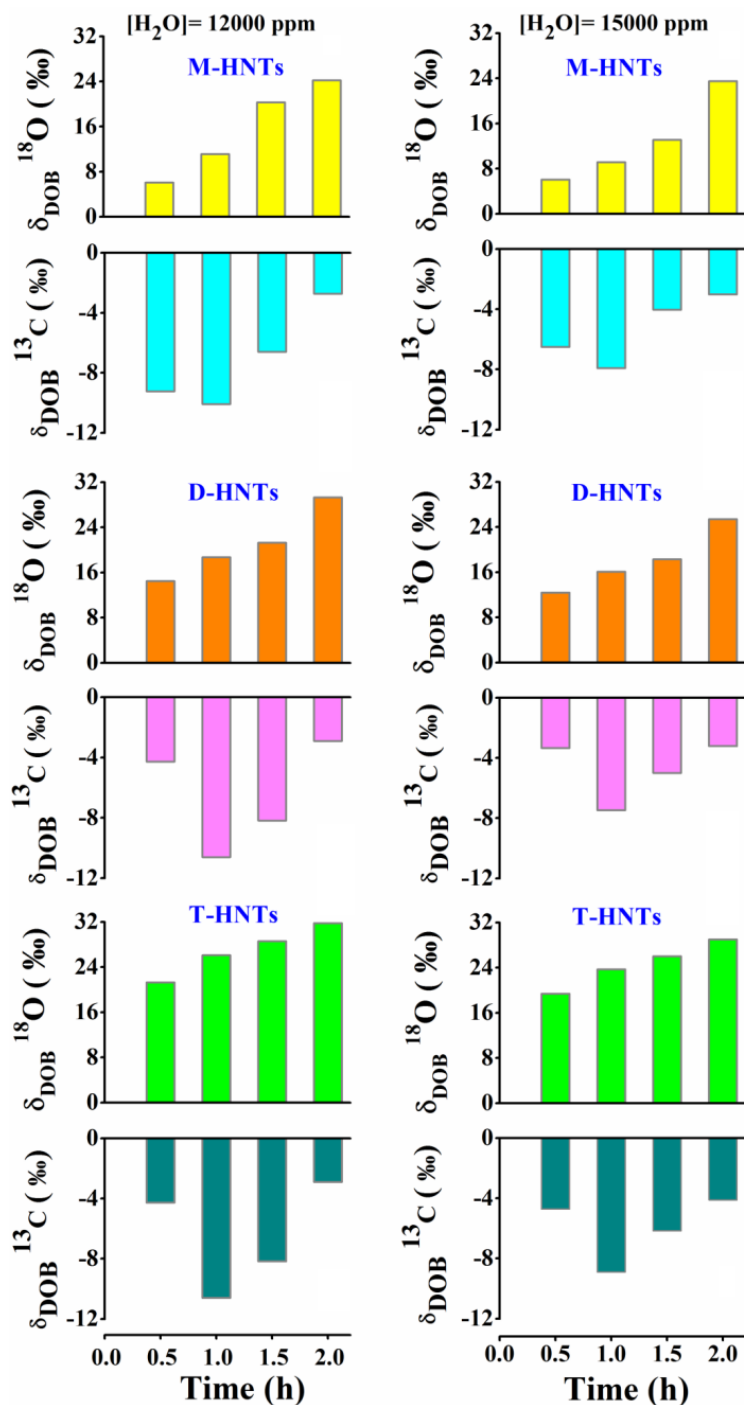


Figure 3.15: Adsorption kinetics of $^{13}\text{C}^{16}\text{O}_2$ and $^{12}\text{C}^{16}\text{O}^{18}\text{O}$ isotopes present in the seasonal ambient (12000 and 15000 ppm respectively), demonstrating similar characteristics of $\delta_{\text{DOB}}^{13}\text{C}$ and $\delta_{\text{DOB}}^{18}\text{O}$ in M-HNTs, D-HNTs and T-HNTs.

Alternatively, $^{12}\text{C}^{16}\text{O}^{18}\text{O}$ isotope is heavier than $^{13}\text{CO}_2$ and $^{12}\text{CO}_2$ isotopes, suggesting a comparatively rapid adsorption of $^{12}\text{C}^{16}\text{O}^{18}\text{O}$ isotopes within the sample flask, leading to a decrease in $\delta_{\text{DOB}}^{18}\text{O}$ value; however, results obtained from the isotopic CO_2 uptake study demonstrate a reverse trend in case of $^{12}\text{C}^{16}\text{O}^{18}\text{O}$ isotope. Early study suggests that oxygen-16 isotope and oxygen-18 isotope are rapidly exchanged between atmospheric CO_2 and ^{18}O water to produce $^{12}\text{C}^{16}\text{O}^{18}\text{O}$ inside the glass flask;³⁸ $\text{C}^{16}\text{O}^{16}\text{O} + \text{H}_2^{18}\text{O} \longrightarrow \text{C}^{16}\text{O}^{18}\text{O} + \text{H}_2^{16}\text{O}$. In our study, there is no external source for incorporation of ^{18}O isotope of CO_2 . Therefore, the enrichment of this isotope in sample flask may be due to the real time production of ^{18}O isotope from the isotopic exchange between $^{12}\text{CO}_2$ and H_2^{18}O in the ambient air of the sample flask. Hence, an increase in $\delta_{\text{DOB}}^{18}\text{O}$ values was found during the isotopic CO_2 adsorption from the ambient air.

3.3.2.4 Reusability of the Adsorbents

From the practical rather economical point of view, an adsorbent should not only possess the fast CO_2 adsorption and desorption capability at a low desorption temperature but also have an intact CO_2 uptake capacity in the course of persistent adsorption/desorption cycling experiments. To address the issue regarding cycling adsorption behaviour of an adsorbent, a consecutive 2 h adsorption and 1.5 h desorption cycling experiments for CO_2 were performed after regeneration of the adsorbents upon heating at $120\text{ }^\circ\text{C}$ under the flow of nitrogen and subsequently pulled down the vacuum before every new set of adsorption/desorption study. The reversible CO_2 adsorption ability of all the three clay based adsorbents at two different experimental conditions indicates a slightly decreasing trend in the adsorption efficacy after repetitive cyclic experiments (Figure 3.16). The low desorption temperature further suggests that the compounds formed between CO_2 and the amine are not stable enough and thus it is easier to regenerate the adsorbents by liberating adsorbed CO_2 under reduced pressure, ensuring the sustainability of the atmospheric CO_2 capture procedure even under oxidative environment. Table 3.4 demonstrates the CO_2 uptake efficacy of these clay based adsorbents compared to that of the reported adsorbents, although the adsorption condition and feed gas concentration which

actually regulate the adsorption property, are quite different. However, all our clay based adsorbents exhibit reasonably higher efficiency for CO₂ capture even when present in low concentration especially in the ambient air (~ 400 ppm).

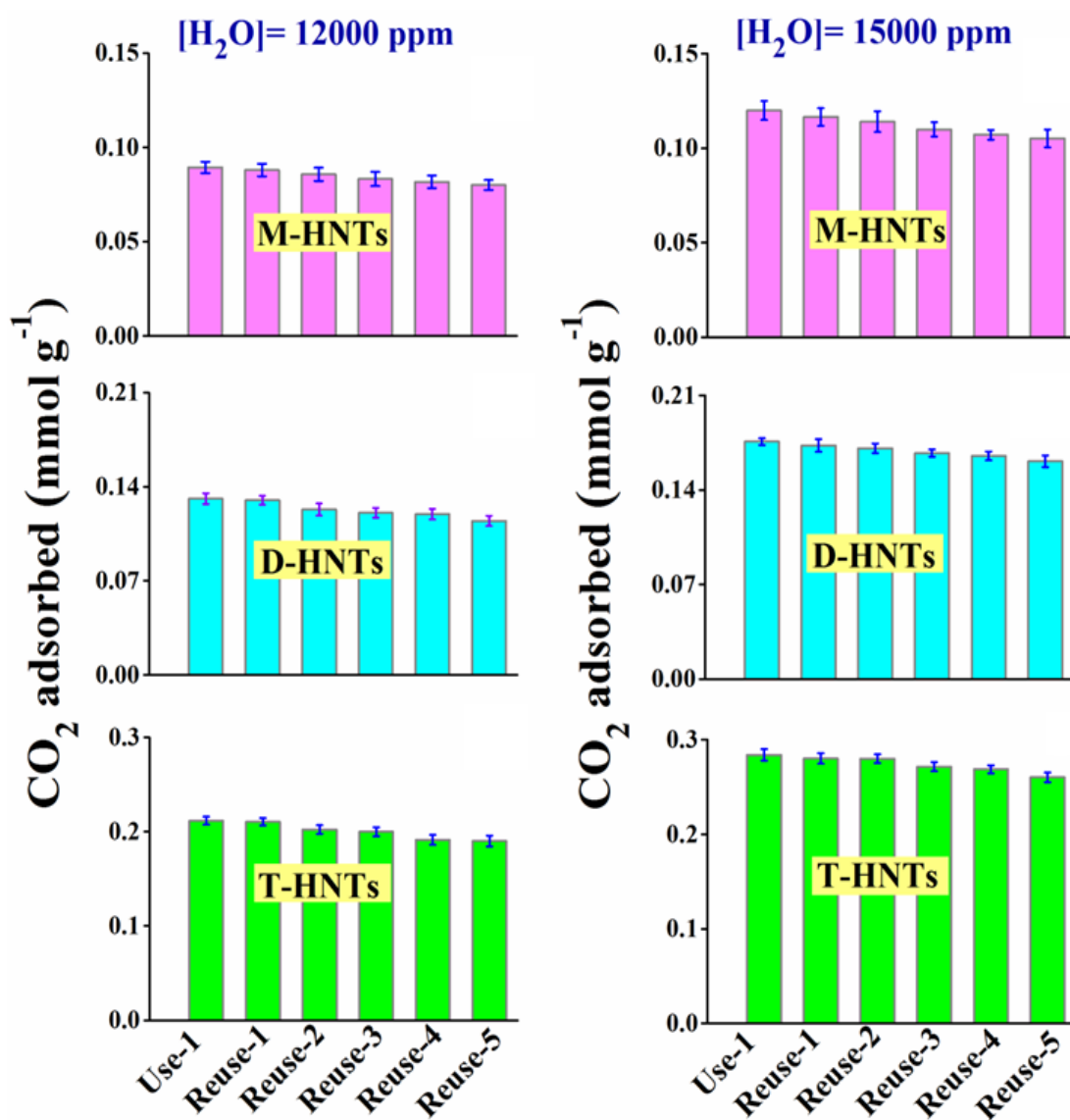


Figure 3.16: The regeneration and recyclability of M-HNTs, D-HNTs, and T-HNTs adsorbents for atmospheric CO₂ capture at different moisture concentration, signifying the good thermal stability and reusability of all adsorbents even under oxidative environment.

Table 3.4: Comparison of CO₂ uptake efficacy of these clay based adsorbents with the reported amine based solid adsorbents.

Adsorbents	Feed gas conc. [CO ₂] in vol %	Amine loading (mmol _N g ⁻¹)	Amine efficiency (mmol _{CO2} mmol _N ⁻¹)	References
APTES ₃₉ /MCM	100	1.79	0.26	39
A2-SBA-15	100	4.20	0.34	8
A2-BPMO	100	4.90	0.44	8
DWSNT-NH ₂	100	2.93	0.49	25
DWSNT-NH-(CH ₂) ₂ -NH ₂	100	4.57	0.41	25
DWSNT-NH-(CH ₂) ₂ -NH-(CH ₂) ₂ -NH ₂	100	4.93	0.45	25
APS-MCM-48	100	2.45	0.32	40
NH ₂ -mag ^a	100	2.20	0.16	41
NH ₂ -C ₁₈ -mag ^a	100	2.30	0.52	41
APS/SBA(1)	15.4	1.11	0.14	37
AEAPS/SBA(1)	15.4	2.26	0.12	37
TA/SBA(1)	15.4	2.75	0.13	37
SBA-NH ₂	10	1.90	0.21	42
SBA-diamine	10	2.50	0.28	42
APTMS/SBA-ex	10	2.43	0.44	43
AEAPS/SBA-ex	10	3.41	0.29	43
TA/SBA-ex	10	4.76	0.25	43
AMPTS/Magnesium Phyllosilicate ^b	5	2.56	0.89	44
TMSPEDA/Magnesium Phyllosilicate ^b	5	3.37	0.84	44
TMSPETA/Magnesium Phyllosilicate ^b	5	3.24	0.71	44

HYB-maga28 ^c	5	0.220	0.60	45
γ -maga28	5	0.276	0.37	45
M-HNTs	0.04	0.36	0.36	present work
D-HNTs	0.04	0.75	0.25	present work
T-HNTs	0.04	1.14	0.25	present work

a: Relative humidity of the gas stream is ~74%. The presence of octadecyl groups in NH₂-C₁₈-maga expanded the interlayer space and help to increase CO₂ adsorption capacity; **b:** Besides alkylammonium carbamate other compounds, like silylpropylcarbamates and hydrogen-bonded propylcarbamic acids were formed, increasing the efficiency above 0.5; **c:** HYB-maga28 is a pillared layered silicates, where lamellas are separated by pillars, allowing CO₂ to reach to amine site and also the surface SiOH groups also take part in the adsorption process by forming silylpropylcarbamates, hydrogen-bonded propylcarbamic acids etc, increasing the efficiency beyond 0.5.

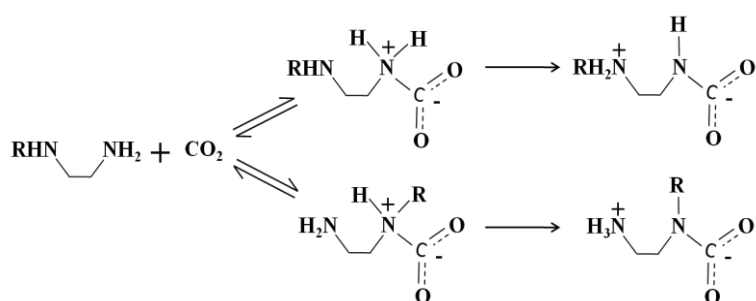
APTES: 3-aminopropyltriethoxysilane; A2-SBA-15: N-[3-(trimethoxysilyl)propyl]ethylene-diamine modified SBA-15; A2-BPMO: N-[3-(trimethoxysilyl)propyl]-ethylenediamine-modified benzene periodic mesoporous organosilica; DWSNTs: double-walled silica nanotubes; APS: 3-aminopropyltriethoxysilane; NH₂-maga: 3-aminopropyltriethoxysilane modified magadiite; NH₂-C₁₈-maga: 3-aminopropyltriethoxysilane and octadecyltrichlorosilane modified magadiite; AEAPS: N-(2-aminoethyl)-3-aminopropyltrimethoxysilane; TA: (3-trimethoxysilylpropyl)diethylenetriamine; SBA-NH₂: 3-aminopropyltriethoxysilane functionalized SBA silica; SBA-diamine: N-[3-(trimethoxysilyl)propyl] ethylenediamine functionalized aminosilicas; AMPTS: 3-aminopropyltriethoxysilane; TMSPEDA: N-[3-(trimethoxysilyl)propyl]-ethylenediamine; TMSPETA: N-[3-(trimethoxysilyl)propyl]-diethylenetriamine; γ -maga28: γ -aminopropyltriethoxysilane functionalized magadiite; HYB-maga28: γ -aminopropyltriethoxysilane functionalized magadiite i.e.; pillared layered silicates.

3.3.2.5 CO₂ Adsorption Mechanism

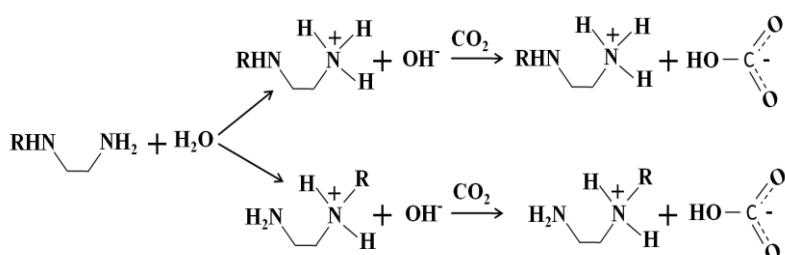
The reaction pathway of CO₂ adsorption onto the surface of these solid adsorbents under anhydrous condition predominantly proceeds through the carbamate mechanism,^{46,47} whereas in humid condition it follows the formation of bicarbonates,^{48,49} ascribed in Scheme 3.2. Basically CO₂ adsorption is an acid-base

reaction where carbamate was produced due to the nucleophilic attack of the lone pair on nitrogen of both primary and secondary amines to CO_2 to form zwitterions, followed by the deprotonation of those zwitterions by a base i.e.; another amine molecule in case of anhydrous condition.^{50,51} Hence, two amine groups are required to capture one molecule of CO_2 under dry condition, while a stoichiometric CO_2/N ratio of 1 in humid condition.⁴⁸⁻⁵⁰

(a) Anhydrous Condition:

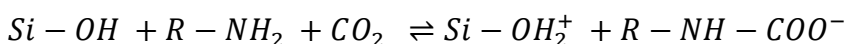
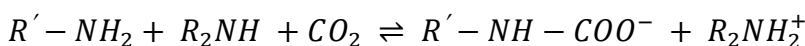
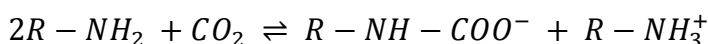


(b) Humid Condition:



Scheme 3.2: Schematic presentation of CO_2 adsorption on the clay based adsorbents having both primary and secondary amine sites under (a) anhydrous and (b) humid conditions.

It is also reported that if CO_2 and amine modified solid adsorbents were contacted significant time under very dry conditions; they formed an additional product, silylalkylcarbamate.^{44,52-54} Hence, silanol groups may assist CO_2 adsorption to the amine based silica adsorbents under very dry condition by forming silylalkylcarbamate which is not formed in humid condition. The proposed mechanism has been presented below:



However, FTIR spectra of the amine based adsorbents exposed to seasonal air attribute to the formation of alkylammonium carbamate species (Figure 3.17, Table 3.5). We could not find any evidence for the formation of silylalkylcarbamate from the recorded FTIR spectra. Therefore, we believe the carbamate mechanism is dominant although the increase in amine efficiency when the ambient air containing relative humidity of 42% was introduced as feed gas, suggests that there may be two operable mechanisms with different intrinsic kinetics for the enhancement of adsorption efficacy of these adsorbents.

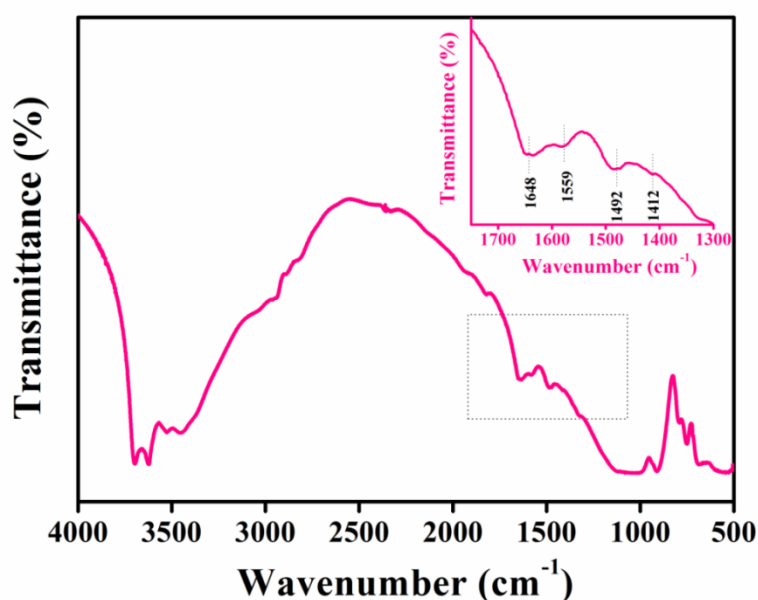


Figure 3.17: FTIR spectrum after the adsorption of CO₂ on T-HNTs demonstrates the formation of alkylammonium carbamate species owing to the adsorption of atmospheric CO₂ onto the surface of the adsorbent.

Table 3.5: Assignment of FTIR bands after the adsorption of atmospheric CO₂ over the surface of adsorbent.

Wavenumber (cm ⁻¹)	Assignment	Species	References
1412	Symmetric stretching COO-	Carbamate	47,55,56
1492	Symmetric NH ⁺ deformation	Ionic carbamate	39,47,56
1559	N-H deformation	Aminosilane	28
1648	C=O stretching	Carbamic acid	53,57
2937	C-H stretching vibration	Aminosilane	28,58
3451	N-H stretching vibration	Aminosilane	28

3.4 Conclusions

In conclusion, we have developed three clay based solid adsorbents grafted with several viable amines having varied amine densities and adsorption sites for isotopic CO₂ capture from ambient air under standard temperature and pressure using a spectroscopic technique, keeping an eye on the preferential adsorption of the three major abundant isotopes of CO₂ which comprises of ¹²CO₂ (98.42%), ¹³CO₂ (1.1%) and ¹²C¹⁶O¹⁸O (0.394%) isotopes. Relative humidity in terms of moisture regulates the isotopic atmospheric CO₂ adsorption and the adsorption kinetics describing CO₂ uptake rate was studied to evaluate the efficacy of the adsorbents as well as to explore the underlying mechanism behind the adsorption. The efficiency along with excellent stability of these novel adsorbents even after prolonged cyclic adsorption-desorption experiments has been attributed by their repetitive use in oxidative environment. Therefore, our findings point to a preferential isotopic CO₂ uptake even in an ultra-dilute concentration as well as under dry and moist conditions, introducing a new pathway in the frontier area of CO₂ capture and sequestering study in a wide range of areas including academic to industry.

3.5 References

1. Sumida, K.; Rogow, D. L.; Mason, J. A.; McDonald, T. M.; Bloch, E. D.; Herm, Z. R.; Bae, T.-H.; Long, J. R. Carbon Dioxide Capture in Metal Organic Frameworks. *Chem. Rev.* **2012**, *112*, 724-781.
2. Pachauri, R. K.; Reisinger, A. IPCC Fourth Assessment Report, Intergovernmental Panel on Climate Change, **2007**.
3. Goepfert, A.; Czaun, M.; May, R. B.; Prakash, G. K. S.; Olah, G. A.; Narayanan, S. R. Carbon Dioxide Capture from the Air Using a Polyamine Based Regenerable Solid Adsorbent. *J. Am. Chem. Soc.* **2011**, *133*, 20164-20167.
4. Rao, A. B.; Rubin, E. S. A Technical, Economic, and Environmental Assessment of Amine-Based CO₂ Capture Technology for Power Plant Greenhouse Gas Control. *Environ. Sci. Technol.* **2002**, *36*, 4467-4475.
5. Kohl, A.; Nielsen, R. Alkanolamines for Hydrogen Sulfide and Carbon Dioxide Removal. *Gas Purification*, Gulf Publishing Company, Houston, Texas, **1997**, 40-186.
6. Zeman, F. Energy and Material Balance of CO₂ Capture from Ambient Air. *Environ. Sci. Technol.* **2007**, *41*, 7558-7563.
7. McDonald, T. M.; Lee, W. R.; Mason, J.A.; Wiers, B. M.; Hong, C. S.; Long, J. R. Capture of Carbon Dioxide from Air and Flue Gas in the Alkylamine-Appended Metal-Organic Framework mmen-Mg₂(dobpdc). *J. Am. Chem. Soc.* **2012**, *134*, 7056-7065.
8. Sim, K.; Lee, N.; Kim, J.; Cho, E.-B.; Gunathilake, C.; Jaroniec, M. CO₂ Adsorption on Amine-Functionalized Periodic Mesoporous Benzenesilicas. *ACS Appl. Mater. Interfaces* **2015**, *7*, 6792-6802.
9. Adeniran, B.; Masika, E.; Mokaya, R. A Family of Microporous Carbons Prepared Via a Simple Metal Salt Carbonization Route with High Selectivity for Exceptional Gravimetric and Volumetric Post-Combustion CO₂ Capture. *J. Mater. Chem. A* **2014**, *2*, 14696-14710.
10. Alkhabbaz, M. A.; Bollini, P.; Foo, G. S.; Sievers, C.; Jones, C. W. Important Roles of Enthalpic and Entropic Contributions to CO₂ Capture from Simulated
11. Flue Gas and Ambient Air Using Mesoporous Silica Grafted Amines. *J. Am. Chem. Soc.* **2014**, *136*, 13170-13173.
12. Li, Y.; Xin, Q.; Wu, H.; Guo, R.; Tian, Z.; Liu, Y.; Wang, S.; He, G.; Pan, F.; Jiang, Z. Efficient CO₂ Capture by Humidified Polymer Electrolyte Membranes with Tunable Water State. *Energy Environ. Sci.* **2014**, *7*, 1489-1499.
13. Lee, K. B.; Beaver, M. G.; Caram, H. S.; Sircar, S. Reversible Chemisorbents for Carbon Dioxide and Their Potential Applications. *Ind. Eng. Chem. Res.* **2008**, *47*, 8048-8062.
14. Nikulshina, V.; Ayesa, N.; Galvez, M. E.; Steinfeld, A. Feasibility of Na-based Thermochemical Cycles for the Capture of CO₂ from Air-Thermodynamic and Thermogravimetric Analyses. *Chem. Eng. J.* **2008**, *140*, 62-70.
15. Stuckert, N. R.; Yang, R. T. CO₂ Capture from the Atmosphere and Simultaneous Concentration Using Zeolites and Amine-Grafted SBA-15. *Environ. Sci. Technol.* **2011**, *45*, 10257-10264.

16. Rezaei, F.; Lively, R. P.; Labreche, Y.; Chen, G.; Fan, Y.; Koros, W. J.; Jones, C. W. Aminosilane-Grafted Polymer/Silica Hollow Fiber Adsorbents for CO₂ Capture from Flue Gas. *ACS Appl. Mater. Interfaces* **2013**, *5*, 3921-3931.
17. Sun, L.-B.; Li, A.-G.; Liu, X.-D.; Liu, X.-Q.; Feng, D.; Lu, W.; Yuan, D.; Zhou, H.-C. Facile Fabrication of Cost-Effective Porous Polymer Networks for Highly Selective CO₂ Capture. *J. Mater. Chem. A* **2015**, *3*, 3252-3256.
18. Neti, V. S. P. K.; Wang, J.; Deng, S.; Echegoyen, L. High and Selective CO₂ Adsorption by a Phthalocyanine Nanoporous Polymer. *J. Mater. Chem. A* **2015**, *3*, 10284-10288.
19. Arab, P.; Parrish, E.; İslamoğlu, T.; El-Kaderi, H. M.. Synthesis and Evaluation of Porous Azo-Linked Polymers for Carbon Dioxide Capture and Separation. *J. Mater. Chem. A* **2015**, *3*, 20586-20594.
20. Neti, V. S. P. K.; Wu, X.; Deng, S.; Echegoyen, L. Selective CO₂ Capture in an Imine Linked Porphyrin Porous Polymer. *Polym. Chem.* **2013**, *4*, 4566-4569.
21. Zare, R. N.; Kuramoto, D. S.; Haase, C.; Tan, S. M.; Crosson, E. R.; Saad, N. M. R. High-Precision Optical Measurements of ¹³C/¹²C Isotope Ratios in Organic Compounds at Natural Abundance. *PNAS* **2009**, *106*, 10928-10932.
22. Ghosh, C.; Mukhopadhyay, P.; Ghosh, S.; Pradhan, M. Insulin Sensitivity Index (ISI_{0, 120}) Potentially Linked to Carbon Isotopes of Breath CO₂ for Pre-Diabetes and Type 2 Diabetes. *Sci. Rep.* **2015**, *5*, 11959.
23. Yah, W. O.; Takahara, A.; Lvov, Y. M. Selective Modification of Halloysite Lumen with Octadecylphosphonic Acid: New Inorganic Tubular Micelle. *J. Am. Chem. Soc.* **2012**, *134*, 1853-1859.
24. Jana, S.; Das, S.; Ghosh, C.; Maity, A.; Pradhan, M. Halloysite Nanotubes Capturing Isotope Selective Atmospheric CO₂. *Sci. Rep.* **2015**, *5*, 8711.
25. Das, S.; Jana, S. A Facile Approach to Fabricate Halloysite/Metal Nanocomposites with Preformed and In Situ Synthesized Metal Nanoparticles: A Comparative Study of their Enhanced Catalytic Activity. *Dalton Trans.* **2015**, *44*, 8906-8916.
26. Ko, Y. G.; Lee, H. J.; Oh, H. C.; Choi, U. S. Amines Immobilized Double-Walled Silica Nanotubes for CO₂ Capture. *J. Hazard. Mater.* **2013**, *250*, 53-60.
27. Yokoi, T.; Yoshitake, H.; Tatsumi, T. Synthesis of Amino-Functionalized MCM-41 Via Direct Co-Condensation and Post-Synthesis Grafting Methods Using Mono-, Di- and Tri-Amino-Organoalkoxysilanes. *J. Mater. Chem.* **2004**, *14*, 951-957.
28. Abdullayev, E.; Sakakibara, K.; Okamoto, K.; Wei, W.; Ariga, K.; Lvov, Y. Natural Tubule Clay Template Synthesis of Silver Nanorods for Antibacterial Composite Coating. *ACS Appl. Mater. Interfaces* **2011**, *3*, 4040-4046.
29. Yuan, P.; Southon, P. D.; Liu, Z.; Green, M. E. R.; Hook, J. M.; Antill, S. J.; Kepert, C. J. Functionalization of Halloysite Clay Nanotubes by Grafting with γ -Aminopropyltriethoxysilane. *J. Phys. Chem. C* **2008**, *112*, 15742-15751.
30. Zhu, H.; Du, M. L.; Zou, M. L.; Xu, C. S.; Fu, Y. Q. Green Synthesis of Au Nanoparticles Immobilized on Halloysite Nanotubes for surface-Enhanced Raman Scattering Substrates. *Dalton Trans.* **2012**, *41*, 10465-10471.

31. Barker, S. L. L.; Dipple, G. M.; Dong, F.; Baer, D. S. Use of Laser Spectroscopy to Measure the $^{13}\text{C}/^{12}\text{C}$ and $^{18}\text{O}/^{16}\text{O}$ Compositions of Carbonate Minerals. *Anal. Chem.* **2011**, *83*, 2220-2226.
32. Ho, Y. S.; McKay, G. Pseudo-Second Order Model for Sorption Processes. *Process Biochem.* **1999**, *34*, 451-465.
33. Ho, Y. S.; McKay, G. The Sorption of Lead (II) Ions on Peat. *Water Res.* **1999**, *33*, 578-584.
34. Heydari-Gorji, A.; Sayari, A. CO₂ Capture on Polyethylenimine-Impregnated Hydrophobic Mesoporous Silica: Experimental and Kinetic Modeling. *Chem. Eng. J.* **2011**, *173*, 72-79.
35. Harlick, P. J. E.; Sayari, A. Applications of Pore-Expanded Mesoporous Silica. 5. Triamine Grafted Material with Exceptional CO₂ Dynamic and Equilibrium Adsorption Performance. *Ind. Eng. Chem. Res.* **2007**, *46*, 446-458.
36. Didas, S. A.; Kulkarni, A. R.; Sholl, D. S.; Jones, C. W. Role of Amine Structure on Carbon Dioxide Adsorption from Ultradilute Gas Streams such as Ambient Air. *ChemSusChem* **2012**, *5*, 2058-2064.
37. Ko, Y. G.; Shin, S. S.; Choi, U. S. Primary, Secondary, and Tertiary Amines for CO₂ Capture: Designing for Mesoporous CO₂ Adsorbents. *J. Colloid Interface Sci.* **2011**, *361*, 594-602.
38. Hiyoshi, N.; Yogo, K.; Yashima, T. Adsorption Characteristics of Carbon Dioxide on Organically Functionalized SBA-15. *Microporous Mesoporous Mater.* **2005**, *84*, 357-365.
39. Gemery, P. A.; Trolier, M.; White, J. W. C. Oxygen Isotope Exchange between Carbon Dioxide and Water Following Atmospheric Sampling Using Glass Flasks. *J. Geophys. Res.* **1996**, *101*, 14415-14420.
40. Tumuluri, U.; Isenberg, M.; Tan, C.; Chuang, S. S. C. In Situ Infrared Study of the Effect of Amine Density on the Nature of Adsorbed CO₂ on Amine-Functionalized Solid Sorbents. *Langmuir* **2014**, *30*, 7405-7413.
41. Kim, S.; Ida, J.; Gulians, V. V.; Lin, J. Y. S. Tailoring Pore Properties of MCM-48 Silica for Selective Adsorption of CO₂. *J. Phys. Chem. B* **2005**, *109*, 6287-6293.
42. Ide, Y.; Kagawa, N.; Sadakane, M.; Sano, T. Precisely Designed Layered Silicate as an Effective and Highly Selective CO₂ Adsorbent. *Chem. Commun.* **2013**, *49*, 9027-9029.
43. Hicks, J. C.; Drese, J. H.; Fauth, D. J.; Gray, M. L.; Qi, G.; Jones, C. W. Designing Adsorbents for CO₂ Capture from Flue Gas-Hyperbranched Aminosilicas Capable of Capturing CO₂ Reversibly. *J. Am. Chem. Soc.* **2008**, *130*, 2902-2903.
44. Li, Y.; Sun, N.; Li, L.; Zhao, N.; Xiao, F.; Wei, W.; Sun, Y.; Huang, W. Grafting of Amines on Ethanol-Extracted SBA-15 for CO₂ Adsorption. *Materials* **2013**, *6*, 981-999.
45. Moura, K. O.; Pastore, H. O. Comparative Adsorption of CO₂ by Mono-, Di-, and Triamino-Organofunctionalized Magnesium Phyllosilicates. *Environ. Sci. Technol.* **2013**, *47*, 12201-12210.
46. Moura, H. M.; Pastore, H. O. Functionalized Mesoporous Solids Based on Magadiite and [Al]-Magadiite. *Dalton Trans.* **2014**, *43*, 10471-10483.

47. Caplow, M. Kinetics of Carbamate Formation and Breakdown, *J. Am. Chem. Soc.* **1968**, *90*, 6795-6803.
48. Hahn, M. W.; Steib, M.; Jentys, A.; Lercher, J. A. Mechanism and Kinetics of CO₂ Adsorption on Surface Bonded Amines. *J. Phys. Chem. C* **2015**, *119*, 4126-4135.
49. Sayari, A.; Belmabkhout, Y. Stabilization of Amine-Containing CO₂ Adsorbents: Dramatic Effect of Water Vapor. *J. Am. Chem. Soc.* **2010**, *132*, 6312-6314.
50. Wang, X.; Schwartz, V.; Clark, J. C.; Ma, X.; Overbury, S. H.; Xu, X.; Song, C. Infrared Study of CO₂ Sorption over “Molecular Basket” Sorbent Consisting of Polyethylenimine-Modified Mesoporous Molecular Sieve. *J. Phys. Chem. C* **2009**, *113*, 7260-7268.
51. Xu, X.; Song, C.; Miller, B. G.; Scaroni, A. W. Influence of Moisture on CO₂ Separation from Gas Mixture by a Nanoporous Adsorbent Based on Polyethylenimine-Modified Molecular Sieve MCM-41. *Ind. Eng. Chem. Res.* **2005**, *44*, 8113-8119.
52. Drese, J. H.; Choi, S.; Lively, R. P.; Koros, W. J.; Fauth, D. J.; Gray, M. L.; Jones, C. W. Synthesis–Structure–Property Relationships for Hyperbranched Aminosilica CO₂ Adsorbents. *Adv. Funct. Mater.* **2009**, *19*, 3821-3832.
53. Vieira, R. B.; Pastore, H. O. Polyethylenimine-Magadiite Layered Silicate Sorbent for CO₂ Capture. *Environ. Sci. Technol.* **2014**, *48*, 2472-2480.
54. Bacsik, Z.; Ahlsten, N.; Ziadi, A.; Zhao, G.; Garcia-Bennett, A. E.; Martín-Matute, B.; Hedin, N. Mechanisms and Kinetics for Sorption of CO₂ on Bicontinuous Mesoporous Silica Modified with n-Propylamine. *Langmuir* **2011**, *27*, 11118-11128.
55. Danon, A.; Stair, P. C.; Weitz, E. FTIR Study of CO₂ Adsorption on Amine-Grafted SBA-15: Elucidation of Adsorbed Species. *J. Phys. Chem. C* **2011**, *115*, 11540-11549.
56. Wilfong, W. C.; Srikanth, C. S.; Chuang, S. S. C. In Situ ATR and DRIFTS Studies of the Nature of Adsorbed CO₂ on Tetraethylenepentamine Films. *ACS Appl. Mater. Interfaces* **2014**, *6*, 13617-13626.
57. Al-Marri, M. J.; Khader, M. M.; Tawfik, M.; Qi, G.; Giannelis, E. P. CO₂ Sorption Kinetics of Scaled-Up Polyethylenimine-Functionalized Mesoporous Silica Sorbent. *Langmuir* **2015**, *31*, 3569-3576.
58. Knöfel, C.; Martin, C.; Hornebecq, V.; Llewellyn, P. L. Study of Carbon Dioxide Adsorption on Mesoporous Aminopropylsilane-Functionalized Silica and Titania Combining Microcalorimetry and In Situ Infrared Spectroscopy. *J. Phys. Chem. C* **2009**, *113*, 21726-21734.
59. Zhao, A.; Samanta, A.; Sarkar, P.; Gupta, R. Carbon Dioxide Adsorption on Amine-Impregnated Mesoporous SBA-15 Sorbents: Experimental and Kinetics Study. *Ind. Eng. Chem. Res.* **2013**, *52*, 6480-6491.

Synthesis of Mesoporous Silica Nanoflowers for CO₂ Capture

4.1 Introduction

Porous silica with large surface area is a fascinating material in modern nanoscience and nanotechnology owing to its unique property, functionality and potential application in the field of catalysis, adsorption, separation and chemical sensors together with its proficiency to be a hard template for the substructure of other materials.¹⁻⁴ Porous silica in the nano regime is attractive as it possesses high surface area, well-defined pore structure, tunable pore size, unprecedented stability and chemical inertness, together with an ecofriendly inexpensive inorganic framework.⁵⁻⁹ Apart from these advantages, porous silica materials have withdrawn immense research interest as drug delivery system owing to their high permeability and biocompatibility.¹⁰⁻¹² However, synthesis of silica nanomaterials with well-defined morphology, controllable size and readily available large surface area is still a challenging task to the researcher and thus effort should be put forward to develop simple and cost effective routes to succeed in fabrication of porous silica with these aforesaid merits.

The excessive emission of anthropogenic carbon dioxide (CO₂) as a result of the human activity and industrial revolution adversely affects the global temperature and hence contributes to the global climate change, which is considered to be a long lasting environmental issue in the twenty-first century.¹³⁻¹⁶ It is therefore essential to implement the carbon capture and sequestration as an imperious alternative in reducing CO₂ emissions into the environment, which in turn restricts CO₂ from entering into carbon cycle. To address these environmental concerns, early studies demonstrate exploration of several solid adsorbents varying from metal-organic frameworks, porous organic polymer, covalent organic polymers, activated carbon, resins, mesoporous silica, aerogel, metal oxides, alkali hydroxide to zeolites for CO₂ adsorption,¹⁷⁻²⁷ as opposed to the liquid

phase amine scrubbing process owing to its poor thermal stability, high regeneration cost, oxidative degradation of amines, together with equipment corrosion and contamination of the gas with the solvent vapour. Even though several solid adsorbents were employed for CO₂ capture, the adsorption capacity of most of the solid materials was severely affected due to their low moisture tolerance during high temperature adsorption and sometimes because of their thermal and chemical instability,²⁸⁻³⁰ which provoke to the researcher in developing durable and recyclable solid adsorbents with easily attainable adsorption sites per mass of the materials that assist to their excellent CO₂ capture efficacy.

Herein, our objective is to significantly increase the surface area of the silica materials with large scale production keeping the size and morphology intact. In the present work, we demonstrate a simple and new route to synthesize high surface area porous silica materials with flower-like morphology through a light-assisted hydrolysis of a silica precursor. We have ascribed the phenomenological elucidation of growth of the flowery silica materials on the basis of transmission electron microscopy. We have then fabricated porous adsorbents via grafting of several viable amines having varied amino group densities and adsorption sites over the silica nanoflowers for CO₂ adsorption under standard temperature and pressure. The efficiency together with stability of these silica nanoflowers has been examined over multiple adsorption-desorption cycles to describe their recyclability from the practical rather economical viewpoint.

4.2 Experimental Section

4.2.1 Synthesis of Silica Nanomaterials

Silica nanomaterials were synthesized via hydrolysis-polycondensation of tetraethyl orthosilicate using a light assisted method. In this typical procedure, cetyltrimethyl ammonium bromide (CTAB, 0.7 mmol) and urea (2.5 mmol) were taken together and dissolved in 5 mL of water. Tetraethyl orthosilicate (TEOS, 0.5 mL) was added in the mixture of methyl phenyl ether (5.0 mL) and hexanol (0.25 mL). All the solutions were

then transferred to a vial fitted with cap and stirred vigorously to mix them properly. After that the vial was placed under visible light for 12 h under stirring condition and the reaction temperature was monitored as 90 °C. Once the solution was cooled down to room temperature, the product was obtained by simple filtration and washed several times with millipore water. The obtained product was air-dried, followed by calcination at 575 °C for 5 h in air.

4.2.2 Functionalization of Silica Nanoflowers

Functionalization of silica nanoflowers was carried out under nitrogen atmosphere using standard air free technique.³¹ Silica nanoflowers (2.0 g) were added into a 50 mL three-necked round bottom flask containing 20.0 mL of toluene. The flask was fixed with rubber septum, condenser and thermocouple adaptor. The reaction mixture was then deaerated under stirring condition for 30 min, subsequently heated with a heating mantle. Aminosilane (10.6 mmol) was injected into the flask at 60 °C and the reaction mixture was refluxed for 20 h at 110 °C. As soon as the temperature of the solution cooled down to room temperature, the product was collected through simple filtration and washed several times with toluene and ethanol respectively. The product was then dried at 100 °C overnight under vacuum. Three different aminosilanes were chosen for functionalization of silica nanoflowers. The products were abbreviated as SNF-1, SNF-2 and SNF-3 for (3-aminopropyl)triethoxysilane, N-[3-(trimethoxysilyl) propyl]ethylenediamine and N1-(3-trimethoxysilylpropyl)diethylenetriamine grafted silica nanoflowers respectively. All the amine functionalized silica nanoflowers were used as adsorbent to study their CO₂ adsorption efficacy.

4.2.3 CO₂ Adsorption Study

CO₂ adsorption capacity of amine loaded silica nanoflowers was performed using a volumetric method. For this study, 0.1 g of adsorbent was taken in a sample holder.

Before the adsorption experiment, the adsorbent was outgassed in vacuum at 383 K for 2 h to complete the desorption of pre-adsorbed CO₂ if any. The adsorption experiment was then carried out using pure CO₂ between 0 to 1 atmospheric pressure at 295 K. Their multi-cycle adsorption-desorption study was performed after regeneration of the adsorbents by heating at 383 K under the flow of nitrogen.

4.3 Results and Discussion

4.3.1 Characterization of Silica Nanoflowers

Large surface area porous silica nanomaterials were synthesized based on a facile strategy involving light-assisted hydrolysis of a tetraethyl orthosilicate (TEOS) at low temperature in presence of urea as hydrolyzing agent, cetyltrimethylammonium bromide (CTAB) as the structure-directing agent, methyl phenyl ether as solvent and hexanol as co-solvent.

4.3.1.1 FESEM and TEM Analyses

To gain insight into their morphology and size, field emission scanning electron microscopy (FESEM) and transmission electron microscopy (TEM) analyses were carried out at different magnifications. Figure 4.1A-C represents FESEM images of silica nanomaterials having diameter of 385 ± 5 nm with uniform hierarchical flower-like morphology. All the nanoflowers are made up of assemblies of thin intersected petals. TEM images attribute to the monodispersity rather narrow size distribution of the synthesized silica nanoflowers (SiO₂ NFs) organized uniformly in all directions, as shown in Figure 4.1D-F. However, TEM image of the edge of the NFs clearly demonstrates that they composed of elongated spikes oriented outwards in three dimensions.

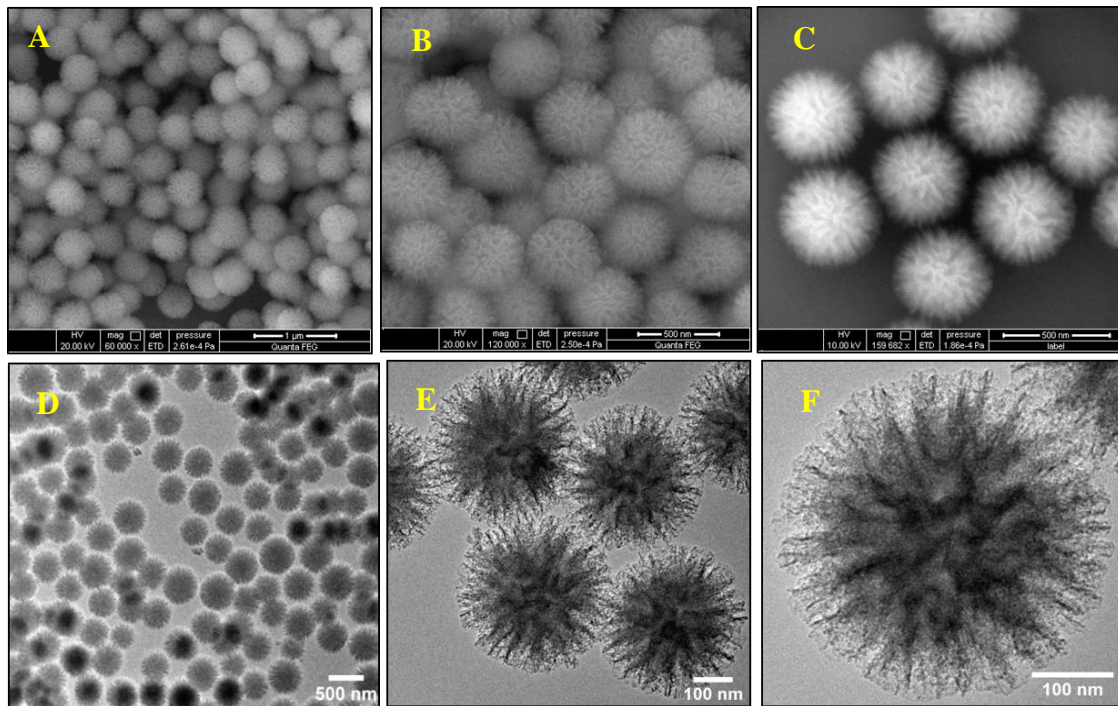


Figure 4.1: FESEM micrographs (A-C) of silica nanomaterials at different magnifications, representing their hierarchical flower-like morphology. TEM images (D-F) of SiO₂ NFs, demonstrating that these nanoflowers are composed of elongated spikes that assembled in a divergent way, leading to the formation of dandelion-like nanoflowers.

4.3.1.2 STEM-EDS Analysis

To directly envisage the chemical composition and distribution of the constituents, scanning transmission electron microscopy-energy dispersive spectroscopy (STEM-EDS) elemental mapping was carried out on a single nanoflower. STEM images of flower-like SiO₂ NFs are illustrated in Figure 4.2. The elemental maps represent homogeneous distribution of all the basic elements Si and O throughout the body and petals of the nanoflower. Hence, the nanopetals assembled in a divergent way and developed radially from the core, leading to the formation of nanoflowers with dandelion-like morphology that allowing us in obtaining accessible large specific surface area together with easy fine tuning of their chemico-physical properties.

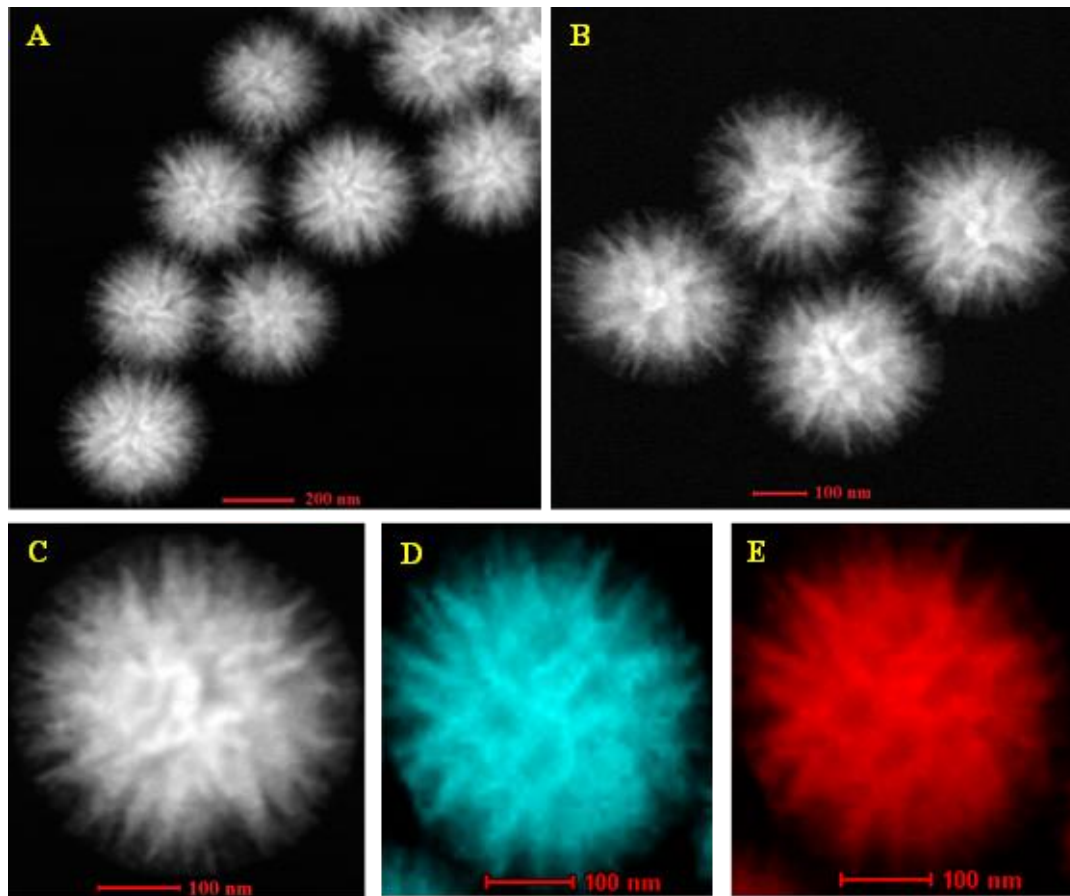
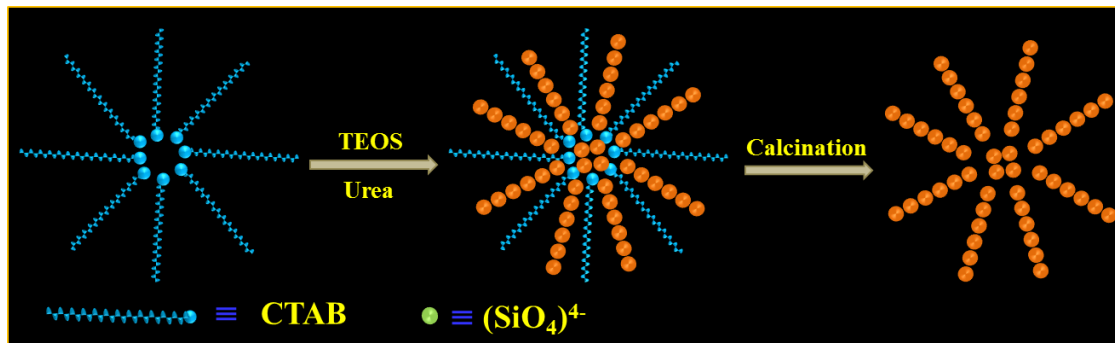


Figure 4.2: STEM images (A, B) of a bunch of SiO₂ NFs, oriented radially from the core. (C) STEM image of a single SiO₂ nanoflower and its elemental mapping of (D) Si (blue zone) and (E) O (red zone) respectively.

4.3.1.3 Growth Mechanism of the SiO₂ Nanoflowers

In addition to the morphological characterization, growth mechanism of the SiO₂ NFs as well as their structural and thermal stability has also been elucidated in detailed. Scheme 4.1 illustrates the possible growth and formation mechanism of nanoflowers. Here, CTAB molecules organized to form micelles that play a pivotal role by providing proper template arising out of the micellar aggregates, which in turn regulate the shape and size of the nanoparticles (NPs). Under irradiation of visible light (90 °C), urea decomposes in water to form NH₄OH and the produced hydroxyl ions hydrolyze the tetraethyl orthosilicate

(TEOS). The silicate molecules then self-assembled and upon condensation results in the nucleation, followed by formation of SiO₂ NFs with divergent structure. The structure-directing agent, CTAB, was completely removed by calcination of SiO₂ NFs at 575 °C under atmospheric condition.



Scheme 4.1: The probable formation mechanism of SiO₂ NFs in presence of a structure-directing agent under irradiation of visible light.

4.3.1.4 NMR Analysis

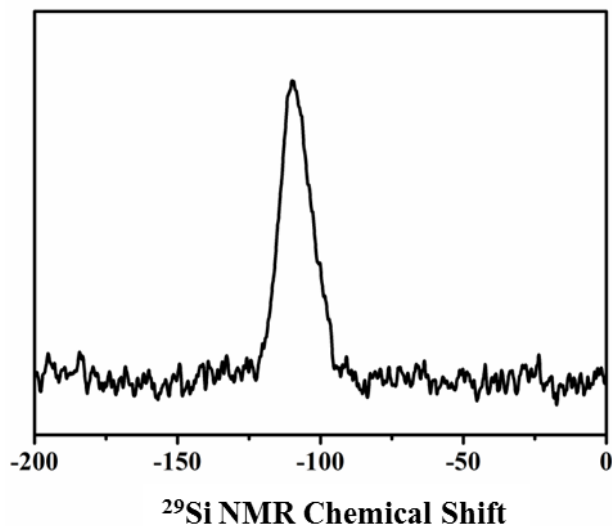


Figure 4.3: ²⁹Si CPMAS NMR spectrum of silica nanoflowers.

Formation of silica nanomaterials was substantiated by solid state ^{29}Si cross-polarization magic-angle spinning (CPMAS) NMR spectroscopy. ^{29}Si CP-MAS NMR spectrum depicted in the Figure 4.3 indicates a resonance peak at -110.44 ppm, attributing to the Q^4 sites of SiO_4 structure. ^{13}C CPMAS NMR spectrum further confirms the absence of any Si-C bonds formation in the silica materials during calcination at 575 °C.

4.3.1.5 FTIR Analysis

Fourier transform infrared (FTIR) spectroscopy analysis shown in the Figure 4.4 represents two characteristic peaks at 1098 and 799 cm^{-1} which are ascribed to the asymmetric and symmetric stretching vibration of Si-O-Si respectively.

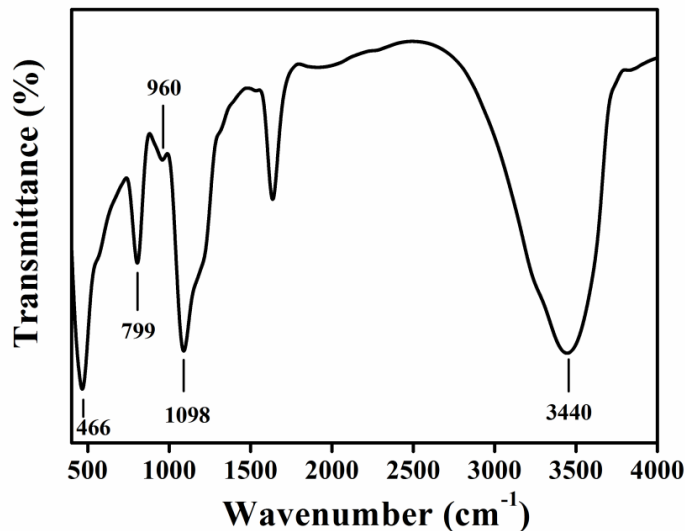


Figure 4.4: Fourier transform infrared (FTIR) spectrum of silica nanoflowers.

4.3.1.6 Surface Area Measurement

In order to demonstrate the specific surfaces of SiO_2 NFs, nitrogen adsorption-desorption study was performed at 77 K, shown in Figure 4.5. The isotherms of SiO_2 NFs demonstrate characteristic type-IV according to the IUPAC classification, indicating the

signature of mesoporous material.³² The specific surface area of the SiO₂ NFs estimated by Brunauer-Emmett-Teller (BET) method was found to be 705 m² g⁻¹ with pore volume of 0.996 cm³ g⁻¹ and an average pore size of 3.44 nm, signifying the formation of mesoporous silica materials having large specific surface area.

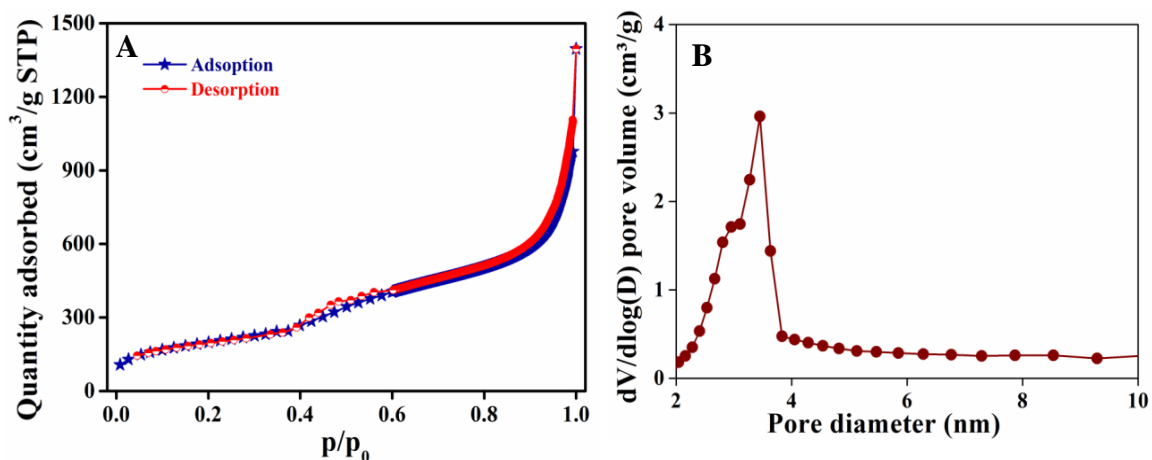


Figure 4.5: (A) Nitrogen adsorption-desorption isotherms performed at 77 K and (B) pore size distribution of SiO₂ NFs, indicating the signature of mesoporous material.

4.3.1.7 XRD Analysis

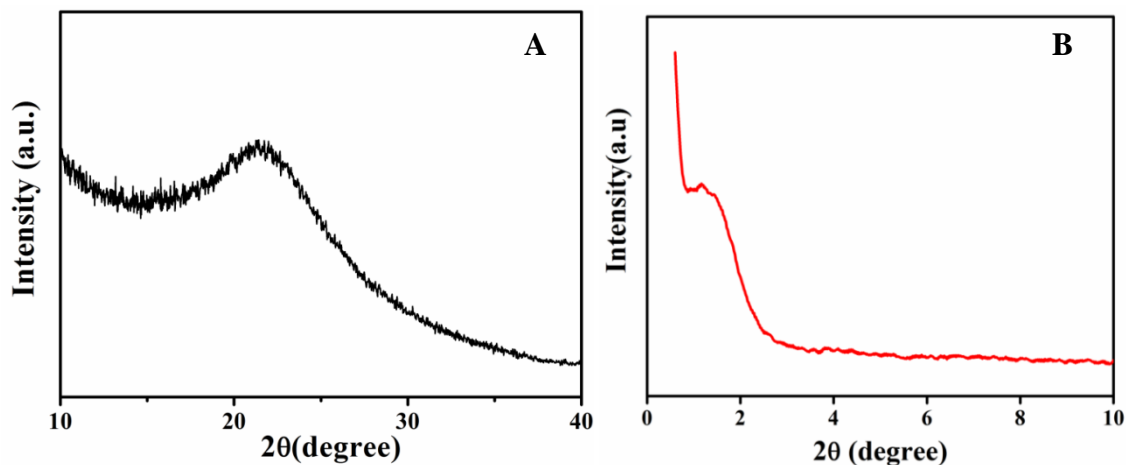


Figure 4.6: (A) X-ray diffraction (XRD) pattern of silica nanoflowers, representing their amorphous nature. (B) Low angle XRD pattern of SiO₂ NFs, confirming the formation of partially ordered mesoporous structures of the NFs.

The presence of a broad peak at 22° in the powder X-ray diffraction (XRD) pattern (Figure 4.6A) accredited to their amorphous nature. Low angle XRD pattern (Figure 4.6B) further authenticates the formation of partially ordered mesoporous structures of the NFs, owing to the presence of a distinctive peak at 1.26° .³³

4.3.1.8 TGA Study

Thermogravimetric analysis (TGA) was carried out under nitrogen atmosphere from 30 to 1000 °C to demonstrate the stability of the silica NFs (Figure 4.7). The weight loss of 2.9% between 40-150 °C corresponds to the desorption of physisorbed water and hydroxyl groups from the surface of the NFs, after which no weight loss was observed. It is also interesting to note that there is no change in morphology and size of the NFs or agglomerated after heating at high temperature and even upon mechanical compression. All these findings clearly substantiate to their good thermal and mechanical stability, which may instigate to the researchers to explore them for diverse applications.

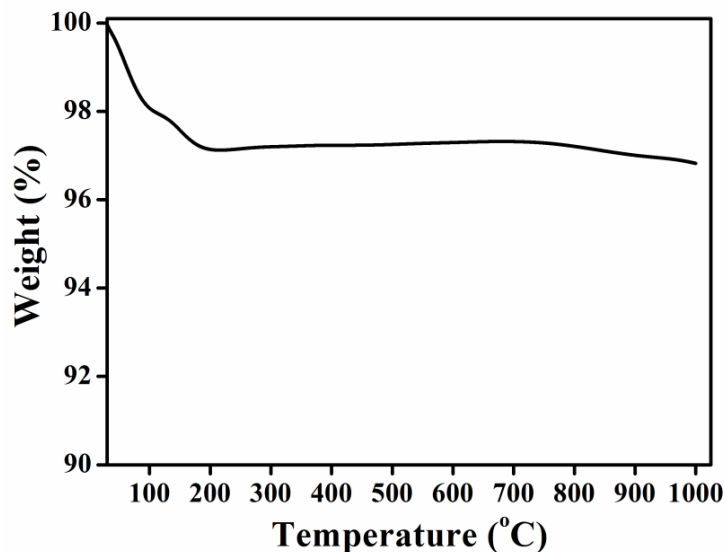
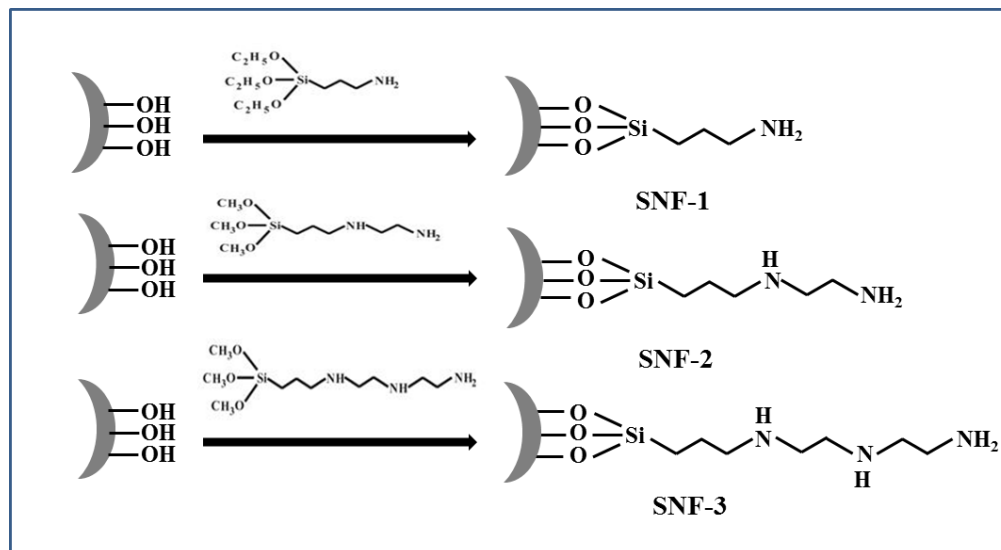


Figure 4.7: Thermogravimetric analysis (TGA) data of silica nanoflowers carried out under nitrogen atmosphere from room temperature to 1000 °C.

4.3.2 Characterization of Amine-Loaded SiO₂ Nanoflowers

Scheme 4.2: Schematic presentation of the functionalization of SiO₂ NFs through the immobilization of aminosilanes based on the grafting reaction.

SiO₂ NFs with dandelion-like morphology, synthesized in methyl phenyl ether as solvent and hexanol as co-solvent, facilitate us in attaining the high specific surface area and easy tuning of their chemico-physical properties through the modification of the accessible large surface silanol group densities. To explore SiO₂ NFs as an adsorbent for CO₂ capture, they have been functionalized using (3-aminopropyl)triethoxysilane (SNF-1), N-[3-(trimethoxysilyl)propyl]ethylenediamine (SNF-2) and N1-(3-trimethoxysilylpropyl)diethylenetriamine (SNF-3) respectively through grafting reaction, The schematic presentation of the functionalization of SiO₂ NFs using is presented in Scheme 4.2.

4.3.2.1 Solid State NMR Analysis

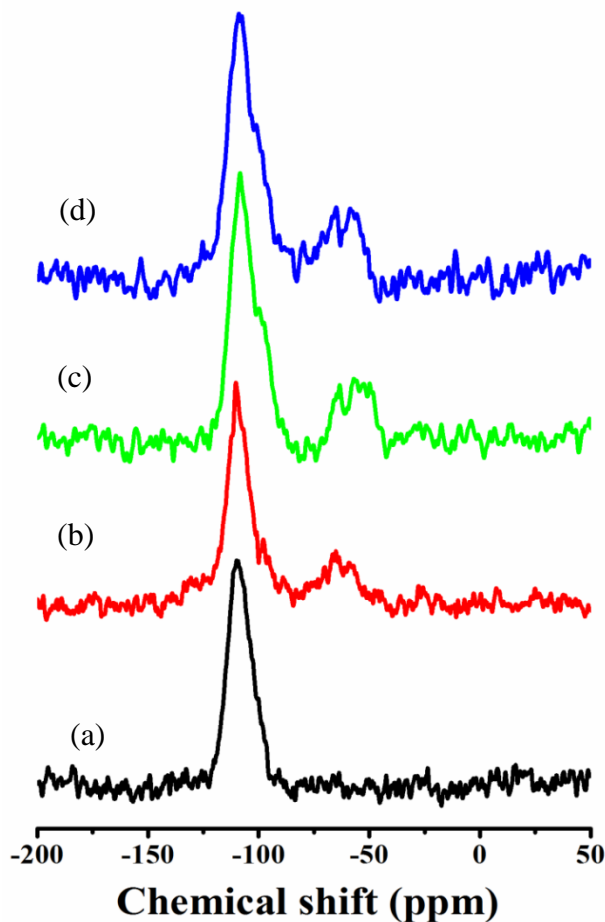


Figure 4.8: ^{29}Si CPMAS NMR spectra of (a) pristine SiO_2 NFs and amine loaded SiO_2 NFs, (b) SNF-1, (c) SNF-2 and (d) SNF-3 respectively.

The solid state ^{29}Si CPMAS NMR spectroscopy ascribed to the successful grafting of aminosilanes through covalent attachment over the surface of nanoflowers, owing to the presence of two new resonance peaks at -65.88 and -58.74 ppm due to T³ {(C–Si(OSi)₃} and T² {(C–Si(OSi)₂OH)} sites (Figure 4.8) in addition to the signal for Q⁴ sites of SiO_4 structure of the constituent silica.^{34,35} ^{13}C CPMAS NMR spectra (Figure 4.9) recorded for amine loaded SiO_2 NFs also substantiate the functionalization of SiO_2 NFs using different aminosilanes via grafting.

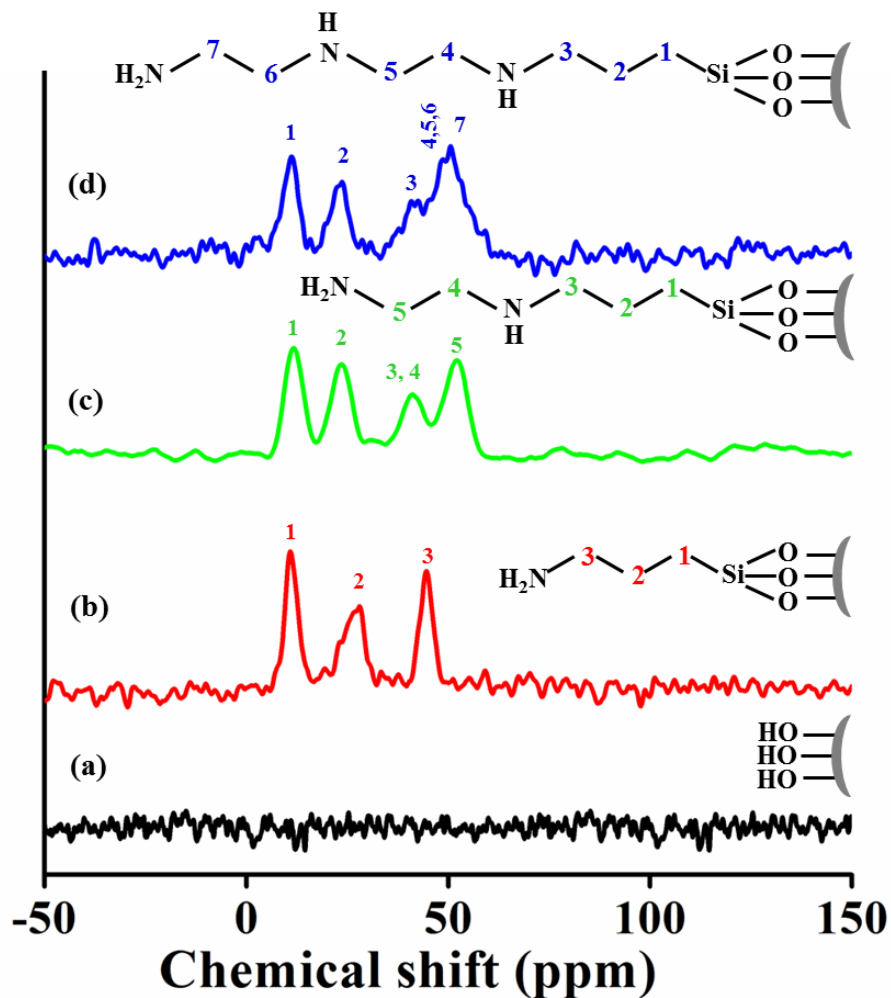


Figure 4.9: ^{13}C CPMAS NMR spectra of (a) pristine SiO_2 NFs and amine loaded SiO_2 NFs, (b) SNF-1, (c) SNF-2 and (d) SNF-3 respectively. The possible structures after functionalization of the SiO_2 NFs with aminosilanes were also presented for each material.

4.3.2.2 FTIR Analysis

FTIR spectra (Figure 4.10) further authenticate the immobilization of amine molecules over nanoflowers surfaces, since two new peaks were observed at 1561 and 2935 cm^{-1} for N-H deformation and stretching vibration of C-H respectively.^{36,37} Despite their

chemical change due to grafting of aminosilane, there is no change in the morphology or size of the NFs.

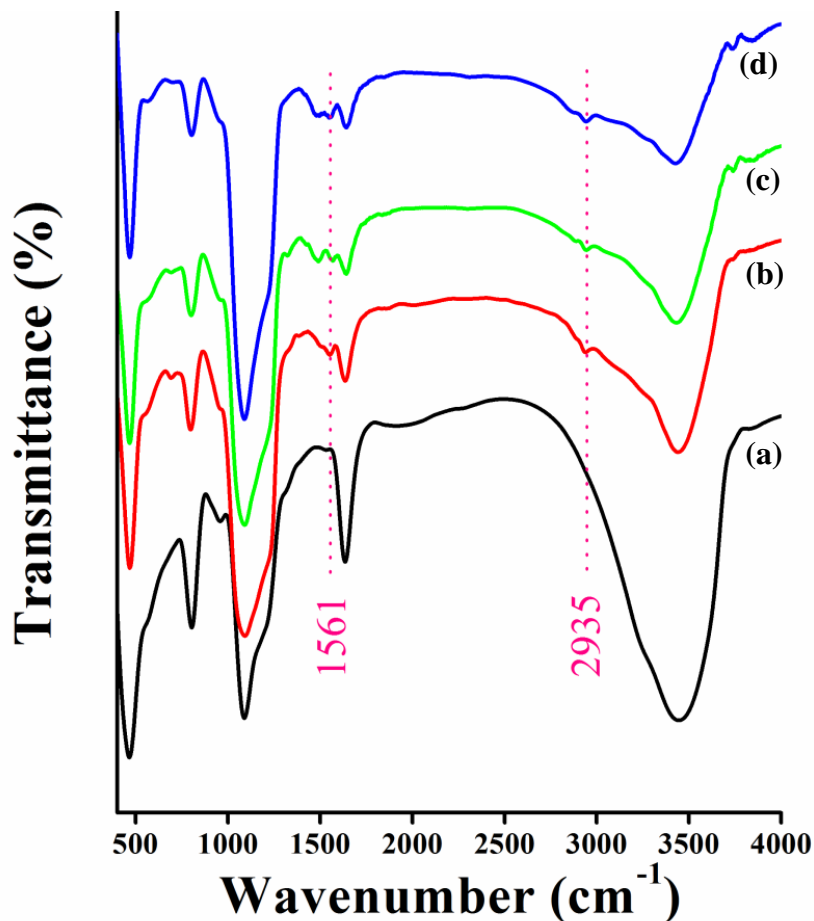


Figure 4.10: (a) FTIR spectrum of pristine SiO₂ NFs. (b-d) FTIR spectra of SNF-1, SNF-2 and SNF-3 respectively, substantiating the immobilization of amine molecules over the surface of SiO₂ NFs through grafting.

4.3.2.3 CHN Elemental Analysis

We have then performed CHN elemental analysis to estimate the actual concentration of immobilized amino groups after functionalization of the nanoflowers. The loaded nitrogen was estimated to be 1.66, 2.78 and 3.51 mmol g⁻¹ in SNF-1, SNF-2 and SNF-3 respectively under the aforesaid experimental condition. The change in the concentration

of nitrogen occurs as the functionalization was carried out using three different aminosilanes with varied amino group densities.

4.3.3 CO₂ Adsorption by Amine-Loaded SiO₂ Nanoflowers

4.3.3.1 CO₂ Adsorption Study

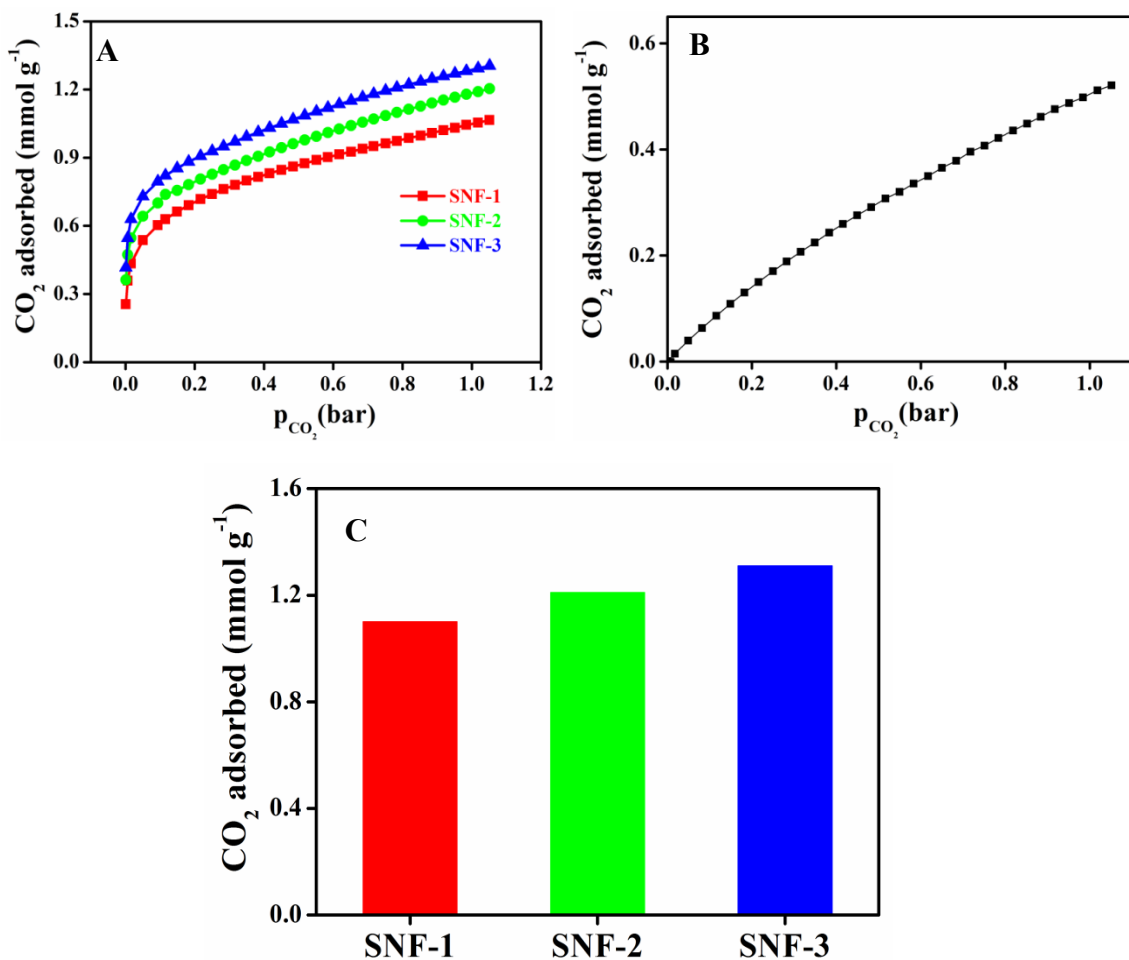


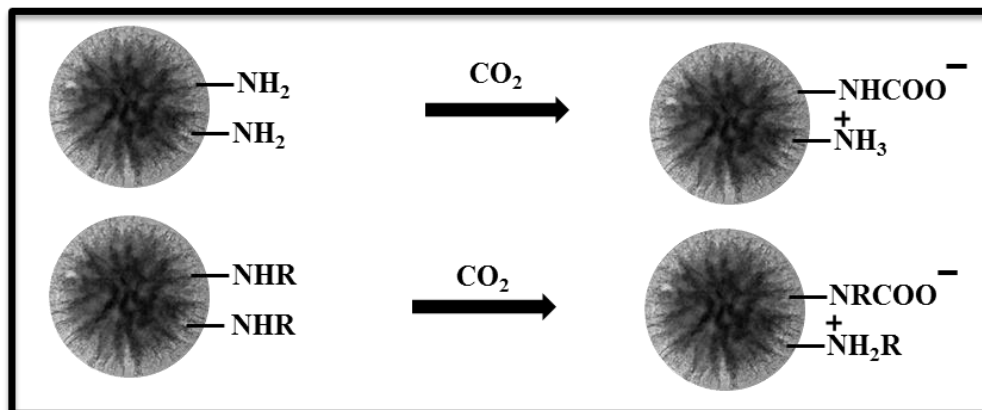
Figure 4.11: (A) CO₂ adsorption behavior of SNF-1, SNF-2 and SNF-3 at 295 K respectively. (B) CO₂ adsorption behavior of pristine SiO₂ NFs as a function of pressure and (C) working capacity of SNF-1, SNF-2 and SNF-3 at 295 K respectively.

Keeping the adverse effect of CO₂ emissions in mind, amine grafted NFs were explored as solid adsorbent for CO₂ adsorption. To demonstrate their CO₂ uptake capacity, the adsorption study was carried out based on the volumetric method using pure CO₂ between 0 to 1 atmospheric pressure at 295 K. CO₂ adsorption behavior of SNF-1, SNF-2 and SNF-3 were compared at 295 K and plotted in Figure 4.11. The adsorption isotherms over the surface of these adsorbents (Figure 4.11A) are distinctive of chemisorption, attributing to the precise nature of interaction between CO₂ molecules and amino groups loaded onto the adsorbents, whereas CO₂ uptake in pristine SiO₂ NFs is an indicative of physisorption as they demonstrate a linear correlation during CO₂ adsorption capacity as a function of pressure (Figure 4.11B). As shown in Figure 4.11C, SNF-3 (1.32 mmol g⁻¹) showed higher CO₂ adsorption than SNF-2 (1.21 mmol g⁻¹) and SNF-1 (1.12 mmol g⁻¹), as they comprised of three different grafted aminosilanes with varied amino group densities, whereas pristine SiO₂ NFs possess a working capacity of 0.51 mmol g⁻¹.

4.3.3.2 CO₂ Adsorption Mechanism

As stated by the early studies, amine efficiency described as the ratio of the moles of CO₂ adsorbed to the moles of amine present in an adsorbent, increases with increasing amine loading onto the adsorbents, which results in stronger CO₂ binding for a high density of amine loading.^{38,39} In the present study, contrary to their amine content, primary amine containing SNF-1 has higher amine efficiency compared to SNF-2 or SNF-3 encompassing both primary and secondary amine sites. The lower amine efficiency of SNF-2 and SNF-3 could be ascribed to the little interaction of the secondary amine groups with CO₂ molecules during adsorption, further signifying that high surface density of covalently attached amine molecules is not only the determining parameter to estimate CO₂ working capacity of an adsorbent, it also significantly rely on the nature of the immobilized amine. CO₂ working capability of the amine functionalized NFs predominantly proceeds via carbamate mechanism,^{40,41} through the formation of zwitterions due to the nucleophilic attack of the lone pair of nitrogen of amines on CO₂ molecules, as illustrated in Scheme 4.3. These zwitterions finally transformed to

alkylammonium carbamate species via deprotonation in presence of another amine under anhydrous condition.



Scheme 4.3: Schematic presentation of CO₂ adsorption mechanism over the surface of amine functionalized SiO₂ NFs having both primary and secondary amine sites.

4.3.3.3 Recyclability Study of these Adsorbents

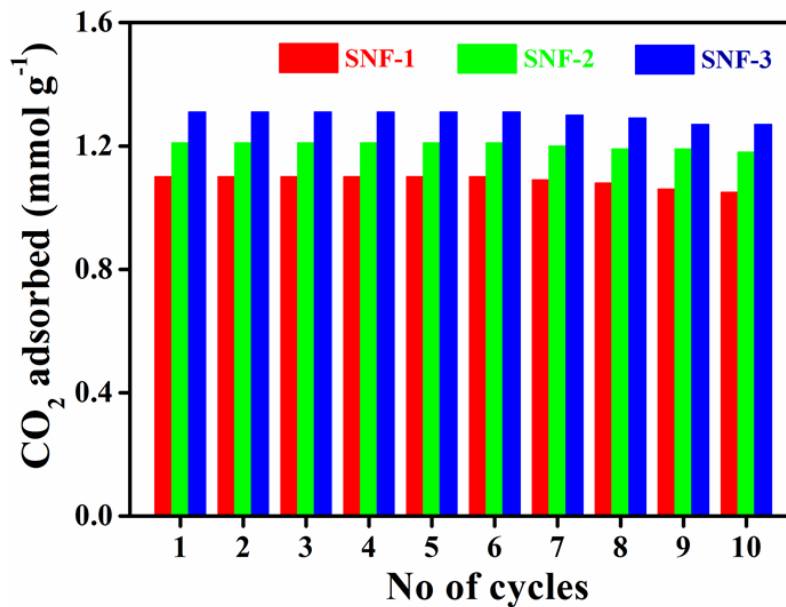


Figure 4.12: Multi-cycle usage of SNF-1, SNF-2 and SNF-3 demonstrates their stability and sustainability.

Towards the end, recyclability of these adsorbents was examined by their multi-cycle usage to demonstrate their stability and sustainability. Figure 4.12 represents multi-cycle CO₂ working capability of these amine grafted SiO₂ NFs based adsorbents. Interestingly, no change in their capture capacity was noticed even after repetitive use.

4.3.3.4. Comparison of Amine Efficiency

CO₂ uptake efficiency of these adsorbents was verified with the reported amine-based adsorbents and presented in Table 4.1. The results indicate to the higher CO₂ uptake efficacy of the amine immobilized SiO₂ NFs.

Table 4.1: CO₂ uptake efficiency of these adsorbents was demonstrated in associated with the reported amine-based adsorbents.

Adsorbents	Nitrogen Content (mmol g ⁻¹)	CO ₂ Capture Capacity (mmol g ⁻¹)	Amine efficiency (mmol _{CO₂} mmol _N ⁻¹)	References
SBA-NH ₂	1.90	0.40	0.21	38
SBA-Diamine	2.50	0.07	0.28	38
APTES ₃₉ /MCM	1.79	0.46	0.26	42
A2-SBA-15	4.20	1.42	0.34	43
A2-BPMO	4.90	2.15	0.44	43
APS-MCM-48	2.45	0.78	0.32	44
APS/SBA	1.11	0.15	0.14	45
AEAPS/SBA	2.26	0.27	0.12	45
TA/SBA	2.75	0.35	0.13	45
TRI-SBA-15-10.2-48S	3.2	0.80	0.25	23
M-HNTs	0.36	0.13	0.36	36

KCC-1-N700	4.86	1.84	0.38	46
KCC-1-PA	2.59	0.46	0.18	34
KCC-1-PEDA	4.55	0.73	0.16	34
KCC-1-PDETA	4.79	0.52	0.11	34
EB-PEI/SiO ₂	9.9	2.67	0.27	47
PEI/SiO ₂	6.8	2.78	0.41	11
SNF-1	1.66	1.10	0.66	Present Work
SNF-2	2.78	1.20	0.43	Present Work
SNF-3	3.51	1.33	0.38	Present Work

4.4 Conclusions

In summary, we have demonstrated the synthesis of monodispersed mesoporous silica nanoflowers with large surface area through a novel, low temperature and cost effective light-assisted hydrolysis route. The developed synthetic route provides uniform silica nanoparticles with precise control over their morphology and size along with good thermal and mechanical stability and may be generalized for the synthesis of other nanoparticles. Tuning the surface chemistry of silica nanoflowers using several amines having varied amine densities and adsorption sites, they have been exploited as solid adsorbent to study their CO₂ working capacity and their long term durability and sustainability have also been accredited by their multi-cycle adsorption-desorption. Up until now, the unique flowery nanostructure with uniform size produced through a light-assisted hydrolysis route has never been reported. This simplistic strategy may provide a new environmental friendly and cost-effective way for up-scaling of dandelion-like silica nanoflowers, which may find potential applications in selective adsorption of contaminants, targeted drug delivery, biosensing, as a support for catalysts and hard templates for the substructure of other materials to form nanocomposites due to their exceptional stability and durability as well as presence of active sites with accessible large surface area.

4.5 References

1. Wan, Y.; Zhao, D. Y. On the Controllable Soft-Templating Approach to Mesoporous Silicates. *Chem. Rev.* **2007**, *107*, 2821-2860.
2. Lebeau, B.; Galarneau, A.; Linden, M. Introduction for 20 Years of Research on Ordered Mesoporous Materials. *Chem. Soc. Rev.* **2013**, *42*, 3661-3662.
3. Sharma, K. K.; Asefa, T. Efficient Bifunctional Nanocatalysts by Simple Postgrafting of Spatially Isolated Catalytic Groups on Mesoporous Materials. *Angew. Chem. Int. Ed.* **2007**, *46*, 2879-2882.
4. Kresge, C. T.; Roth, W. J. The Discovery of Mesoporous Molecular Sieves from the Twenty Year Perspective. *Chem. Soc. Rev.* **2013**, *42*, 3663-3670.
5. Liu, N.; Dunphy, D. R.; Atanassov, P.; Bunge, S. D.; Chen, Z.; Lo'pez, G. P.; Boyle, T. J.; Brinker, C. J. Photoregulation of Mass Transport through a Photoresponsive Azobenzene-Modified Nanoporous Membrane. *Nano Lett.* **2004**, *4*, 551-554.
6. Kim, H. J.; Lee, S. J.; Park, S. Y.; Jung, J. H.; Kim, J. S. Detection of Cu^{II} by a Chemodosimeter-Functionalized Monolayer on Mesoporous Silica. *Adv. Mater.* **2008**, *20*, 3229-3234.
7. Wu, Z.; Zhao, D. Ordered Mesoporous Materials as Adsorbents. *Chem. Commun.* **2011**, *47*, 3332-3338.
8. Torney, F.; Trewyn, B. G.; Lin, V. S. Y.; Wang, K. Mesoporous Silica Nanoparticles Deliver DNA and Chemicals into Plants. *Nat. Nanotechnol.* **2007**, *2*, 295-300.
9. Zhao, D.; Huo, Q.; Feng, J.; Chmelka, B. F.; Stucky, G. D. Nonionic Triblock and Star Diblock Copolymer and Oligomeric Surfactant Syntheses of Highly Ordered, Hydrothermally Stable, Mesoporous Silica Structures. *J. Am. Chem. Soc.* **1998**, *120*, 6024-6036.
10. Lee, J. E.; Lee, N.; Kim, H.; Kim, J.; Choi, S. H.; Kim, J. H.; Kim, T.; Song, I. C.; Park, S. P.; Moon, W. K.; Hyeon, T. Uniform Mesoporous Dye-Doped Silica Nanoparticles Decorated with Multiple Magnetite Nanocrystals for Simultaneous Enhanced Magnetic Resonance Imaging, Fluorescence Imaging, and Drug Delivery. *J. Am. Chem. Soc.* **2010**, *132*, 552-557.
11. Mal, N. K.; Fujiwara, M.; Tanaka, Y. Photocontrolled Reversible Release of Guest Molecules from Coumarin-Modified Mesoporous Silica. *Nature* **2003**, *421*, 350-353.
12. Shi, M.; Ho, K.; Keating, A.; Shoichet, M. S. Doxorubicin-Conjugated Immuno-Nanoparticles for Intracellular Anticancer Drug Delivery. *Adv. Funct. Mater.* **2009**, *19*, 1689-1696.
13. Busch, A.; Alles, S.; Gensterblum, Y.; Prinz, D.; Dewhurst, D. N.; Raven, M. D.; Stanjek, H.; Krooss, B. M. Carbon Dioxide Storage Potential of Shales. *Int. J. Greenhouse Gas Control* **2008**, *2*, 297-308.
14. Rogelj, J.; Hare, W.; Lowe, J.; Van Vuuren, D. P.; Riahi, K.; Matthews, B.; Hanaoka, T.; Jiang, K.; Meinshausen, M. Emission Pathways Consistent with a 2 °C Global Temperature Limit. *Nat. Clim. Change* **2011**, *1*, 413-418.
15. Stern, N. *Stern Review on the Economics of Climate Change*. Cambridge University Press, Cambridge, **2006**.

16. D'Alessandro, D. M.; Smit, B.; Long, J. R. Carbon Dioxide Capture: Prospects for New Materials. *Angew. Chem. Int. Ed.* **2010**, *49*, 6058-6082.
17. McDonald, T. M.; Lee, W. R.; Mason, J. A.; Wiers, B. M.; Hong, C. S.; Long, J. R. Capture of Carbon Dioxide from Air and Flue Gas in the Alkylamine-Appended Metal-Organic Framework mmen-Mg₂(dobpdc). *J. Am. Chem. Soc.* **2012**, *134*, 7056-7065.
18. Das, S.; Heasman, P.; Ben, T.; Qiu, S. Porous Organic Materials: Strategic Design and Structure-Function Correlation. *Chem. Rev.* **2017**, *117*, 1515-1563.
19. Cote, A. P.; Benin, A. I.; Ockwig, N. W.; O'Keeffe, M.; Matzger, A. J.; Yaghi, O. M. Porous, Crystalline, Covalent Organic Frameworks. *Science* **2005**, *310*, 1166-1170.
20. Xiang, Z.; Zhou, X.; Zhou, C.; Zhong, S.; He, X.; Qin, C.; Cao, D. Covalent-Organic Polymers for Carbon Dioxide Capture. *J. Mater. Chem.* **2012**, *22*, 22663-22669.
21. Plaza, M. G.; García, S.; Rubiera, F.; Pis, J. J.; Pevida, C. Post-Combustion CO₂ Capture with a Commercial Activated Carbon: Comparison of Different Regeneration Strategies. *Chem. Eng. J.* **2010**, *163*, 41-47.
22. Chen, Z.; Deng, S.; Wei, H.; Wang, B.; Huang, J.; Yu, G. Polyethylenimine-Impregnated Resin for High CO₂ Adsorption: An Efficient Adsorbent for CO₂ Capture from Simulated Flue Gas and Ambient Air. *ACS Appl. Mater. Interfaces* **2013**, *5*, 6937-6945.
23. Jahandar Lashaki, M.; Ziaei-Azad, H.; Sayari, A. New Insights into the Hydrothermal Stability of Triamine-Functionalized SBA-15 Silica for CO₂ Adsorption, *ChemSusChem* **2017**, *10*, 4037-4045.
24. Kong, Y.; Shen, X.; Cui, S.; Fan, M. Development of Monolithic Adsorbent via Polymeric Sol-Gel Process for Low-Concentration CO₂ Capture. *Appl. Energy* **2015**, *147*, 308-317.
25. Harada, T.; Simeon, F.; Hamad, E. Z.; Hatton, T. A. Alkali Metal Nitrate-Promoted High-Capacity MgO Adsorbents for Regenerable CO₂ Capture at Moderate Temperatures. *Chem. Mater.* **2015**, *27*, 1943-1949.
26. Stolaroff, J. K.; Keith, D. W.; Lowry, G. V. Carbon Dioxide Capture from Atmospheric Air Using Sodium Hydroxide Spray. *Environ. Sci. Technol.* **2008**, *42*, 2728-2735.
27. Wang, B.; Côté, A. P.; Furukawa, H.; O'Keeffe, M.; Yaghi, O. M.; Colossal Cages in Zeolitic Imidazolate Frameworks as Selective Carbon Dioxide Reservoirs. *Nature* **2008**, *453*, 207-211.
28. Kumar, A.; Madden, D. G.; Lusi, M.; Chen, K. J.; Daniels, E. A.; Curtin, T.; Perry, J. J.; Zaworotko, M. J. Direct Air Capture of CO₂ by Physisorbent Materials, *Angew. Chem. Int. Ed.* **2015**, *54*, 14372-14377.
29. Sayari, A.; Belmabkhout, Y. Stabilization of Amine-Containing CO₂ Adsorbents: Dramatic Effect of Water Vapor, *J. Am. Chem. Soc.* **2010**, *132*, 6312-6314.
30. Wang, Q.; Luo, J.; Zhong, Z.; Borgna, A. CO₂ Capture by Solid Adsorbents and Their Applications: Current Status and New Trends. *Energy Environ. Sci.* **2011**, *4*, 42-55.
31. Jana, S.; Chang, J. W.; Rioux, R. M.. Synthesis and Modeling of Hollow Intermetallic Ni-Zn Nanoparticles Formed by the Kirkendall Effect. *Nano Lett.* **2013**, *13*, 3618-3625.

32. Wang, C.; Zhou, Y.; Ge, M. Y.; Xu, X. B.; Zhang, Z. L.; Jiang, J. Z. Large-Scale Synthesis of SnO₂ Nanosheets with High Lithium Storage Capacity. *J. Am. Chem. Soc.* **2010**, *132*, 46-47.
33. Zhang, H.; Li, Z.; Xu, P.; Wu, R.; Jiao, Z. A Facile Two Step Synthesis of Novel Chrysanthemum-Like Mesoporous Silica Nanoparticles for Controlled Pyrene Release. *Chem. Commun.* **2010**, *46*, 6783-6785.
34. Singh, B.; Polshettiwar, V. Design of CO₂ Sorbents Using Functionalized Fibrous Nanosilica (KCC-1): Insights into the Effect of the Silica Morphology (KCC-1 vs. MCM-41). *J. Mater. Chem. A* **2016**, *4*, 7005-7019.
35. Dos Santos, T. C.; Bourrelly, S.; Llewellyn, P. L.; Carneiro, J. W. D. M.; Ronconi, C. M. Adsorption of CO₂ on Amine-Functionalised MCM-41: Experimental And Theoretical Studies. *Phys. Chem. Chem. Phys.* **2015**, *17*, 11095-11102.
36. Das, S.; Ghosh, C.; Jana, S. Moisture Induced Isotopic Carbon Dioxide Trapping from Ambient Air. *J. Mater. Chem. A* **2016**, *4*, 7632-7640.
37. Yokoi, T.; Yoshitake, H.; Tatsumi, T. Synthesis of Amino-Functionalized MCM-41 via Direct Co-Condensation and Post-Synthesis Grafting Methods Using Mono-, Di- and Tri-Amino-Organosiloxanes. *J. Mater. Chem.* **2004**, *14*, 951-957.
38. Hicks, J. C.; Drese, J. H.; Fauth, D. J.; Gray, M. L.; Qi, G.; Jones, C. W. Designing Adsorbents for CO₂ Capture from Flue Gas-Hyperbranched Aminosilicas Capable of Capturing CO₂ Reversibly. *J. Am. Chem. Soc.* **2008**, *130*, 2902-2903.
39. Das, S.; Maity, A.; Pradhan, M.; Jana, S. Assessing Atmospheric CO₂ Entrapped in Clay Nanotubes using Residual Gas Analyzer. *Anal. Chem.* **2016**, *88*, 2205-2211.
40. Caplow, M. Kinetics of Carbamate Formation and Breakdown. *J. Am. Chem. Soc.* **1968**, *90*, 6795-6803.
41. Hahn, M. W.; Steib, M.; Jentys, A.; Lercher, J. A. Mechanism and Kinetics of CO₂ Adsorption on Surface Bonded Amines, *J. Phys. Chem. C* **2015**, *119*, 4126-4135.
42. Tumuluri, U.; Isenberg, M.; Tan, C.; Chuang, S. S. C. In Situ Infrared Study of the Effect of Amine Density on the Nature of Adsorbed CO₂ on Amine-Functionalized Solid Sorbents. *Langmuir* **2014**, *30*, 7405-7413.
43. Sim, K.; Lee, N.; Kim, J.; Cho, E. B.; Gunathilake, C.; Jaroniec, M. CO₂ Adsorption on Amine-Functionalized Periodic Mesoporous Benzenesilicas. *ACS Appl. Mater. Interfaces* **2015**, *7*, 6792-6802.
44. Kim, S.; Ida, J.; Gulians, V. V.; Lin, J. Y. S. Tailoring Pore Properties of MCM-48 Silica for Selective Adsorption of CO₂. *J. Phys. Chem. B* **2005**, *109*, 6287-6293.
45. Hiyoshi, N.; Yogo, K.; Yashima, T. Adsorption Characteristics of Carbon Dioxide on Organically Functionalized SBA-15. *Microporous and Mesoporous Mater.* **2005**, *84*, 357-365.
46. Patil, U.; Fihri, A.; Emwas, A. H.; Polshettiwar, V. Silicon Oxynitrides of KCC-1, SBA-15 and MCM-41 for CO₂ Capture with Excellent Stability and Regenerability. *Chem. Sci.* **2012**, *3*, 2224-2229.
47. Min, K.; Choi, W.; Kim, C.; Choi, M. Oxidation-Stable Amine-Containing Adsorbents for Carbon Dioxide Capture. *Nat. Commun.* **2018**, *9*, 726-732.

Development of Hybrid Nanocomposites for Hg(II) Removal from Aqueous Solution

5.1 Introduction

The contamination of toxic heavy metal ions discharged from textile, fertilizer, mining, refining, and printing industries into water has been identified as a serious threat not only to the public health but also to the environment and natural ecosystems, as the toxic heavy metals present in liquid effluents are considered as persistent, non-biodegradable, and bioaccumulative.¹⁻³ Among the several toxic heavy metals, mercury is one of the most harmful pollutants, having permissible limit of 2.0 ppb in drinking water. Mercury exposure via direct contact or gradual bioaccumulation leads to the severe damage to the human nerves, lungs, kidneys, and other organs. Currently, mercury has been excessively released into environment through rapid discharge of industrial waste, including fossil fuel combustion, batteries, electronic materials, and chemicals. Up-to-now, several techniques have been adopted for heavy metals removal, e.g.; adsorption, precipitation, ion exchange, reverse osmosis, and nanofiltration.⁴⁻⁸

Among the various techniques, adsorption is fascinating to the researchers owing to its simplicity, low-cost, and a reliable chemical engineering process, which has potential to overcome these environmental issues.⁹ For efficient mercury removal from water, several potential adsorbents were reported in the literature, like activated carbon,^{10,11} graphene,¹² chelate incorporated fibers,^{13,14} chitosan,^{15,16} cellulose,^{17,18} and porous silica.^{19,20} Although activated carbon is highly porous with large specific surface area and high adsorption efficiency, it is expensive to use and regenerate, thus limiting its large-scale synthesis for industrial application.¹⁹ Besides activated carbon, graphene based adsorbents having large effective surface areas possess excellent adsorption

capacity and selectivity but the synthesis of such materials involves time consuming steps to achieve well-dispersed nano carbon flakes and their functional derivatives.¹⁷ The potential toxicity of nanoscale adsorbents as well as difficulties for repossessing the adsorbents after metal ions adsorption is the major limitation in some techniques.²¹ Again, adsorbents synthesized based on chelate-modified wool or polyester fibers, consist of either high temperature processes or special instruments during their synthesis.^{13,14} For template-based mesoporous silica materials synthesis, an inherent drawback is that it is not a cost-effective route owing to the use of rather expensive sacrificial templates, like surfactants, block copolymers etc., which in turn restricts their wide usage as advanced adsorbents.²² The pressing need is therefore to develop environmentally friendly and reusable adsorbents in a large scale based on low-cost materials and simple synthetic route for the efficient removal of toxic heavy metal ions.

Recently, inorganic-organic hybrid nanocomposites (NCs) consisting of clay materials, provide a new direction in the frontier area of materials science because of their high abundance in nature together with high mechanical and thermal stability as well as diverse applications in the field of environmental remediation, which includes adsorption of toxic inorganic contaminants since they possess good chemical affinity and excellent adsorption efficiency even at low concentration. Halloysite nanotubes (HNTs) are naturally occurring and economically sustainable two-layered aluminosilicate clay ($\text{Al}_2\text{Si}_2\text{O}_5(\text{OH})_4 \cdot n\text{H}_2\text{O}$), containing tetrahedral SiO_2 sheets and the octahedral AlO_6 sheets. HNTs having a hollow tubular structure, demonstrate positive inner surface and negative outer surface charges, which regulate their physicochemical properties through the control of the chemistry of these constituent elements. However, the disadvantages of such material are the less metal loading capabilities and quite low metal ion binding constants, which can be resolved through the functionalization of these materials using active organic functional groups that immobilized over their surfaces. Thus, functionalization of HNTs by organosilanes gives rise to low-cost adsorbents for the adsorption of toxic heavy metal ions, which in turn open a new route for the treatment of industrial heavy metal contaminated wastewater.

We have developed hybrid NCs consisting mercapto ($-SH$) and amino ($-NH_2$ and $-NHR$) groups for surface functionalization HNTs and explored them as cost-effective sorbents for the removal of toxic heavy metal ions from the aqueous solution. The chemical analysis of the NCs was carried out by FTIR and NMR spectroscopies, whereas morphological characterization was performed using scanning electron microscopy. We have studied their adsorption capacity, toward Hg(II) ions, dependence of functional groups, contact time and initial metal ion concentration. Adsorption kinetics and isotherms for Hg (II) ions were studied using three different adsorbents. The adsorption capacity of all the NCs was examined even at low concentration of adsorbate. Subsequently, stability of these NCs was illustrated by their repetitive use and their efficacy was compared with the reported amine based adsorbents.

5.2 Experimental Section

5.2.1 Synthesis of Inorganic-Organic Hybrid Nanocomposites

Inorganic-organic hybrid NCs were synthesized by grafting of organosilanes over the outer surfaces of HNTs.²³ The grafting reaction was performed under nitrogen atmosphere using standard air free technique. A 50 mL three-necked round bottom flask containing 15.0 mL of toluene, 3.0 g of HNTs was added to the flask which was fixed with a rubber septum, condenser, and a thermocouple adaptor. The reaction mixture was de-aerated for 30 minutes under nitrogen at room temperature, followed by heated with a heating mantle. After that organosilane (6.0 mmol) was injected into the flask at 60 °C under stirring condition, subsequently the reaction mixture was heated to 120 °C and refluxed for 20h at that temperature. Finally, the as-synthesized product was collected through filtration and washed several times with toluene and ethanol respectively to remove unreacted aminosilanes if any and then dried at 100 °C overnight under vacuum. The products were abbreviated as M-HNTs, S-HNTs and SH-HNTs for 3-(aminopropyl)triethoxysilane, trimethoxy[3-(methylamino)propyl]silane, and (3-

mercaptopropyl) trimethoxysilane functionalized HNTs respectively and explored them as adsorbent to capture toxic metal ions.

5.2.2 Batch Adsorption Study

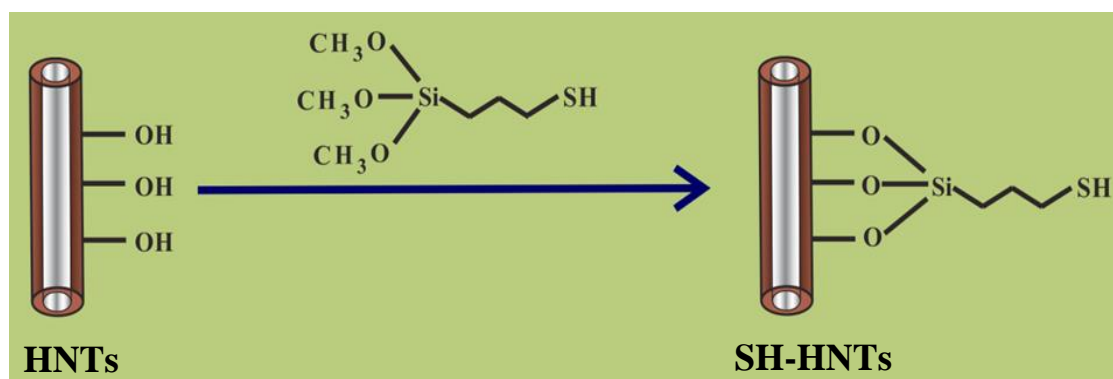
To demonstrate the adsorption capacity of these NCs towards toxic metal ions from aqueous solution, Hg(II) solution was taken in a beaker containing adsorbent (SH-HNTs or M-HNTs or S-HNTs). Adsorption experiments were carried out taking different concentration of Hg(II) solution and the adsorbent concentration was maintained to 3.0 g L^{-1} . The solution was stirred on a magnetic stirrer up to a desired time and then the solution was filtered off once the adsorption was over and collected for further study. The resulting solutions were analyzed by inductive coupled plasma optical emission spectroscopy (ICP-OES). The amount of unbound Hg(II) ions present in the filtrate was also estimated using diphenylthiocarbazone (dithizone), which formed a complex with Hg(II) ions. The absorption spectra of mercury-dithizone complexes have been recorded using a UV-Visible spectrophotometer in a standard quartz cuvette of 1 cm path length. All the isotherms and kinetics were carried out at pH 4 at $25 \text{ }^\circ\text{C}$. For adsorption kinetics and initial concentration of Hg(II) solution was taken to be 200 mg L^{-1} with an adsorbent concentration of 3.0 g L^{-1} . For the regeneration and reuse of the NCs, the used SH-HNTs, M-HNTs and S-HNTs were treated with 10% thiourea in 0.05 M HCl solution for 2 h and then washed with plenty of water. After being regenerated, the adsorbents were added into the Hg(II) solution to check their reusability. Keeping all the experimental condition the same, we have also studied the adsorption capacity of these NCs for other heavy metals ions present in the aqueous solution.

5.3 Results and Discussion

5.3.1 Hg (II) Removal from Aqueous Solution Using SH-HNTs NCs

5.3.1.1 Characterization of the SH-HNTs

Due to the presence of negatively charged outer surfaces of HNTs, we can tune the properties by the selective modification of the surface through grafting of an organosilane, (3-mercaptopropyl) trimethoxysilane (MPTMS) as shown in Scheme 5.1. As the surface defects generally occur on the external surface of HNTs, the hydroxyl groups at those defects become available for surface modification.²⁴ Unlike the untreated HNTs, aqueous solution of modified HNTs doesn't show any colloidal stability, indicating hydrophobic nature of the outermost surfaces after the modification with organosilane.



Scheme 5.1: Schematic presentation of the synthesis of SH-HNTs through the grafting of (3-mercaptopropyl) trimethoxysilane over the outer surfaces of HNTs.

5.3.1.1.1 TGA Study

To estimate the silane/HNTs ratio, we have studied the thermal decomposition behavior of both HNTs and SH-HNTs with the help of thermogravimetric analysis (TGA) under nitrogen flow. TGA curves (Figure 5.1) of HNTs before and after surface modification represent the mass loss in the temperature range 50-600 °C. Weight loss between 50-150

°C corresponds to the desorption of physisorbed water from the surface and in the region of 150-250 °C, is due to the loss of hydrogen bonded MPTMS or removal of residual template. Decomposition of MPTMS which was grafted over HNTs surface occurs around 250-475 °C. Above 375 °C, the weight loss observed in HNTs and SH-HNTs, ascribes to the dehydroxylation of the residual structural AlOH groups.²⁴ The mass loss estimated by TGA analysis for SH-HNTs is in accordance with the amount of ligand covalently bound to the HNTs.

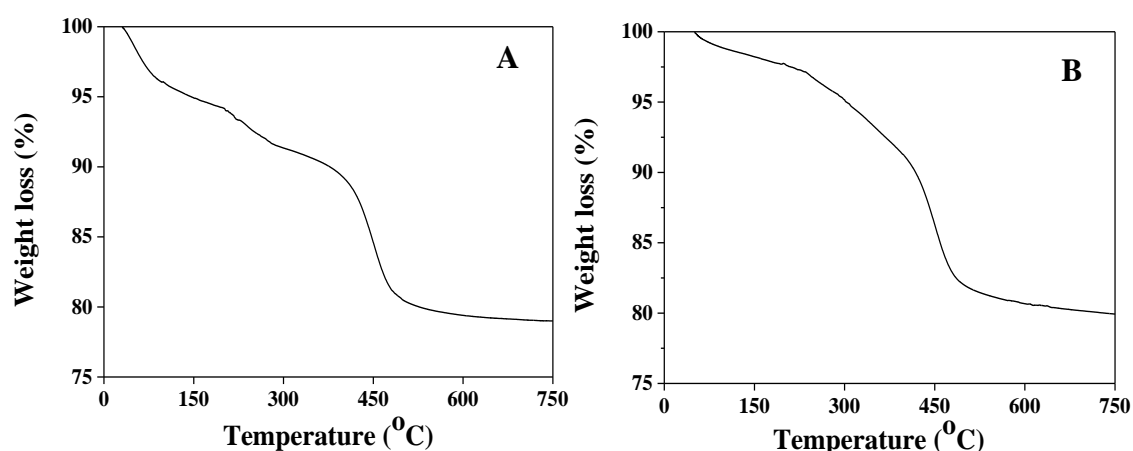


Figure 5.1: Thermogravimetric analysis (TGA) data of (A) HNTs and (B) SH-HNTs measured under nitrogen from room temperature to 750 °C.

5.3.1.1.2 FTIR Study

Fourier transform infrared (FTIR) spectra of HNTs and SH-HNTs exhibit (Figure 5.2) the well-defined peaks at 1635, 3621, and 3694 cm^{-1} , demonstrating deformation of water, O-H stretching of inner hydroxyl groups, and O-H stretching of inner surface hydroxyl groups respectively. All the above mentioned peaks are observed with a slight decrease in intensity in SH-HNTs, indicating that the basic structure of halloysite remains unaltered even after surface modification by MPTMS. Two newly emerged bands at 2931 cm^{-1} and 2550 cm^{-1} in SH-HNTs are assigned to the stretching vibration of C-H and S-H respectively, suggesting the grafting of MPTMS over the surface of HNTs.

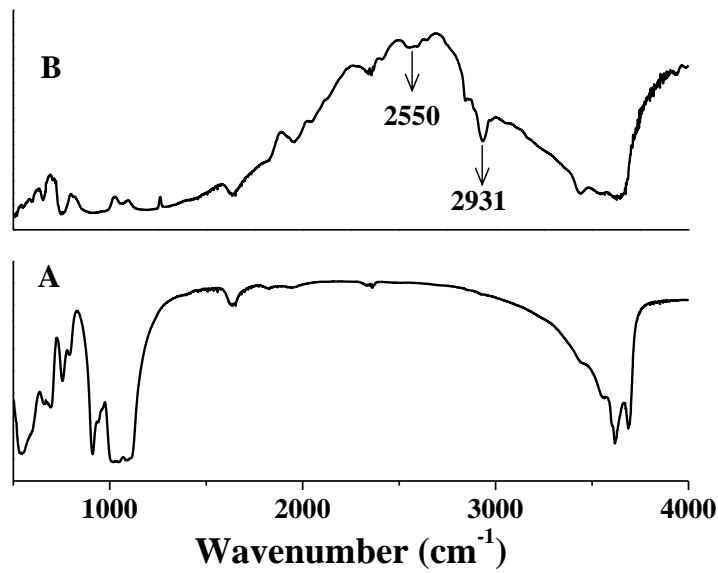


Figure 5.2: FTIR spectra of (A) HNTs and (B) surface modified HNTs by (3-mercaptopropyl) trimethoxysilane.

5.3.1.1.3 XRD Analysis

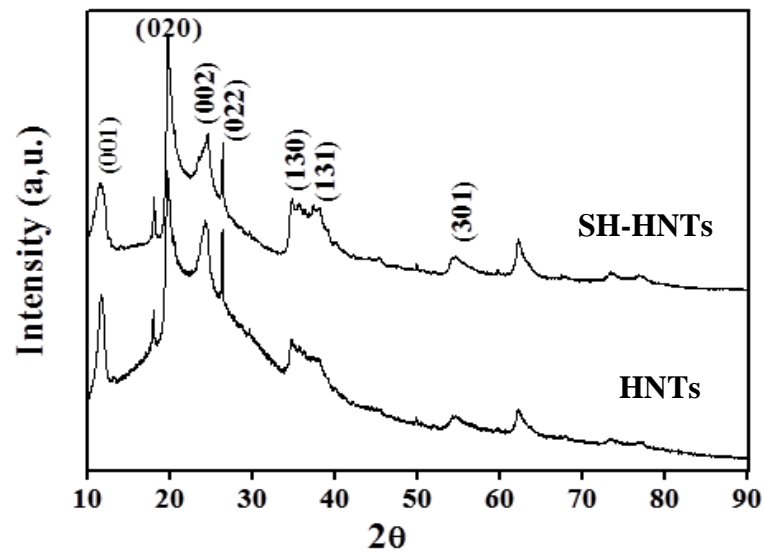


Figure 5.3: XRD patterns of HNTs before and after surface modification

We have studied the phase and purity of HNTs before and after modification of the surface by X-ray diffraction (XRD). Even after surface modification, the XRD pattern of SH-HNTs remains the same demonstrating no intercalation of MPTMS into the interlayer of HNTs and is in concordance with the reported pattern of HNTs (Figure 5.3).^{25,26}

5.3.1.1.4 FESEM and TEM Study

The morphology and the size of HNTs and SH-HNTs were determined with the help of field emission scanning electron microscopy (FESEM) and transmission electron microscopy (TEM) respectively. FESEM images of HNTs (Figure 5.4A and B) before and after modification demonstrate that they consist of cylindrical shaped tubes with an open-ended lumen. TEM images of HNTs and SH-HNTs (Figure 5.5A and B) demonstrate that the cylindrical shaped tubes composed of multilayer walls with the lumen, have irregularity in both length and wall thickness which results in variation in inner and outer diameter. The length of the tubes is 1.0 to 1.5 μm . The outer diameter of the tubes is 50-100 nm whereas lumen size is around 15-20 nm. The observed defects on the surface of HNTs may be due to the mechanical damage or by crystallographic defects.²⁴

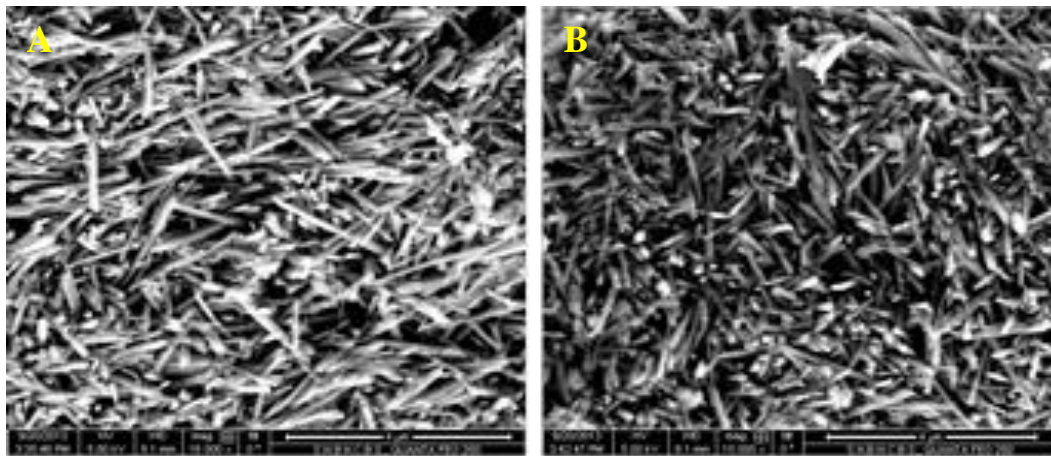


Figure 5.4: FESEM images of HNTs (A) before and (B) after surface modification.

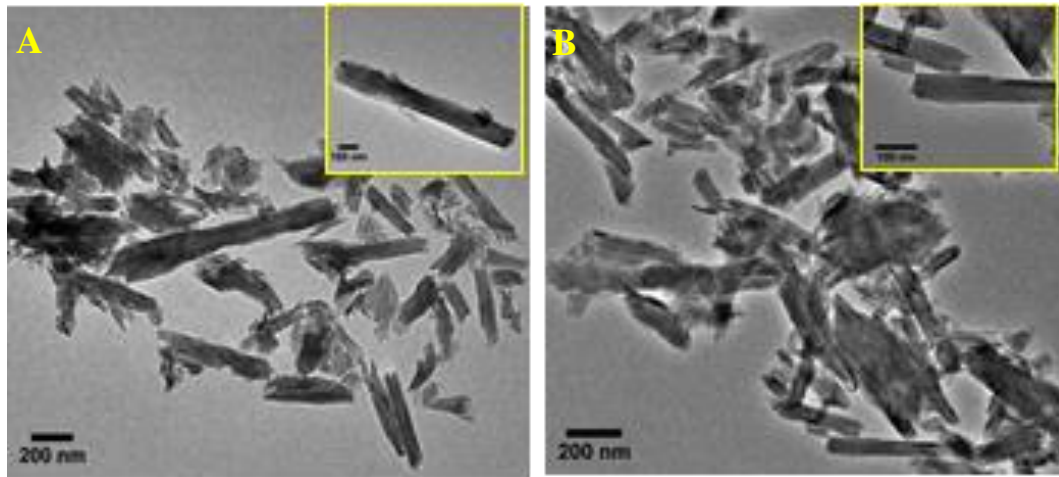


Figure 5.5: TEM images of (A) HNTs and (B) SH-HNTs. Inset of A and B shows a single HNT.

5.3.1.1.5 EDS Study

Energy dispersive X-ray spectroscopy (EDS) further corroborates the presence sulphur and carbon with the three main constituents, oxygen, aluminium, and silicon in SH-HNTs whereas pure HNTs contain only oxygen, aluminium, and silicon (Figure 5.6). EDS ensured the presence of sulphur and carbon in SH-HNTs owing to the surface modification of HNTs by MPTMS. The concentration of sulphur in the SH-HNTs is 1.04 wt % which was also confirmed by TGA analysis.

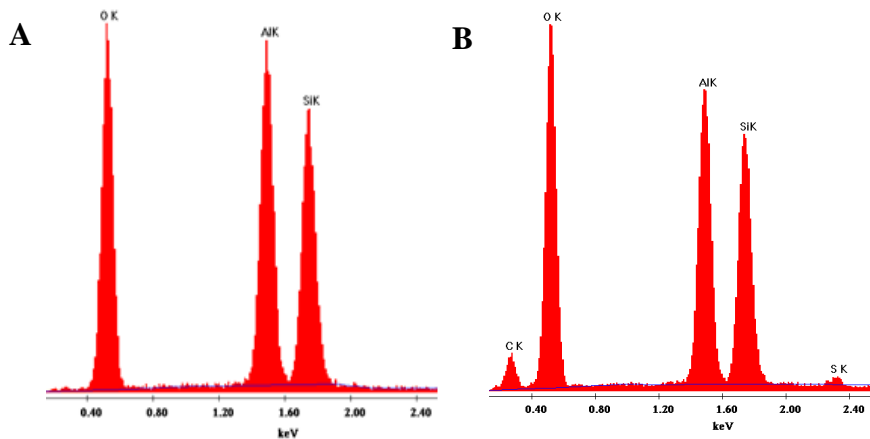


Figure 5.6: EDS spectra of (A) HNTs and (B) SH-HNTs.

5.3.1.1.6 Analysis of Sulphur (S) Content

We have performed CS analysis using carbon/sulphur analyzer to know the exact amount of sulphur present in the SH-HNTs and it has been estimated to be 1.08 wt %.

5.3.1.2 Mercury Adsorption Study by SH-HNTs

Mercury is one of the main pollutants in water. Inorganic mercury compounds are rapidly accumulated in the kidney and also cause neurological and renal disturbances. Thus, there is a desire to develop a low-cost adsorbent to extract these pollutants from the ground water. A new solid-phase adsorbent was synthesized by the surface modification of HNTs with MPTMS for the removal of heavy metals ions. Multiple sets of batch experiments were performed to study the mercury adsorption isotherms. To determine the adsorption capacity, SH-HNTs were added to Hg(II) solution and the reaction mixture was equilibrated at room temperature under neutral condition. After the adsorption of Hg(II) ions by SH-HNTs, the amount of unbound Hg(II) ions present in the solution was estimated using a UV-Visible spectrophotometer at different time intervals.

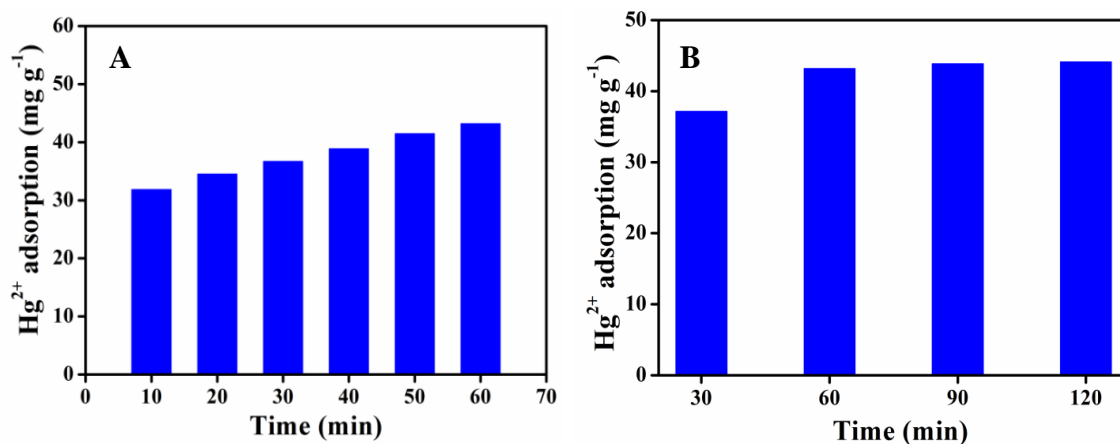


Figure 5.7: Adsorption of Hg(II) ions from the aqueous solution (200 mg/L) by SH-HNTs as a function of time, at an interval of (A) 10 min and (B) 30 min, indicating adsorption of Hg(II) increases with time and finally reaches to a maximum 1h after the addition of the above adsorbent.

The uptake of Hg(II) ions by SH-HNTs as a function of time was estimated and presented in Figure 5.7A. It is evident that the adsorption of Hg(II) increases with time and finally reaches to a maximum, 1h after the addition of adsorbent (Figure 5.7B). However, unmodified HNTs hardly show adsorption even after 24 h. The calculated Hg/S molar ratio indicates 1:1 complexation mechanism between Hg(II) and thiol and also demonstrates the presence of sufficient amounts of active adsorption sites in the SH-HNTs. Therefore, we can affirm that all the thiol groups are located on the external surfaces of HNTs.

The adsorption isotherm of Hg(II) on SH-HNTs was studied by static equilibrium adsorption to know the binding property and the experimental data were fitted with Freundlich²⁷ as well as Langmuir isotherm model.²⁸ Langmuir isotherm theory which assumes monolayer coverage of adsorbate over a homogenous adsorbent surface can be expressed as follows: models.

$$Q_e = \frac{K_L Q_m C_e}{1 + K_L C_e} \quad (5.1)$$

The Freundlich equilibrium isotherm which is used for the description of multilayer adsorption with interaction between adsorbed molecules can be expressed as follows:

$$Q_e = K_F C_e^{\frac{1}{n}} \quad (5.2)$$

where, Q_e is the equilibrium adsorption capacity of an adsorbent and Q_m is the maximum adsorption capacity of that adsorbent (mg g^{-1}). C_e is the equilibrium concentration of adsorbate (mg L^{-1}), K_L is the Langmuir equilibrium constant (L mg^{-1}) associated to the free energy of adsorption. K_F is the Freundlich equilibrium constant ($\text{mg g}^{-1})(\text{L mg}^{-1})^{1/n}$ and n is the adsorption equilibrium constant. Based on Langmuir and Freundlich model we have analyzed the experimental data obtained for equilibrium adsorption isotherm of Hg(II) (Figure 5.8A). The experimental data was well fitted with Langmuir model than the Freundlich model, demonstrating monolayer molecular adsorption over SH-HNTs. The maximum Hg(II) adsorption capacity of 62.19 mg g^{-1} of adsorbent was achieved.

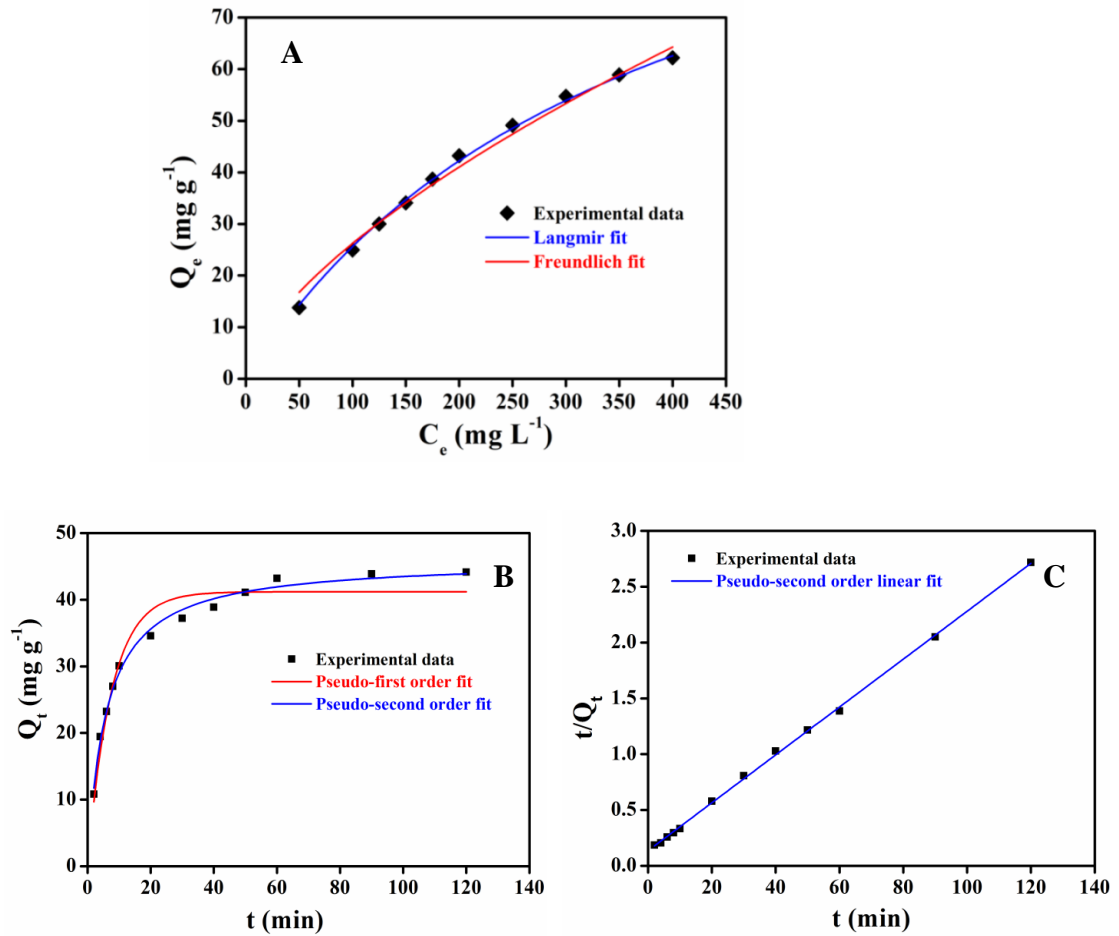


Figure 5.8: (A) Adsorption isotherms of Hg(II) ions over the surfaces of SH-HNTs demonstrating monolayer coverage of the adsorbate. (B) Adsorption kinetics of Hg(II) and corresponding (C) pseudo-second-order linear fit for SH-HNTs, representing that SH-HNTs follow pseudo-second order adsorption model.

The adsorption kinetics of Hg (II) ions was then studied based on the pseudo-first order and pseudo-second order rate equations:^{29,30}

Pseudo-first-order rate equation is given by

$$Q_t = Q_e - Q_e e^{-k_1 t} \quad (5.3)$$

Pseudo-second-order rate equation is:

$$Q_t = \frac{k_2 Q_e^2 t}{1 + k_2 Q_e t} \quad (5.4)$$

where, Q_e is the equilibrium adsorption capacity of an adsorbent (mg g^{-1}), Q_t is the amount of adsorbate (mg g^{-1}) at time t . k_1 is the pseudo-first order reaction rate constant (min^{-1}) and k_2 is the rate constant for pseudo-second order reaction ($\text{g mg}^{-1} \text{min}^{-1}$). Figure 5.8B represents uptake of Hg(II) ions by SH-HNTs as a function of time. Linear fitting of pseudo second-order kinetics for the adsorption of Hg(II) by SH-HNTs was presented in Figure 5.8C. It was observed that the adsorption kinetics of Hg(II) follows pseudo-second-order rate equation (with $R^2 = 0.997$), assuming the chemical adsorption process is the rate-limiting step.

5.3.1.3 Chemical Stability and Regenerability of SH-HNTs

To find out the chemical stability and regenerability of the adsorbent, several adsorption/desorption test were carried out using 10 % thiourea in 0.05M HCl solution as eluent. After successive regeneration, the adsorption efficacy of SH-HNTs remains almost the same up to 5th cycle and then gradually decreases probably due to the irreversible Hg(II) adsorption or due to oxidation of thiol groups (Figure 5.9). Its ability to restore high mercury uptake capacity for a number of cycles even after regeneration and reuse makes SH-HNTs a new alternative as an adsorbent.

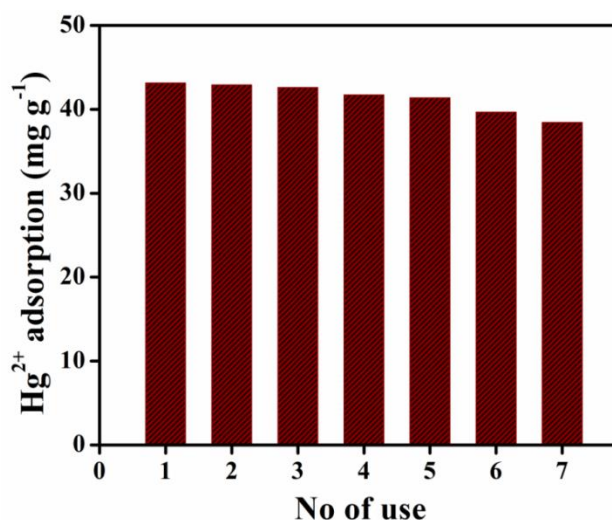


Figure 5.9: Adsorption efficiency of SH-HNTs for Hg(II) ions from the aqueous solution (200 mg/L) using the same batch of SH-HNTs.

5.3.1.4 Adsorption of Different Toxic Metals by SH-HNTs

The adsorption efficiency of SH-HNTs has also been extended for the adsorption of Pb(II) and Cd(II) ions from the aqueous solution. For a comparative study, the same experiment was performed taking the adsorbate solution of three different heavy metal ions. We found that SH-HNTs adsorbed maximum Hg(II) among the three adsorbates and the adsorption efficiency follows the order: Hg(II) > Cd(II) > Pb(II) (Figure 5.10). The above observation can be explained with the help of Pearson's Hard and Soft Acids and Bases (HSAB) theory.³¹ According to HSAB principle "hard acids prefer to bind with the hard bases to give ionic complexes, whereas the soft acids prefer to bind with soft bases to give covalent complexes". As per the theory, the Lewis acid and bases are divided into hard, soft, and border line types. In our study, MPTMS (RSH) is a soft base which prefers to bind with Hg(II), a soft acid, compared to Pb(II) which is a border line acid. Though Cd(II) belongs to soft acid type, we observed the higher selectivity of RSH towards Hg(II) than Cd(II). The smaller ionic radii of Cd(II) presumably makes it less softer than Hg(II), as larger ionic radii is another characteristic to become a soft acid. Thus, the SH-HNTs may be a new alternative to meet the requirements of a sensor or an adsorbent for the detection as well as adsorption of Hg(II), Pb(II), and Cd(II) from aqueous solution.

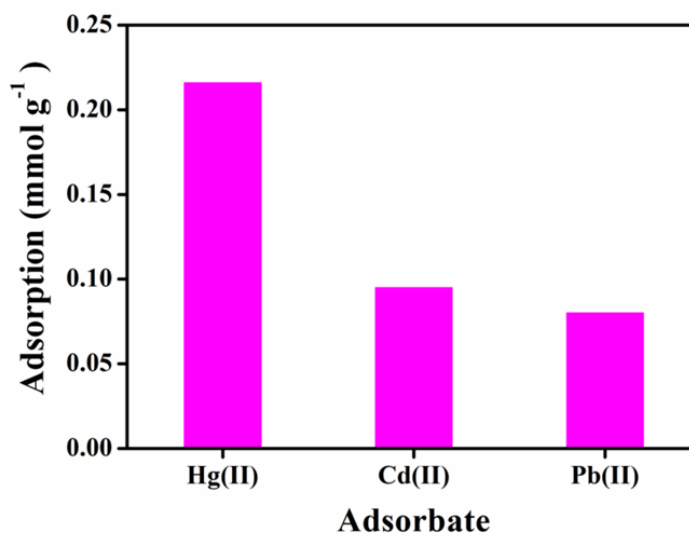
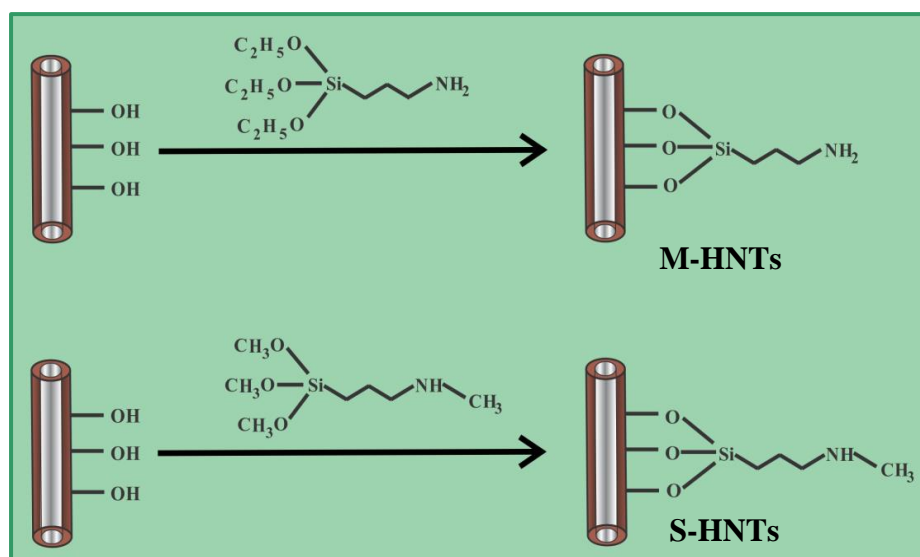


Figure 5.10: Adsorption efficiency of SH-HNTs for the different adsorbates from their aqueous solution (200 mg/L).

5.3.2 Hg (II) Removal from Aqueous Solution Using Amine Functionalized HNTs

5.3.2.1 Characterization of M-HNTs and S-HNTs

The nanocomposites were synthesized based on the selective modification of the outer surfaces of HNTs using aminosilanes, having primary or secondary amine sites through the grafting of 3-(aminopropyl)triethoxysilane (M-HNTs) and trimethoxy[3-(methylamino)propyl]silane (S-HNTs) respectively, as ascribed in Scheme 5.2.



Scheme 5.2: Schematic presentation of the synthesis of M-HNTs and S-HNTs through the grafting of 3-(aminopropyl)triethoxysilane and trimethoxy[3-(methylamino)propyl]silane over the outer surfaces of HNTs respectively.

5.3.2.1.1 FTIR Study

The chemical modification of HNTs surfaces due to the grafting of aminosilanes was characterized by FTIR spectroscopy. Figure 5.11 represents FTIR spectra of HNTs, M-HNTs, and S-HNTs, indicating the presence of two well-defined peaks at 3621 and 3697 cm⁻¹ owing to the stretching vibrations of inner hydroxyl and inner surface hydroxyl groups respectively.³² Three new bands at 1556, 2935, and 3453 cm⁻¹ were observed in

case of M-HNTs and S-HNTs for N-H deformation and stretching vibration of C-H and N-H respectively, signifying grafting of aminosilanes.^{33,34}

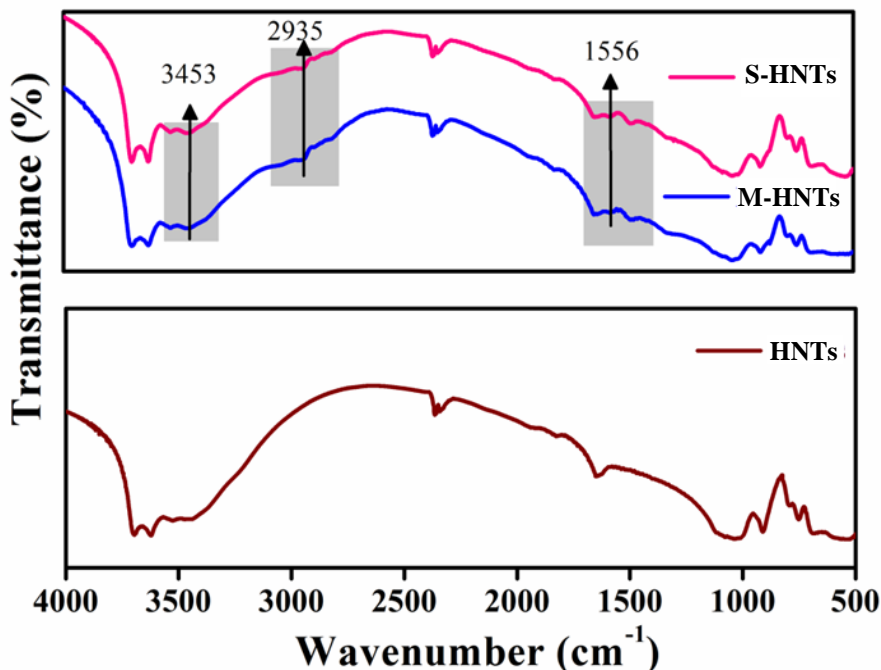


Figure 5.11: FTIR spectra of HNTs, M-HNTs and S-HNTs. FTIR spectra of M-HNTs and S-HNTs demonstrate the presence of amino groups in the nanocomposites due to the grafting of aminosilanes onto the surface of HNTs.

5.3.2.1.2 NMR Study

Additionally, we have performed solid state ^{29}Si NMR spectroscopy to further demonstrate the grafting of these aminosilanes over the surface of HNTs. ^{29}Si CP-MAS NMR spectra of HNTs, M-HNTs and S-HNTs are illustrated in Figure 5.12. In ^{29}Si CP-MAS NMR spectra, the chemical shift at -91 ppm arises from the constituent silicon present in HNTs, M-HNTs, and S-HNTs. The new peak appeared at -67 ppm in both M-HNTs and S-HNTs is due to the tridentate (T^3) bonded silicon, indicating the formation of a new chemical bond between the surface hydroxyl groups of HNTs and the organosilanes.³⁵

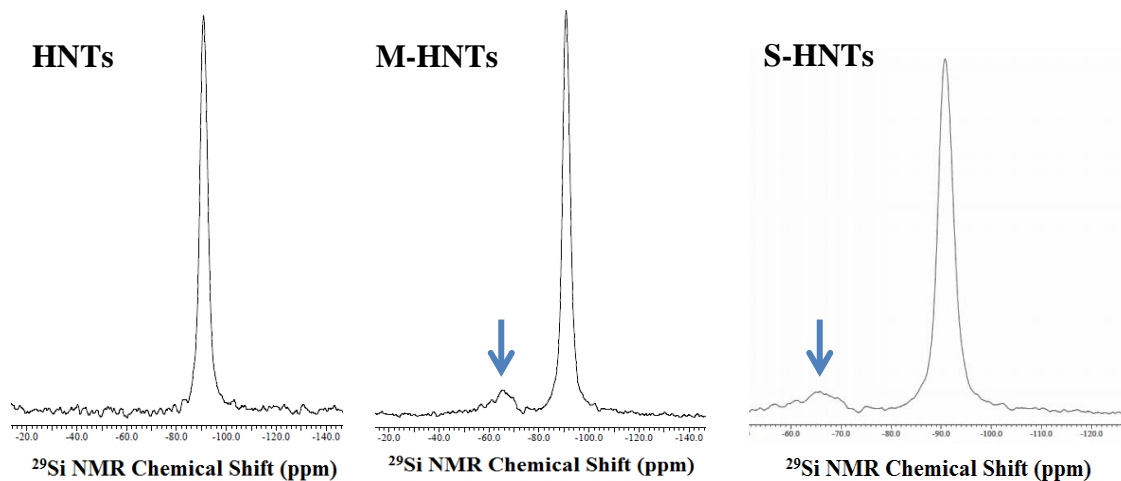


Figure 5.12: ^{29}Si CP-MAS NMR spectra of HNTs, M-HNTs and S-HNTs respectively.

5.3.2.1.3 FESEM Study

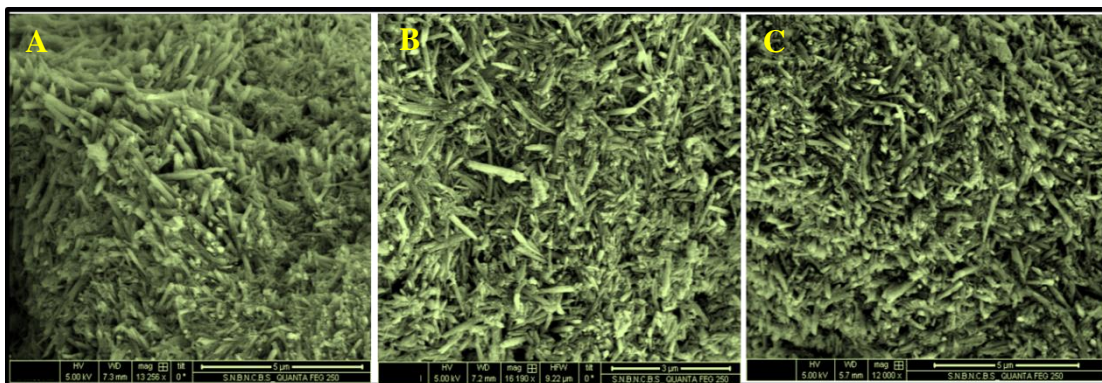


Figure 5.13: FESEM images of (A) HNTs, (B) M-HNTs, and (C) S-HNTs respectively, indicating that they are composed of cylindrical shaped tubes with no change in their morphology even after grafting of aminosilanes.

The field emission scanning electron microscopy (FESEM) images of HNTs, M-HNTs and S-HNTs are shown in Figure 5.13. HNTs are composed of cylindrical shaped tubes having lengths between 1.0 - 1.5 μm with outer and inner diameters of 50-100 nm and 15-20 nm respectively, demonstrating polydispersity in their sizes. The morphology of

M-HNTs and S-HNTs is analogous to the morphology of pristine HNTs even after grafting of aminosilanes.

5.3.2.1.4 XRD Study

X-ray diffraction pattern (XRD) of HNTs is similar to that of P-HNTs or S-HNTs (Figure 5.14). The characteristic (001) reflection remains unaltered after grafting of organosilanes, further demonstrating the absence of any intercalation of aminosilane into the interlayer of HNTs.^{35,36}

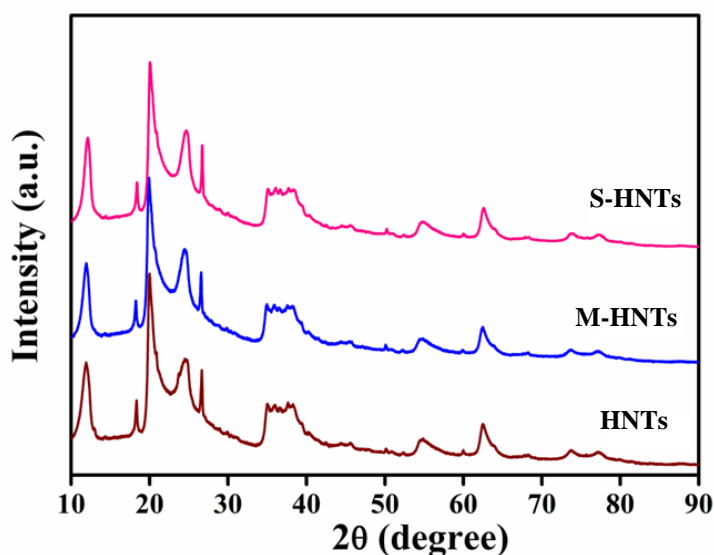


Figure 5.14: XRD patterns of HNTs, M-HNTs and S-HNTs respectively, indicating the absence of any intercalation of aminosilanes into the interlayer of HNTs.

5.3.2.1.5 CHN Elemental Analysis

CHN elemental analysis was carried out to achieve the exact concentration of grafted amino groups in M-HNTs and S-HNTs. The loaded N was assessed to be 0.51 and 0.53 wt% in M-HNTs and S-HNTs respectively under the present experimental condition.

These organosilane functionalized surfaces of HNTs are stable enough and impervious to remove the aminosilanes from the surface by any organic solvents or water.

5.3.2.1.6 Surface Area Analysis

The specific surface area assessed by the Brunauer-Emmett-Teller (BET) method was found to be 22 and 19 m² g⁻¹ for M-HNTs and S-HNTs respectively. The isotherms of the adsorbents are of type II with H3 hysteresis loops (Figure 5.15) according to IUPAC classification, representing the signature of mesoporous materials.

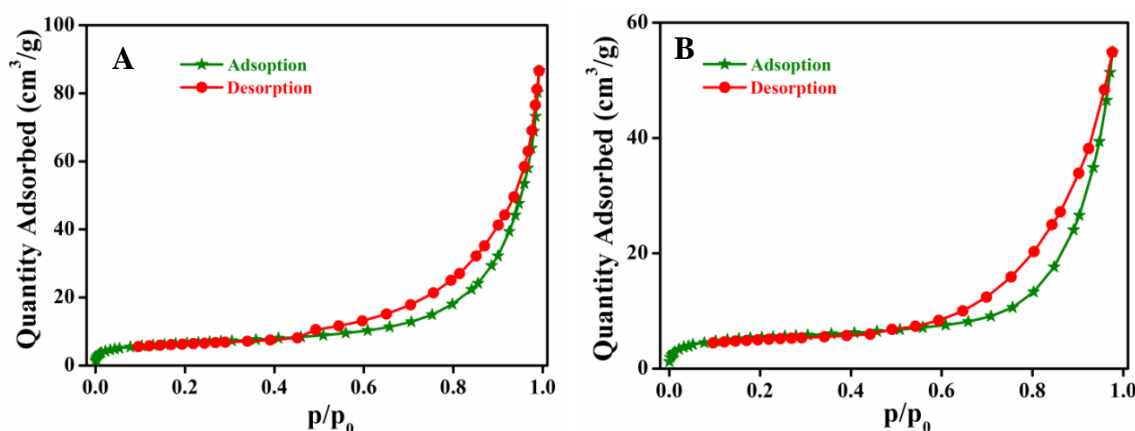


Figure 5.15: The nitrogen adsorption-desorption isotherms of (A) M-HNTs and (B) S-HNTs respectively, representing the signature of mesoporous materials. The specific surface area was estimated using nitrogen adsorption-desorption study at 77 K.

5.3.2.2 Mercury Adsorption Study using M-HNTs and S-HNTs

To explore the adsorption capacity of the NCs, mercury-containing aqueous solutions was considered as a pollutant, since mercury has been established as one of the most harmful pollutants in the environment owing to its high toxicity, volatility, and bioaccumulation. The adsorption kinetics describing Hg(II) uptake rate was governed by

the contact time during adsorption reaction, which in turn determines the efficiency of Hg(II) sorption of these adsorbents. To study the adsorption kinetics, the reaction mixture was equilibrated at room temperature and then the amount of adsorbed Hg(II) ions by M-HNTs and S-HNTs was estimated as a function of time. We found that the apparent adsorption equilibrium reached around 60 min of the adsorption process, after which no significant change in adsorption capacity was observed even until 2 h (Figure 5.16). The adsorption kinetics of Hg(II) ions was then studied based on the pseudo-first order and pseudo-second order rate equations. In Table 5.1, we have summarized kinetic parameters for Hg(II) adsorption based on the pseudo-first order and pseudo-second order models. Based on the extracted correlation coefficient (R^2), the adsorption kinetics of Hg(II) follows pseudo-second order model for both M-HNTs and S-HNTs, where the chemical adsorption process is the rate-limiting step. Again Q_e values obtained from the pseudo-second order model fitting are comparable to that of the experimental values, further suggesting pseudo-second order adsorption kinetics of Hg(II).

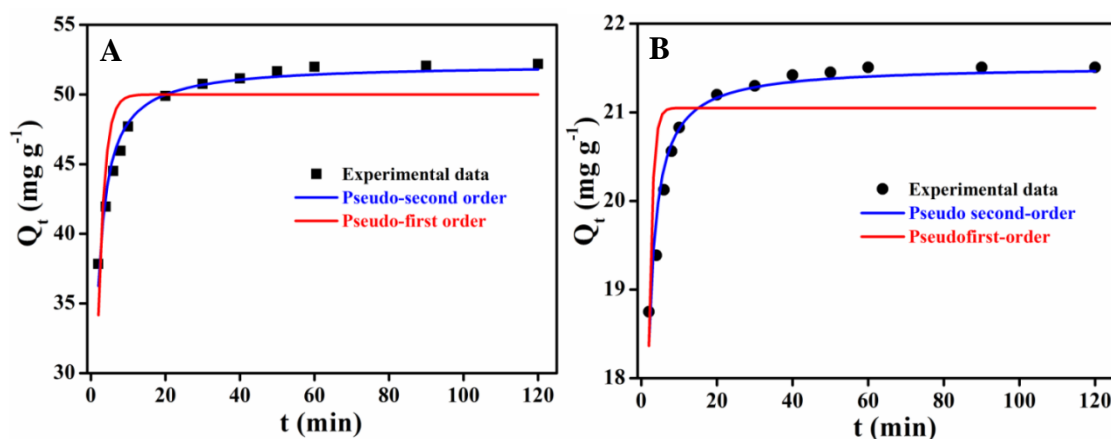


Figure 5.16: Adsorption kinetics of Hg(II) for both (A) M-HNTs and (B) S-HNTs, representing that both M-HNTs and S-HNTs follow pseudo-second order adsorption model.

Table 5.1: Kinetic parameters for Hg(II) uptake obtained from pseudo-first order and pseudo-second order models.

Adsorbent	$Q_{e\text{-exp}}$ (mg g^{-1})	Pseudo-First Order			Pseudo-Second Order		
		Q_{cal} (mg g^{-1})	$k_1(\text{min}^{-1})$	R^2	Q_{cal} (mg g^{-1})	k_2 ($\text{g mg}^{-1}\text{min}^{-1}$)	R^2
M-HNTs	52.18	49.99	0.575	0.71	52.18	0.02181	0.99
S-HNTs	21.50	21.08	1.029	0.69	21.52	0.13614	0.98

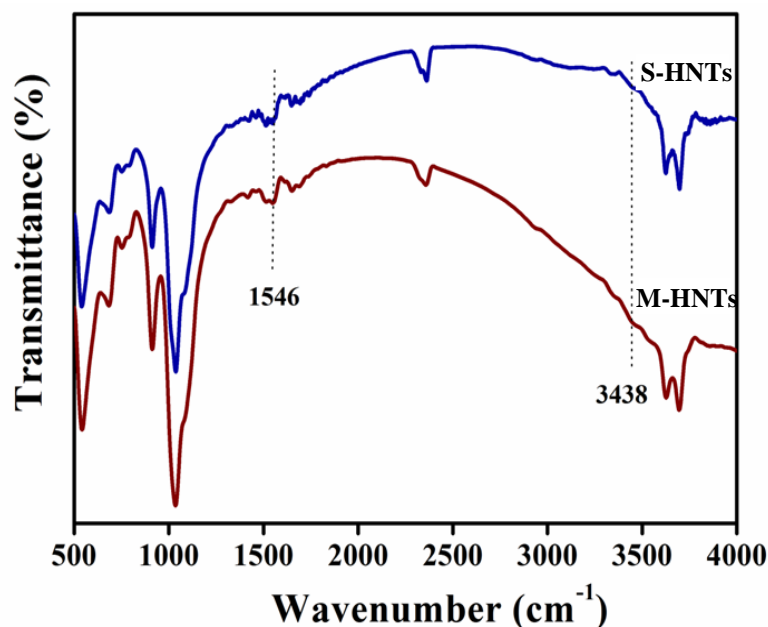
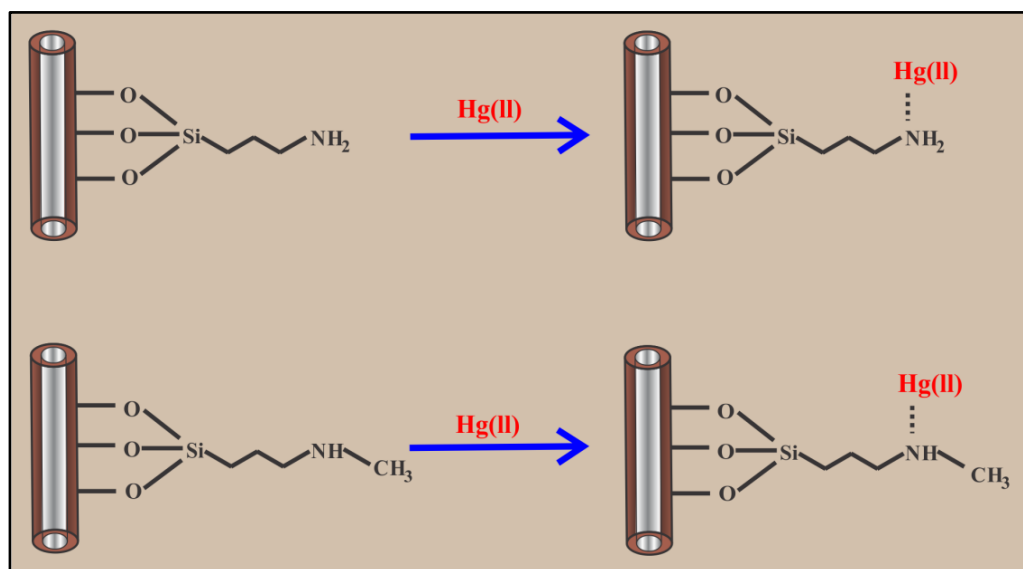


Figure 5.17: FTIR spectra of M-HNTs and S-HNTs after adsorption of Hg(II) ions, indicating metal-ligand complex formation between Hg(II) and the reactive functional groups ($-\text{NH}_2$ or $-\text{NHR}$) present in the adsorbents, since the lone pair of electrons on the nitrogen are the key adsorption sites for Hg(II) capture.

FTIR analysis was performed after the adsorption of Hg(II) ions over the surface of M-HNTs and S-HNTs (Figure 5.17), which demonstrated that the stretching and deformation vibrations of N-H at 3453 and 1556 cm^{-1} were shifted to 3438 and 1546 cm^{-1} respectively, authenticating an interaction of Hg(II) ions with the adsorption sites ($-\text{NH}_2$

or -NHR) present in the adsorbents. The probable mechanism behind the binding of toxic Hg(II) ions is attributed to the metal-ligand complex formation between Hg(II) and the reactive functional groups (-NH₂ or -NHR) of the adsorbents, since they provide effective adsorption sites, as shown in Scheme 5.3. Again, Hg(II) ions prefer to coordinate with amine sites, resulting in a strong coordination with Hg(II) ions.



Scheme 5.3: Schematic presentation of the probable mechanism of the binding of toxic Hg(II) ions with the reactive functional groups (-NH₂ or -NHR) present in the adsorbents.

To demonstrate the adsorption isotherm of Hg(II), multiple sets of batch experiments were carried out at room temperature for M-HNTs and S-HNTs respectively. The adsorption isotherm of Hg(II) was studied to indicate the binding properties, as shown in Figure 5.18. Both the adsorption isotherms initially show a very sharp increase, signifying high-energy adsorption sites that facilitate strong adsorption at low equilibrium concentrations. The resultant data sets on mercury ion removal were fitted according to Langmuir and Freundlich isotherm models. It is known to all that Freundlich equilibrium isotherm demonstrates multi-layer adsorption with interaction between adsorbed

molecules and is related to the heterogeneous surfaces, whereas Langmuir isotherm describes the monolayer coverage of the adsorbate and valid for dynamic equilibrium adsorption over a homogenous adsorbent surface.^{37,38} Thus, Langmuir isotherm suggests adsorption on a homogeneous surface with uniform energy by monolayer coverage without any interaction between adsorbed ions, while different sites with several adsorption energies are involved in case of Freundlich isotherm. The Langmuir and Freundlich models parameters obtained for each adsorbent after fitted with experimental data are summarized in Table 5.2. It is interesting to note that correlation coefficient obtained from the Langmuir model was better fitted than that of Freundlich isotherm for mercury ions, suggesting a characteristic monolayer molecular adsorption of Hg(II) ions over the surfaces of M-HNTs and S-HNTs. The maximum adsorption capacity (Q_M) of M-HNTs and S-HNTs for Hg (II) was estimated to be 83.48 and 45.22 mg g⁻¹ respectively, indicating higher adsorption capacity of M-HNTs for Hg(II) ions than that of S-HNTs. It should be pointed out that M-HNTs consist of primary amine sites, while S-HNTs are composed of secondary amine sites. Thus, lower adsorption capacity of S-HNTs for Hg(II) ions is possibly due to the little interaction of the adsorbate with the secondary amines during the adsorption process, since amino groups present in the adsorbent are the effective adsorption sites.

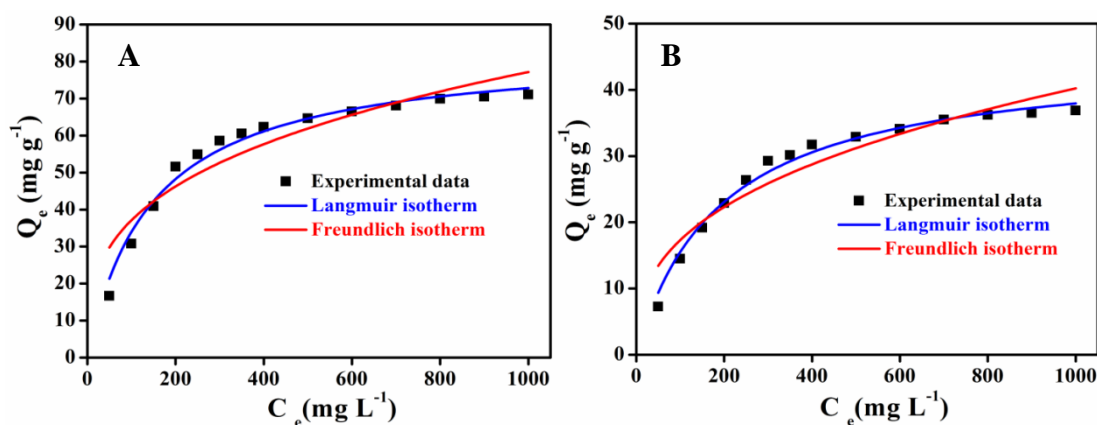


Figure 5.18: Adsorption isotherms of Hg(II) ions over the surfaces of (A) M-HNTs and (B) S-HNTs respectively, demonstrating monolayer coverage of the adsorbate.

Table 5.2: Langmuir and Freundlich isotherm models fitting parameters for the adsorption of Hg(II) over the adsorbents.

Adsorbent	Q _{e-exp} (mg g ⁻¹)	Langmuir Model			Freundlich Model		
		K _L (L mg ⁻¹)	Q _M (mg g ⁻¹)	R ²	K _F (mg g ⁻¹) (L mg ⁻¹) ^{1/n}	n	R ²
M-HNTs	71.4	0.00681	83.48	0.987	8.505	3.132	0.868
S-HNTs	37.1	0.00522	45.22	0.991	3.201	2.73	0.901

5.3.2.3 Temperature Dependence of Adsorption Capacity

Temperature dependent adsorption kinetics of these adsorbents was performed by carrying out the adsorption experiment in different temperature, keeping all other experimental condition unaltered. Figure 5.19A represents change in adsorption capacity of M-HNTs and S-HNTs as a function of temperature. The maximum adsorption was noticed around 40 °C. To determine spontaneous adsorption process, it is necessary to consider both the enthalpy and free energy change. The free energy change can be obtained from the equilibrium constant (K_d) which is estimated experimentally. The overall reaction equilibrium constant (K_d) can be obtained from the experiment as,

$$K_d = \frac{C_0 - C_e}{C_e} \times \frac{V}{W} \quad (5.5)$$

where, V is the working volume in mL and W is the adsorbent mass in g. C_0 and C_e are the initial and equilibrium concentrations of the adsorbate respectively.

Plot of $\ln K_d$ vs. $1/T$ was shown in Figure 5.19B. From this plot, one can subsequently measure the enthalpy change (ΔH^0) and entropy change (ΔS^0), as shown in Table 5.3 and Table 5.4. How the free energy change is affected due to endothermicity and disorderness of a process can be obtained using the following equation.

$$\Delta G^0 = \Delta H^0 - T\Delta S^0 \quad (5.6)$$

$$\Delta G^0 = -RT \ln K_d \quad (5.7)$$

where, R is the gas constant ($8.314 \text{ J mol}^{-1} \text{ K}^{-1}$), T is the absolute temperature in Kelvin (K), K_d is the equilibrium constant in mL g^{-1} . As equilibrium constant (K_d) can be obtained experimentally from $K_d = Q_e/C_e$ for various temperatures, one can find $-\Delta H^0/R$ as the slope and $\Delta S^0/R$ as the intercept from $\ln K_d$ vs. $1/T$ plot.

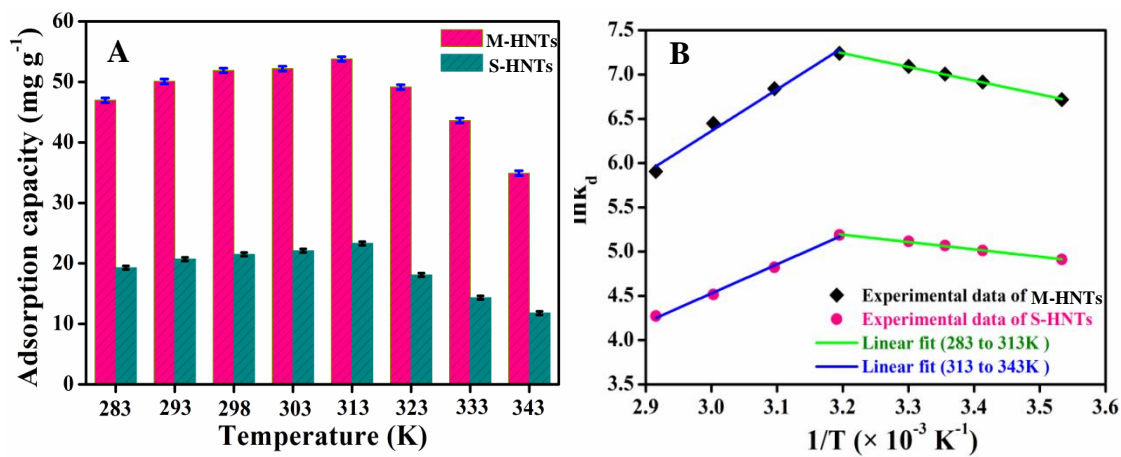


Figure 5.19: (A) Plot of adsorption capacity of M-HNTs and S-HNTs as a function of temperature and (B) corresponding $\ln K_d$ vs. $1/T$ plot.

For the spontaneous process, ΔG^0 is negative which is a resultant of ΔH^0 and $T\Delta S^0$, where ΔH^0 as +ve means endothermicity and positive intercept means ΔS^0 positive as an increase in randomness happens. This is due to the fact that Hg(II) adsorbs to the primary or secondary amine structure relative to its standard state. At higher temperature above 40°C , the surface adsorption of Hg actually governs the overall temperature dependence of rate.

Table 5.3: Thermodynamic parameters of Hg(II) adsorption onto M-HNTs and S-HNTs as a function of temperature (283K to 313K).

Adsorbent	T (K)	Q_e (mg g ⁻¹)	ΔG^0 (kJmol ⁻¹)	ΔH^0 (kJmol ⁻¹)	ΔS^0 (Jmol ⁻¹ K ⁻¹)
M-HNTs	283	46.98	-15.80	12.87	101.37
	293	50.10	-16.84		
	298	52.18	-17.35		
	303	52.20	-17.86		
	313	53.80	-18.84		
S-HNTs	283	19.29	-11.55	6.9	65.23
	293	20.70	-12.21		
	298	21.50	-12.55		
	303	22.10	-12.88		
	313	23.3	-13.50		

Table 5.4: Thermodynamic Parameters of Hg(II) Adsorption onto M-HNTs and S-HNTs as a Function of Temperature (313K to 343K).

Adsorbent	T(K)	Q_e (mg g ⁻¹)	ΔG^0 (kJmol ⁻¹)	ΔH^0 (kJmol ⁻¹)	ΔS^0 (Jmol ⁻¹ K ⁻¹)
M-HNTs	313	53.80	-18.84	-39.15	-64.54
	323	49.15	-18.37		
	333	43.63	-17.85		
	343	34.93	-16.84		
S-HNTs	313	23.30	-13.50	-27.32	-44.31
	323	18.10	-12.95		
	333	14.34	-12.50		
	343	11.10	-12.18		

5.3.2.4 Relation between Kinetics and Thermodynamics

The pseudo second order rate of the overall adsorption reaction, r_d can be written as,

$$r_d \propto r_s r_c \quad (5.8)$$

where, r_s is the rate proportional to the number of Hg atom adsorbed on the surface and r_c is the rate proportional to the number of Hg atoms involved in the primary or secondary amine complexation. Usually, adsorption of Hg on the surface of an adsorbent is an adsorption process governed by the rate,

$$r_s = r_s^0 e^{-\Delta G_s^\ddagger / RT} \quad (5.9)$$

$$r_c = r_c^0 e^{\Delta G_c^\ddagger / RT} \quad (5.10)$$

where, ΔG_s^\ddagger is change in free energy of activation of adsorption process and r_s^0 depends on the number of Hg atom on the adsorbent. ΔG_c^\ddagger is the amount of energy of interaction due to amine complexation with Hg and r_c^0 is proportional to the number or a size of Hg-amine complexes.

However, the critical size of the amine complexation actually controls the lowering of the thermal activation energy barrier of the adsorption process from the adsorbent. So, the overall adsorption rate, r_d can be written from the collision theory as,

$$r_d = f \left(\frac{k_B T}{h} \right) r_s^0 r_c^0 e^{-(\Delta G_s^\ddagger - \Delta G_c^\ddagger) / RT} \quad (5.11)$$

where, f is a proportionality constant which depends on the frequency factor of collision of Hg with the adsorbent and includes other approximate rate factors independent of temperature. The breaking of Hg amine complex is also a thermally activated process, where activation energy is negative of the interaction energy to make the appropriate size of the Hg-amine complex formation. We consider the overall process as,



so that

$$K_d = \frac{k_f}{k_b} \quad (5.12)$$

As the k_b is not affected by the Hg-amine complexation interaction energy, K_d is affected only by the ΔG_C^\ddagger in ΔG^0 . Free energy of activation for the adsorption of Hg-amine complex is given by

$$\Delta G_f^\ddagger = \Delta G_S^\ddagger - \Delta G_C^\ddagger \quad (5.13)$$

But the backward activation process, ΔG_b^\ddagger doesn't depend on the complexation, so that

$$\Delta G^0 = \Delta G_f^\ddagger - \Delta G_b^\ddagger = \Delta G_{ads}^\ddagger - \Delta G_C^\ddagger \quad (5.14)$$

where, ΔG_{ads}^\ddagger is the free energy change only due to the Hg(II) surface adsorption process. The mechanism of temperature dependent adsorption process is very similar in primary and secondary amine cases except the fact that the primary amine complexation is more favoured than the secondary one at any temperature by the obvious reason of steric hindrance on the surface.

At lower temperature below 40 °C, one can find $\Delta G_C^\ddagger > \Delta G_S^\ddagger$. At 40 °C, ΔG_C^\ddagger is almost zero and the value of $\ln K_d$ falls on the normal adsorption straight line with $1/T$ at higher temperature. As below 40 °C, $(\Delta G_S^\ddagger - \Delta G_C^\ddagger)$ is negative so the $\ln K_d$ increases with increasing $1/T$. However, it is beyond our limit to demonstrate the temperature dependence of decomplexation or decrease in size of the Hg amine complex with increase in temperature from the present experiment. In the high temperature range ($> 40^\circ\text{C}$), from the straight line curve with +ve slope one finds $\Delta H^0 = -ve$. Hg adsorption is an exothermic process and $\Delta S^0 = -ve$, i.e.; disorderness decreases. Therefore, the decrease in the adsorption capacity of our adsorbents at high temperature is possibly due to the weakening of the interaction between the active sites of the adsorbents and adsorbate.³⁷⁻³⁹ However, in the lower temperature range ($< 40^\circ\text{C}$), straight line curve with negative slope, ΔH^0 of the amine-Hg complexation is positive, indicating an endothermic process, whereas ΔS^0 is positive, so disorderness increases due to complexation process, which is also supported by the experimental data (Table 5.3 and Table 5.4).

5.3.2.5 Adsorption of Different Toxic Metals

In addition to Hg(II), we have studied the adsorption kinetics of M-HNTs and S-HNTs for several toxic metals (Cd(II), Pb(II), and Cu(II)) present in the aqueous solution, keeping all the experimental condition the same. The functional groups of the adsorbent and the adsorbate (metal ions) play an important role in the adsorption process, which in turn regulate the adsorption efficiency of the adsorbent. From Figure 5.20A, it can be found that the uptake of Hg(II) from aqueous solution by both M-HNTs and S-HNTs is remarkably higher compared to other metal ions, demonstrating insignificant adsorption of these metal ions possibly due to the physico-chemical properties of the metal ions, such as electro-negativity and ionic radius. Hence, we may conclude that M-HNTs has exceptional selectivity for Hg(II) adsorption and is capable of removal them from aqueous solution.

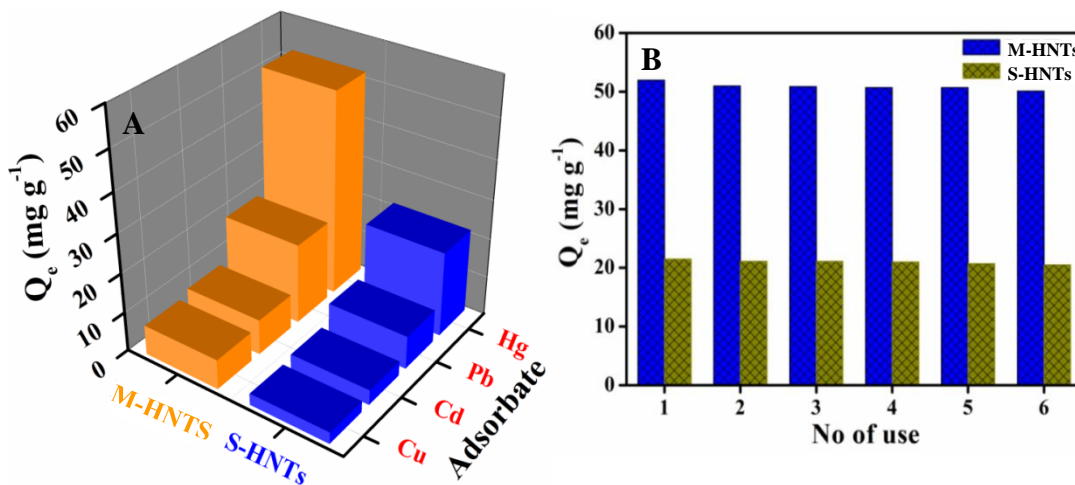


Figure 5.20: (A) Adsorption efficiency of M-HNTs and S-HNTs towards different adsorbates (200 mg L⁻¹) and (B) their uptake efficacy for Hg(II) after repetitive cyclic experiments.

The stability and recyclability of M-HNTs and S-HNTs were demonstrated by carrying out a number of adsorption/desorption experiments using 10% thiourea in 0.05 M HCl solution as an eluent. After successive regeneration, the uptake efficiency of these

adsorbents was found to be almost same up to six cycles (Figure 5.20B). After 6th cycle, a slight decrease in adsorption efficacy was observed both for M-HNTs and S-HNTs, which is possibly due to the irreversible adsorption of Hg(II) or may be due to the oxidation of amino groups during repetitive adsorption experiments.

5.3.2.6 Effect of Solution pH

It is important to note that the solution pH imparts a significant role during the adsorption process of Hg(II). To demonstrate pH dependent adsorption capacity of both M-HNTs and S-HNTs, we have carried out the adsorption study in the pH range 2-11, as shown in Figure 5.21A. With increasing solution pH from 2 to 7, the adsorption capacity of these adsorbents for Hg(II) ion increased noticeably and became highest at pH 7. This is possible due to the higher concentration of hydrogen ions at lower pH, which results in the protonation of the amino groups, leading to the weak binding ability of amino groups towards Hg(II) ions at lower pH. Additionally, a competitive adsorption between Hg(II) ions and hydrogen ions with the amine binding sites of the adsorbents occurs at low pH, which further encumbers the sequestration of Hg(II) ions. At higher pH (>7), an increase in adsorption efficiency of the adsorbents should occur since the deprotonated amines are available for binding with Hg(II). This observation has also been corroborated with our experimental findings for zero point charge pH (pH_{zpc}). It should be noted that pH_{zpc} is an important factor during adsorption of ionic species where the adsorbent surface has net electrical neutrality. The zero point charge pH (pH_{zpc}) of M-HNTs and S-HNTs was calculated by the pH drift method. In this method, the pH_{zpc} of the adsorbent was estimated by adding 10 mL of 0.05 M NaCl solution to the several vials (15 mL) and the pH was adjusted to a desired value (in the pH range of 2 – 12) using aqueous solutions of either HCl or NaOH. Then, 0.03 g of the adsorbent was added to the each vial and closed properly and mixed well using a vortexer for 30 min. After that, the vials were allowed to equilibrate for 48 h at room temperature. The suspensions were centrifuged to measure the final pH of the supernatant. The difference between final and initial pH (ΔpH) was

plotted against initial pH. The point of intersection of the resulting curve at which $\Delta\text{pH} = 0$, gives rise to the exact value of pH_{zpc} of an adsorbent. Figure 5.21B depicts pH_{zpc} of both M-HNTs and S-HNTs respectively. The pH_{zpc} of M-HNTs was estimated to be 7.6, whereas it is 7.2 for S-HNTs. Therefore, $\text{pH} > \text{pH}_{\text{zpc}}$, the surface of the adsorbents should be negatively charged, which may facilitate to adsorb cationic species. However, a decrease in adsorption efficacy was observed for both the adsorbents. This may be due to the formation of $\text{Hg}(\text{OH})_3^-$ complex with increasing concentration of hydroxyl ions in the solution,^{40,41} resulting in an electrostatic repulsion between the lone pair of nitrogen of amino groups with the negatively charged metal complexes and leading to the lowering of the Hg adsorption efficiency of the adsorbents.

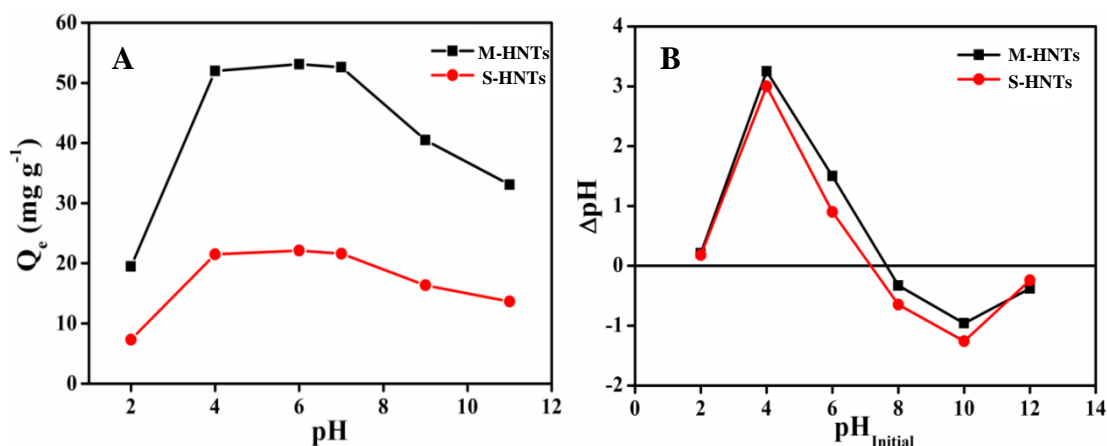
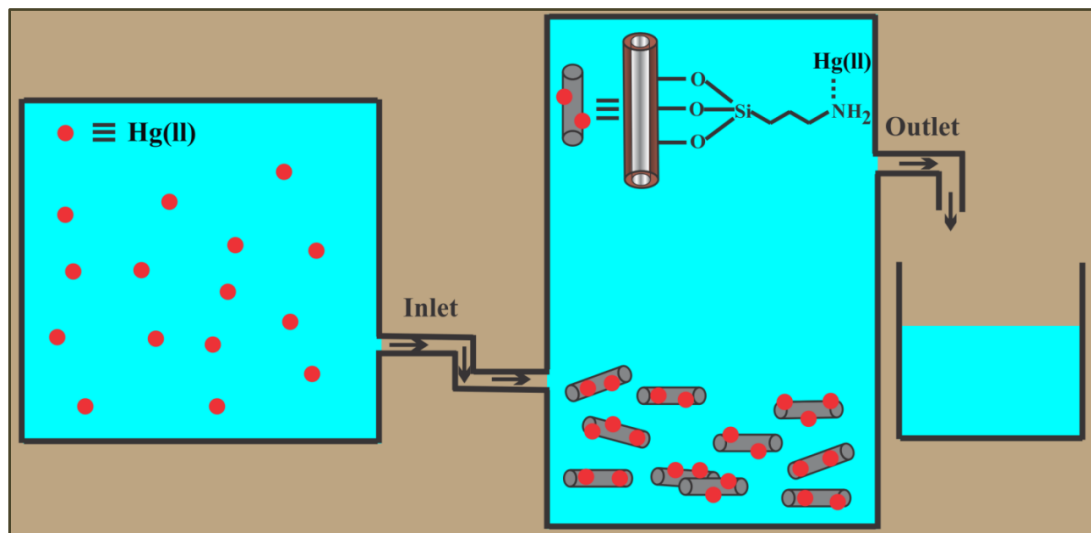


Figure 5.21: (A) Adsorption capacity of M-HNTs and S-HNTs estimated in the pH range 2-11, having concentration of Hg(II) solution 200 mg L^{-1} . (B) pH at zero point charge (pH_{zpc}) for M-HNTs and S-HNTs respectively.

Finally, we have compared Hg(II) uptake efficiency of M-HNTs with the reported amine based adsorbents (Table 5.5), illustrating significant adsorption efficacy of M-HNTs. Thus, exceptional sorption capacity together with easy synthetic route to achieve these nanocomposites may be an alternative pathway for developing prospective adsorbents to capture toxic metals present in drinking water (Scheme 5.4).

Table 5.5: Comparison of Hg(II) uptake efficiency of M-HNTs with the reported amine based adsorbents.

Adsorbents	Conc. of Hg(II) (mg L ⁻¹)	Adsorption Capacity (mg g ⁻¹)	References
P-C-CTS-(Hg)	50	12.5	42
MWCNT-AA	50	45.05	43
GO	100	16.7	44
MGO	100	59.9	44
Bent-NH ₂	100	39.0	45
NM 1	150	68.8	46
MIL-101-Thymine	200	51.75	47
MIL-101-NH ₂	200	30.67	47
M-HNTs	200	52.18	This work



Scheme 5.4: Schematic presentation of the sorption of Hg(II) ions by these clay based nanocomposites leaving behind clean water free from toxic metal ions.

5.4 Conclusions

In conclusion, we have fabricated three hybrid nanocomposites containing thiol or primary amine or secondary amine site to explore them as cost-effective sorbents for the removal of toxic heavy metal ions from the aqueous solution. Adsorption kinetics of Hg(II) ions follows pseudo-second-order rate equation as compared to pseudo-first-order model. The adsorption isotherms were well fitted with Langmuir isotherm model having high value of correlation coefficient compared to Freundlich isotherm model, confirming monolayer adsorption of the mercury ions on the surface of amine-functionalized clay nanomaterials. With increasing solution pH, the adsorption efficiency of these adsorbents for Hg(II) ion increased up to pH 7, followed by a gradual decrease in adsorption efficiency was noticed in alkaline pH in case of amine functionalized HNTs. Thermodynamic analysis indicates that Hg(II) ions adsorption by these adsorbents is highly favorable, spontaneous, and endothermic in nature at low temperature, further corroborated by theoretical study. All the adsorbents show excellent adsorption capacity even at low concentration and multi-cycle Hg(II) uptake capability. Owing to the outstanding adsorption efficiency and good recyclability, these nanocomposites may be explored as an adsorbent for industrial heavy metal contaminated wastewater treatment, which in turn may find application in the field of environmental remediation.

5.5 References

1. McNutt, M. Mercury and Health. *Science* **2013**, *341*, 1430.
2. Krabbenhoft, D. P.; Sunderland, E.M. Global Change and Mercury. *Science* **2013**, *341*, 1457-1458.
3. Boening, D.W. Ecological Effects, Transport, and Fate of Mercury: A General Review. *Chemosphere* **2000**, *40*, 1335-1351.
4. Aguado, J.; Arsuaga, J. M.; Arencibia, A.; Lindo, M.; Gascón, V. Aqueous Heavy Metals Removal by Adsorption on Amine-Functionalized Mesoporous Silica. *J. Hazard. Mater.* **2009**, *163*, 213-221.
5. Prabhu, V.; Lee, S.; Clack, H. L. Electrostatic Precipitation of Powdered Activated Carbon and Implications for Secondary Mercury Adsorption within Electrostatic Precipitators. *Energy Fuels* **2011**, *25*, 1010–1016.
6. Babel, S.; Kurniawan, T.A. Low-Cost Adsorbents for Heavy Metals Uptake from Contaminated Water: A Review. *J. Hazard. Mater.* **2003**, *97*, 219-243.

7. Oehmen, A.; Vergel, D.; Fradinho, J.; Reis, M. A. M.; Crespo, J. G.; Velizarov, S. Mercury Removal from Water Streams through the Ion Exchange Membrane Bioreactor Concept. *J. Hazard. Mater.* **2014**, *264*, 65-70.
8. Samanta, A.; Das, S.; Jana, S. Exploring b-FeOOH Nanorods as an Efficient Adsorbent for Arsenic and Organic Dyes. *ChemistrySelect* **2018**, *3*, 2467– 2473.
9. Benhamou, A.; Baudu, M.; Derriche, Z.; Basly, J. P. Aqueous Heavy Metals Removal on Amine-Functionalized Si-MCM-41 and Si-MCM-48. *J. Hazard. Mater.* **2009**, *171*, 1001–1008.
10. Morris, E.A.; Kirk, D.W.; Jia, C.Q.; Morita, K. Roles of Sulfuric Acid in Elemental Mercury Removal by Activated Carbon and Sulfur-Impregnated Activated Carbon. *Environ. Sci. Technol.* **2012**, *46*, 7905–7912.
11. Fischer, C.; Oschatz, M.; Nickel, W.; Leistenschneider, D.; Kaskel, S.; Brunner, E. Bioinspired Carbide-Derived Carbons with Hierarchical Pore Structure for the Adsorptive Removal of Mercury from Aqueous Solution. *Chem. Commun.* **2017**, *53*, 4845-4848.
12. Chandra, V.; Kim, K. S. Highly Selective Adsorption of Hg²⁺ by a Polypyrrole–Reduced Graphene Oxide Composite. *Chem. Commun.* **2011**, *47*, 3942– 3944.
13. Monier, M.; Nawar, N.; Abdel-Latif, D. A. Preparation and Characterization of Chelating Fibers Based on Natural Wool for Removal of Hg(II), Cu(II) and Co(II) Metal Ions from Aqueous Solutions. *J. Hazard. Mater.* **2010**, *184*, 118-125.
14. Monier, M.; Abdel-Latif, D. A. Modification and Characterization of PET Fibers for Fast Removal of Hg (II), Cu (II) and Co (II) Metal Ions from Aqueous Solutions. *J. Hazard. Mater.* **2013**, *250*, 122-130.
15. Miretzky, P.; Cirelli, A. F. Hg (II) Removal from Water by Chitosan and Chitosan Derivatives: A Review. *J. Hazard. Mater.* **2009**, *167*, 10-23.
16. Zhang, A.; Xiang, J.; Sun, L.; Hu, S.; Li, P.; Shi, J.; Fu, P.; Su, S. Preparation, Characterization, and Application of Modified Chitosan Sorbents for Elemental Mercury Removal. *Ind. Eng. Chem. Res.* **2009**, *48*, 4980–4989.
17. Hanif, Z.; Lee, S.; Qasim, G. H.; Ardiningsih, I.; Kim, J. A.; Seon, J.; Han, S.; Hong, S.; Yoon, M. H. Polypyrrole Multilayer-Laminated Cellulose for Large-Scale Repeatable Mercury Ion Removal. *J. Mater. Chem. A* **2016**, *4*, 12425-124334.
18. Zhou, Y.; Hu, X.; Zhang, M.; Zhuo, X.; Niu, J. Preparation and Characterization of Modified Cellulose for Adsorption of Cd (II), Hg (II), and Acid Fuchsin from Aqueous Solutions. *Ind. Eng. Chem. Res.* **2013**, *52*, 876-884.
19. Da'na, E. Adsorption of Heavy Metals on Functionalized-Mesoporous Silica: A Review. *Microporous Mesoporous. Mater.* **2017**, *247*, 145-157.
20. Yantasee, W.; Rutledge, R.D.; Chouyyok, W.; Sukwarotwat, V.; Orr, G.; Warner, C.L.; Warner, M.G.; Fryxell, G.E.; Wiacek, R.J.; Timchalk, C.; Addleman, R.S. Functionalized Nanoporous Silica for the Removal of Heavy Metals from Biological Systems: Adsorption and Application. *ACS Appl. Mater. Interfaces* **2010**, *2*, 2749–2758.
21. Liao, K. H.; Lin, Y. S.; Macosko, C. W.; Haynes, C. L. Cytotoxicity of Graphene Oxide and Graphene in Human Erythrocytes and Skin Fibroblasts. *ACS Appl. Mater. Interfaces* **2011**, *3*, 2607–2615.

22. Walcarius, A.; Mercier, L. Mesoporous Organosilica Adsorbents: Nanoengineered Materials for Removal of Organic and Inorganic Pollutants. *J. Mater. Chem.* **2010**, *20*, 4478–4511.
23. Das, S.; Maity, A.; Pradhan, M.; Jana, S. Assessing Atmospheric CO₂ Entrapped in Clay Nanotubes using Residual Gas Analyzer. *Anal. Chem.* **2016**, *88*, 2205–2211.
24. Yuan, P.; Southon, P. D.; Liu, Z.; Green, M. E. R.; Hook, J. M.; Antill, S. J.; Kepert, C. J. Functionalization of Halloysite Clay Nanotubes by Grafting with γ -Aminopropyltriethoxysilane. *J. Phys. Chem. C* **2008**, *112*, 15742–15751.
25. Yah, W. O.; Takahara, A.; Lvov, Y.M. Selective Modification of Halloysite Lumen with Octadecylphosphonic Acid: New Inorganic Tubular Micelle. *J. Am. Chem. Soc.* **2012**, *134*, 1853–1859.
26. Brindley, G. W. Order-Disorder in the Clay Mineral Structures. In *Crystal Structures of Clay Minerals and Their X-ray Identification*; Brindley, Mineralogist Society: London, **1980**.
27. Antochshuk, V.; Olkhovyk, O.; Jaroniec, M.; Shin, H. J.; Ryoo, R. Benzoylthiourea-Modified Mesoporous Silica for Mercury (II) Removal. *Langmuir* **2003**, *19*, 3031–3034.
28. Thomas, J. M.; Thomas, W. J. Introduction to the Principles of Heterogeneous Catalysis. *Academic Press*, **1967**.
29. Ho, Y. S.; McKay, G. The Sorption of Lead (II) Ions on Peat. *Water Res.* **1999**, *33*, 578–584.
30. Ho, Y.-S. Review of Second-Order Models for Adsorption Systems. *J. Hazard. Mater.* **2006**, *136*, 681–689.
31. J. E. Huheey, E. A. Keiter, R. L. Keiter, *Inorganic Chemistry: Principles of Structure and Reactivity*, 4th Ed, **2002**.
32. Jana, S.; Das, S. Development of Novel Inorganic–Organic Hybrid Nanocomposites as a Recyclable Adsorbent and Catalyst. *RSC Adv.* **2014**, *4*, 34435–34442.
33. Das, S.; Samanta, A.; Jana, S. Light-Assisted Synthesis of Hierarchical Flower-Like MnO₂ Nanocomposites with Solar Light Induced Enhanced Photocatalytic Activity. *ACS Sustainable Chem. Eng.* **2017**, *5*, 9086–9094.
34. Das, S.; Jana, S. A Facile Approach to Fabricate Halloysite/Metal Nanocomposites with Preformed and *In Situ* Synthesized Metal Nanoparticles: A Comparative Study of Their Enhanced Catalytic Activity. *Dalton Trans.* **2015**, *44*, 8906–8916.
35. Yuan, P.; Southon, P. D.; Liu, Z.; Green, M. E. R.; Hook, J. M.; Antill, S. J.; Kepert, C. J. Functionalization of Halloysite Clay Nanotubes by Grafting with γ -Aminopropyltriethoxysilane. *J. Phys. Chem. C* **2008**, *112*, 15742–15751.
36. Das, S.; Ghosh, C.; Jana, S. Moisture Induced Isotopic Carbon Dioxide Trapping from Ambient Air. *J. Mater. Chem. A* **2016**, *4*, 7632–7640.
37. Niu, Y.; Qu, R.; Sun, C.; Wang, C.; Chen, H.; Ji, C.; Zhang, Y.; Shao, X.; Bu, F. Adsorption of Pb (II) from Aqueous Solution by Silica-Gel Supported Hyperbranched Polyamidoamine Dendrimers. *J. Hazard. Mater.* **2013**, *244*, 276–286.
38. Song, X.; Niu, Y.; Qiu, Z.; Zhang, Z.; Zhou, Y.; Zhao, J.; Chen, H. Adsorption of Hg (II) and Ag (I) from Fuel Ethanol by Silica Gel Supported Sulfur-Containing

- PAMAM Dendrimers: Kinetics, Equilibrium and Thermodynamics. *Fuel* **2017**, *206*, 80-88.
39. Niu, Y.; Qu, R.; Chen, H.; Mu, L.; Liu, X.; Wang, T.; Zhang, Y.; Sun, C. Synthesis of Silica Gel Supported Salicylaldehyde Modified PAMAM Dendrimers for the Effective Removal of Hg (II) from Aqueous Solution. *J. Hazard. Mater.* **2014**, *278*, 267-278.
 40. Perry, R. H.; Green, D. *Perry's Chemical Engineering Handbook*, 6th Ed., McGraw-Hill, New York, **1984**.
 41. Kabiri, S.; Tran, D. N. H.; Azari, S.; Losic, D. Graphene-Diatom Silica Aerogels for Efficient Removal of Mercury Ions from Water. *ACS Appl. Mater. Interfaces* **2015**, *7*, 11815-11823.
 42. Tang, X.; Niu, D.; Bi, C.; Shen, B. Hg²⁺ Adsorption from a Low-Concentration Aqueous Solution on Chitosan Beads Modified by Combining Polyamination With Hg²⁺-Imprinted Technologies. *Ind. Eng. Chem. Res.* **2013**, *52*, 13120-13127.
 43. Deb, A. S.; Dwivedi, V.; Dasgupta, K.; Ali, S. M.; Shenoy, K. T.; Novel Amidoamine Functionalized Multi-Walled Carbon Nanotubes for Removal of Mercury (II) Ions from Wastewater: Combined Experimental and Density Functional Theoretical Approach. *Chem. Eng. J.* **2017**, *313*, 899-911.
 44. Guo, Y.; Deng, J.; Zhu, J.; Zhou, X.; Bai, R. Removal of Mercury (II) and Methylene Blue from a Wastewater Environment with Magnetic Graphene Oxide: Adsorption Kinetics, Isotherms and Mechanism. *RSC Adv.* **2016**, *6*, 82523-82536.
 45. Anirudhan, T. S.; Jalajamony, S.; Sreekumari, S. S. Adsorption of Heavy Metal Ions from Aqueous Solutions by Amine and Carboxylate Functionalised Bentonites. *Appl Clay Sci.* **2012**, *65*, 67-71.
 46. Zhu, Z.; Yang, X.; He, L. N.; Li, W. Adsorption of Hg²⁺ from Aqueous Solution on Functionalized MCM-41. *RSC Adv.* **2012**, *2*, 1088-1095.
 47. Luo, X.; Shen, T.; Ding, L.; Zhong, W.; Luo, J.; Luo, S.; Novel Thymine-Functionalized MIL-101 Prepared by Post-Synthesis and Enhanced Removal of Hg²⁺ from Water. *J. Hazard. Mater.* **2016**, *306*, 313-322.

Fabrication of Halloysite/Metal Nanocomposites with Preformed and *In-Situ* Synthesized Metal Nanoparticles: A Comparative Study of Their Enhanced Catalytic Activity

6.1 Introduction

The modern synthesis of the advanced functional materials with enhanced properties involves hybrid NCs, comprised of nanoscale inorganic materials and organic derivatives, where controlling the molecular structure at the atomic and macroscopic dimensions is a key aspect with a major effect on the performance. The quantum leap in hybrid NCs generally arises by reducing the domain size of the inorganic phase to several nanometers and generating huge interfacial areas, which introduces various covalent bonds or other compatibilization between the phases. Inorganic-organic hybrid NCs are astonishingly versatile and well known for their outstanding properties, such as high mechanical strength, thermal stability, high refractive index, low coefficient of thermal expansion etc.¹⁻⁴ These hybrid NCs can be synthesized from the diverse inorganic solids, like layered silicates clay, hydroxyapatite, silica, metal oxides, and a variety of biopolymers, e.g.; polysaccharides, polypeptides, proteins, nucleic acids and so on.⁵⁻⁸ The synthetic approach includes the structural templating of the inorganic component typically via self-assembly, preparation and surface modification of nanoscale inorganic particles, and use of nanometer-sized containers for synthesis.⁹⁻¹¹ They are of particular interest in advanced catalysis, controlled drug delivery, food processing, water purification, optics, electronics, mechanics, and sensors.¹²⁻¹⁵ Development of halloysite based inorganic-organic hybrid NCs opened up a new direction for the fabrication of novel materials and compound which will be explored as anti-corrosion agents, biocides, nanoreactor to host reactants for nanosynthesis and biomimetic synthesis. Halloysite nanotubes (HNTs) is a naturally occurring two-layered aluminosilicate clay ($\text{Al}_2\text{Si}_2\text{O}_5(\text{OH})_4 \cdot n\text{H}_2\text{O}$) with a hollow tubular structure, formed by the surface

weathering of aluminosilicate minerals, having constituent elements of aluminium, silicon, and oxygen. The adjacent alumina and silica layers with their water of hydration, result in a packing disorder and make the nanotubes to curve and roll up to form multilayers.^{16,17} Formation of hollow tube is impelled by the mismatch in the periodicity between the oxygen sharing tetrahedral SiO₂ sheets and the adjacent octahedral AlO₆ sheets which also determine the inner positive and outer negative surface charges of the HNTs.^{18,19} Thus, they possess different inner/outer surface chemistry which helps to manipulate the chemico-physical properties of these naturally available clay nanotubes through the control of the chemistry of the constituent elements as well as their morphology. Since hydrophilic surface of HNTs sometimes restricts their widespread applications in different fields, modification of the outer surfaces of these nanotubes with some organosilanes demonstrates improved dispersal of clay materials as well as enhances their physical, mechanical, and chemical properties. Furthermore, functionalization of HNTs by these organosilanes facilitates to immobilize metal nanoparticles (NPs) over the surface where HNTs behave as a solid support and organosilane acts as linker molecule and thus lead to the easy formation of HNTs/metal NCs.

Metallic nanoparticles have become the focus of basic research in modern nanoscience because of their unique properties which allows their efficient use in catalysis, photonics, electronics, and information storage.²⁰⁻²³ Their properties and activity can be highly affected and reduced once they started agglomeration which tends to be bulk like materials. To prevent agglomeration and achieve well dispersed particles, we can either immobilized these NPs on solid supports or synthesize them directly over the supports.^{12,24-28} However, a number of fundamental studies have been performed based on the supported noble metal NPs catalysts due to their high catalytic activity under mild condition, such as CO oxidation, hydrocarbon combustion, selective oxidation and hydrogenation, and water gas shift reaction.²⁸⁻³⁴ Halloysite nanoclay, a cheap and an abundant natural resource, provides an alternative solid support for the immobilization of metal NPs to be utilized as a heterogeneous catalyst which subsequently gets separated from the reaction mixture at the end of the reaction and the use of HNTs as catalyst support is still very few.

The primary objectives of our present study are to fabricate HNTs/metal NCs, probe the formation of the NCs, and then evaluate and compare their catalytic activity. HNTs/metal NCs were synthesized based on the immobilization of metal precursors over the surface of aminosilane modified HNTs followed by the reduction of the metal precursors to achieve NPs and the other approach involved direct immobilization of previously prepared metal NPs over HNTs surfaces. Exploiting these two approaches, HNTs/Au and HNTs/Ag NCs have successfully been synthesized and were authenticated by different physical methods. The spherical morphology of preformed Au and Ag NPs remained intact even after immobilization. The catalytic efficiency of all NCs has been demonstrated for the reduction of 4-nitrophenol by sodium borohydride and compared with the reported heterogeneous catalysts. We have estimated activation energy and entropy of activation for this reduction reaction. A detailed kinetic study represents that *in-situ* synthesized HNTs/Ag NCs are catalytically more active amongst the four NCs, although their catalytic efficiency is almost comparable and all these catalysts can be reused and recycled repetitively for this reduction reaction.

6.2 Experimental Section

6.2.1 Synthesis of Aminosilane Modified Halloysite Nanotubes

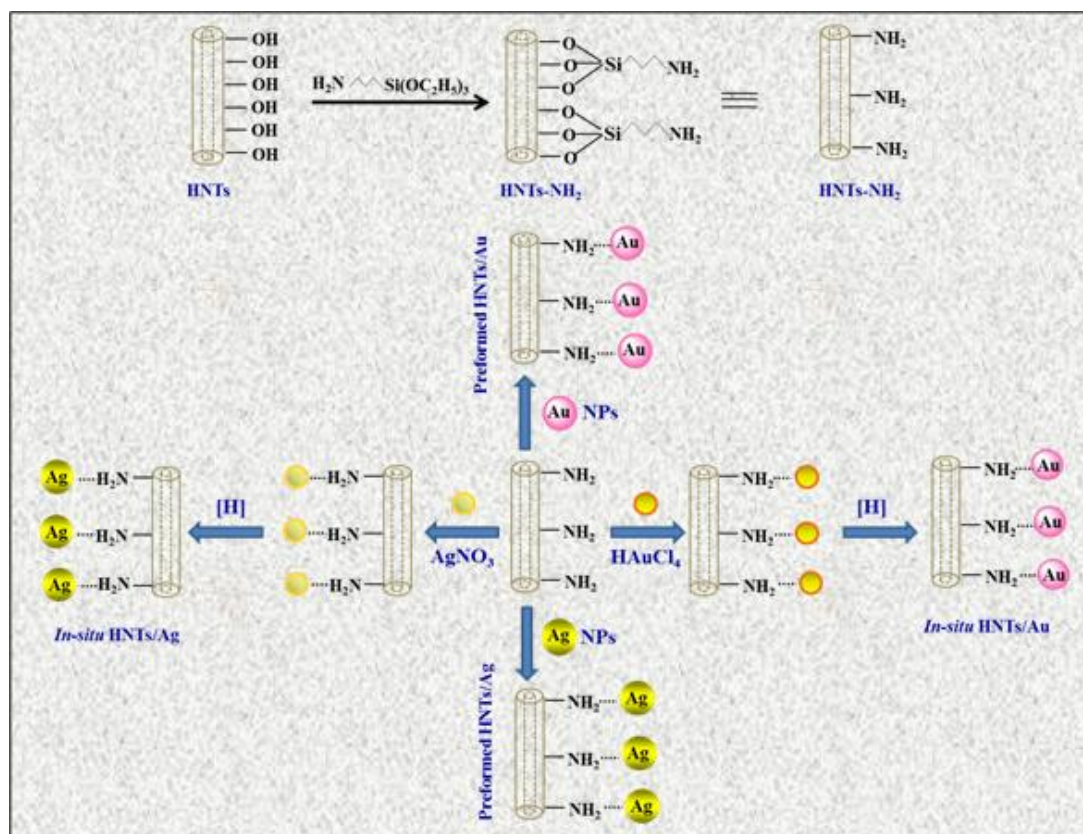
For surface modification of HNTs, a three-necked round bottom flask containing 2.0 g of HNTs and 20 mL of toluene, was fitted with a condenser, rubber septum, thermocouple adaptor, and quartz sheath in which a thermocouple was inserted. At 60 °C, 2.5 mL of (3-aminopropyl) triethoxysilane was injected to the flask which was heated with a heating mantle and the reaction solution was refluxed at 120 °C for 12 h. Afterwards the product was washed with toluene and ethanol respectively and dried at 100 °C under vacuum. The aminosilane modified HNTs were represented as HNTs-NH₂.

6.2.2 Fabrication of HNTs/Metal NCs with Preformed Metal Nanoparticles

First, metal NPs were synthesized based on the thermal decomposition of a metal salt in a hot organoamine solvent.³⁵ All the reactions were carried out under a nitrogen atmosphere using standard air-free techniques. Gold(III) chloride trihydrate (0.12 mmol) was dissolved in a mixture of oleylamine (12 mM) and 1-octadecene (22mM) in a flask which was fitted with a condenser, rubber septum, thermo-couple adaptor, and quartz sheath in which a thermocouple was inserted. The reaction flask was heated with a heating mantle to 120 °C and aged for 30 min. Consequently, colour of the solution changed from yellow to orange to pink indicating the formation of Au NPs. In a similar way, Ag NPs were synthesized from silver nitrate (0.12 mmol). Once the flask cooled down to room temperature, particles were collected by centrifugation after the addition of acetone-hexane (3:1) mixture and were redispersed in toluene and used as a stock solution for the immobilization over HNTs-NH₂. HNTs/metal nanocomposites were synthesized based on the immobilization of preformed metal NPs over the surface of silane modified HNTs. First, 0.5 g of HNTs-NH₂ was added to a beaker containing the previously synthesized Au NPs (6 mL) and stirred for 1 h to complete the immobilization of Au NPs onto the surface of HNTs-NH₂. A gradual fading of the intense pink colour of Au NPs solution to almost colourless while HNTs-NH₂ themselves turned pink, illustrated complete immobilization of Au NPs. Once the HNTs-NH₂ doesn't uptake additional Au NPs solution, the product was washed several times with toluene. Likewise, HNTs-NH₂ turned to yellow after the fabrication with Ag NPs, leaving behind a colourless supernatant solution. After the immobilization of Au and Ag NPs over HNTs-NH₂, the synthesized NCs are denoted as preformed HNTs/Au and HNTs/Ag respectively (Scheme 6.1).

6.2.3 Fabrication of HNTs/Metal NCs with *In-Situ* Synthesized Metal Nanoparticles

Alternatively, HNTs/metal nanocomposites were also synthesized based on the immobilization of metal precursors over the surface of HNTs-NH₂ followed by



Scheme 6.1: Schematic presentation of the surface modification of halloysite nanotubes using (3-aminopropyl) triethoxysilane, subsequently fabrication of Au and Ag NPs decorated HNTs i.e.; HNTs/Au and HNTs/Ag nanocomposites which were achieved through the immobilization of (1) corresponding metal precursors followed by *in-situ* reduction and (2) previously synthesized metal NPs, over the surface of aminosilane modified HNTs.

the reduction with ice cold aqueous solution of sodium borohydride. A beaker containing HAuCl₄ (6 mL, 10⁻² M) and HNTs-NH₂ (0.5 g) was stirred on a magnetic stirrer for 6 h which in turn results a fading of the yellow colour of the solution, indicating immobilization of HAuCl₄ onto the surface of HNTs-NH₂. Once the HNTs-NH₂ get saturated with HAuCl₄, the product was washed several times with Mili-Q H₂O to remove the unadsorbed HAuCl₄ if any and reduced with ice cold aqueous solution of NaBH₄ to achieve *in-situ* HNTs/Au NCs. Similarly, HNTs/Ag NC was synthesized using AgNO₃ as a precursor, followed by the reduction with aqueous solution of NaBH₄ (Scheme 6.1). The

catalytic activity of these nanocomposites has been studied taking the reduction of 4-nitrophenol (4-NP) to 4-aminophenol (4-AP) as a model reaction.

6.2.4 Catalytic Reaction

Catalytic activity of these four NCs has been studied for the reduction of 4-NP to 4-AP. In a standard quartz cuvette of 1 cm path length, 2.0 mg of HNTs/metal nanocomposites was taken along with 2.7 mL of aqueous solution of 4-NP (0.1 mM). Aqueous solution NaBH₄ (0.3 mL of 0.1M) was added to the reaction mixture and the time dependent absorption spectra were recorded at room temperature using a UV-Visible spectrophotometer.

6.3 Results and Discussion

The different inner/outer surface chemistry of the clay nanotubes facilitates to manipulate the chemico-physical properties of HNTs through the control of the chemistry of their constituent elements. Hence, selective modification of the outer surface of HNTs has been performed through the grafting of an aminosilane which has been characterized by various physical methods.

6.3.1 Characterization of HNTs-NH₂

6.3.1.1 FESEM and TEM Study

Field emission scanning electron microscopy (FESEM) and transmission electron microscopy (TEM) images of HNTs before and after surface modification with APTES are presented in Figure 6.1. Transmission electron microscopy (TEM) images of HNTs before and after surface modification represents the cylindrical shaped tube composed of multilayer walls with an open-ended lumen, having defects on the outer surface of HNTs which are presumably due to the mechanical damage or by

crystallographic defects. HNTs composed of cylindrical shaped tubes with a typical length between 1.0 and 1.5 μm , having outer diameter of 50-100 nm and inner diameter of 15-20 nm. However, surface functionalization of HNTs doesn't alter their morphology or size.

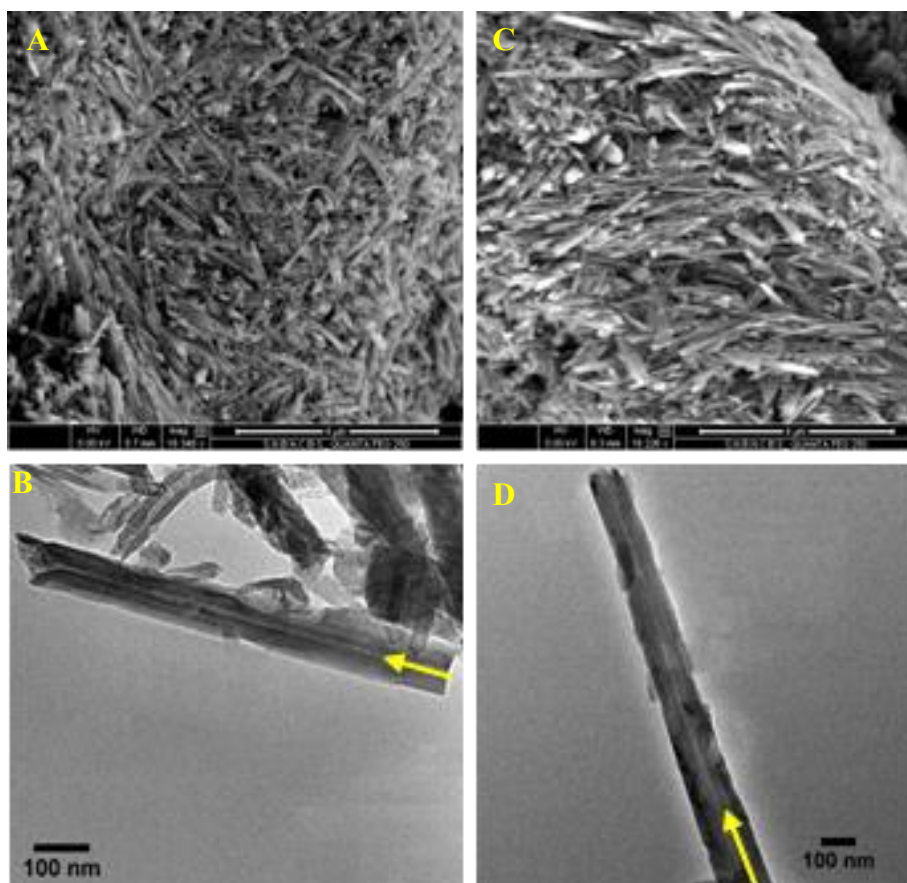


Figure 6.1: FESEM and TEM images of HNTs (A & B) before and (C & D) after surface modification with an aminosilane, HNTs-NH₂.

6.3.1.2 EDX Study

Compositional analysis by Energy dispersive X-ray analysis (EDX) indicates the presence of aminosilane after the surface modification of HNTs as they contain carbon and nitrogen along with the three main constituents of HNTs; oxygen, aluminium, and silicon (Figure 6.2).

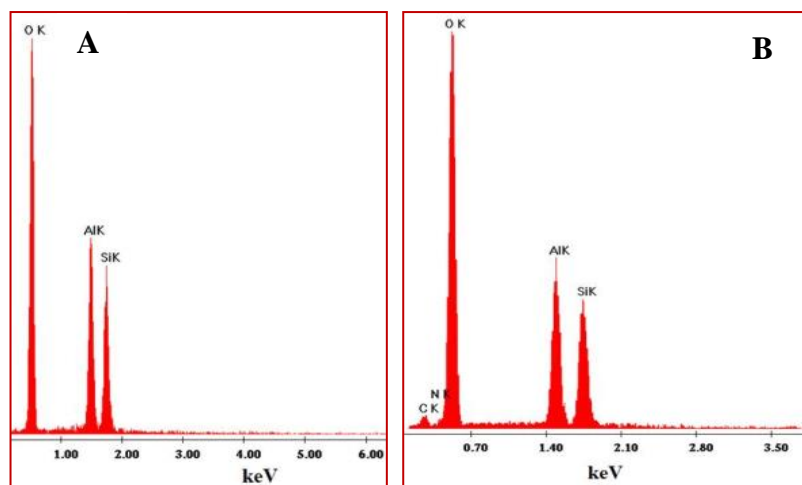


Figure 6.2: EDX spectra of (A) HNTs and (B) HNTs-NH₂.

6.3.1.3 CHN Elemental Analysis

CHN elemental analysis was carried after the functionalization of HNTs with APTES. The result demonstrates the immobilization of 0.39 mmol amino groups per gram of HNTs-NH₂.

6.3.1.4 FTIR Study

Fourier transform infrared (FTIR) spectroscopy ascertains the grafting of (3-aminopropyl) triethoxysilane (APTES) over the surface of HNTs. FTIR spectra of HNTs and HNTs-NH₂ shown in Figure 6.3, indicate two characteristic bands at 3621 and 3697 cm⁻¹ which can be attributed to the stretching vibrations of inner hydroxyl group and inner surface hydroxyl group respectively.³⁶ All these peaks further demonstrate the unaltered basic structure of HNTs even after surface modification though some new peaks are observed in HNTs-NH₂. Grafting of APTES over the surface of HNTs was confirmed due to the presence of new peaks at 2932 and 3453 cm⁻¹ for the stretching vibration of C-H and N-H and at 1562 cm⁻¹ for the N-H deformation.

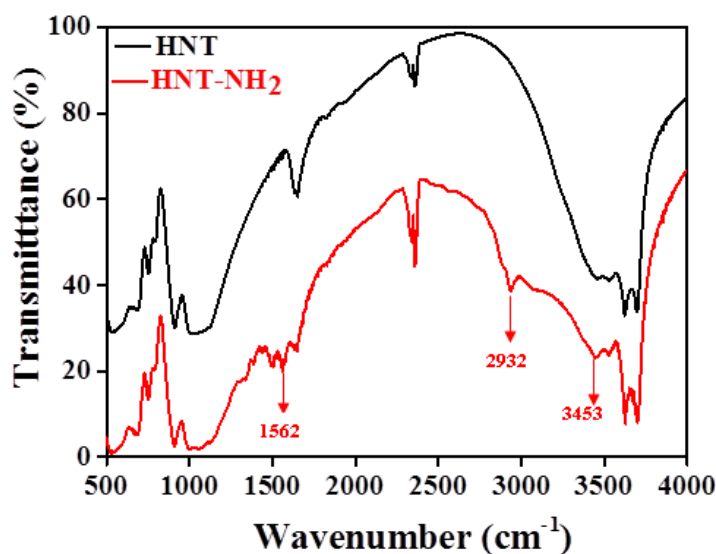


Figure 6.3: FTIR spectra of HNTs and HNTs-NH₂ respectively.

6.3.1.5 XRD Study

Figure 6.4 represents the diffraction pattern of HNT-NH₂ which is similar to that of bare HNTs. The observed (020) reflection is the characteristic of tubular halloysite clay in both bare HNTs and HNTs-NH₂.³⁷ There is no intercalation of APTES into the interlayer of HNTs, as (001) reflection does not shift to the lower angles. This further assures that most of the hydroxyl groups are embedded and unavailable for grafting because of the multi-layer structure of HNTs.

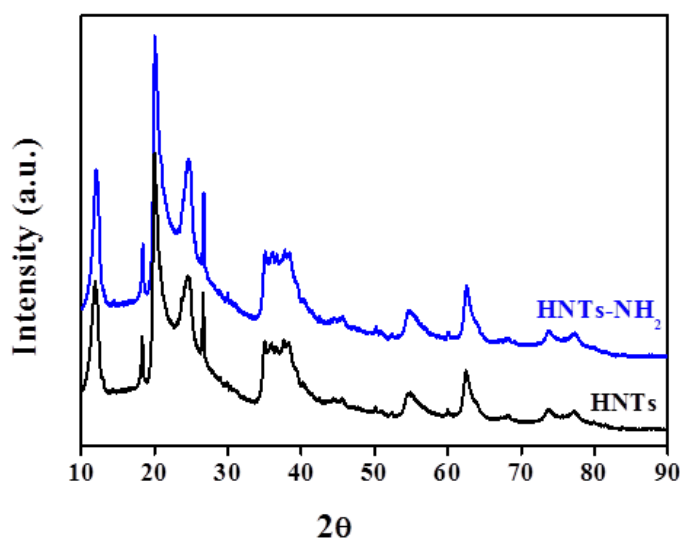


Figure 6.4: XRD patterns of HNTs and HNTs-NH₂ respectively.

6.3.2 Characterization of the HNTs/Metal NCs

The process of fabricating HNTs/metal NCs was elucidated in Scheme 6.1. After the surface modification of HNTs using APTES, HNTs/metal NCs were synthesized through the immobilization of both preformed and *in-situ* synthesized metal NPs over the surface of the clay nanotubes where the aminosilane behaves as a linker molecule and strengthen the interfacial adhesion of NPs over HNTs.

6.3.2.1 FTIR Study

FTIR analysis further demonstrates the immobilization of metal NPs over the surface of HNTs-NH₂. After the immobilization of Ag NPs, the intensity of the peak at 1562 cm⁻¹ for N-H deformation in HNTs-NH₂ has been decreased and shifted to 1555 cm⁻¹ (Figure 6.5), which further demonstrated that the aminosilane behaves as a linker molecule and strengthen the interfacial adhesion of NPs over HNTs surfaces.

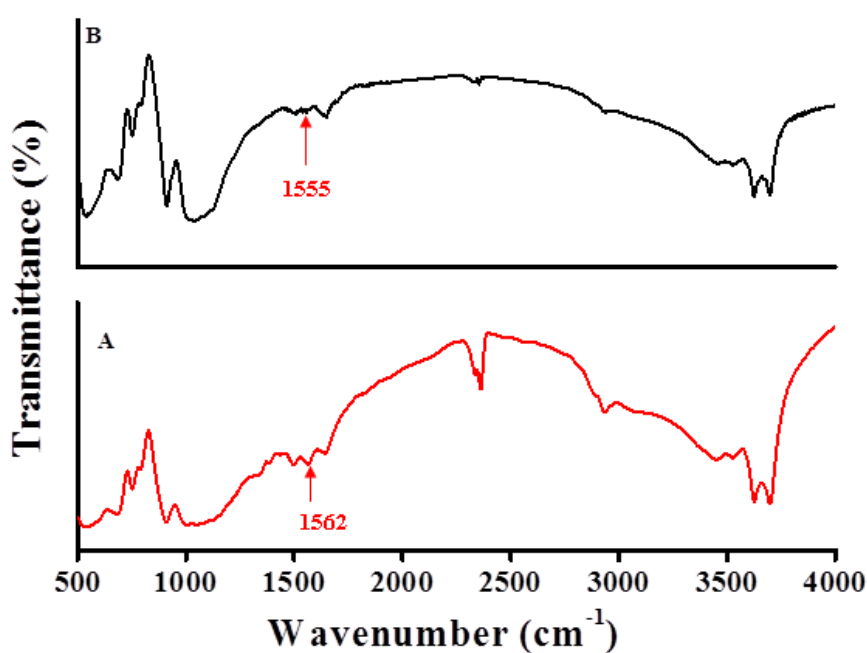


Figure 6.5: FTIR spectra of (A) HNTs-NH₂ and (B) HNTs/Ag NCs, synthesized after immobilization of Ag NPs over the surface of HNTs-NH₂.

6.3.2.2 XRD Analysis

A comparison between the XRD patterns of HNTs and HNTs/Au or HNTs/Ag (Figure 6.6A) establishes the presence of newly emerged peaks of (111) and (200) planes for face centered cubic (fcc) Au or Ag,³⁸ which further corroborate the loading of preformed Au and Ag NPs respectively, on the surface of amine modified HNTs. XRD patterns again determine fcc structure of the loaded Au or Ag NPs (Figure 6.6B) in case of *in-situ* synthesized HNTs/Ag and HNTs/Au NCs.

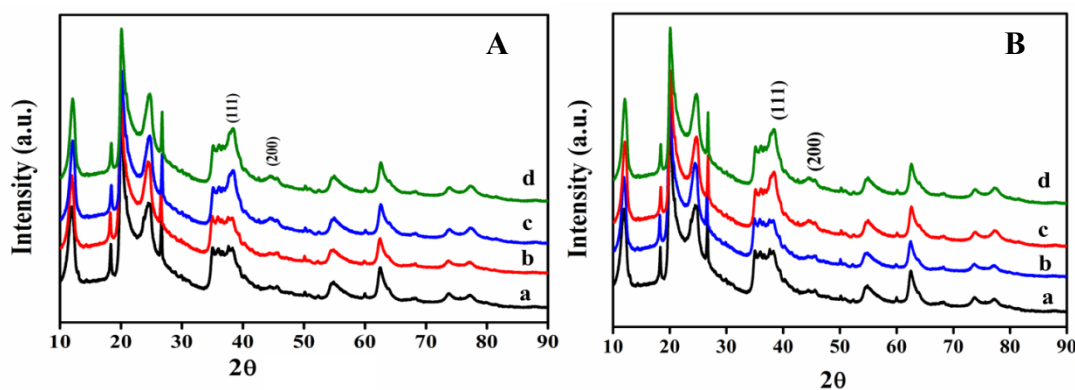


Figure 6.6: (A) XRD patterns of (a) HNTs, (b) HNTs-NH₂ and HNTs/metal NCs synthesized with preformed (c) Ag and (d) Au NPs. (B) XRD patterns of (a) HNTs and (b) HNTs-NH₂ and *in-situ* synthesized (c) HNTs/Ag and (d) HNTs/Au NCs.

6.3.2.3 UV-Visible and TEM Analyses

Based on the thermal decomposition of the metal salt in a hot organoamine solvent, we have synthesized Au and Ag NPs from their respective metal precursors. UV-Visible absorption spectra of colloidal Au and Ag nanoparticles before immobilization over the surface of HNTs-NH₂ are presented Figure 6.7A. The TEM image of Au NPs, shown in Figure 6.7B, demonstrates nearly monodispersed spherical morphology with an average particle size of 9 ± 0.5 nm. Figure 6.6C-E represents TEM images of preformed HNTs/Au at

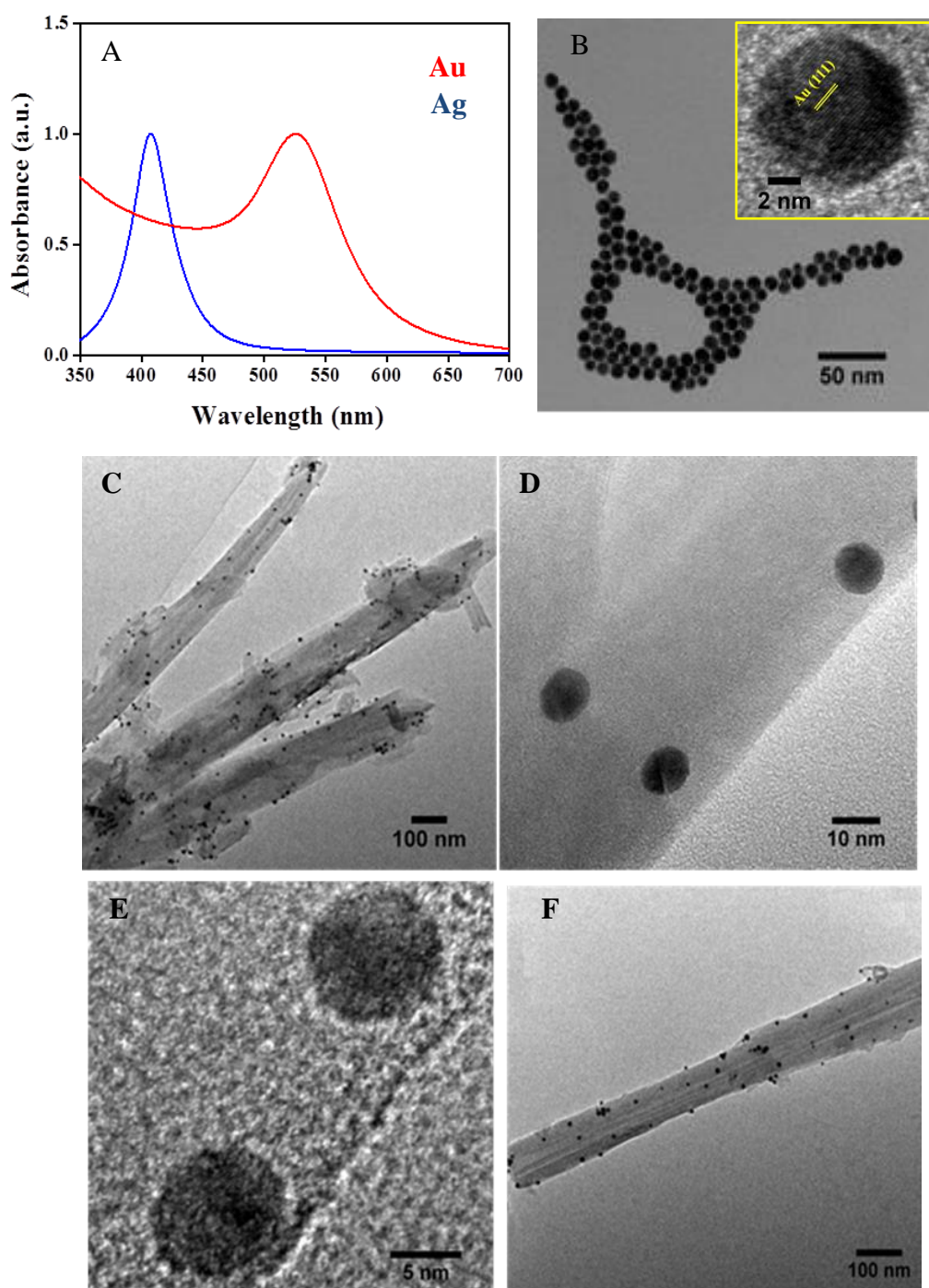


Figure 6.7: (A) UV-Visible absorption spectra of colloidal Au and Ag nanoparticles before immobilization over the surface of aminosilane modified HNTs (HNTs-NH₂). TEM images of (B) Au nanoparticles before and (C-E) after immobilization on the surface of aminosilane modified HNTs (HNTs/Au NCs) at different magnifications. HRTEM image of single Au, demonstrating (111) planes of the fcc Au (Inset of Figure B). (F) TEM image of HNTs/Ag NCs prepared with preformed Ag NPs.

different magnifications, indicating the immobilization of well-dispersed Au NPs over the surface of HNTs-NH₂ with no change in their size, shape, and morphology. TEM image of preformed HNTs/Ag shown in Figure 6.7F, also exhibits well-distribution of Ag NPs (8.5 ± 0.5 nm) over HNTs-NH₂ without any agglomeration.

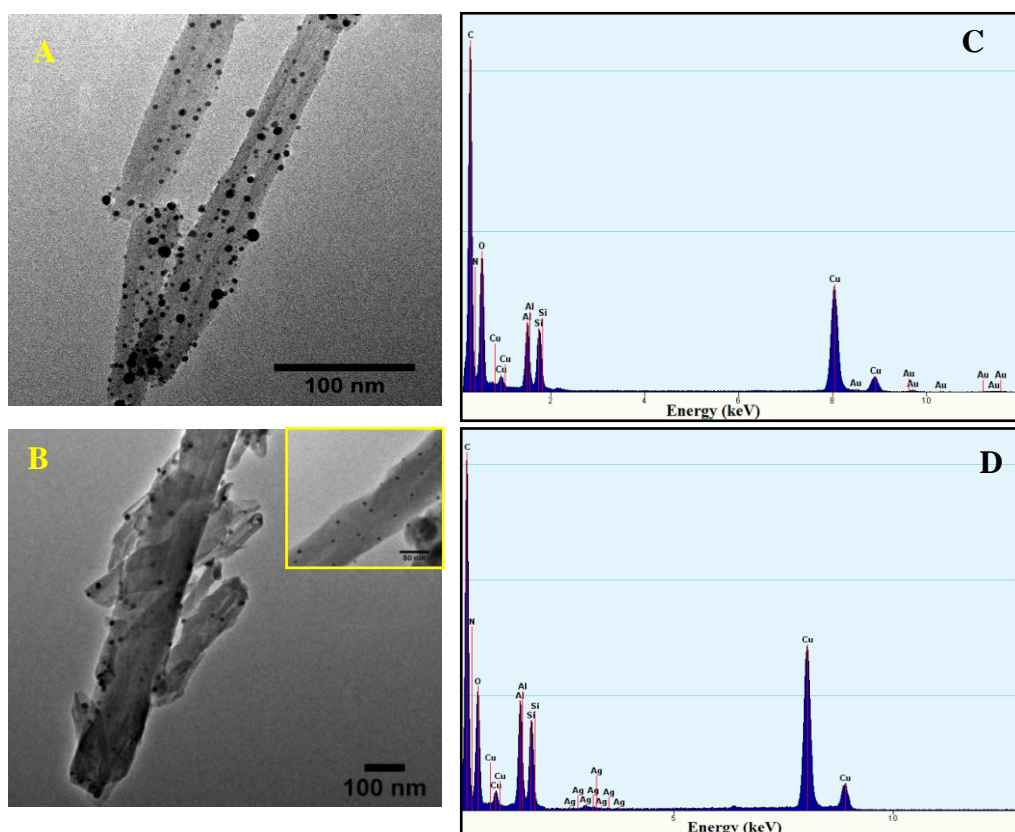


Figure 6.8: TEM images of *in-situ* synthesized (A) HNT/Au and (B) HNT/Ag NCs and (C, D) their corresponding EDX spectra, demonstrating the presence of Au and Ag in HNT/Au and HNT/Ag NCs respectively.

In contrast to the fabrication of HNTs/metal NCs with preformed Au and Ag NPs, another synthetic strategy involved immobilization of their metal precursors over the surface of HNTs and then subsequent reduction to the corresponding metal NPs. In this approach, Au and Ag NPs were directly grown on the outer surface of HNTs-NH₂ to achieve HNTs/Au and HNTs/Ag NCs. After the addition and subsequent immobilization of HAuCl₄ or AgNO₃

on the surface of HNTs-NH₂, the adsorbed ions were reduced using aqueous solution of NaBH₄ which results in the formation of HNTs/Au and HNTs/Ag NCs respectively. The morphology and chemical composition of these *in-situ* synthesized NCs have also been characterized with the help of TEM and EDX analysis (Figure 6.8). EDX analysis again demonstrates the *in-situ* formation of HNTs/Au and HNTs/Ag NCs. All the NPs are entirely immobilized and well dispersed over the surface of HNTs having particle sizes 9.0 ± 1.5 for Au and 9.0 ± 1.0 for Ag NPs respectively.

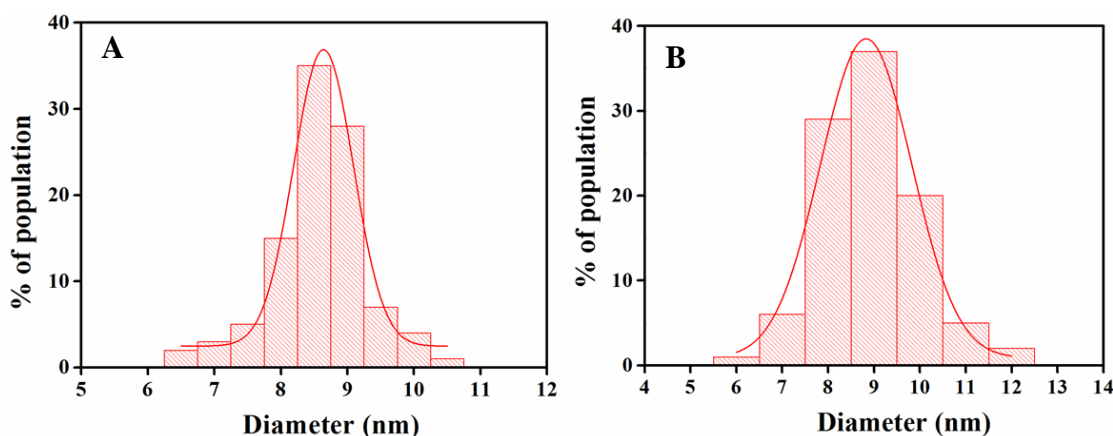


Figure 6.9: Histograms of particle size distribution of Ag NPs immobilized in (A) preformed and (B) *in-situ* synthesized HNTs/Ag NCs.

Therefore, our both the synthetic routes (preformed and *in-situ*) helps to synthesize almost monodispersed spherical Au and Ag NPs with precise control over particle growth and morphology and are well distributed on the HNTs-NH₂ surfaces (Figure 6.9). In our preformed HNTs/metal NCs, all the embedded NPs retain their size, shape, and morphology even after the immobilization. Thus, we have developed two different synthetic approaches to fabricate HNTs/metal NCs through the immobilization of preformed NPs as well as direct *in-situ* reduction with subsequent growth of the metal NPs over the surface modified HNTs, which in turn produce the heterogeneous catalysts.

6.3.3 Catalytic Activity of the HNTs/Metal Nanocomposites

6.3.3.1 Catalytic Activity Study

Owing to the high surface-to-volume ratio, a potential application of metal nanoparticle is to catalyze certain reactions which would not be feasible otherwise. To evaluate and compare the catalytic activity of these NCs we have considered reduction of 4-nitrophenol (4-NP) by sodium borohydride (NaBH_4) as a model reaction. The reaction kinetics could be monitored using UV-Visible spectroscopy as colour changes involved during the course of this reaction. An aqueous solution of 4-NP has a strong absorption (λ_{max}) at 317 nm under a neutral or acidic condition. After immediate addition of freshly prepared ice-cold aqueous solution of NaBH_4 , the absorption peak was red shifted to 400 nm owing to the formation of 4-nitrophenolate ions as the alkalinity of the solution increased. In absence of any catalyst, though the reduction of 4-NP by NaBH_4 (E^0 for 4-NP/4-AP = -0.76 V and $\text{H}_3\text{BO}_3/\text{BH}_4^- = -1.33\text{V}$ vs. NHE) is thermodynamically feasible but kinetically restricted. Thus, absorption intensity at 400 nm remained unaltered even for a couple of days without any fading and ultimate bleaching of the yellow colour, as well as the intensity of the absorption peak at 400 nm gradually decreased and a new absorption peak at ~300 nm appeared for 4-aminophenol (4-AP) which steadily increased in intensity as the reaction proceeded.^{39,40} Time-dependent UV-Visible absorption spectra of 4-NP reduction reaction as a function of time in presence of *in-situ* and preformed synthesized HNTs/Ag NCs have been demonstrated in Figure 6.10A & B. Two isosbestic points at 280 and 315 nm are observed in the UV-Visible spectra, suggesting the precise conversion of 4-NP to 4-AP without any side reaction.^{40,41} Sometimes the small bubbles of H_2 gas evolved from NaBH_4 during the reaction would retard the optical measurement and might lead to a shift of the UV-Visible spectra, resulting in the loss of the isosbestic points.

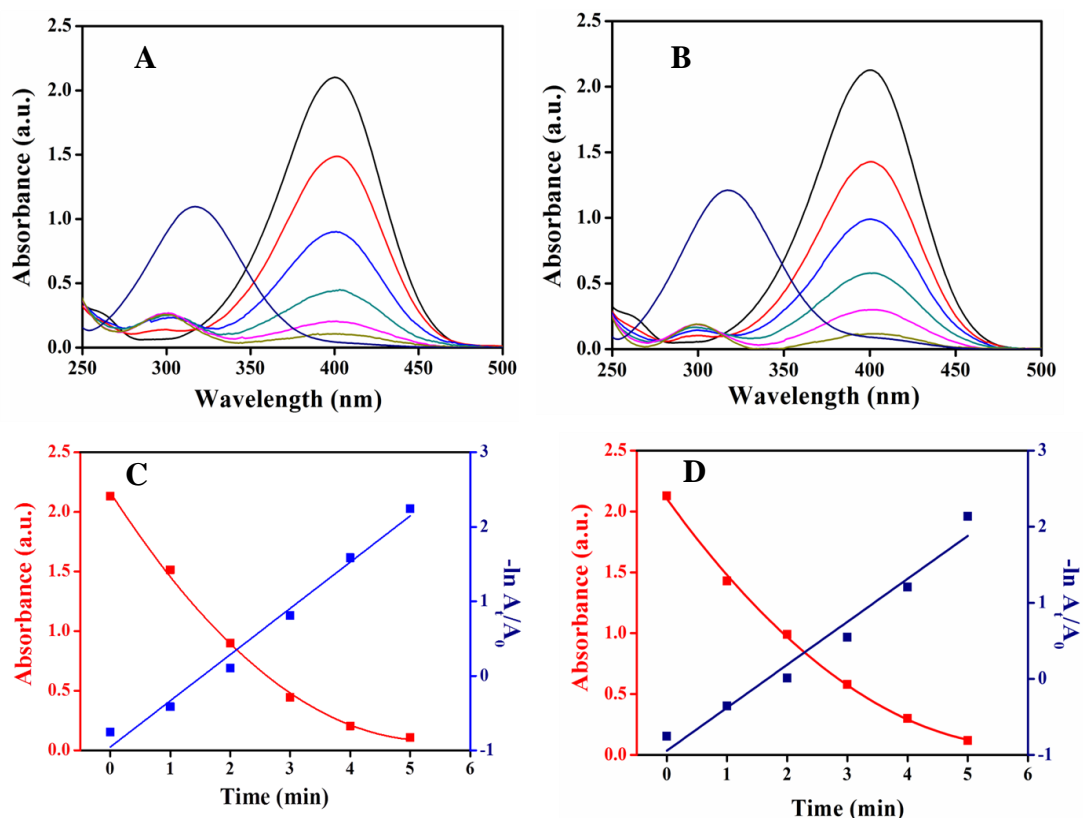


Figure 6.10: UV–Visible spectra for the successive reduction of 0.1 mM 4-NP using 0.1 M NaBH₄, catalyzed by 2.0 mg of (A) *in-situ* synthesized HNTs/Ag and (B) preformed HNTs/Ag NCs at an interval of 1 min and corresponding plot of (C) and (D) absorbance and $\ln A_t/A_0$ against the reaction time for pseudo-first-order kinetics of 4-NP.

In the present study, the concentration of the reductant, borohydride ion largely exceeds to that of 4-NP. For all the experiments, concentration of 4-NP and NaBH₄ were maintained to 0.1 and 10 mM respectively. Once we added NaBH₄ into the reaction solution, the metal particles embedded over HNTs started the catalytic reduction by relaying electrons from the donor BH₄⁻ to the acceptor 4-NP only after the adsorption of both onto the particle surfaces. The evolved H₂ from BH₄⁻ purged out air and prevented the aerial oxidation of 4-AP. Furthermore, evolution of gas bubbles of H₂ surrounding the catalyst particles helped in stirring the solution which facilitated to disperse the catalyst particles in the reaction mixture for a smooth reaction to occur throughout the reduction process. As the initial concentration of NaBH₄ was very high, it remained constant throughout the reaction. Hence, we have used pseudo-first-

order kinetics with respect to 4-NP to determine the average catalytic rate constant (k) of this reaction. The reaction conversion was estimated from the ratio of the concentration C_t/C_0 , which was proportional to the relative intensity of the UV-Vis absorbance (A_t/A_0) at 400 nm. Here, C_t and C_0 are the concentrations of 4-NP at reaction time t and the initial stage; A_t and A_0 are the corresponding absorbance at 400 nm respectively. As shown in Figure 6.10C & D, the linear correlation between $\ln(A_t/A_0)$ and reaction time (t) was confirmed through pseudo-first-order kinetics.

6.3.3.2 Catalytic Efficiency of Preformed and *In-situ* Synthesized Catalysts

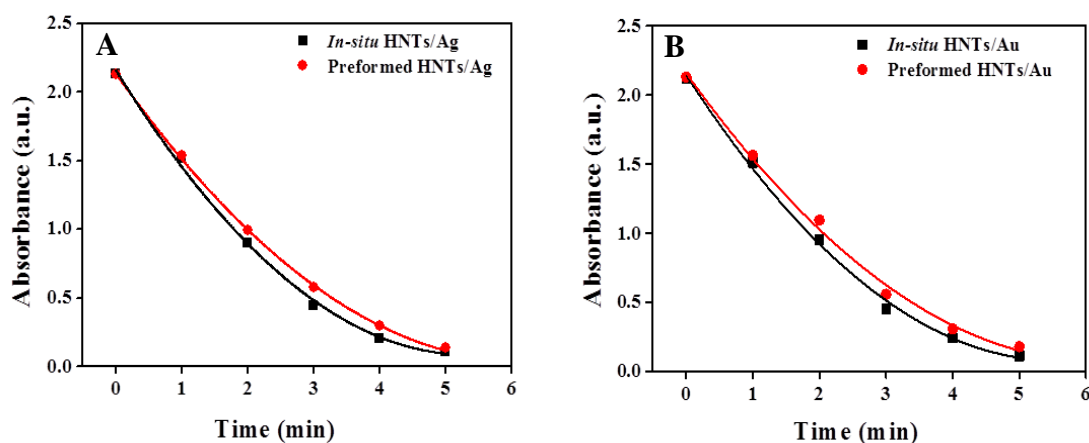


Figure 6.11: Plot of absorbance as a function of reaction time for 2.0 mg preformed and *in situ* synthesized (A) HNTs/Ag and (B) HNTs/Au NCs respectively, to compare their catalytic activity.

Figure 6.11A & B demonstrate the absorbance versus time plot for preformed and *in-situ* synthesized HNTs/Ag NCs and HNTs/Au NCs catalysts respectively. The catalytic rate constant k , which determines the reaction rate for 4-NP reduction, was obtained from the linear plot of $\ln(A_t/A_0)$ against reaction time (t) for all NCs catalysts. As shown in Table 6.1, the catalytic rate constant k for *in-situ* synthesized HNTs/Ag NCs (0.62 min^{-1}) is significantly higher among the four NCs catalysts, having the lowest value of k for

performed HNTs/Au NCs. It should be pointed out that we didn't observe any induction time for this reduction reaction upon the addition of any NCs catalysts at room temperature. At lower temperature, regardless of the NCs catalysts, there is an induction time i.e.; a certain period of time required to proceed the reduction reaction.

Table 6.1: Summary of the particle size, rate constant (k), activation energy (E_a), pre-exponential factor (A), and entropy of activation (ΔS) for four different nanocomposites.

Nanocomposites	Particle Size (nm)	First-Order Rate Constant (k, min^{-1})	E_a (kJmol^{-1})	A (min^{-1})	ΔS ($\text{Jmol}^{-1}\text{K}^{-1}$)
<i>In-situ</i> HNTs/Ag	9.0 ± 1	0.62033	22.7	6.3×10^3	72.75
<i>In-situ</i> HNTs/Au	9.0 ± 1.5	0.57049	27.3	3.8×10^4	87.63
Preformed HNTs/Ag	8.5 ± 0.5	0.5649	28.1	5.8×10^4	91.12
Preformed HNTs/Au	9.0 ± 0.5	0.53765	29.8	1.2×10^5	97.27

6.3.3.3 Activation Energy of the Reaction

To estimate the apparent activation energy of this reaction, we have carried out the reaction at four different temperatures and evaluated the corresponding k which increases with increase in temperature, signifying the dependency of this reduction reaction on temperature. Based on the linear correlation between $\ln k$ and the reciprocal of T and following the Arrhenius equation: $\ln k = \ln A - E_a/RT$, we have measured the apparent activation energy (E_a) from the slope and the pre-exponential factor (A) from the intercept. Figure 6.12 represents the Arrhenius plot for all the catalysts as well as plot of pre-exponential factors against activation energy of this reaction. The activation energy of the *in situ*

synthesized HNTs/Ag was estimated to be 23 kJ/mol, which is lower compared to preformed HNTs/Ag (28 kJ/mol) or HNTs/Au (30 kJ/mol) and even than that of *in situ* synthesized HNTs/Au NCs (27 kJ/mol).

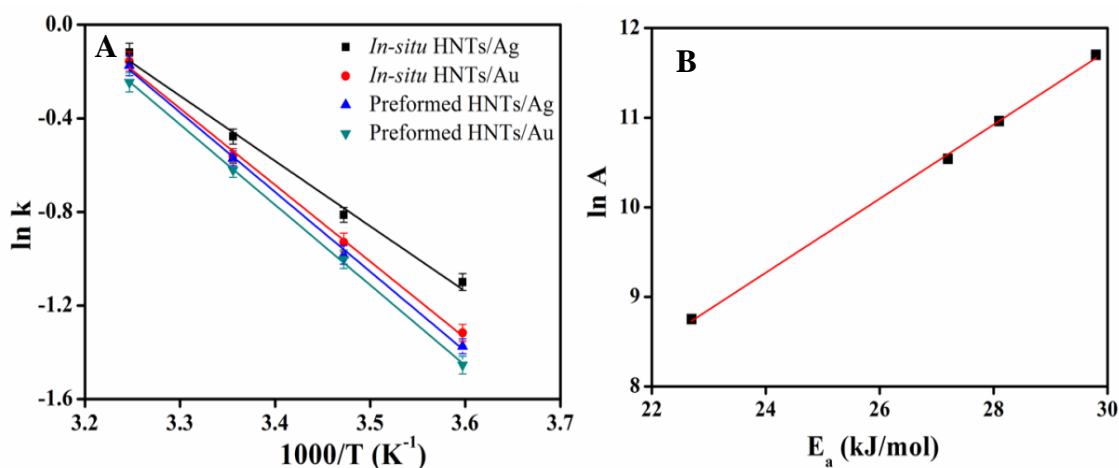


Figure 6.12: (A) Arrhenius plots for the reduction reaction catalysed by preformed and *in-situ* synthesized HNTs/Ag and HNTs/Au NCs. Based on the linear correlation between $\ln k$ and the reciprocal of T , activation energy (E_a) has been calculated from the slope and pre-exponential factor from the intercept. (B) Plot $\ln A$ against E_a of the Arrhenius equation demonstrating the compensation effect for the catalysts.

The calculated values of activation energy reported in the literature vary considerably for different catalysts. Zeng et al. measured E_a for Au partially hollow nanoboxes (55 kJ/mol), hollow nanoboxes (44 kJ/mol) and nanocages (28 kJ/mol).⁴³ Pal and co-workers reported E_a of 21 kJ/mol for Au/calcium-alginate and 31 kJ/mol for Au NPs loaded on resin beads and their dependency on particle size.^{44,45} Activation energy has also been found to be 14 kJ/mol for colloidal Pt nanocubes and it became 12 kJ/mol after supported them on polystyrene microsphere.⁴⁶ Ballauff and co-workers demonstrated E_a of 40, 44 and 43 kJ/mol for Pt, Pd and Au NPs embedded in polyelectrolyte brushes respectively.^{42,47} Activation energy has also been reported to be 38 kJ/mol for Au NPs deposited on commercially available poly(methyl methacrylate)⁴⁸ and 45 kJ/mol for Ag-deposited Fe₂O₃ NPs.⁴⁹ Based on the equation $\ln A = \Delta S/R$,⁵⁰ we have estimated the entropy of activation (ΔS) and presented in Table 6.1. It

is worth noting that the lowest pre-exponential factor and the entropy of activation were observed for *in situ* synthesized HNTs/Ag NCs, whereas preformed HNTs/Au NCs had the highest pre-exponential factor and the entropy of activation.

Thus, the present study demonstrates that E_a indicates the temperature dependence of the catalytic rate constant k and enhanced catalytic activity of *in situ* synthesized HNTs/Ag among the four NCs. The linear correlation between $\ln A$ and E_a perceived in this catalytic system, clearly attributes to the compensation effect which is generally found in both heterogeneous and a large number of homogeneous catalytic systems^{43,51} and could be precisely explained with the help of switching theory. Based on the switching theory,⁵² this effect may be associated with the switching in kinetics from a regime where the overall rate is dominated by the rate of activation of the reactant to a regime where the stability of the reaction product adsorbed on the surface of the catalyst becomes more important.

6.3.3.4 Recyclability Study of the Catalyst

In any catalysis, feasible recovery of catalysts is a crucial step to make the process cost-effective and eco-friendly. At the end of the catalytic reduction, all the NCs catalysts remain active and recycled for this reduction reaction after separated them from the product through a simple filtration and with proper washing using distilled water and drying at room temperature. However, even after repetitive use no leaching of metal NPs into the reaction solution was observed, ascribing the stability of the NCs catalysts. Figure 6.13 exhibits plot of catalytic rate constant k for 4-NP reduction over a number of cycles using the same batch of NCs catalysts, attributing the stability and recyclability of the catalysts. The catalytic reduction of other isomers of nitrophenol, picric acid, and nitrobenzoic acid was also successful in presence of these NCs catalysts and even after repetitive use they retained their size, shape, and morphology.

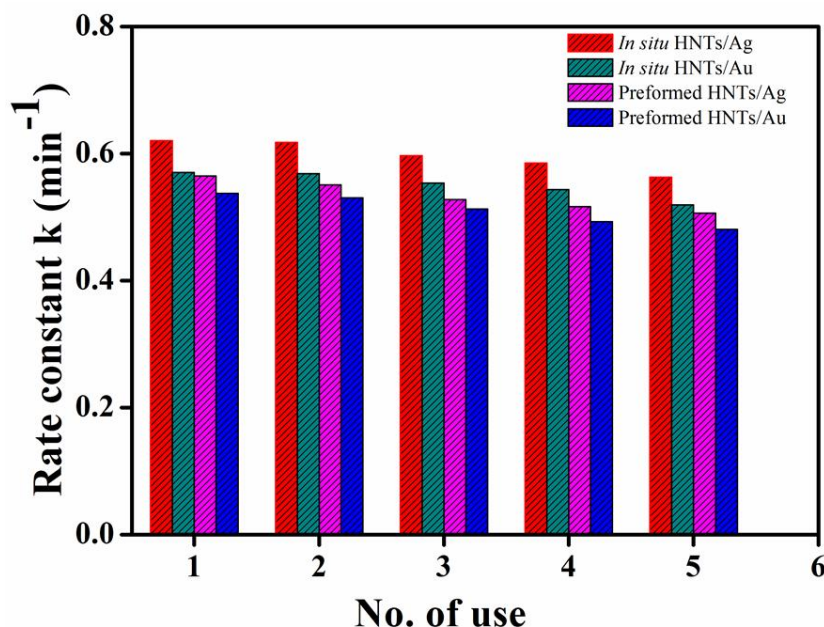


Figure 6.13: Reusability of HNTs/Ag and HNTs/Au nanocomposites as catalysts for the reduction of 4-NP by NaBH₄, demonstrating the stability and recyclability of the nanocomposites.

6.3.3.5 Mechanism of the Reduction Reaction

Metallic nanoparticles strongly catalyze the redox reactions, which can be explained in terms of electrochemical current potential.^{53,54} The mechanism of this reduction reaction using HNTs/metal NCs as catalyst can be explained based on the Langmuir–Hinshelwood model,^{47,55} as shown in Figure 6.14. Borohydride ions (BH₄⁻) get adsorb onto the surface of metal and transfer a surface hydrogen species to the surface of the metal NPs. The adsorption of both BH₄⁻ and 4-NP molecules onto the surface of metal NPs are reversible and can be modeled by Langmuir isotherm. In this reaction, electron transfer takes place from BH₄⁻ to 4-NP only after the adsorption of both onto the surface of the metal NPs. The rate of electron transfer at the catalyst surface can be influenced by the adsorption of 4-nitrophenolate ion onto the catalyst surface and then interfacial electron transfer followed by desorption of the product, 4-aminophenol away from the surface, leaving a free metal surfaces which thus, accessible for a new catalytic cycle to proceed. It should be noted that the

adsorption/desorption equilibria and the diffusion of reactant molecules to the NPs are considered to be fast. The reaction between the adsorbed 4-NP and the metal NPs surface bound hydrogen atoms is the rate-determining step.

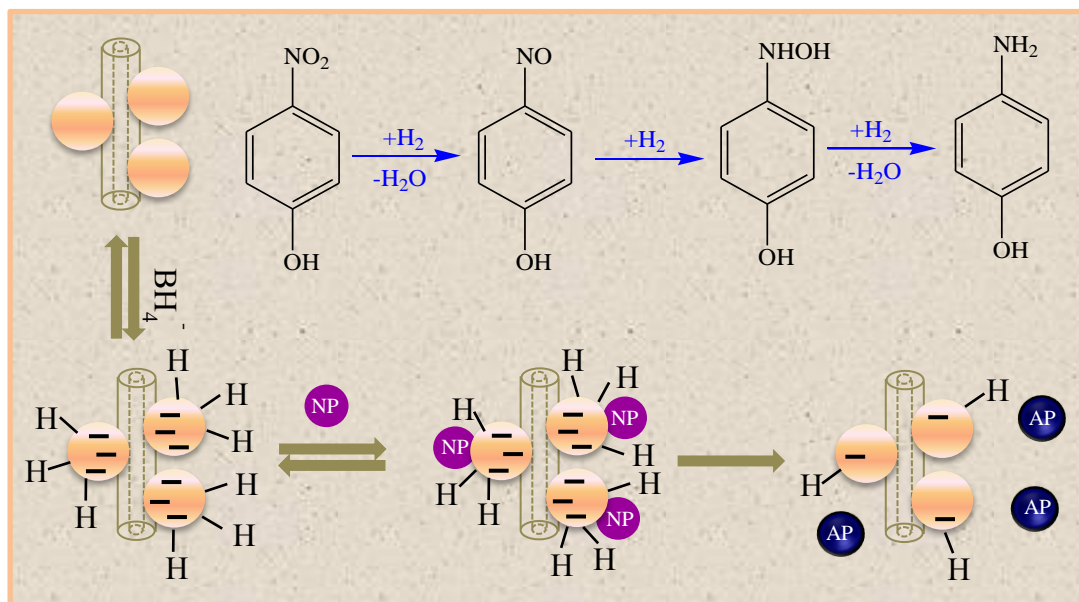


Figure 6.14: Mechanistic model based on Langmuir–Hinshelwood mechanism for the reduction of 4-nitrophenol (4-NP) to 4-aminophenol (4-AP) using sodium borohydride (NaBH_4), catalyzed by metal nanoparticles (NPs) which were immobilized over the surface of aminosilane modified halloysite nanotubes (HNTs). Catalytic reaction takes place on the surface of metal NPs, once borohydride ions and 4-NP get adsorb onto the metal surface.

6.3.3.6 Comparison of Catalytic Activity

In order to compare the catalytic activity of our NCs catalysts with the catalysts reported in the literature, k was normalized to the concentration of Au or Ag, where k_{nor} ($k_{nor} = k/C_{metal}$) represents the intrinsic catalytic activity of the catalysts.⁵⁶ In Table 6.2, we have demonstrated the catalytic efficiency of our HNTs/metal NCs and compared with that of the reported catalysts, which comprised of Au and Ag NPs loaded on a support for the reduction of 4-NP. A remarkable catalytic activity for *in situ* synthesized HNTs/Ag NCs was observed for this reduction reaction, having highest k_{nor} of $0.184 \text{ s}^{-1} \text{ mM}^{-1}$ in contrast to other Ag catalysts, like Ag-NP/C composite ($9.9 \times 10^{-4} \text{ s}^{-1} \text{ mM}^{-1}$),⁵⁷

$\text{Fe}_3\text{O}_4@\text{SiO}_2\text{-Ag}$ magnetic nanocomposite ($4.9 \times 10^{-2} \text{ s}^{-1} \text{ mM}^{-1}$),⁵⁸ $\text{Fe}_3\text{O}_4@\text{C}@\text{Ag}$ composite microspheres ($8.1 \times 10^{-2} \text{ s}^{-1} \text{ mM}^{-1}$),⁵⁹ AgNP-PG-5K (polyguanidino oxanorbornene, $0.149 \text{ s}^{-1} \text{ mM}^{-1}$)⁶⁰ etc. HNTs/Au NCs also have a reasonable catalytic activity for this reduction reaction and is higher than that of other heterogeneous Au catalysts e.g.; R-Au (Au NPs loaded on resin beads),⁴⁵ dendrimer-encapsulated gold nanoparticles,⁶¹ Au-Chitosan/ Fe_3O_4 (Au NPs on chitosan-coated iron oxide),⁶² Au- Fe_3O_4 heterostructure,⁶³ and so on. *In situ* synthesized HNTs/Au NCs shows a comparable catalytic activity, having k_{nor} of $0.17 \text{ s}^{-1} \text{ mM}^{-1}$, to that of preformed HNTs/Au ($0.16 \text{ s}^{-1} \text{ mM}^{-1}$) and HNTs/Ag ($0.168 \text{ s}^{-1} \text{ mM}^{-1}$) NCs catalysts. Though the catalytic activity of preformed and *in situ* synthesized HNTs/Au and HNTs/Ag NCs (i.e.; in presence and absence of stabilizing agent) are almost comparable, there is a still bit difference in their efficiency. The particle sizes of these four different NCs are almost similar, thus, the variation in their catalytic activity could be due to a difference in the available surface area of the metallic NPs during catalysis as well as a difference in the ability of the reactants to reach the NPs surfaces. In case of preformed HNTs/metal NCs, the presence of capping materials which are anchored over the surface of the NPs could make it sterically more difficult for the reactant molecules to reach the surface of the NPs and consequently they collide with each other. The considerable enhancement in the catalytic activity of *in situ* synthesized HNTs/Ag NCs presumably ascribed to the higher affinity of Ag-N than that of Au-N, as well as the absence of any capping agent over the surface of NPs which results in the availability of the more exposed Ag atoms on the surface to get adsorb of the reactant molecules for a smooth reaction to occur. Hence, the efficacy of the NCs for the reduction of 4-NP follow the order: *in situ* HNTs/Ag > *in situ* HNTs/Au > preformed HNTs/Ag > preformed HNTs/Au. However, all HNTs/Au and HNTs/Ag NCs demonstrated such an outstanding catalytic efficiency, whereas bare HNTs or organosilane modified HNTs didn't exhibits any catalytic activity for this reduction reaction.

Table 6.2: Comparison of the catalytic rate constant (k) and normalized rate constants (k_{nor}) for different Ag and Au heterogeneous catalysts for the reduction of 4-nitrophenol (4-NP). C_{NP} : concentration of 4-NP, C_{Metal} : concentration of Ag or Au in the catalyst. Data were taken or calculated from the respective papers.

Catalysts	C_{NP} (mM)	C_{Metal} (mM)	k (s^{-1})	k_{nor} ($s^{-1} mM^{-1}$)	References
Ag-NP/C composite	4.67×10^{-2}	1.7	1.69×10^{-3}	9.9×10^{-4}	57
$Fe_3O_4@SiO_2$ -Ag	6.1×10^{-2}	0.157	7.67×10^{-3}	4.9×10^{-2}	58
$Fe_3O_4@C@Ag$	5.0×10^{-2}	4.6×10^{-2}	3.72×10^{-3}	8.1×10^{-2}	59
AgNP-PG-5K	0.12	3.7×10^{-2}	5.5×10^{-3}	0.149	60
<i>In situ</i> HNTs/Ag	0.1	5.6×10^{-2}	1.03×10^{-2}	0.184	Present work
Preformed HNTs/Ag	0.1	5.6×10^{-2}	9.42×10^{-3}	0.168	Present work
R-Au	0.1	1.4	5.85×10^{-5}	4.18×10^{-5}	45
Au/PAMAM	4.0×10^{-2}	0.95	2.0×10^{-3}	2.1×10^{-3}	61
Au-Chitosan/ Fe_3O_4	0.1	0.17	1.2×10^{-2}	7.1×10^{-2}	62
Au- Fe_3O_4	4.33	0.88	1.05×10^{-2}	1.19×10^{-2}	63
<i>In situ</i> HNTs/Au	0.1	5.6×10^{-2}	9.51×10^{-3}	0.17	Present work
Preformed HNTs/Au	0.1	5.6×10^{-2}	8.96×10^{-3}	0.16	Present work

6.4 Conclusions

In the present study, based on the two different synthetic approaches, we have fabricated HNTs/metal NCs through the immobilization of preformed as well as direct *in situ* growth of the metal NPs over the surface modified HNTs, which in turn develop efficient and low-cost heterogeneous catalysts. Thus, we have successfully prepared uniformly distributed Au and Ag NPs over the surface of HNTs in presence and absence of any coupling materials. Catalytic efficacy of these NCs has been studied for the reduction of nitroaromatics using $NaBH_4$ as

a model reaction and the overall reaction mechanism was explained in terms of Langmuir-Hinshelwood model. Although their catalytic activity is almost comparable, a detailed kinetic study demonstrated the higher catalytic efficiency of *in situ* synthesized HNTs/Ag NCs amongst the four NCs because of the absence of any capping agent over the surface of NPs. Activation energy, pre-exponential factor, and entropy of activation have been estimated for this reduction reaction. All these catalysts have been reused repetitively for this reduction reaction owing to their convenient recovery from the reaction solution through a simple filtration. This procedure demonstrates an added advantage for the efficient separation and recycling of the catalyst once the reaction completed, which is still a challenging task for homogeneous metal catalysts from both the economical and ecological point of view. Therefore, the process should be attractive because of its simplicity and large-scale production of the heterogeneous catalysts. The clay based nanocatalysts are relatively green catalysts, environmentally benign in nature, and a promising candidate for Au or Ag NPs based other catalytic applications in industrial syntheses.

6.5 References

1. Sanchez, C.; Julián, B.; Belleville, P.; Popall, M. Applications of Hybrid Organic-Inorganic Nanocomposites. *J. Mater. Chem.* **2005**, *15*, 3559-3592.
2. Drisko, G. L.; Sanchez, C. Hybridization in Materials Science-Evolution, Current State, and Future Aspirations. *Eur. J. Inorg. Chem.* **2012**, 5097–5105.
3. Ahmad, Z.; Mark, J. E. Biomimetic Materials: Recent Developments in Organic-Inorganic Hybrids. *Mater. Sci. Eng. C* **1998**, *6*, 183-196.
4. Wu, K. H.; Chang, T. C.; Wang, Y. T.; Chiu, Y. S. Organic-Inorganic Hybrid Materials. I. Characterization and Degradation of Poly (Imide-Silica) Hybrids. *J. Polym. Sci. A Polym. Chem.* **1999**, *37*, 2275-2284.
5. Theng, B. K. G. Formation and Properties of Clay-Polymer Complexes. *Elsevier, New York*, **1979**.
6. Ding, X.; Henrichs, S. M. Adsorption and Desorption of Proteins and Polyamino Acids by Clay Minerals and Marine Sediments. *Mar. Chem.* **2002**, *77*, 225-237.
7. Chen, Y.; Iroh, J. O. Synthesis and Characterization of Polyimide/Silica Hybrid Composites. *Chem. Mater.* **1999**, *11*, 1218-1222.
8. Chang, C. C.; Chen, W. C. Synthesis and Optical Properties of Polyimide-Silica Hybrid Thin Films. *Chem. Mater.* **2002**, *14*, 4242-4248.
9. Burkett, S. L.; Sims, S. D.; Mann, S. Synthesis of Hybrid Inorganic-Organic Mesoporous Silica by Co-Condensation of Siloxane and Organosiloxane Precursors. *Chem. Commun.* **1996**, 1367-1368.

10. Ogawa, M. A. A Simple Sol-Gel Route for the Preparation of Silica–Surfactant Mesostructured Materials. *Chem. Commun.* **1996**, 1149-1150.
11. Shchukin, D. G.; Sukhorukov, G. B.; Price, R. R.; Lvov, Y. M. Halloysite Nanotubes as Biomimetic Nanoreactors. *Small* **2005**, *1*, 510-513.
12. Jana, S.; Praharaj, S.; Panigrahi, S.; Basu, S.; Pande, S.; Chang, C. -H.; Pal, T. Light-Induced Hydrolysis of Nitriles by Photoproduced α -MnO₂ Nanorods on Polystyrene Beads. *Org. Lett.* **2007**, *9*, 2191-2193.
13. Thunemann, A. F.; Schutt, D.; Kaufner, L.; Pison, U.; Mohwald, H. Maghemite Nanoparticles Protectively Coated with Poly(ethylene imine) and Poly(ethylene oxide)-block-poly(glutamic acid). *Langmuir* **2006**, *22*, 2351-2357.
14. Tans, S. J.; Verschueren, A. R. M.; Dekker, C. Room-Temperature Transistor Based on a Single Carbon Nanotube. *Nature* **1998**, *393*, 49-52.
15. Lelu, S.; Novat, C.; Graillat, C.; Guyot, A.; Bourgeat-Lami, E. Encapsulation of an Organic Phthalocyanine Blue Pigment into Polystyrene Latex Particles Using a Miniemulsion Polymerization Process. *Polym. Int.* **2003**, *52*, 542-547.
16. Joussein, E.; Pitit, S.; Churchman, J.; Theng, B.; Righi, D.; Delvaux, B. Halloysite Clay Minerals-A Review. *Clay Miner.* **2005**, *40*, 383-426.
17. Lvov, Y. M.; Shchukin, D. G.; Möhwald, H.; Price, R. R. Halloysite Clay Nanotubes for Controlled Release of Protective Agents. *ACS Nano* **2008**, *2*, 814-820.
18. Abdullayev, E.; Joshi, A.; Wei, W.; Zhao Y.; Lvov, Y. Enlargement of Halloysite Clay Nanotube Lumen by Selective Etching of Aluminum Oxide. *ACS Nano* **2012**, *6*, 7216-7226.
19. Cavallaro, G.; Lazzara, G.; Milioto, S. Exploiting the Colloidal Stability and Solubilization Ability of Clay Nanotubes/Ionic Surfactant Hybrid Nanomaterials. *J. Phys. Chem. C* **2012**, *116*, 21932-21938.
20. Ingram, D. B.; Christopher, P.; Bauer, J. L.; Linic, S. Predictive Model for the Design of Plasmonic Metal/Semiconductor Composite Photocatalysts. *ACS Catal.* **2011**, *1*, 1441-1447.
21. Lee, J. S.; Ulmann, P. A.; Han, M. S.; Mirkin, C. A. A DNA-Gold Nanoparticle-Based Colorimetric Competition Assay for the Detection of Cysteine. *Nano Lett.* **2008**, *8*, 529-533.
22. Hirsch, L. R.; Stafford, R. J.; Bankson, J. A.; Sershen, S. R.; Rivera, B.; Price, R. E.; Hazle, J. D.; Halas, N. J.; West, J. L. Nanoshell-Mediated Near-Infrared Thermal Therapy of Tumors Under Magnetic Resonance Guidance. *Proc. Natl. Acad. Sci.* **2003**, *100*, 13549-13554.
23. Murphy, C. J.; Gole, A. M.; Hunyadi, S. E.; Orendorff, C. J. One-Dimensional Colloidal Gold and Silver Nanostructures. *Inorg. Chem.* **2006**, *45*, 7544-7554.
24. Dai, J.; Bruening, M. L. Catalytic Nanoparticles formed by Reduction of Metal Ions in Multilayered Polyelectrolyte Films. *Nano Lett.* **2002**, *2*, 497-501.
25. Ivanova, S.; Pitchon, V.; Zimmermann, Y.; Petit, C. Preparation of Alumina Supported Gold Catalysts: Influence of Washing Procedures, Mechanism of Particles Size Growth. *Appl. Catal. A* **2006**, *298*, 57-64.
26. Jana, S.; Das, S. Development of Novel Inorganic-Organic Hybrid Nanocomposites as a Recyclable Adsorbent and Catalyst. *RSC Adv.* **2014**, *4*, 34435-34442.

27. Esumi, K.; Isono, R.; Yoshimura, T. Preparation of PAMAM- and PPI-Metal (Silver, Platinum, and Palladium) Nanocomposites and Their Catalytic Activities for Reduction of 4-Nitrophenol. *Langmuir* **2004**, *20*, 237-243.
28. Garcia-Martinez, J. C.; Lezutekong, R.; Crooks, R. M. Dendrimer-Encapsulated Pd Nanoparticles as Aqueous, Room-Temperature Catalysts for the Stille Reaction. *J. Am. Chem. Soc.* **2005**, *127*, 5097-5103.
29. Haruta, M.; Tsubota, S.; Kobayashi, T.; Kageyama, H.; Genet, M. J.; Delmon, B. Low-Temperature Oxidation of CO over Gold Supported on TiO₂, α -Fe₂O₃, and Co₃O₄. *J. Catal.* **1993**, *144*, 175-192.
30. Jana, S.; Pande, S.; Panigrahi, S.; Praharaj, S.; Basu, S.; Pal, A.; Pal, T. Exploitation of Electrostatic Field Force for Immobilization and Catalytic Reduction of o-Nitrobenzoic Acid to Anthranilic Acid on Resin-bound Silver Nanocomposites. *Langmuir* **2006**, *22*, 7091-7095.
31. Rodriguez, J. A.; Ma, S.; Liu, P.; Hrbek, J.; Evans, J.; Pérez, M. Activity of CeO_x and TiO_x Nanoparticles Grown on Au (111) in the Water-Gas Shift Reaction. *Science* **2007**, *318*, 1757-1760.
32. Fujitani, T.; Nakamura, I.; Akita, T.; Okumura, M.; Haruta, M. Hydrogen Dissociation by Gold Clusters. *Angew. Chem. Int. Ed.* **2009**, *48*, 9515-9518.
33. Green, I. X.; Tang, W.; Neurock, M.; Yates, Jr. J. T. Low-Temperature Catalytic H₂ Oxidation over Au Nanoparticle/TiO₂ Dual Perimeter Sites, *Angew. Chem. Int. Ed.* **2011**, *50*, 10186-10189.
34. Shimizu, K.; Sato, R.; Satsuma, A. Direct C-C Cross-Coupling of Secondary and Primary Alcohols Catalyzed by a γ -Alumina-Supported Silver Subnanocluster. *Angew. Chem. Int. Ed.* **2009**, *48*, 3982-3986.
35. Wang, R.; Jiang, G.; Ding, Y.; Wang, Y.; Sun, X.; Wang, X.; Chen, W. Photocatalytic Activity of Heterostructures Based on TiO₂ and Halloysite Nanotubes. *ACS Appl. Mater. Interfaces* **2011**, *3*, 4154-4158.
36. Jana, S.; Chang, J. W.; Rioux, R. M. Synthesis and Modeling of Hollow Intermetallic Ni-Zn Nanoparticles Formed by the Kirkendall Effect. *Nano Lett.* **2013**, *13*, 3618-3625.
37. Yuan, P.; Southon, P. D.; Liu, Z.; Green, M. E. R.; Hook, J. M.; Antill, S. J.; Kepert, C. J. Functionalization of Halloysite Clay Nanotubes by Grafting with γ -Aminopropyltriethoxysilane. *J. Phys. Chem. C* **2008**, *112*, 15742-15751.
38. Yah, W. O.; Xu, H.; Soejima, H.; Ma, W.; Lvov, Y.; Takahara, A. Biomimetic Dopamine Derivative for Selective Polymer Modification of Halloysite Nanotube Lumen. *J. Am. Chem. Soc.* **2012**, *134*, 12134-12137.
39. Jana, S.; Pande, S.; Sinha, A. K.; Sarkar, S.; Pradhan, M.; Basu, M.; Saha, S.; Pal, T. A Green Chemistry Approach for the Synthesis of Flower-like Ag-Doped MnO₂ Nanostructures Probed by Surface-Enhanced Raman Spectroscopy. *J. Phys. Chem. C* **2009**, *113*, 1386-1392.
40. Pradhan, N.; Pal, A.; Pal, T. Silver Nanoparticle Catalyzed Reduction of Aromatic Nitro Compounds. *Colloids Surf. A: Physicochem. Eng. Aspects* **2002**, *196*, 247-257.
41. Jana, S.; Ghosh, S. K.; Nath, S.; Pande, S.; Praharaj, S.; Panigrahi, S.; Basu, S.; Endo, T.; Pal, T. Synthesis of Silver Nanoshell-Coated Cationic Polystyrene Beads: A Solid Phase Catalyst for the Reduction of 4-Nitrophenol. *Appl. Catal. A: General* **2006**, *313*, 41-48.

42. Mei, Y.; Lu, Y.; Polzer, F.; Ballauff, M. Catalytic Activity of Palladium Nanoparticles Encapsulated in Spherical Polyelectrolyte Brushes and Core-Shell Microgels. *Chem. Mater.* **2007**, *19*, 1062-1069.
43. Zeng, J.; Zhang, Q.; Chen, J.; Xia, Y. A Comparison Study of the Catalytic Properties of Au-Based Nanocages, Nanoboxes, and Nanoparticles. *Nano Lett.* **2010**, *10*, 30-35.
44. Saha, S.; Pal, A.; Kundu, S.; Basu, S.; Pal, T. Photochemical Green Synthesis of Calcium-Alginate-Stabilized Ag and Au Nanoparticles and Their Catalytic Application to 4-Nitrophenol Reduction. *Langmuir* **2010**, *26*, 2885-2893.
45. Panigrahi, S.; Basu, S.; Praharaj, S.; Pande, S.; Jana, S.; Pal, A.; Ghosh, S. K.; Pal, T. Synthesis and Size-Selective Catalysis by Supported Gold Nanoparticles: Study on Heterogeneous and Homogeneous Catalytic Process. *J. Phys. Chem. C* **2007**, *111*, 4596-4605.
46. Mahmoud, M. A.; Snyder, B.; El-Sayed, M. A. Polystyrene Microspheres: Inactive Supporting Material for Recycling and Recovering Colloidal Nanocatalysts in Solution. *J. Phys. Chem. Lett.* **2010**, *1*, 28-31.
47. Wunder, S.; Polzer, F.; Lu, Y.; Mei, Y.; Ballauff, M. Kinetic Analysis of Catalytic Reduction of 4-Nitrophenol by Metallic Nanoparticles Immobilized in Spherical Polyelectrolyte Brushes. *J. Phys. Chem. C* **2010**, *114*, 8814-8820.
48. Kuroda, K.; Ishida, T.; Haruta, M. Reduction of 4-Nitrophenol to 4-Aminophenol over Au Nanoparticles Deposited on PMMA. *J. Mol. Catal. A: Chem.* **2009**, *298*, 7-11.
49. Shin, K. S.; Choi, J.-Y.; Park, C. S.; Jang, H. J.; Kim, K. Facile Synthesis and Catalytic Application of Silver-Deposited Magnetic Nanoparticles. *Catal. Lett.* **2009**, *133*, 1-7.
50. Narayanan, R.; El-Sayed, M. A. Shape-Dependent Catalytic Activity of Platinum Nanoparticles in Colloidal Solution. *Nano Lett.* **2004**, *4*, 1343-1348.
51. Rooney, J. J. The Extended Eyring Kinetic Equation and the Compensation Effect in Catalysis. *J. Mol. Catal. A: Chem.* **1998**, *129*, 131-134.
52. Bligaard, T.; Honkala, K.; Logadottir, A.; Norskov, J. K.; Dahl, S.; Jacobsen, C. J. H. On the Compensation Effect in Heterogeneous Catalysis. *J. Phys. Chem. B* **2003**, *107*, 9325-9331.
53. Freund, P. L.; Spiro, M. Colloidal Catalysis: the Effect of Sol Size and Concentration. *J. Phys. Chem. B* **1985**, *89*, 1074-1077.
54. Miller, D. S.; Bard, A. J.; McLendon, G.; Ferguson, J. Catalytic Water Reduction At Colloidal Metal" Microelectrodes". 2. Theory and Experiment. *J. Am. Chem. Soc.* **1981**, *103*, 5336-5341.
55. Vannice, M. A. *Kinetics of Catalytic Reactions*, Springer Science. Philadelphia, PA, **2005**.
56. Fang, Y.; Wang, E. Simple and Direct Synthesis of Oxygenous Carbon Supported Palladium Nanoparticles with High Catalytic Activity. *Nanoscale* **2013**, *5*, 1843-1848.
57. Tang, S.; Vongehr, S.; Meng, X. Carbon Spheres with Controllable Silver Nanoparticle Doping. *J. Phys. Chem. C* **2010**, *114*, 977-982.
58. Chi, Y.; Yuan, Q.; Li, Y.; Tu, J.; Zhao, L.; Li, N.; Li, X. Synthesis of Fe₃O₄@SiO₂-Ag Magnetic Nanocomposite Based on Small-Sized and Highly Dispersed Silver Nanoparticles for Catalytic Reduction of 4-Nitrophenol. *J. Colloid Interface Sci.* **2012**, *383*, 96-102.

-
59. An, Q.; Yu, M.; Zhang, Y.; Ma, W.; Guo, J.; Wang, C. Fe₃O₄@Carbon Microsphere Supported Ag-Au Bimetallic Nanocrystals with the Enhanced Catalytic Activity and Selectivity for the Reduction of Nitroaromatic Compounds. *J. Phys. Chem. C* **2012**, *116*, 22432-22440.
 60. Baruah, B.; Gabriel, G. J.; Akbashev, M. J.; Booher, M. E. Facile Synthesis of Silver Nanoparticles Stabilized by Cationic Polynorbornenes and Their Catalytic Activity in 4-Nitrophenol Reduction. *Langmuir* **2013**, *29*, 4225-4234.
 61. Wu, H.; Liu, Z.; Wang, X.; Zhao, B.; Zhang, J.; Li, C. Preparation of Hollow Capsule-Stabilized Gold Nanoparticles through the Encapsulation of the Dendrimer. *J. Colloid Interface Sci.* **2006**, *302*, 142-148.
 62. Chang, Y. -C.; Chen, D. -H. Catalytic Reduction of 4-Nitrophenol by Magnetically Recoverable Au Nanocatalyst. *J. Hazard. Mater.* **2009**, *165*, 664-669.
 63. Lin, F.; Doong, R. Bifunctional Au-Fe₃O₄ Heterostructures for Magnetically Recyclable Catalysis of Nitrophenol Reduction. *J. Phys. Chem. C* **2011**, *115*, 6591-6598.

**Light-Assisted Synthesis of Hierarchical Flower-Like MnO₂
Nanocomposites with Solar Light Induced Enhanced
Photocatalytic Activity**

7.1 Introduction

Environmental pollution has become one of the greatest concerns in the recent past owing to its grave and irreparable damage to the earth. Wastewater effluents from industries are defined as primary sources of water pollution as they are discharged sometimes even untreated or inadequately treated before being released into the environment, resulting in increased level of water pollution that causes a severe impact on the natural environment as well as on human health.^{1,2} Nowadays, organic dyes used in textile and food industries are the major sources of environmental contamination due to their non-biodegradability, high toxicity and carcinogenic effects.^{3,4} Additionally, wastewater treatment of pollutants produced from dye processing industries demonstrates a major challenge to attain desired effluent discharge standards, followed by appropriate recycle and reuse of those products in manufacturing processes. Therefore, the degradation of these refractory pollutants has drawn adequate interest and become the need of the hour in the on-going effort to diminish their environmental impact. Simultaneously, cost-effective procedures need to be developed for the transformation of hazardous substances into the benign forms.⁵ The photocatalytic degradation, a rapidly expanding process for wastewater treatment, is capable of the removing organic dyes through the degradation or by transforming them into harmless chemicals in the contaminated water, together with it is a low cost, complete mineralization and a low temperature route.⁶⁻⁸ Furthermore, the effective and inimitable way to utilize the renewable and never-ending solar energy would be the photocatalysis, driven by well-known photocatalysis principle of the redox reaction induced by photogenerated electron and holes on photocatalysts.⁹

Among the transition metal oxides, manganese oxides represent one of the diverse classes of materials having fundamental and technological significance. Nanostructured manganese dioxides (MnO_2) kept their signature in the field of catalysis,¹⁰⁻¹² ion exchange,¹³ molecular adsorption,¹⁴⁻¹⁵ biosensors,^{16,17} energy storage,^{18,19} and electrode materials for batteries^{20,21} owing to their high abundance and outstanding structural flexibility. However, a special mention is needed for MnO_2 in environmental remediation, where it is being used as a catalyst for the degradation of organic dyes. MnO_2 occurs in several polymorphic forms, such as α - MnO_2 ,^{22,23} β - MnO_2 ,^{22,23} γ - MnO_2 ,²⁴ δ - MnO_2 ,²⁵ and ϵ - MnO_2 ²⁶ depending on how the basic MnO_6 octahedral units in MnO_2 share their face and edge. A variety of approaches such as hydrothermal,^{21,27,28} sol-gel,^{29,30} co-precipitation,^{31,32} thermal decomposition,³³ electrodeposition³⁴ etc. have been established to synthesize nanostructures of MnO_2 with different morphologies, like spheres, cubes, rods, wires, belts, tubes, plates, flowers, urchinlike structures and so on. Alternatively, fabrication of multi-dimensional ordered nanostructured oxides is especially desirable for advanced catalytic, electronic, and optoelectronic applications. However, the structural and morphological complexity in MnO_2 nanostructures makes the synthesis procedure more difficult and is still challenging to achieve pure crystallographic phase and uniform morphology, which is indispensable for any MnO_2 nanostructures to demonstrate their efficacy. Moreover, precise control over self-assembly of nanostructures with hierarchy is desirable to fabricate novel materials. Besides these difficulties, low-temperature solution chemistry route always represents an alternative user-friendly approach in terms of practical significance.

Fabrication of novel nanocomposites (NCs) based on nanoclays invokes a new direction in the frontier area of materials science to synthesize novel materials for varied applications including advanced catalysis, environmental remediation, water purification, anti-corrosion agents, pseudocapacitors, nanoreactors to host reactants for nanosynthesis and biomimetic synthesis, drug delivery, and in energy storage.³⁵⁻⁴⁰ HNTs are environmental friendly, less expensive, and naturally occurring layered aluminosilicate clay with a well-defined hollow tubular structure, formed due to the mismatch in the

periodicity between the oxygen sharing tetrahedral SiO_2 sheets and the octahedral AlO_6 sheets.^{41,42} The adjacent alumina and silica layers along with their water of hydration induce a packing disorder, making the nanotubes curve and roll up to form multilayers. The unique surface chemistry in HNTs, originating from their positive octahedral array of Al–OH groups at the inner surfaces and negative Si–O–Si groups at the outer surfaces, fascinates to fabricate novel hybrid nanocomposites with exceptional physical or chemical properties.

The objective of this work is to prepare nanoscale hierarchical MnO_2 over the surface of halloysite clay nanotubes (HNTs) using a novel green chemistry route through a light-assisted decomposition of a manganese precursor and investigate the photocatalytic activity of HNTs/ MnO_2 NCs under natural sunlight irradiations for the degradation several organic dyes. Flower-like $\delta\text{-MnO}_2$ nanostructures comprising of assemblies of intersected nanosheets were grown over the outer surfaces of HNTs. The growth mechanism together with the morphological and crystalline evolution of $\delta\text{-MnO}_2$ nanoflowers has been demonstrated through controlled synthesis, along with X-ray diffraction and electron microscopy studies. Methylene blue (MB) and eosin yellow (EY) were chosen as model contaminants to study their catalytic efficacy. Effects of organic dye type, irradiation source and time, photocatalytic stability, and the crystal phase of the photocatalyst were also examined. The underlying mechanism for the degradation of dyes has also been established through quenching experiments, suggesting the formation of reactive oxygen species which are responsible for the dye degradation.

7.2 Experimental Section

7.2.1 Surface Functionalization of Halloysite Nanotubes

Organosilanes grafted halloysite nanotubes (HNTs) were synthesized according to the following procedure.^{43,44} The grafting reaction was carried out under nitrogen atmosphere using standard air free techniques. 3.0 g of HNTs was taken in a 50 mL three-necked

round bottom flask containing 15.0 mL of toluene. Afterwards, the reaction flux was fixed with a rubber septum, condenser, thermocouple adaptor and an additional quartz sheath in which a thermocouple was inserted. The reaction mixture was de-aerated for 30 minutes under nitrogen at room temperature, followed by heated with a heating mantle. Then, 1.5 mL of (3-aminopropyl) triethoxysilane was injected into the reaction flask at 60°C under stirring condition and refluxed for 20 h. Finally, the as-synthesized product was collected through filtration and washed several times with toluene and ethanol respectively. The obtained product was dried at 100°C overnight under vacuum.

7.2.2 Fabrication of HNTs/MnO₂ Nanocomposites

The HNTs/MnO₂ nanocomposites were prepared using a light-assisted decomposition technique. In a typical process, 1.0 mmol of potassium permanganate was dissolved in 7.0 mL of millipore water in a vials containing 0.1 g of amine functionalized HNTs. Next, 3.0 mL of NaOH solution (3 wt %) was added drop-wise into the above reaction solution and was mixed well using a vortexer for 10 min. The vials was then closed properly and placed under visible light for 6 h and the reaction temperature was monitored to be 90°C. Once the solution was cooled to room temperature, the product was obtained by simple filtration and washed several times with millipore water to remove NaOH and unreacted KMnO₄ if any. The product was dried in air for 1 day and abbreviated as HNTs/MnO₂ nanocomposites.

7.2.3 Photocatalytic Reaction

The photocatalytic activity of HNTs/MnO₂ nanocomposites was explored towards the degradation of aqueous solution of methylene blue (MB) and eosin yellow (EY) under solar light and UV light irradiation respectively. All photocatalytic reactions were performed in a photocatalytic reactor system, consisting of a cylindrical borosilicate glass

reactor vessel with an effective volume of 50 mL and a cooling water jacket. UV-A lamp (8 W medium-pressure mercury lamp of $\lambda = 254$ nm) positioned axially at the center as a UV light radiation source in a photocatalytic reactor system. The reaction temperature was maintained at 25°C by circulating the cooling water during the photodegradation of the dyes. During the photocatalysis using natural solar radiation, we have placed the photocatalytic reactor under the solar light radiation keeping all other experimental condition the same. The photocatalytic experiment was carried out taking 25.0 mL of 0.03 mM aqueous solution of dye in a 50 mL glass reactor, having catalyst concentration of 40 mg L⁻¹. First, the reaction mixture was stirred using a magnetic stirrer in the dark overnight to attain a complete adsorption-desorption equilibrium. Then, the solutions were exposed to light irradiation with a constant stirring up to a desired time. The time dependent photocatalytic degradation of MB and EY at room temperature was monitored using UV-Visible spectrophotometer, taking 3.0 mL of the suspension at specific time intervals. Prior to UV-visible absorption study, the suspension was centrifuged each time to separate the photocatalyst from the dye solution and recorded the spectrum. Once the spectrum was recorded, the solution was transferred back to the reaction vessel. Absorption spectra of exposed MB solution at 664 nm and EY solution at 515 nm have been analyzed quantitatively at definite time interval during the degradation study. Similarly, control experiment was carried out in presence of nanocomposites under dark. Subsequently, the degradation rate was evaluated in terms of changes in absorption intensity of the dye solution. The efficiency (%) towards the degradation of dyes using HNTs/MnO₂ nanocomposites was estimated as follows:

$$(\%) \text{ Degradation} = \frac{C_0 - C_t}{C_0} \times 100 \quad (7.1)$$

where, C_t is the concentration of dye after irradiation of light at a specific time and C_0 is the initial concentration.

7.3 Results and Discussion

7.3.1 Characterization of the Surface Modified HNTs

HNTs are naturally occurring and environmentally benign layered aluminosilicate clay having a well-defined hollow tubular structure, consisting of tetrahedral SiO_2 sheets and the octahedral AlO_6 sheets. Owing their positive inner surfaces and negative outer surfaces facilitates to tune their surface chemistry, which in turn assists to fabricate novel hybrid nanocomposites. Selective modification of the outer surfaces of HNTs with aminosilane assists immobilization of metal or metal oxides over their surfaces, resulting in the formation of metal or metal oxide NCs.

7.3.1.1 FTIR Analysis

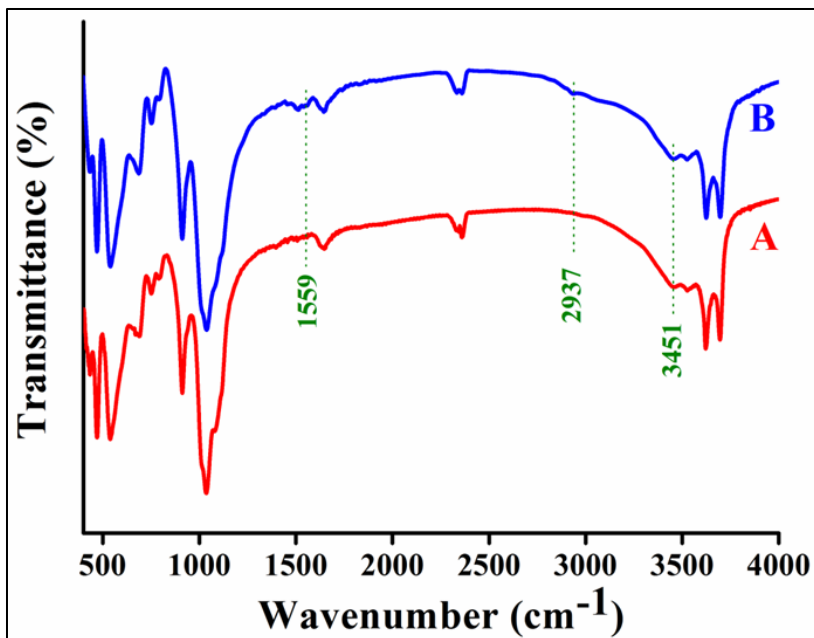


Figure 7.1: FTIR spectra of (A) HNTs and (B) after surface functionalization with (3-aminopropyl) triethoxysilane, demonstrating the presence of amino group due to the grafting of aminosilane onto the surface of HNTs.

The functionalization of HNTs with aminosilane was carried out through grafting reaction. Fourier transform infrared (FTIR) spectroscopy substantiates the formation of amine functionalized HNTs owing to the presence of three new bands at 1559, 2937, and 3451 cm^{-1} for N–H deformation and stretching vibration of C–H and N–H respectively (Figure 7.1), along with two characteristic peaks at 3621 and 3697 cm^{-1} for the stretching vibrations of the inner hydroxyl group and inner surface hydroxyl group respectively.^{45,46}

7.3.1.2 FESEM Study

Field emission scanning electron microscopy (FESEM) analysis demonstrated that HNTs are composed of cylindrical shaped tubes with an open-ended lumen along the tube (Figure 7.2). The length of the tube generally varies between ~ 1.0 to $1.5 \mu\text{m}$ with an outer diameter of 50-100 nm and an inner diameter of 15-20 nm. However, it is important to note that surface functionalization of HNTs doesn't alter their morphology or size.

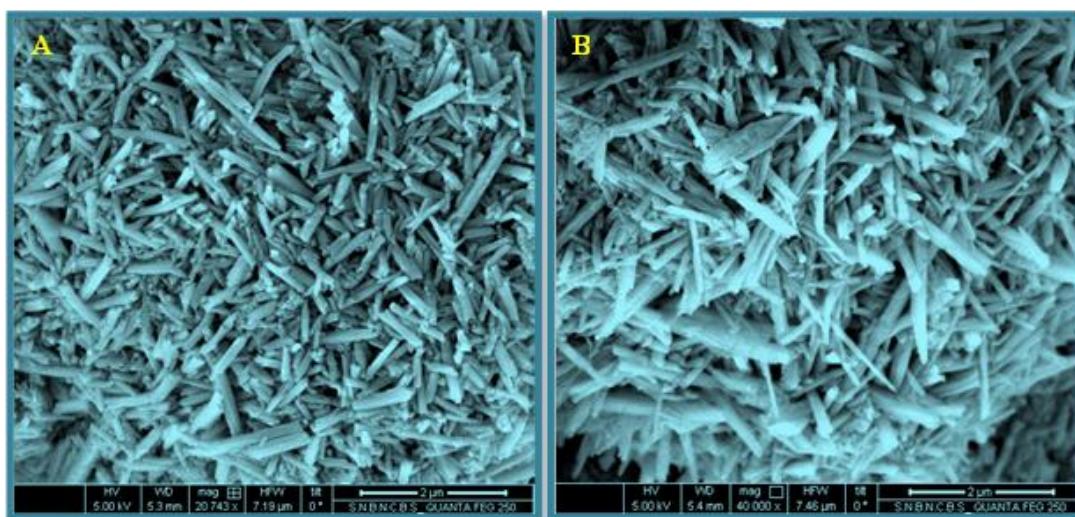


Figure 7.2: FESEM micrographs of halloysite clay nanotubes (HNTs) before (A) and after (B) surface functionalization with (3-aminopropyl) triethoxysilane, indicating no change in their size or morphology.

7.3.1.3 CHN Elemental Analysis

The grafted amino groups on to the surface of HNTs were assessed using carbon, hydrogen and nitrogen (CHN) analyzer. It was estimated to be 0.38 mmol per gram of amine functionalized HNTs.

7.3.1.4 Zeta-potential Measurement

The zeta (ζ)-potential measurements demonstrated that the surface of pristine HNTs is negatively charged, having ζ - potential of -18.6 mV. After functionalization with aminosilane, the surface became positive with ζ - potential of + 24.5 mV, signifying the surface coverage of HNTs with amine groups. Hence, the selective surface modification of HNTs basically tunes their surface chemistry.

7.3.2 Characterization of HNTs/MnO₂ NCs

The synthesis of MnO₂ nanostructures has been carried out through light-assisted decomposition reactions of an aqueous solution of potassium permanganate (KMnO₄) in alkaline condition. Upon addition of alkaline KMnO₄ solution on to the amine functionalized HNTs under visible light irradiation (~90°C), it was reduced to MnO₂ and immobilized over the HNTs surfaces and thus produces HNTs/MnO₂ NCs.

7.3.2.1 FESEM Analysis

The morphology of the HNTs/MnO₂ NCs is illustrated in Figure 7.3. The FESEM images demonstrate a panoramic morphology, consisting of hierarchical flower-like MnO₂ nanostructures and made up of assemblies of thin intersected nanosheets.

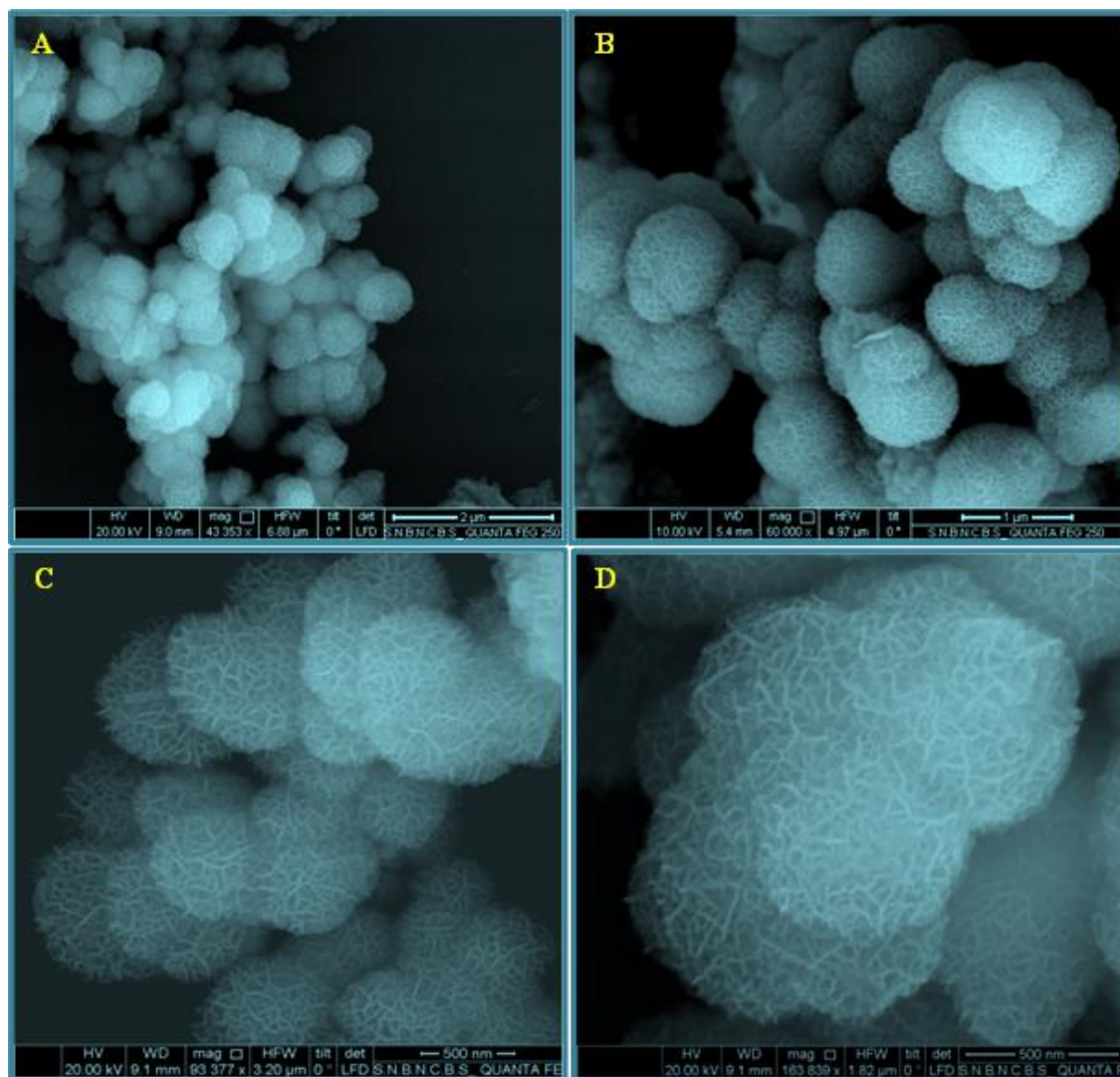


Figure 7.3: FESEM micrographs of HNTs/MnO₂ nanocomposites at different magnifications (A-D), demonstrating hierarchical flower-like MnO₂ nanostructures were grown over the outer surfaces of halloysite clays (HNTs).

7.3.2.2 TEM and HRTEM Analyses

To gain insight further into their morphology and detailed crystalline structure, transmission electron microscopy (TEM) images of HNTs/MnO₂ NCs at different magnifications are demonstrated in Figure 7.4. Analogous to FESEM images, TEM

image also points to the formation of flower-like morphology of MnO_2 , Figure 7.4A and B. Many wrinkled and intersected nanosheets of ~ 4 nm thickness self-assemble and finally grow in all directions to produce MnO_2 nanoflowers (Figure 7.4C and D). The high resolution TEM (HRTEM) image of the edge (Figure 7.5) indicates lattice fringes with spacing of ~ 0.71 nm corresponding to the (001) plane of $\delta\text{-MnO}_2$.

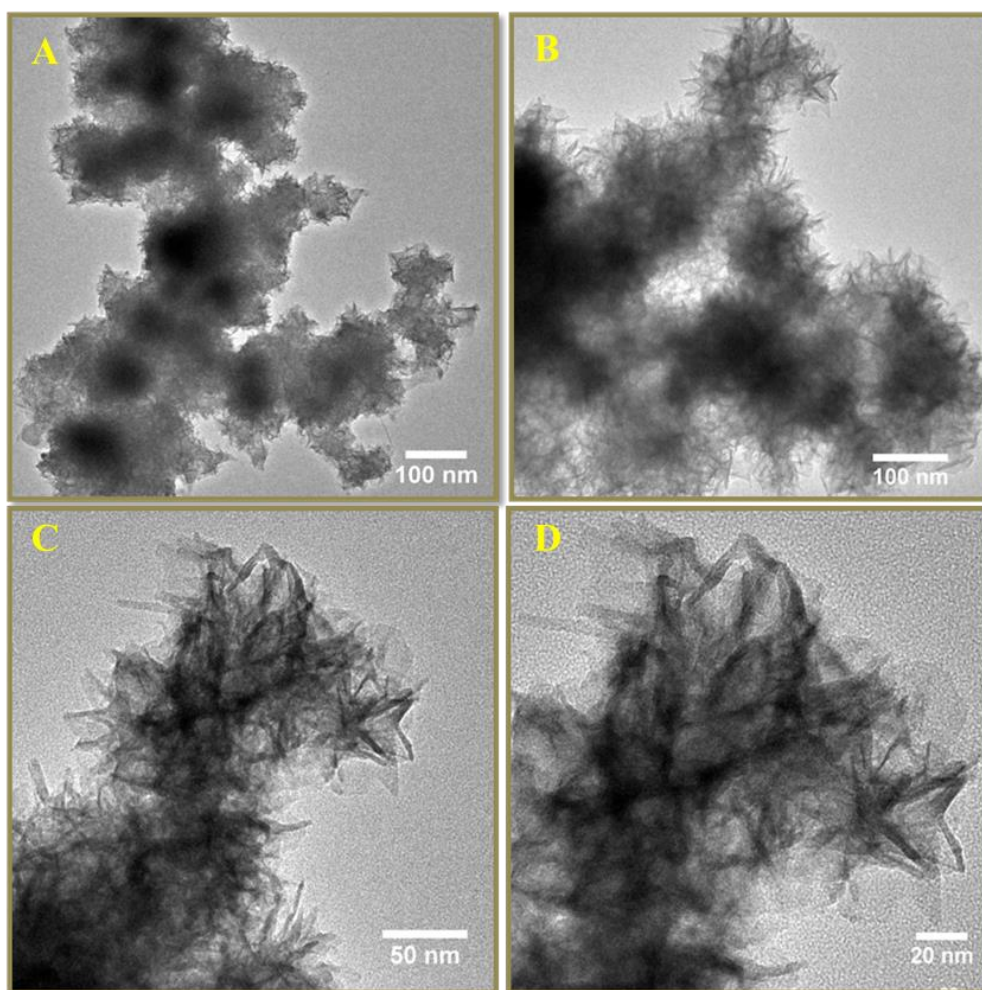


Figure 7.4: (A, B) TEM images of hierarchical flower-like HNTs/ MnO_2 nanocomposites. (C, D) TEM images of MnO_2 nanoflowers demonstrating that they made up of assemblies of thin intersected nanosheets.

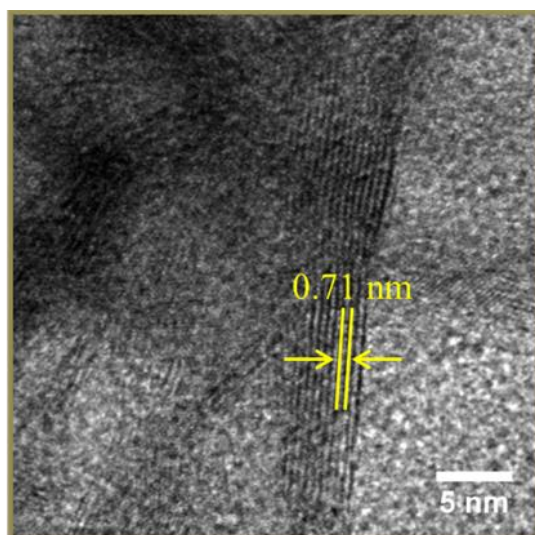


Figure 7.5: HRTEM image of the nanosheets of hierarchical flower-like HNTs/MnO₂ nanocomposites

7.3.2.3 EDS Analysis

The compositional analysis of HNTs/MnO₂ NCs by energy dispersive X-ray spectroscopy (EDS) authenticates the presence of Mn as signals from Mn are evident with the three main constituents of HNTs; oxygen, alumina, and silicon (Figure 7.6).

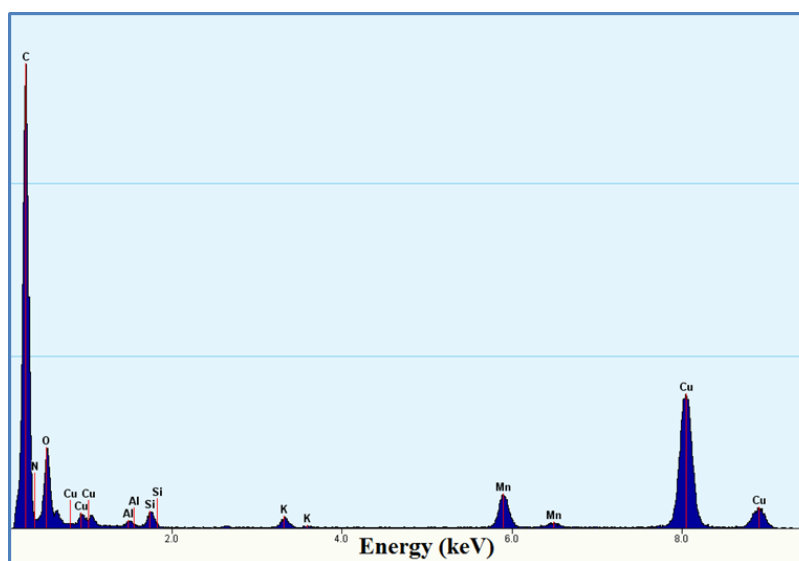


Figure 7.6: EDS spectrum of HNTs/MnO₂ NCs demonstrating the presence of Mn as signals from Mn are evident with the three main constituents of HNTs, i.e.; O, Al and Si.

7.3.2.4 STEM-EDS Elemental Mapping Analysis

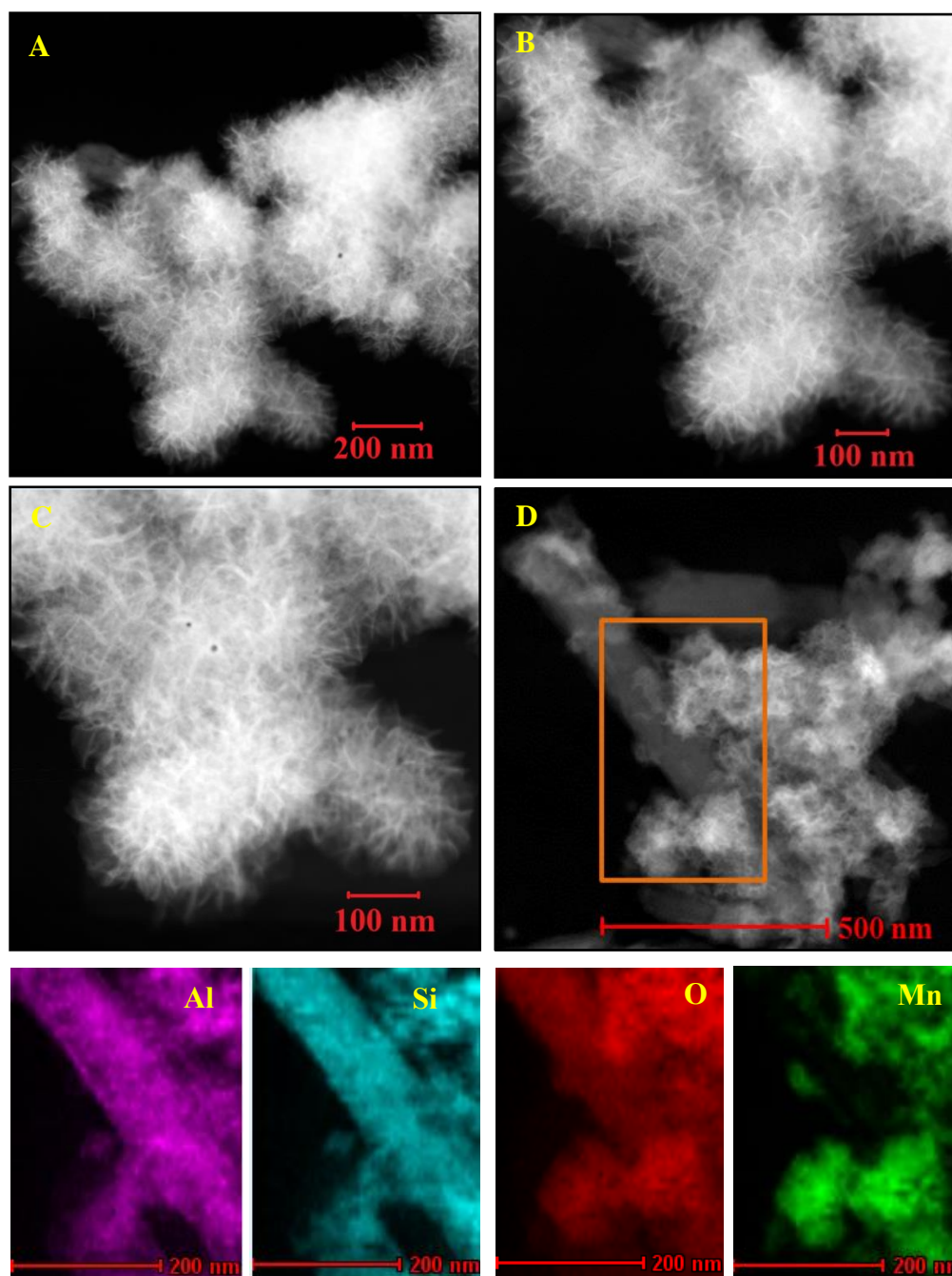


Figure 7.7: (A-C) STEM images of hierarchical flower-like MnO₂ nanostructures grown over the outer surfaces of HNTs at different magnifications. (D) STEM image of MnO₂ nanoflowers onto the surface of a single cylindrical shaped halloysite nanotube (HNT) and corresponding elemental mapping of the Al (pink zone), Si (blue zone), O (red zone), and Mn (green zone) respectively.

To directly visualize the formation of MnO_2 nanoflowers over the surface of HNTs, scanning transmission electron microscopy-energy dispersive spectroscopy (STEM-EDS) elemental mapping was carried out on the HNTs/ MnO_2 NCs. STEM images of hierarchical flower-like MnO_2 nanostructures immobilized over the surface of HNTs are presented in Figure 7.7A-C. STEM image of MnO_2 nanoflowers onto the surface of a single cylindrical shaped halloysite nanotube is presented in Figure 7.7D. The elemental maps shown in Figure 7.7 represent the distribution of all the basic elements present in the HNTs/ MnO_2 NCs. Each element is specified by a definite color. The elemental mappings of Al and Si demonstrate their homogeneous distribution throughout the body of the cylindrical shaped tubes, whereas Mn is located exclusively over the outer surfaces of the tubes in a flowery architecture and O is quantified through all over the nanocomposites.

7.3.2.5 XRD Study

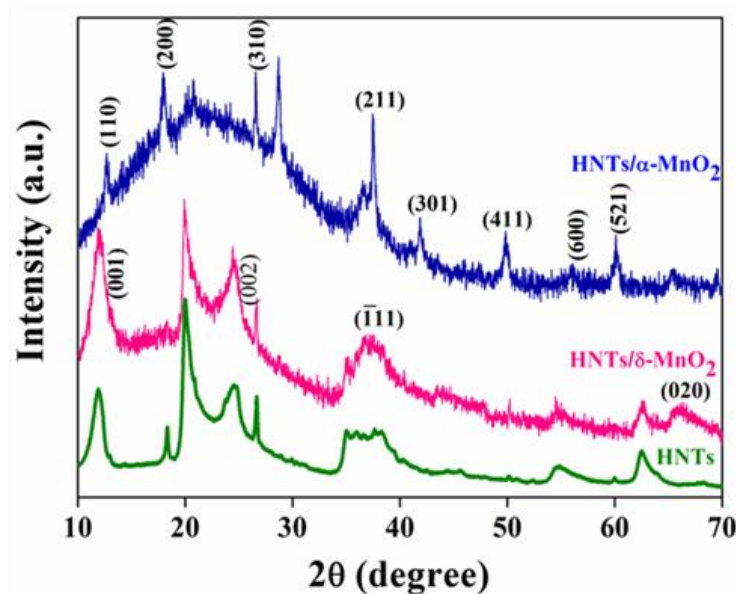


Figure 7.8: XRD patterns of pristine HNTs and δ - MnO_2 nanoflowers grown onto the surface of HNTs, which transform into α - MnO_2 nanoflowers upon heating.

The X-ray diffraction (XRD) pattern of the MnO_2 nanoflowers represents the characteristic signature of the monoclinic structure of layered $\delta\text{-MnO}_2$. All the diffraction peaks correspond to the (001), (002), ($\bar{1}11$), and (020) plane of pure $\delta\text{-MnO}_2$ respectively, as shown in Figure 7.8. This is also in accordance with the HRTEM analysis. No manganese oxides, hydroxides or other impurities were found in XRD, signifying the successful formation of pure $\delta\text{-MnO}_2$ phase. The phase transition of MnO_2 nanoflowers from δ - phase to α -phase occurs upon heating the sample at $450\text{ }^\circ\text{C}$, suggesting the layered crystalline structure of $\delta\text{-MnO}_2$ transforms into the 2×2 tunnels in $\alpha\text{-MnO}_2$.

7.3.2.6 Phase Transition of MnO_2 /HNTs NCs

Upon heating the $\delta\text{-MnO}_2$ MnO_2 nanoflowers at $450\text{ }^\circ\text{C}$, phase transition of MnO_2 nanoflowers occurs from δ -phase to α -phase. However, we could not observe any change in their morphology, as indicated in Figure 7.9.

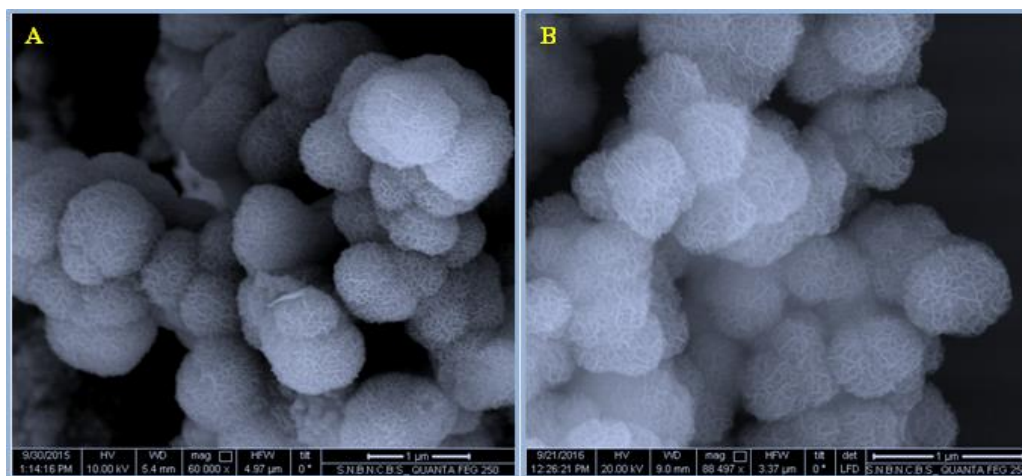


Figure 7.9: FESEM images of MnO_2 nanoflowers (A) before and (B) after heating.

7.3.2.7 Determination of Zeta-potential of δ -MnO₂/HNTs NCs

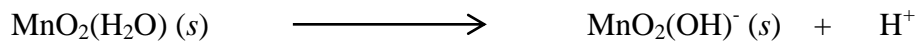
The ζ - potential of δ -MnO₂/HNTs NCs is negative, whereas it is positive for amine functionalized HNTs (Table 7.1). The negative charge of δ -MnO₂ also may arise due to the presence of large amount of vacancies within the Mn(IV) octahedral sheets,⁴⁷ since the estimated vacant site was found to be approximately 6-7 % of the total Mn sites.^{48,49}

Table 7.1: Summary of the ζ - potential of HNTs, functionalized HNTs and HNTs/MnO₂ NCs.

Sample	Zeta-potential (mV)
HNTs	-18.6
Amine functionalized HNTs	24.5
HNTs/MnO ₂ NCs	-39.6

7.3.2.8 Growth Mechanism Study

Selective surface modification of HNTs with aminosilane facilitates the formation and subsequent growth of flower-like metal oxides over their outer surfaces, which in turn produces HNTs/metal oxide NCs. Upon irradiation of alkaline KMnO₄ solution under visible light, the purple color of the reaction solution gradually diminishes with time, demonstrating that MnO₄⁻ ions were reduced photochemically to MnO₂ and immobilized over the amine functionalized HNTs. In an alkaline condition, a hydrogen ion may be lost from hydrated manganese dioxide surfaces, giving rise to negatively charged particles.⁵⁰



Thus, alkaline condition induces the negative charge to the MnO_2 particles which were then assembled over the outer surfaces of amine functionalized HNTs through electrostatic interaction and finally grown as flower-like architecture.

It is also important to note that there is no apparent reaction occurs when the reaction solution is neutral. Figure 7.10 shows FESEM images of the intermediates

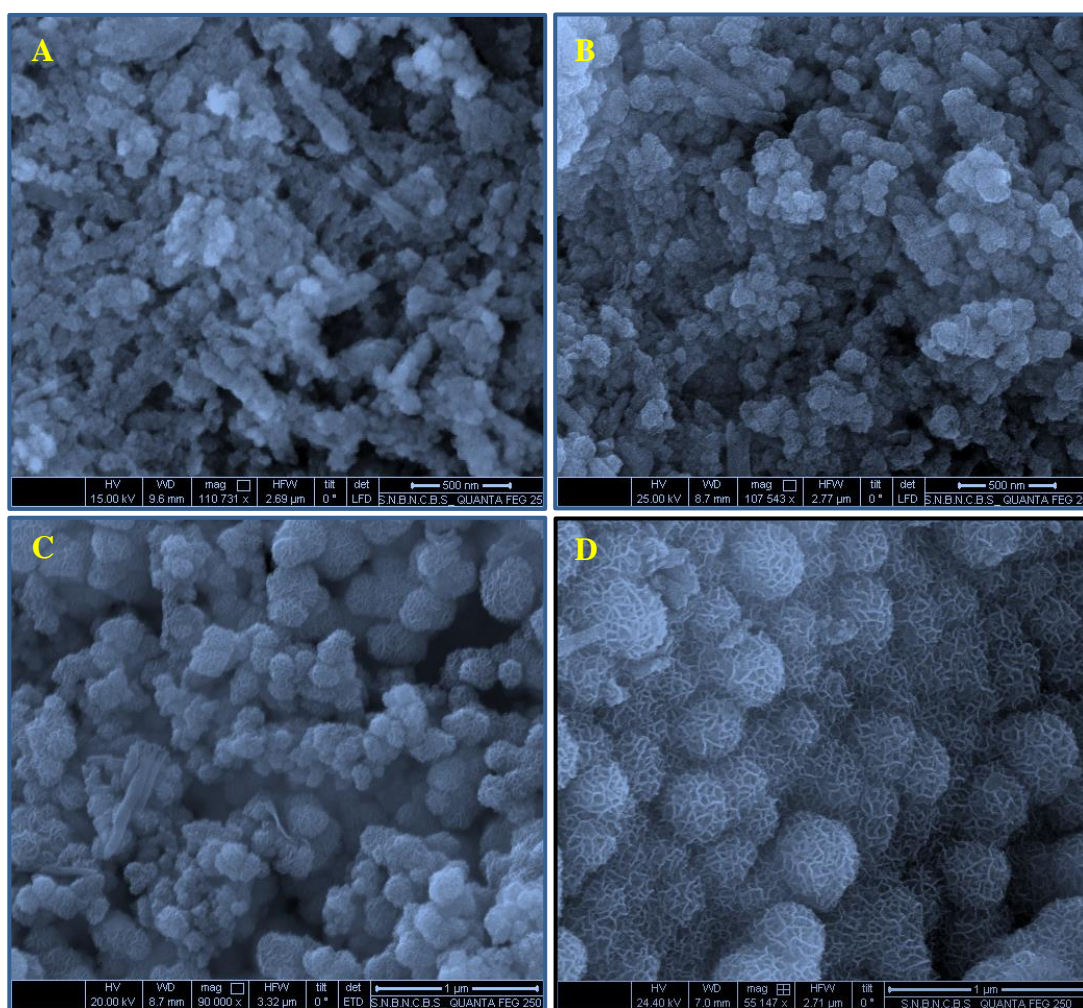


Figure 7.10: FESEM images of the intermediates during the formation of flower-like $\delta\text{-MnO}_2$ nanostructures under the light-assisted decomposition techniques at different time (A) 1 h, (B) 2 h, (C) 4 h, and (D) 6 h respectively, demonstrating the time-dependent evolution of $\delta\text{-MnO}_2$ nanoflowers through the seeded growth procedure.

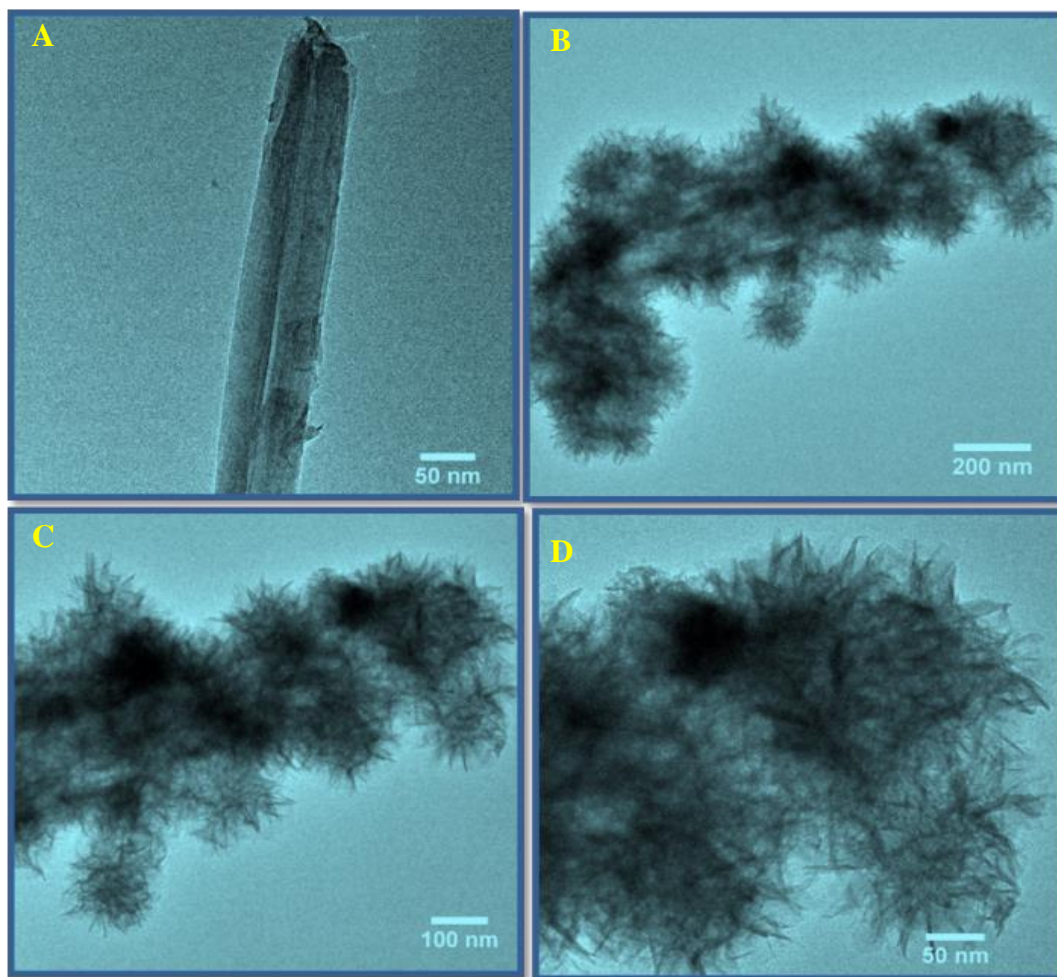


Figure 7.11: TEM micrographs of (A) a single halloysite nanotube (HNT) and (B-D) MnO₂ nanoflowers grow over the surface of the nanotube.

during the formation of flower-like δ -MnO₂ nanostructures under the light-assisted decomposition techniques at different time. As shown in Figure 7.10, the intermediate formed after 1 h is composed of tiny nanoparticles, which are gradually grown into a flower-like architecture as the reaction time progresses and finally well transform nanoflowers are achieved on to the surface of HNTs after 6 h of the reaction time. Therefore, the proposed growth mechanism encompasses the formation of tiny MnO₂ nanoparticle seeds, followed by self-assembles of those seeds through a seeded growth mechanism to produce hierarchical flower-like nanostructures of MnO₂. It is also evident

from the TEM images that all the functionalized HNTs are covered completely by δ -MnO₂ nanoflowers, which are well grown on their outer surfaces. Figure 7.11 demonstrates TEM images of MnO₂ nanoflowers onto the surface of a single cylindrical shaped HNT, leaving aside no empty surfaces. TEM analysis further substantiates strong electrostatic interactions between MnO₂ nanoflowers and functionalized HNTs, since they are firmly attached to the HNTs surfaces and no nanosheets are coming out even after sonication, which further supports the robustness of the structures.

7.3.2.9 BET Surface Area Measurement

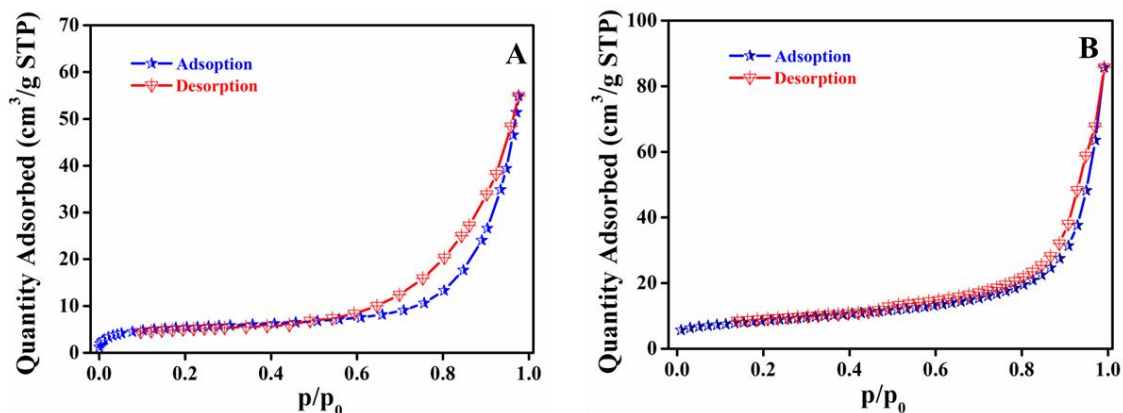


Figure 7.12: The nitrogen adsorption/desorption isotherms of (A) HNTs after functionalization with aminosilane and (B) HNTs/ δ -MnO₂ nanocomposites, signifying the distinctive signature of mesoporous materials.

To demonstrate the specific surfaces of HNTs and HNTs/MnO₂ NCs, nitrogen adsorption/desorption study was performed at 77 K, shown in Figure 7.12. The isotherm of the HNTs is of type II with H3 hysteresis loops according to IUPAC classification, whereas it is of type IV for MnO₂ NCs, indicating the distinctive signature of mesoporous materials. The specific surface area of HNTs and the flower-like NCs was estimated to be 18 and 30 m²g⁻¹ by Brunauer–Emmett–Teller (BET) method. Hence, the increase in surface area in the flower-like NCs will facilitate to enhance their photocatalytic efficacy

7.3.2.10 UV-visible Diffuse Reflectance Study

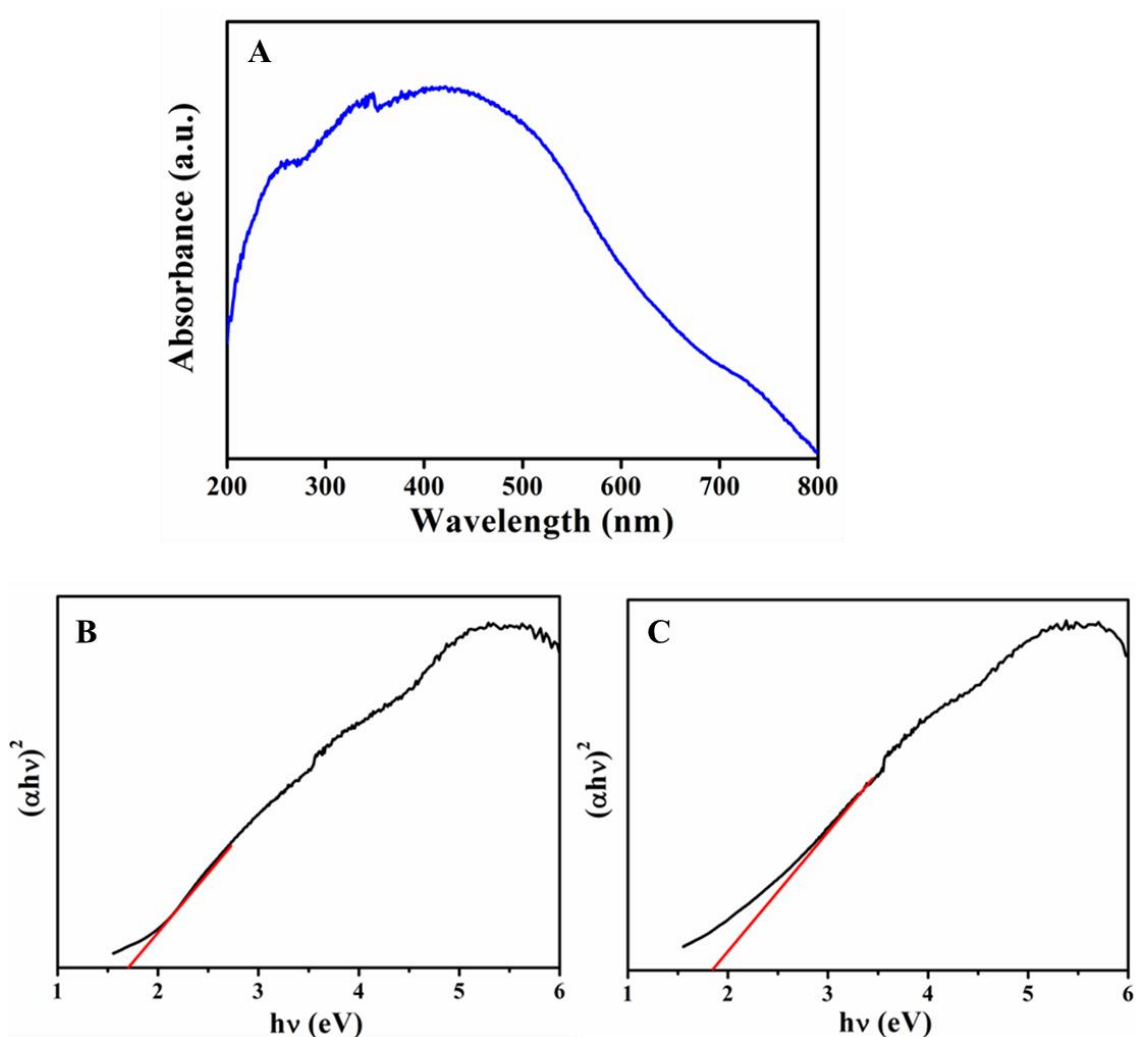


Figure 7.13: (A) UV-visible diffuse reflectance spectrum of flower-like hierarchical δ -MnO₂ nanostructures grow over the surfaces of HNTs. Band gap energy plots for (B) HNTs/ δ -MnO₂ and (C) HNTs/ α -MnO₂ nanocomposites respectively.

UV-visible diffuse reflectance spectrum of HNTs/ δ -MnO₂ NCs exhibits a broad band in the region of 350 - 550 nm with a distinct band edge around 425 nm (Figure 7.13A). The characteristic optical absorption of MnO₂ NCs can be attributed to the $\text{Mn}^{4+} \leftarrow \text{O}_2^-$

charge transfer transitions,⁵¹ together with d-d transitions in Mn ions⁵² originating due to the split of the Mn 3d energy level into higher (e_g) and lower (t_{2g}) energy levels due to the ligand field of MnO_6 octahedra. We have estimated the band gap energy for HNTs/ δ - MnO_2 and HNTs/ α - MnO_2 nanocomposites and is found to be 1.70 and 1.85 eV respectively, as shown in Figure 7.13B & C.

7.3.2.11 ICP-OES Analysis

The concentration of the loaded manganese onto the halloysite clays was assessed to be ~13.37 wt% of the clays estimated using inductively coupled plasma optical emission spectrometry (ICP-OES) technique. The elemental composition analysis obtained by EDS study further demonstrated that 12.92 wt% Mn was immobilized in HNTs/ MnO_2 NCs, which is in good agreement with the result obtained through ICP analysis.

Thus, the present work represents a low-temperature solution chemistry approach for the synthesis of hierarchical flower-like δ - MnO_2 nanostructures over nanoclays to study their photocatalytic efficiency for the degradation of several organic dyes under natural sunlight irradiations.

7.3.3 Photocatalytic Activity of HNTs/ MnO_2 NCs

7.3.3.1 Degradation of Organic Pollutants

The degradation of the refractory pollutants has withdrawn immense interest and become a key challenge to diminish their impact on the environmental health and safety. Keeping the impact of the refractory pollutants in mind, we have studied the catalytic performance of hierarchical flower-like HNTs/ δ - MnO_2 NCs for wastewater treatment by considering the degradation of organic dyes in aqueous solution under sunlight irradiation at room temperature. Methylene blue (MB) and eosin yellow (EY), having complex aromatic

molecular structure, were chosen as model contaminants for this study. Once the dye solution reached an adsorption–desorption equilibrium (Figure 7.14A & B), it was then exposed to the irradiation source and the degradation reaction was studied.

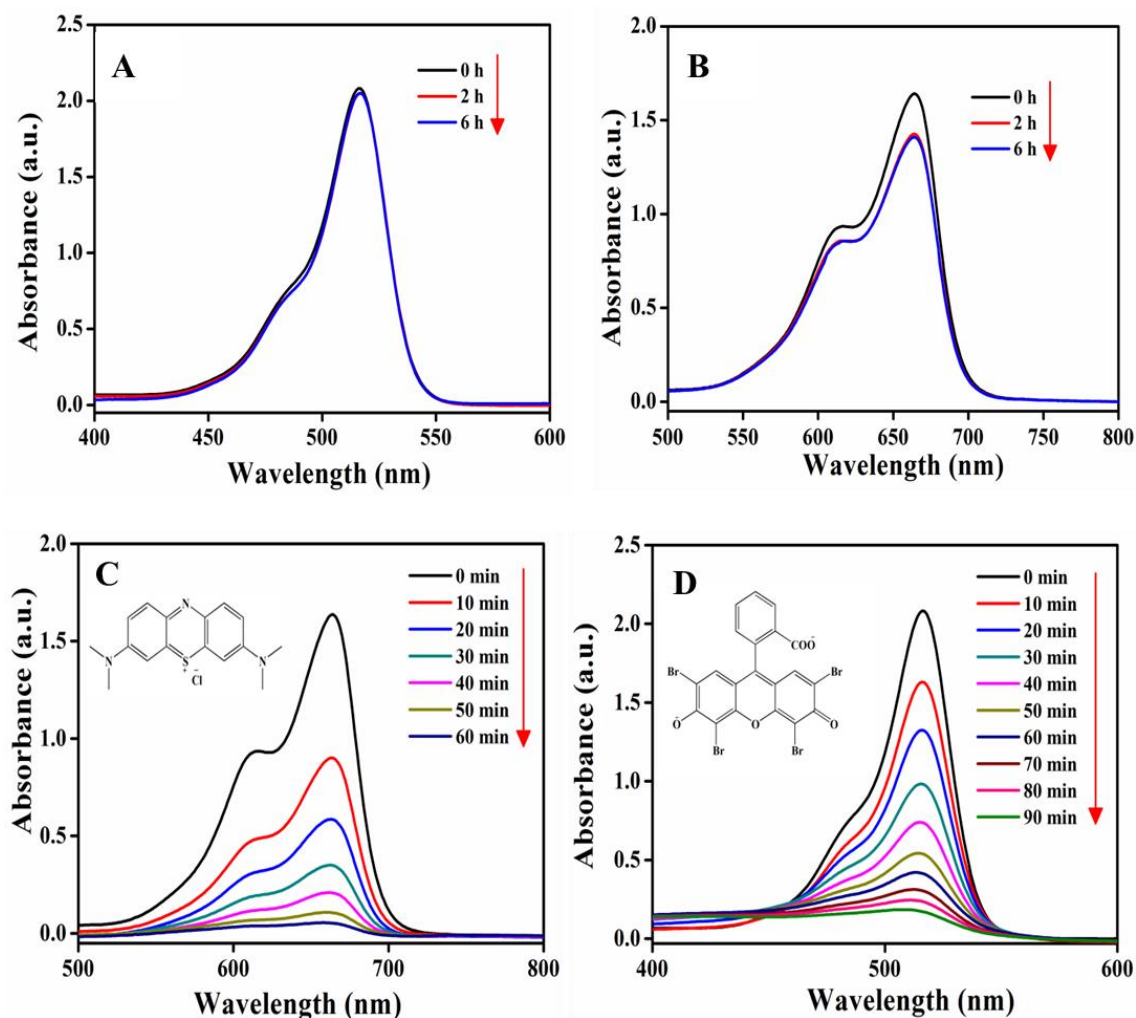


Figure 7.14: UV-Visible absorption spectra for the adsorption–desorption equilibrium study of (A) EY and (B) MB as a function of time. We hardly see any adsorption for EY since it is a negatively charged dye, whereas we have seen some adsorption of MB (~14%) by HNTs/ δ -MnO₂ NCs, since MB is a positively charged dye. The UV-visible absorption spectra of (C) MB and (D) EY as a function of reaction time in the process of photodegradation under solar light using hierarchical flower-like HNTs/ δ -MnO₂ NCs as catalysts.

The UV-visible absorption spectra of MB and EY as function of reaction time in the process of photodegradation and the rate of degradation under solar light are presented in Figure 6. As the reaction proceeds, the characteristic absorbance of MB at 664 nm which was chosen to monitor the catalytic process gradually decreases, demonstrating the degradation of the dye with time (Figure 7.14C). Again, the color of the dye solution changed from blue to light blue and finally to colorless over the degradation process.⁵³ Similarly, the characteristic absorbance of EY at 515 nm steadily decreases and the yellow color of the solution progressively faded away and became colorless upon irradiation of sunlight.⁵⁴ Figure 7.14D shows the absorption spectra of EY dye solution in presence of HNTs/MnO₂ NCs under irradiation of direct sunlight at different time interval.

7.3.3.2 Kinetics of the Degradation Reaction

The photocatalytic efficiency of the NCs has also been verified under UV light irradiation. Figure 7.15A and B indicate the change in concentration of the dye solution with time for UV and sunlight irradiation, suggesting that both the dyes degrade at faster rate under sunlight in comparison to UV light. The kinetics of the degradation process was further explored using HNTs/MnO₂ NCs under these two different irradiation sources based on the pseudo-first-order kinetic model:

$$\ln(C_t/C_0) = -kt \quad (7.2)$$

where, C_0 is the initial concentration of the dyes, C_t is the concentration of dyes with regard to the degradation time t and k is the reaction rate constant. The degradation of MB and EY obeyed the pseudo-first-order kinetic model (Figure 7.15C and D) and the corresponding rate constants of the degradation reactions were assessed for UV and solar irradiation. Degradation efficiency, time, and the reaction rate constants for these dyes are demonstrated in Table 7.2. The higher reaction rate constant under sunlight compared to UV light for both the dyes attributes to their faster degradation under sunlight than that

of UV light irradiation, which further ascribed to the enhanced photocatalytic activity of HNTs/MnO₂ NCs in presence of natural solar light. This may be due to the fact that MnO₂ possesses characteristic optical absorption in the region of 350 - 550 nm with a distinct band edge around 425 nm. With the aim to verify the impact of HNTs towards the degradation process using HNTs/MnO₂ NCs, the photodegradation of the dyes was carried out exclusively using pristine HNTs. However, they hardly show any catalytic efficiency towards photodegradation and hence don't impart any effect during the degradation of dyes (Figure 7.16).

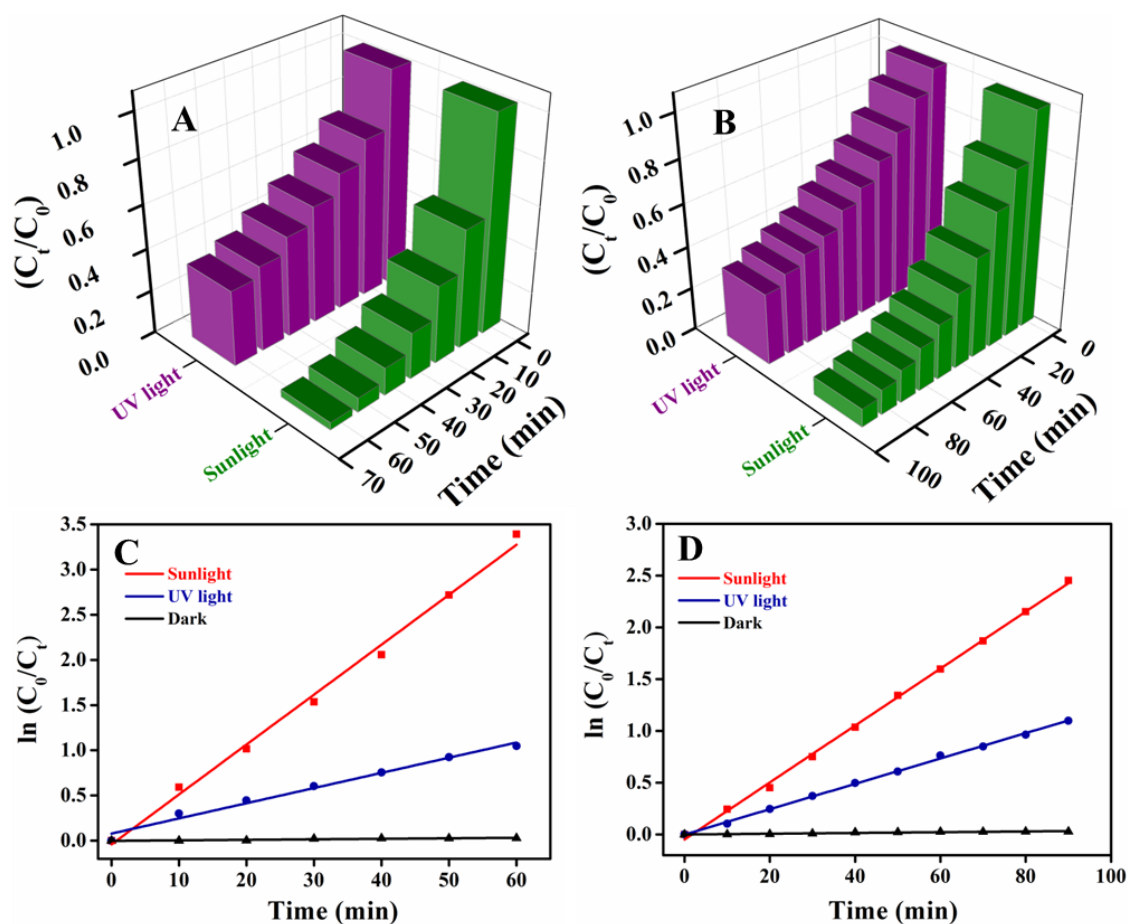


Figure 7.15: (A) and (B) indicate the change in concentration of the MB and EY solution with time under the irradiation of UV and sunlight respectively. Rate of degradation of (C) MB and (D) EY under irradiation of two different light sources, demonstrating their faster degradation under sunlight than that of UV light.

Table 7.2: Summary of the degradation percentage of MB and EY at a specific time and the corresponding rate constants under UV and solar light irradiation using hierarchical flower-like HNTs/ δ -MnO₂ NCs based on the pseudo-first-order kinetic model.

Catalyst	Dyes	Irradiation Source	Degradation Time (min)	% of Degradation	First-Order Rate Constant (k, min ⁻¹)
HNTs/ δ -MnO ₂	MB	Sunlight	60	97	0.05526
		UV light	120	83	0.01679
	EY	Sunlight	90	92	0.02751
		UV light	120	76	0.01224

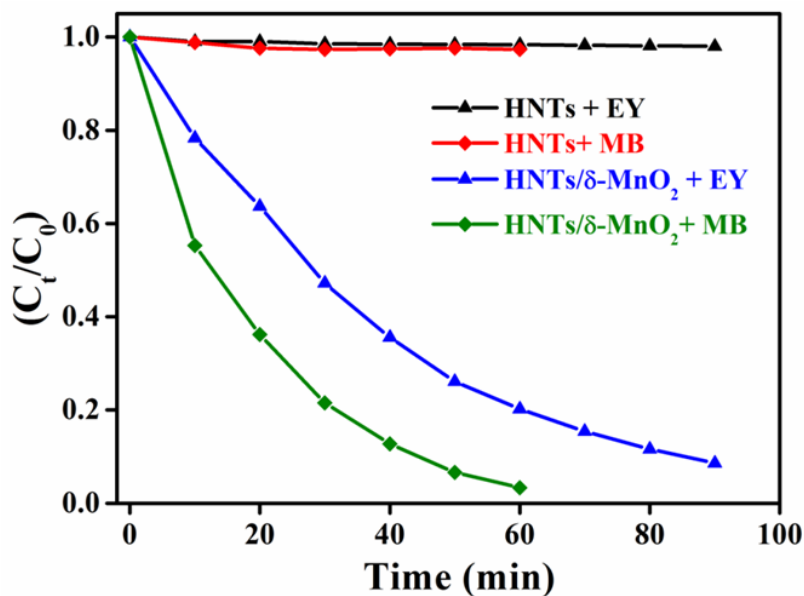


Figure 7.16: Catalytic efficiency of HNTs towards photodegradation of EY and MB, exhibiting that they don't have any catalytic effect during the degradation of dyes.

7.3.3.3 Recyclability Study

From a practical point of view, it is always important for a catalyst to have structural stability during the catalytic process. The repetitive use of HNTs/ δ -MnO₂ NCs toward the degradation of dyes as a function of time demonstrates excellent recycling capability and outstanding degradation performance (Figure 7.17A and B). Apart from their recyclability, easy recovery from the reaction solution through simple filtration is another salient advantage of such heterogeneous catalysts.

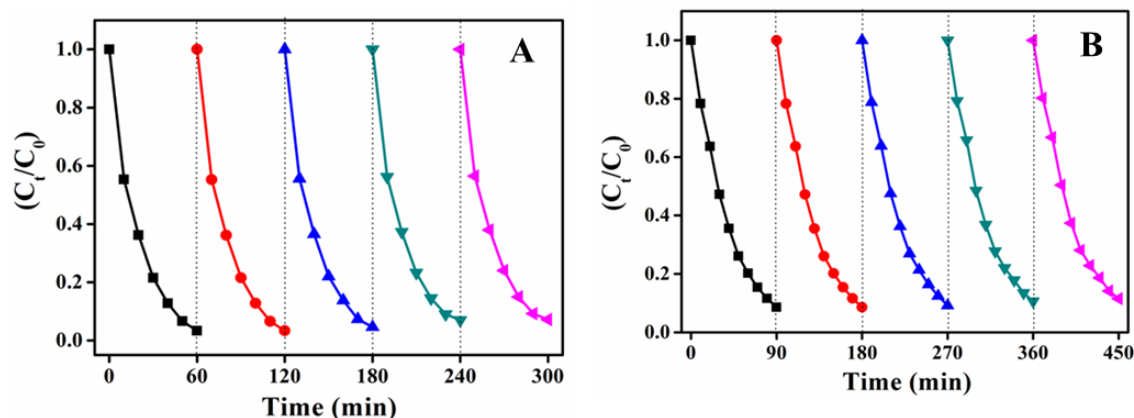


Figure 7.17: Multi-cycle degradation performances of hierarchical flower-like HNTs/ δ -MnO₂ NCs toward the degradation of (A) MB and (B) EY under sunlight irradiation.

7.3.3.4 Comparison of Catalytic Efficiency

Finally, we have compared the catalytic efficiency of HNTs/ δ -MnO₂ NCs with the reported MnO₂ based catalysts (Table 7.3), corroborating their higher catalytic efficacy towards the photodegradation of organic dyes. With the α -phase of HNTs/MnO₂ NCs, obtained upon heating the sample at 450 °C, the photodegradation reaction was also carried out keeping all the other experimental condition the same. It was found that HNTs/ δ -MnO₂ NCs possess higher catalytic efficiency in contrast to HNTs/ α -MnO₂ NCs and thus follow the order: δ -MnO₂ > α -MnO₂ NCs (Figure 7.18). This might be accredited to their different exposed crystallographic facets that showed varied adsorption

ability to the reactants or there may be a slight impact of the band gap energies of the nanocomposites during the degradation of dyes, resulting in their diverse catalytic activity.

Table 7.3: Comparison of the photocatalytic efficacy of HNTs/ δ -MnO₂ NCs with the reported MnO₂ based catalysts for the degradation of MB. Data were taken from the respective papers.

Catalyst	Dye Conc. (mg/L)	Degradation (%) of MB	Catalyst Dose (mg/L)	Time (min)	Weight Ratio [#]	References
Meso-MnO ₂ - MCM-41	100	99	1000	60	0.099	55
δ -MnO ₂	80	92	2000	700	0.0396	56
δ -MnO ₂ /montmorillonite	80	92	2000	700	0.0368	56
Pelagite	50	98	3000	100	0.016	57
MnO ₂	20	93	200	180	0.093	58
MnO ₂ /Fe ₃ O ₄	20	98.2	200	180	0.098	58
MnO ₂	10	51.1	500	60	0.010	59
Mn ₃ O ₄ -MnO ₂	10	93.5	500	60	0.019	59
HNTs/ δ -MnO ₂	10	97	40	60	0.243	Present work

#Weight Ratio indicates a ratio between the degraded MB in mg and corresponding amount of catalyst in mg.

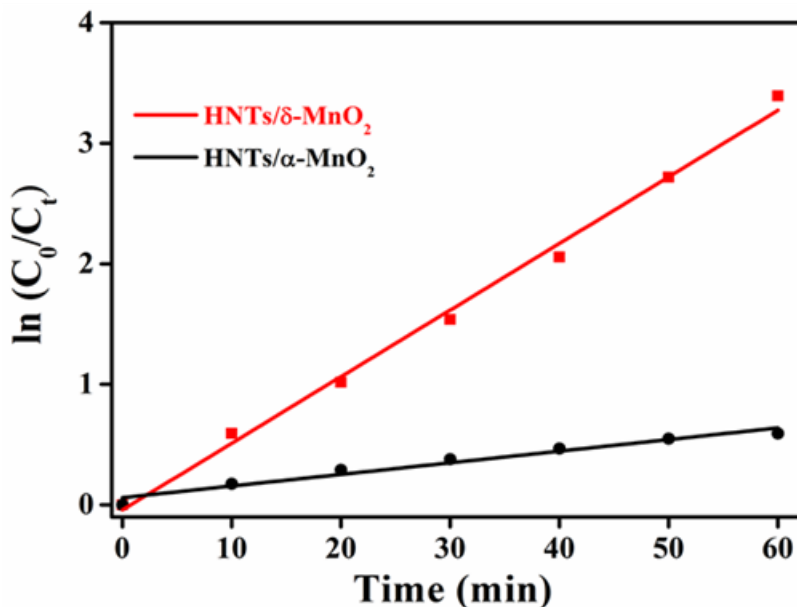


Figure 7.18: Comparison of the photodegradation efficiency of HNTs/ δ -MnO₂ vs. HNTs/ α -MnO₂ NCs, demonstrating HNTs/ δ -MnO₂ NCs possess higher catalytic efficiency than that of HNTs/ α -MnO₂ NCs.

7.3.3.5 Photocatalytic Degradation Mechanism

To demonstrate the degradation reaction proceeds through a photocatalytic pathway via the formation of reactive oxygen species due to the irradiation of light, photodegradation of MB was carried out after the addition of a supplementary oxygen source, H₂O₂, to the dye solution keeping all the experimental condition unaltered and then exposed to the sunlight (Figure 7 D). It was evident that the rate of photodegradation of MB is significantly increased in presence of H₂O₂, signifying the possible formation of reactive oxygen species due to the irradiation of light and thus enhances the degradation rate. To further authenticate the formation of primary active species and their role during photocatalysis, the reaction was performed using *tert*-butyl alcohol (*t*-BA) which is a scavenger of hydroxyl radicals ($\cdot\text{OH}$), and sodium azide, a quencher of both singlet oxygen ($^1\text{O}_2$) and hydroxyl radicals ($\cdot\text{OH}$) respectively, so that they can scavenge the generated reactive oxygen species in the reaction medium (Figure 7.19A). The

degradation reaction was also studied in presence of triethanolamine (TEA), a scavenger of hole (h^+). Figure 7.19B compares the photocatalytic rate in presence of scavengers, which clearly shows that the photocatalytic efficacy of HNTs/ δ -MnO₂ NCs was significantly inhibited, further attributing to the formation of reactive oxygen species during photocatalysis.

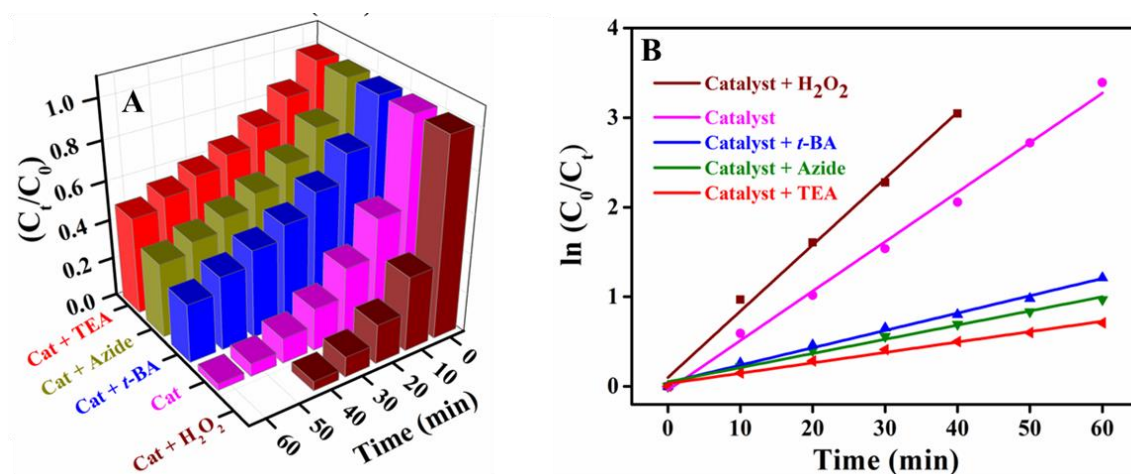


Figure 7.19: (A) Comparison of the change in concentration of MB in presence of a supplementary oxygen source and scavengers under solar light using HNTs/ δ -MnO₂ and (B) corresponding rate of degradation, demonstrating the degradation reaction occurs due to the formation of reactive oxygen species during photocatalysis.

Based on the aforesaid observation, photocatalytic mechanism of MnO₂ NCs is proposed in Scheme 7.1. The predominant photogenerated active species are h^+ , \cdot OH and also 1 O₂, among which last two species originated probably due to the interaction of photoexcited conduction band electrons with molecular oxygen at the surface of the MnO₂ nanoflowers. \cdot OH also may be produced through direct oxidation of surface adsorbed H₂O molecules by h^+ . As a consequence, photogenerated several active species take part in the photocatalytic reaction and thus facilitate to enhance the photocatalytic activity of the catalyst. We have further assessed the conduction band (CB) and valence

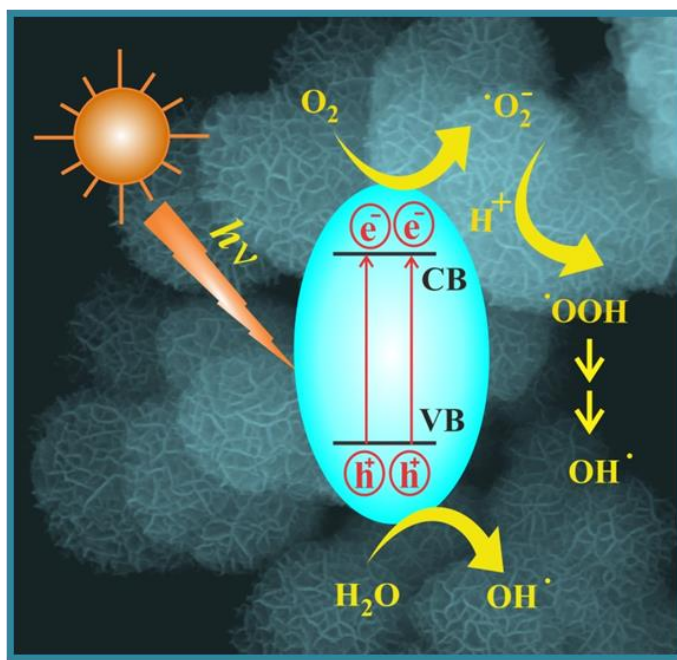
band (VB) potential for MnO₂ NCs to confirm the generation of active species. These energy levels were calculated using the following empirical equations:⁶⁰

$$E_{CB} = \chi - E^e - 0.5E_g \quad (7.3)$$

$$E_{VB} = E_{CB} + E_g \quad (7.4)$$

$$\chi = [\chi(A)^a \chi(B)^b]^{\frac{1}{(a+b)}} \quad (7.5)$$

where, E_{VB} and E_{CB} are the VB and CB potentials and E^e is the energy of free electrons on the hydrogen scale (4.5 eV). E_g is the band gap energy of the semiconductor and χ is the absolute electronegativity of the semiconductor, determined as the geometric mean of the electronegativity of the constituent atoms. A and B are the atoms present in the semiconductor, whereas a and b are the number of those atoms. E_g and χ for MnO₂



Scheme 7.1. Proposed photocatalytic mechanism for the degradation of organic dyes using flower-like MnO₂ nanocomposites in presence of solar light, demonstrating the formation of several reactive oxygen species.

nanostructures are found to be 1.7 and 5.95 eV respectively. Thus, E_{CB} and E_{VB} of MnO_2 nanostructures are estimated to be 0.60 and 2.30 eV, which in turn demonstrate the generation of active species upon irradiation of light and those photogenerated active species assist degradation of dyes. Hence, hierarchical flower-like δ - MnO_2 nanostructured supported on clay nanotubes would be a promising candidate to fabricate photocatalytic reaction devices for environmental remediation by eliminating the organic pollutants from wastewater.

7.4 Conclusions

In summary, we have established a light-assisted solution chemistry route for the synthesis of nanoscale hierarchical flower-like MnO_2 over the surface of aluminosilicate clay nanotubes. Microscopic analysis demonstrates that δ - MnO_2 nanoflowers comprise of assemblies of many wrinkled and intersected nanosheets. The photocatalytic activity of the HNTs/ δ - MnO_2 NCs has been investigated towards the degradation of organic dyes in presence of renewable and never-ending solar energy. The crystallographic phase dependent photocatalytic activity of HNTs/ MnO_2 NCs demonstrated that δ - MnO_2 possess higher catalytic efficiency compared to α - MnO_2 . The underlying photocatalytic mechanism suggests the formation of reactive oxygen species that facilitate the degradation of dyes. Thus the present work points to a low-temperature environment-friendly approach for the synthesis of hierarchical flower-like δ - MnO_2 nanostructures, which may be considered to be an alternative heterogeneous photocatalyst for the degradation of organic pollutants under natural sunlight irradiations. The process should be fascinating because of the easy control over reaction conditions, possible scaling up, and recycling of the nanocomposites, as well as no need of any supplementary oxygen sources during photodegradation, which in turn may open up a broader impact in the area of environmental remediation including clean-up process of the industrial effluents to ground water treatment.

7.5 References

1. Houk, V. S. The Genotoxicity of Industrial Wastes and Effluents. *Mutat. Res.* **1992**, *277*, 91-138.
2. Kyung, H.; Lee, J.; Choi, W. Simultaneous and Synergistic Conversion of Dyes and Heavy Metal Ions in Aqueous TiO₂ Suspensions under Visible-Light Illumination. *Environ. Sci. Technol.* **2005**, *39*, 2376–2382.
3. Grau, P. Textile Industry Wastewater Treatment. *Water Sci. Technol.* **1991**, *24*, 97–103.
4. Sloker, Y. M.; LeMarechal, A. M. Methods of Decolorization of Textile Wastewater. *Dyes Pigm.* **1998**, *37*, 335–356.
5. Kubacka, A.; Fernandez-Garcia, M.; Colon, G. Advanced Nanoarchitectures for Solar Photocatalytic Applications. *Chem. Rev.* **2012**, *112*, 1555–1614.
6. Legrini, O.; Oliveros, E.; Braun, A. M. Photochemical Processes for Water Treatment. *Chem. Rev.* **1993**, *93*, 671–698.
7. Mills, A.; Davies, R. H.; Worsley, D. Water Purification by Semiconductor Photocatalysis. *Chem. Soc. Rev.* **1993**, *22*, 417–425.
8. Wang, T.; Li, C.; Ji, J.; Wei, Y.; Zhang, P.; Wang, S.; Fan, X.; Gong, J. Reduced Graphene Oxide (rGO)/BiVO₄ Composites with Maximized Interfacial Coupling for Visible Light Photocatalysis. *ACS Sustainable Chem. Eng.* **2014**, *2*, 2253–2258.
9. Hoffmann, M. R.; Martin, S. T.; Choi, W. Y.; Bahnemann, D. W. Environmental Applications of Semiconductor Photocatalysis. *Chem. Rev.* **1995**, *95*, 69–96.
10. Djurišić, A. B.; Leunga, Y. H.; Ng, A. M. C. Strategies for Improving the Efficiency of Semiconductor Metal Oxide Photocatalysis. *Mater. Horiz.* **2014**, *1*, 400–410.
11. Espinal, L.; Suib, S. L.; Rusling, J. F. Electrochemical Catalysis of Styrene Epoxidation with Films of MnO₂ Nanoparticles and H₂O₂. *J. Am. Chem. Soc.* **2004**, *126*, 7676–7682.
12. Lin, Y. M.; Li, D. Z.; Hu, J. H.; Xiao, G. C.; Wang, J. X.; Li, W. J.; Fu, X. Z. Highly Efficient Photocatalytic Degradation of Organic Pollutants by PANI-Modified TiO₂ Composite. *J. Phys. Chem. C* **2012**, *116*, 5764–5772.
13. Liu, J. T.; Ge, X.; Ye, X. X.; Wang, G. Z.; Zhang, H. M.; Zhou, H. J.; Zhang Y. X.; Zhao, H. J. 3D Graphene/ δ -MnO₂ Aerogels for Highly Efficient and Reversible Removal of Heavy Metal Ions. *J. Mater. Chem. A* **2016**, *4*, 1970–1979.
14. Crespo, Y.; Seriani, N. A Lithium Peroxide Precursor on the α -MnO₂ (100) Surface. *J. Mater. Chem. A* **2014**, *2*, 16538–16546.
15. Cao, J.; Mao, Q.; Shi, L.; Qian, Y. Fabrication of γ -MnO₂/ α -MnO₂ Hollow Core/Shell Structures and their Application to Water Treatment. *J. Mater. Chem.* **2011**, *21*, 16210–16215.
16. Ou, M.; Huang, J.; Yang, X.; Quan, K.; Yang, Y.; Xie, N.; Wang, K. MnO₂ Nanosheet Mediated “DD–A” FRET Binary Probes for Sensitive Detection of Intracellular mRNA. *Chem. Sci.* **2017**, *8*, 668–673.

17. Yuan, Y.; Wu, S.; Shu, F.; Liu, Z. An MnO₂ Nanosheet as a Label-Free Nanoplatfom for Homogeneous Biosensing. *Chem. Commun.* **2014**, *50*, 1095–1097.
18. Zhang, K.; Han, X.; Hu, Z.; Zhang, X.; Tao, Z.; Chen, J. Nanostructured Mn-based Oxides for Electrochemical Energy Storage and Conversion. *Chem. Soc. Rev.* **2015**, *44*, 699-728.
19. Lang, X. Y.; Hirata, A.; Fujita, T.; Chen, M. W. Nanoporous Metal/Oxide Hybrid Electrodes for Electrochemical Supercapacitors. *Nat. Nanotechnol.* **2011**, *6*, 232–236.
20. Thackeray, M. M. Manganese Oxides for Lithium Batteries. *Prog. Solid State Chem.* **1997**, *25*, 1–71.
21. Truong, T. T.; Liu, Y.; Ren, Y.; Trahey, L.; Sun, Y.; Morphological and Crystalline Evolution of Nanostructured MnO₂ and Its Application in Lithium-Air Batteries. *ACS Nano* **2012**, *6*, 8067-8077.
22. Wang, X.; Li, Y. Selected-Control Hydrothermal Synthesis of α - and β -MnO₂ Single Crystal Nanowires. *J. Am. Chem. Soc.* **2002**, *124*, 2880–2881.
23. Sui, N.; Duan, Y. Z.; Jiao, X. L.; Chen, D. R. Large-Scale Preparation and Catalytic Properties of One-Dimensional α/β -MnO₂ Nanostructures. *J. Phys. Chem. C* **2009**, *113*, 8560–8565.
24. Jung, W. II; Nagao, M.; Pitteloud, C.; Itoh, K.; Yamada, A.; Kanno, R. Chemically Oxidized γ -MnO₂ for Lithium Secondary Batteries; Structure and Intercalation / Deintercalation Properties. *J. Mater. Chem.* **2009**, *19*, 800–806.
25. Zhang, J.; Luan, Y.; Lyu, Z.; Wang, L.; Xu, L.; Yuan, K.; Pan, F.; Lai, M.; Liu, Z.; Chen, W. Synthesis of Hierarchical Porous δ -MnO₂ Nanoboxes as an Efficient Catalyst for Rechargeable Li–O₂ Battery. *Nanoscale* **2015**, *7*, 14881-14888.
26. Poyraz, A. S.; Song, W.; Kriz, D.; Kuo, C.-H.; Seraji, M. S.; Suib, S. L. Crystalline Mesoporous K_{2-x}Mn₈O₁₆ and ϵ -MnO₂ by Mild Transformations of Amorphous Mesoporous Manganese Oxides and Their Enhanced Redox Properties. *ACS Appl. Mater. Interfaces* **2014**, *6*, 10986-10991.
27. Li, W. N.; Yuan, J. K.; Shen, X. F.; Gomez-Mower, S.; Xu, L. P.; Sithambaram, S.; Aindow, M.; Suib, S. L. Hydrothermal Synthesis of Structure- and Shape-Controlled Manganese Oxide Octahedral Molecular Sieve Nanomaterials. *Adv. Funct. Mater.* **2006**, *16*, 1247–1253.
28. Qiu, G.; Huang, H.; Dharmarathna, S.; Benbow, E.; Stafford, L.; Suib, S. L. Hydrothermal Synthesis of Manganese Oxide Nanomaterials and Their Catalytic and Electrochemical Properties. *Chem. Mater.* **2011**, *23*, 3892–3901.
29. Wang, X.; Yuan, A.; Wang, Y. Supercapacitive Behaviors and Their Temperature Dependence of Sol-Gel Synthesized Nanostructured Manganese Dioxide in Lithium Hydroxide Electrolyte. *J. Power Sources* **2007**, *172*, 1007–1011.
30. Ching, S.; Petrovay, D. J.; Jorgensen, M. L.; Suib, S. L. Sol-Gel Synthesis of Layered Birnessite-Type Manganese Oxides. *Inorg. Chem.* **1997**, *36*, 883-890.

31. Brousse, T.; Toupin, M.; Dugas, R.; Athouel, L.; Crosnier, O.; Belanger, D. Crystalline MnO₂ as Possible Alternatives to Amorphous Compounds in Electrochemical Supercapacitors. *J. Electrochem. Soc.* **2006**, *153*, A2171–A2180.
32. Xie, X.; Zhang, C.; Wu, M. B.; Tao, Y.; Lv, W.; Yang, Q. H. Porous MnO₂ for Use in a High Performance Supercapacitor: Replication of a 3D Graphene Network as a Reactive Template. *Chem. Commun.* **2013**, *49*, 11092–11094.
33. Yu, C. C.; Zhang, L. X.; Shi, J. L.; Zhao, J. J.; Gao, J. H.; Yan, D. S. A Simple Template-Free Strategy to Synthesize Nanoporous Manganese and Nickel Oxides with Narrow Pore Size Distribution, and Their Electrochemical Properties. *Adv. Funct. Mater.* **2008**, *18*, 1544–1554.
34. Duay, J.; Sherrill, S. A.; Gui, Z.; Gillette, E.; Lee, S. B. Self-Limiting Electrodeposition of Hierarchical MnO₂ and M(OH)₂/MnO₂ Nanofibril/Nanowires: Mechanism and Supercapacitor Properties. *ACS Nano* **2013**, *7*, 1200–1214.
35. Wang, L.; Chen, J.; Ge, L.; Zhu, Z.; Rudolph, V. Halloysite-Nanotube-Supported Ru Nanoparticles for Ammonia Catalytic Decomposition to Produce CO_x-Free Hydrogen. *Energy Fuels* **2011**, *25*, 3408–3416.
36. Das, S.; Ghosh, C.; Jana, S. Moisture Induced Isotopic Carbon Dioxide Trapping from Ambient Air. *J. Mater. Chem. A* **2016**, *4*, 7632–7640.
37. Liang, J.; Fan, Z.; Chen, S.; Ding, S.; Yang, G. Hierarchical NiCo₂O₄ Nanosheets@Halloysite Nanotubes with Ultrahigh Capacitance and Long Cycle Stability as Electrochemical Pseudocapacitor Materials. *Chem. Mater.* **2014**, *26*, 4354–4360.
38. Abdullayev, E.; Price, R.; Shchukin, D.; Lvov, Y. Halloysite Tubes as Nanocontainers for Anticorrosion Coating with Benzotriazole. *ACS Appl. Mater. Interfaces* **2009**, *1*, 1437–1443.
39. Lvov, Y.; Wang, W.; Zhang, L.; Fakhrullin, R. Halloysite Clay Nanotubes for Loading and Sustained Release of Functional Compounds. *Adv. Mater.* **2016**, *28*, 1227–1250.
40. Das, S.; Jana, S. A Tubular Nanoreactor Directing the Formation of *In-Situ* Iron Oxide Nanorods with Superior Photocatalytic Activity. *Environ. Sci.: Nano* **2017**, *4*, 596–603.
41. Bates, T. F.; Hildebrand, F. A.; Swineford, A. Morphology and Structure of Endellite and Halloysite. *Am. Mineral.* **1950**, *35*, 463–484.
42. Lvov, Y. M.; Shchukin, D. G.; Möhwald, H.; Price, R. R. Halloysite Clay Nanotubes for Controlled Release of Protective Agents. *ACS Nano* **2008**, *2*, 814–820.
43. Das, S.; Maity, A.; Pradhan, M.; Jana, S. Assessing Atmospheric CO₂ Entrapped in Clay Nanotubes using Residual Gas Analyzer. *Anal. Chem.* **2016**, *88*, 2205–2211.
44. Das, S.; Jana, S. A Facile Approach to Fabricate Halloysite/Metal Nanocomposites with Preformed and *In Situ* Synthesized Metal Nanoparticles: A Comparative Study of their Enhanced Catalytic Activity. *Dalton Trans.* **2015**, *44*, 8906–8916.

45. Yuan, P.; Southon, P. D.; Liu, Z.; Green, M. E. R.; Hook, J. M.; Antill, S. J.; Kepert, C. J. Functionalization of Halloysite Clay Nanotubes by Grafting with γ -Aminopropyltriethoxysilane. *J. Phys. Chem. C* **2008**, *112*, 15742–15751.
46. Jana, S.; Das, S.; Ghosh, C.; Maity, A.; Pradhan, M. Halloysite Nanotubes Capturing Isotope Selective Atmospheric CO₂. *Sci. Rep.* **2015**, *5*, 8711.
47. Peacock, C. L.; Sherman, D. M. Sorption of Ni by Birnessite: Equilibrium Controls on Ni in Seawater. *Chem. Geol.* **2007**, *238*, 94–106.
48. Villalobos, M.; Lanson, B.; Manceau, A.; Toner, B.; Sposito, G. Structural Model for the Biogenic Mn Oxide Produced by Pseudomonas Putida. *Am. Mineral.* **2006**, *91*, 489–502.
49. Zhu, M.; Farrow, C. L.; Post, J. E.; Livi, K. J. T.; Billinge, S. J. L.; Ginder-Vogel, M.; Sparks, D. L. Structural Study of Biotic And Abiotic Poorly-Crystalline Manganese Oxides Using Atomic Pair Distribution Function Analysis. *Geochim. Cosmochim. Acta* **2012**, *81*, 39–55.
50. Manahan, S. E. *Environmental Chemistry*, Eighth Edition, **2004**, 118.
51. Gao, T.; Glerup, M.; Krumeich, F.; Nesper, R.; Fjellvag, H.; Norby, P. Microstructures and Spectroscopic Properties of Cryptomelane-type Manganese Dioxide Nanofibers. *J. Phys. Chem. C* **2008**, *112*, 13134–13140.
52. Chacon-Patino, M. L.; Blanco-Tirado, C.; Hinestroza, J. P.; Combariza, M. Y. Biocomposite of Nanostructured MnO₂ and Fique Fibers for Efficient Dye Degradation. *Green Chem.* **2013**, *15*, 2920–2928.
53. Khanchandani, S.; Kumar, S.; Ganguli, A. K. Comparative Study of TiO₂/CuS Core/Shell and Composite Nanostructures for Efficient Visible Light Photocatalysis. *ACS Sustainable Chem. Eng.* **2016**, *4*, 1487–1499.
54. Debnatha, S.; Ballava, N.; Nyonia, H.; Maityb, A.; Pillay, K.; Optimization and Mechanism Elucidation of the Catalytic-photo-Degradation of the Dyes Eosin Yellow (EY) and Naphthol Blueblack (NBB) by a Polyaniline-Coated Titanium Dioxide Nanocomposite. *Appl. Catal. B: Environ.* **2015**, *163*, 330–342.
55. Nanda, B.; Pradhan, A. C.; Parida, K. A Comparative Study on Adsorption and Photocatalytic Dye Degradation under Visible Light Irradiation by Mesoporous MnO₂ Modified MCM-41 Nanocomposite. *Microporous Mesoporous Mater.* **2016**, *226*, 229–242.
56. Zhu, M. X.; Wang, Z.; Xu, S. H.; Li, T. Decolorization of Methylene Blue by δ -MnO₂-Coated Montmorillonite Complexes: Emphasizing Redox Reactivity of Mn-Oxide Coatings. *J. Hazard. Mater.* **2010**, *181*, 57–64.
57. Zhu, M.-X.; Wang, Z.; Zhou, L.-Y. Oxidative Decolorization of Methylene Blue Using Pelagite. *J. Hazard. Mater.* **2008**, *150*, 37–45.
58. Zhang, L.; Lian, J.; Wu, L.; Duan, Z.; Jiang, J.; Zhao, L. Synthesis of a Thin-Layer MnO₂ Nanosheet-Coated Fe₃O₄ Nanocomposite as a Magnetically Separable Photocatalyst. *Langmuir* **2014**, *30*, 7006–7013.
59. Zhao, J.; Nan, J.; Zhao, Z.; Li, N.; Liu, J.; Cui, F. Energy-Efficient Fabrication of a Novel Multivalence Mn₃O₄-MnO₂ Heterojunction for Dye Degradation Under Visible Light Irradiation. *Appl. Catal. B Environ.* **2017**, *202*, 509–517.

60. Mousavi, M.; Habibi-Yangjeh, A.; Abitorabi, M. Fabrication of Novel Magnetically Separable Nanocomposites Using Graphitic Carbon Nitride, Silver Phosphate and Silver Chloride and their Applications in Photocatalytic Removal of Different Pollutants Using Visible-Light Irradiation. *J. Colloid Interface Sci.* **2016**, *480*, 218-231.

**Clay Nanotubes as Nanoreactor for the Synthesis of Iron Oxides
with Enhanced Photocatalytic Activity**

8.1 Introduction

Confinement of molecules and atoms inside the hollow structure provides a promising and unique strategy for studying structures and chemical properties of individual molecules at the nanoscale, which in turn produces a hollow nano-container to carry out any synthesis at the nanolevel. Over the past decades, a wide range of hollow micro- and nano-containers have been developed including hollow silica sphere, porous alumina templates, carbon nanotubes, supramolecular cages, liposomes, DNA, and micelles to physically confine the size and shape of the growing nanoparticles as well as protect them against surrounding environmental effects.¹⁻⁹ Among the several templates, tubular templates have been attracted increasing interest since they provide the internal hollow space for the formation of rod-shaped nanoparticles which bring forth a rich combination of optical, electronic, and magnetic properties because of their anisotropic morphologies.

Halloysite nanotube (HNT) is an environmental friendly, robust and naturally occurring layered aluminosilicate clay ($\text{Al}_2\text{Si}_2\text{O}_5(\text{OH})_4 \cdot n\text{H}_2\text{O}$) with a well-defined hollow tubular structure, has nowadays become the focus of modern research in material science.¹⁰⁻¹² HNTs formed due to the mismatch in the periodicity between the oxygen sharing tetrahedral SiO_2 sheets and the octahedral AlO_6 sheets, where the adjacent alumina and silica layers along with their water of hydration impart a packing disorder and make the nanotubes curve and roll up to form multilayers.^{13,14} As the clay nanotubes consists of a gibbsite-like array of Al–OH groups on the inner surface and Si–O–Si groups on the outer surface, they demonstrate positive charge at their lumen and negative charge at outer surfaces in a wide range of pH, which therefore facilitate to tune their chemico-physical properties by selectively regulating the chemistry of the constituent

elements, resulting in the fabrication of promising new inorganic-organic hybrid nanocomposites (NCs) to find potential applications in catalysis, adsorption, drug delivery, anticorrosion, enzyme immobilization etc.^{10,14-19} Owing to the availability of the hollow tubular structure i.e.; lumen, HNTs have been used for the controlled or sustained release of drugs or bio-molecules, as a host molecule to encapsulate oil and large size enzymes as well as a nanoreactor to hold reactants for biomimetic synthesis and thus helps to confine the size and diameter of the synthesized nanomaterials,^{18,20-24} demonstrating a new candidate for nanoconfined reactions. Apart from these advantages, HNTs are less expensive compared to carbon nanotubes and at the same time they are biocompatible. However, selective modification of lumen to design new inorganic-organic hybrid NCs or to use them as nanoconfined reactor is still a challenging task.

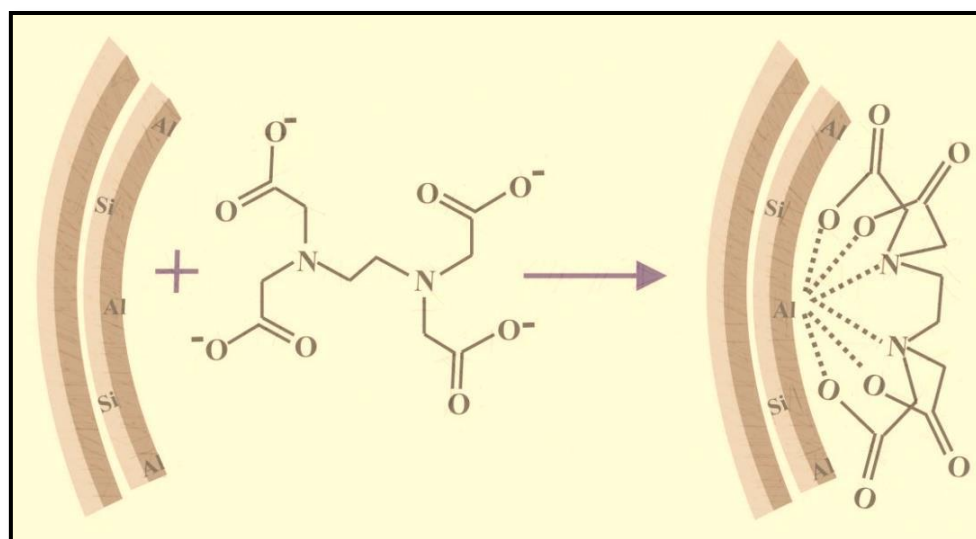
Exploiting the inner lumen of halloysite clays as nanoconfined reactors, we have synthesized nanoscale inorganic materials within the lumen of the nanoclays. After the modification of the lumen using disodium salt of ethylenediaminetetraacetic acid, the selectivity of inner surface modification was characterized by Fourier transform infrared and solid-state nuclear magnetic resonance spectroscopy, demonstrating the binding of EDTA to the alumina site not to the silica site of the tubes. Selective modification of the clay lumen produces an inorganic micelle-like architecture, facilitating the formation of rod-shaped nanoscale iron oxide inside the lumen of the clay nanotubes and finally giving rise to a nanocomposites having α -Fe₂O₃ core with halloysite shell. The as-prepared α -Fe₂O₃/HNTs NCs exhibit enhanced photocatalytic activity in presence of direct sunlight.

8.2 Experimental Section

8.2.1 Lumen Modification of Halloysite Nanotubes

Inner surface modification of halloysite nanotubes (HNTs) using disodium salt of ethylenediaminetetraacetic acid (EDTA) was carried out under nitrogen atmosphere using standard air free techniques.^{12,25} In a 50 mL three-necked round bottom flask, 2.0 g of HNTs and 2.5 g of EDTA-disodium salt dissolved in 20 mL of water were added and the

pH has been adjusted to 8.0 by drop-wise addition of the aqueous solution of NaOH. Once the flask was fitted with rubber septum and cone adapter, it was evacuated for 1h using a vacuum pump at room temperature. To achieve the highest loading of EDTA inside the lumen of halloysite, the process of evacuation and cycling back to atmospheric pressure was repeated for several times under stirring condition for 72 h. Finally, the as synthesized product was obtained after simple filtration and washed several times with Milli-Q water to remove extra EDTA. The product was then dried at 100°C overnight under vacuum and abbreviated as EDTA-HNTs, as shown in Scheme 8.1.



Scheme 8.1: Schematic presentation of the selective modification of the halloysite lumen with ethylenediaminetetraacetic acid (EDTA), resulting in the formation of EDTA-HNTs.

8.2.2 Synthesis of α -Fe₂O₃ within the Lumen of Modified Halloysite Nanotubes

For the synthesis Fe₂O₃ inside the Lumen of EDTA-HNTs, 1.0 g of EDTA-HNTs was re-dispersed into the aqueous solution containing 7.4 mmol of FeCl₃ in around bottom flask, followed by pull down the evacuation. Based on the aforesaid procedure used for EDTA loading, FeCl₃ solution was administered into the lumen by evacuation and cycling back to atmospheric pressure. HNTs-EDTA loaded with Fe³⁺ was washed several times with

Milli-Q water to eliminate unadsorbed FeCl₃ solution and dried at room temperature. The product was now calcined at 400 °C for 10 h in air to prepare Fe₂O₃ within the lumen of EDTA functionalized HNTs and finally produces α -Fe₂O₃/HNTs NCs.

8.2.3 Photocatalytic Reaction

The photocatalytic activity of α -Fe₂O₃/HNTs NCs was investigated toward degradation of aqueous solution of methylene blue (MB) and congo red (CR) under UV, visible as well as solar irradiation. All photocatalytic reactions were carried out in a photocatalytic reactor system, consisting of a cylindrical borosilicate glass reactor vessel with an effective volume of 50 mL, a cooling water jacket, and a UV-A lamp (8 W medium-pressure mercury lamp of $\lambda = 254$ nm) or visible light source (40 W tungsten bulb) positioned axially at the center as a UV light source. The reaction temperature was maintained at 25°C by circulating the cooling water during the experiment. During the photocatalysis using solar radiation, we have placed the reactor under the solar radiation keeping all other experimental condition the same. The time dependent photocatalytic degradation of aqueous MB and CR was monitored by measuring the absorbance of the irradiated solution using UV-Visible spectrophotometer at room temperature. In a typical experiment, 0.01g of α -Fe₂O₃/HNTs nanocomposite was taken in a 50mL glass reactor containing 15 ml of aqueous solution of MB or CR, having an initial concentration of 0.02 mM. Afterward, the reaction solution was exposed to the UV or visible or solar radiation with a constant stirring and studied the degradation reaction by taking out 3.0 mL of the suspension at different time interval. Prior to UV-visible absorption study, each time the suspension was centrifuged to separate the NCs from the dye solution and recorded the spectrum. Absorption intensity of exposed MB solution at 664nm and CR solution at 498 nm has been measured quantitatively throughout the experiments at different time intervals. Consequently, the degradation rate was evaluated according to the change in the absorption intensity of the dye solution. Analogous control experiment was studied with the NCs in dark.

8.3 Results and Discussion

8.3.1 Characterization of the Lumen Modification of HNTs

8.3.1.1 TEM Study

To explore any nanotubule as nanoconfined reactor, it is important to note that the internal diameter of that nanotube has to be at least 0.6 nm wider than the diameter of the guest molecule.²⁶ Since the nanotube diameter is a key factor in determining whether the trapping of molecules inside the tube is feasible, we have performed TEM analysis which demonstrated that HNTs composed of cylindrical shaped tubes with an open ended lumen along the tube, having defects on the outer surface of HNTs possibly caused by the mechanical damage or crystallographic defects (Figure 8.1A). The length of tube is ~ 1.0 to 1.5 μm with an outer diameter of 50-100 nm and inner diameter of 15-20 nm, having the elemental composition of aluminium, silicon and oxygen. It is reported that the halloysite lumen volume is almost 10 vol % of the overall tube and the tubule lumen has a positive inner surface below pH 8.5, which in turn assists in loading of negatively

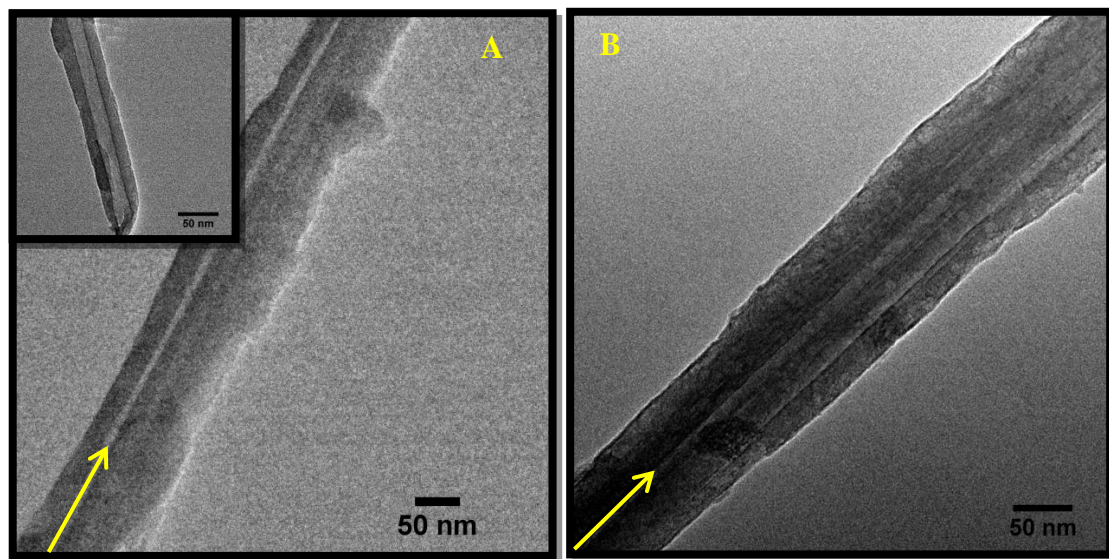


Figure 8.1: TEM images of (A) HNTs and (B) after lumen modification with EDTA. The arrow in (A) and (B) indicates an open ended lumen along the tubes.

charged molecules by averting their adsorption on the negatively charged outer surfaces.¹⁰ After the modification of the inner lumen of HNTs using EDTA, TEM micrographs indicated that there is no change in their size or shape, only a less transparent lumen is observed (Figure 8.1B). This may be because of the incorporation of negatively charged EDTA molecule within the lumen that exists longitudinally along the tubes. The lumen loaded with EDTA molecules now facilitates the incorporation of iron chloride molecules because of the strong binding affinity of EDTA towards iron through chelation.

8.3.1.2 FTIR Analysis

The loading of EDTA molecule was ascertained by Fourier transform infrared (FTIR) spectroscopy owing to the presence of the characteristic C-H and C-O symmetric stretching vibrations at 2840 and 1410 cm^{-1} respectively, as shown in Figure 8.2. Besides

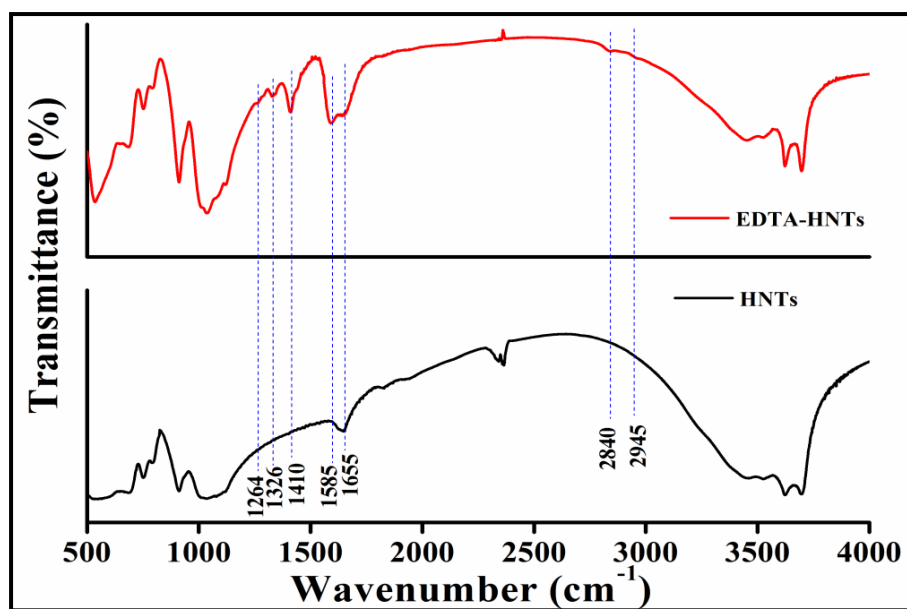


Figure 8.2: FTIR spectra of HNTs before and after lumen modification with EDTA.

these bands, there are few more bands were detected at 1655, 1326 and 1264 cm^{-1} for the stretching vibration of C=O, C-C and C-N respectively in EDTA-HNTs, signifying the immobilization of EDTA molecule in HNTs (the assignment of all vibrational modes are presented in Table 8.1. However, the presence of two distinct bands at 3621 and 3697 cm^{-1} in both HNTs and EDTA-HNTs, are originated from the stretching vibrations of the inner hydroxyl group and inner surface hydroxyl group of HNTs, assuring the unalteration of their basic structure.

Table 8.1: Assignment of FTIR bands after loading of disodium salt of ethylenediaminetetraacetic acid (EDTA) in halloysite nanoclays.

Wavenumber (cm^{-1})	Assignment	Species
3697	Inner surface -OH group	HNTs
3621	Inner -OH group	HNTs
2945	C-H asymmetric stretching	EDTA
2840	C-H symmetric stretching	EDTA
1655	C=O stretching	EDTA
1585	asymmetric stretching C-O	EDTA
1410	Symmetric stretching C-O	EDTA
1326	C-C stretching	EDTA
1264	C-N stretching	EDTA

8.3.1.3 NMR Study

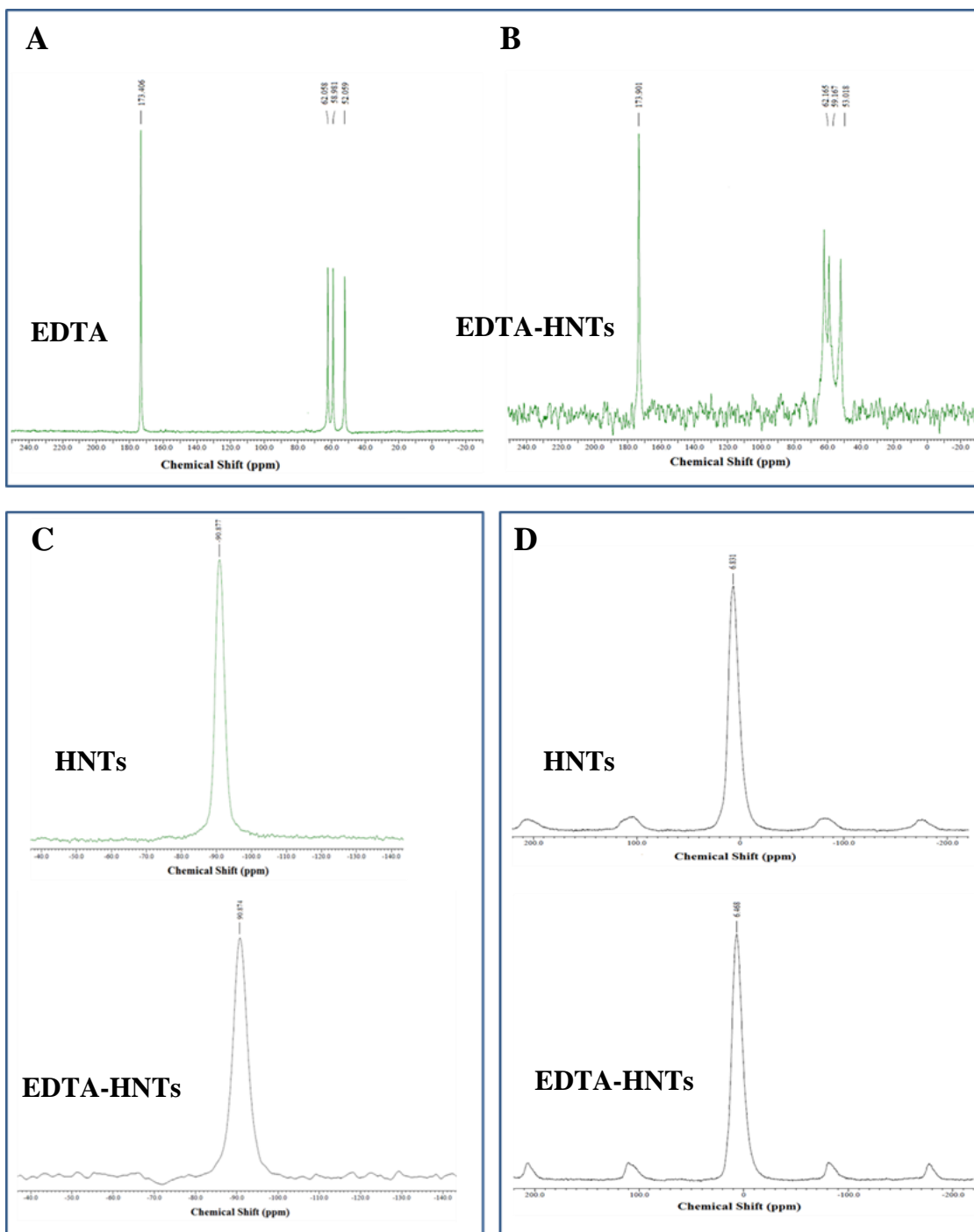


Figure 8.3: (A,B) ^{13}C CPMAS NMR spectra of EDTA and after the loading of EDTA into HNTs, (C) ^{29}Si CPMAS NMR spectra and (D) ^{27}Al CPMAS NMR spectra of pristine HNTs and corresponding EDTA-HNTs respectively.

To gain insight into the precise binding of EDTA with HNTs, we have performed solid state ^{13}C , ^{27}Al and ^{29}Si NMR spectroscopy. The solid state ^{13}C CPMAS NMR spectra of EDTA and EDTA-HNTs are demonstrated in Figure 8.3. The ^{13}C NMR spectrum of EDTA molecule (Figure 8.3A) exhibits three carbon resonances appearing at 173.4, 58.9 and 52 ppm, which can be ascribed to the carbonyl, acetate CH_2 and ethylenic CH_2 of EDTA respectively. After the loading of EDTA into HNTs, all the three carbon resonances were observed and slightly shifted to the downfield, indicating the change in the chemical environment after the immobilization of EDTA inside HNTs. To demonstrate the selective binding aspects of EDTA, we have recorded ^{27}Al and ^{29}Si NMR spectra of both pristine HNTs and EDTA-HNTs. However, we could not find any shift in the resonances at -90.7 ppm originating from silicon, which in turn eliminates the possibility of binding of EDTA to silica surfaces and further suggests the binding of EDTA with alumina surface present in the lumen (Figure 8.3B). The solid state ^{27}Al NMR spectrum of HNTs as depicted in Figure 8.4C, represents that the resonances at 6.8 ppm is due to the octahedral AlO_6 , which is found to be upfielded after binding with EDTA. This is also in accordance with the reported literature.²⁷ The upfield shifts suggest that the chemical environment of aluminium in EDTA-HNTs is different from that in pristine HNTs. Therefore, all the aforesaid findings shed light on the moderate interaction between the negatively charged EDTA with the positively charged alumina surfaces present in the lumen of HNTs.

8.3.1.4 XRD Study

The diffraction pattern illustrates the tubular structure of the clay nanotubes because of the observed (020) reflection (Figure 8.4), and the characteristic (001) reflection in EDTA-HNTs remain unchanged, demonstrating the absence of any intercalation of EDTA molecules into the interlayer of tubes wall, further indicating that the interlayer AlOH groups are not taking part in the modification process.^{28,29}

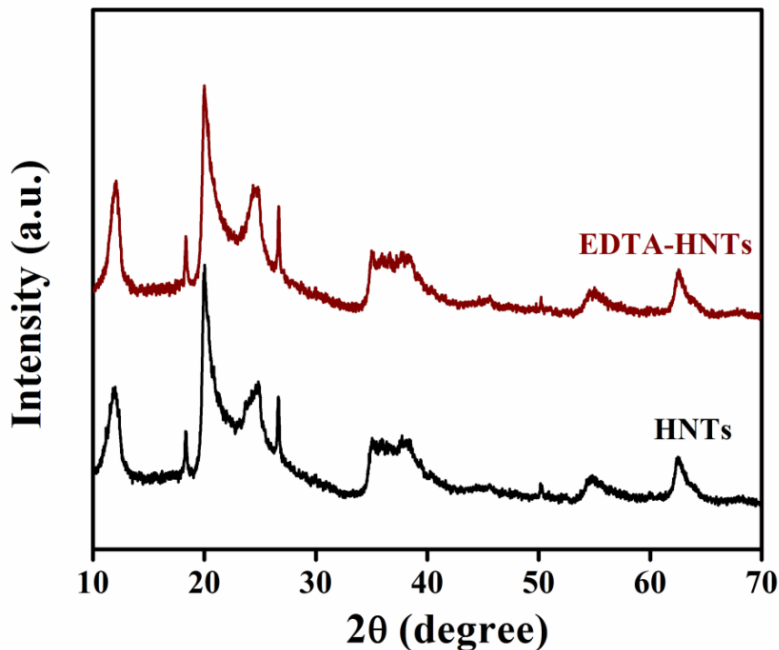


Figure 8.4: XRD patterns of bare HNTs and after loaded with ethylenediaminetetraacetic acid (EDTA), indicating the absence of any intercalation of EDTA into the interlayer of tubes wall.

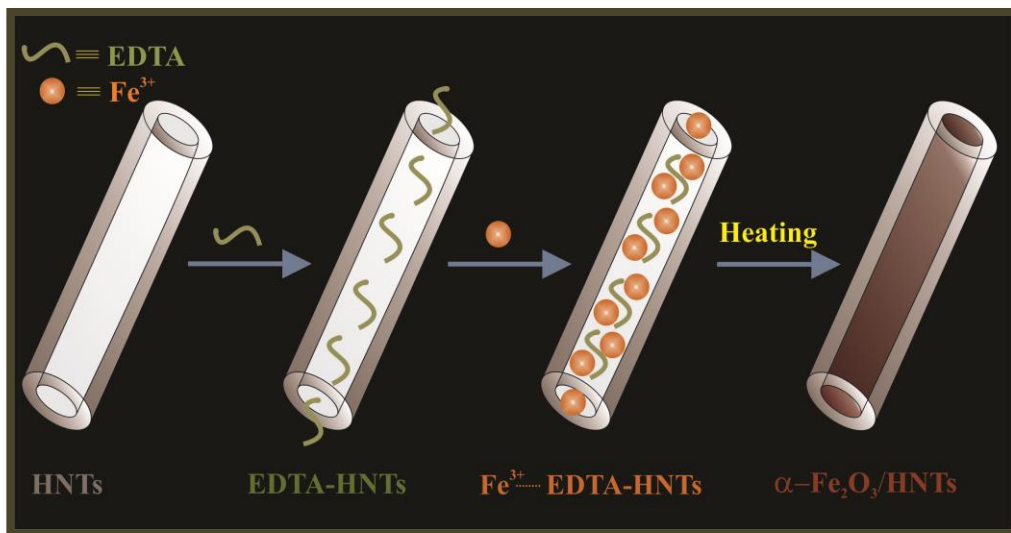
8.3.1.5 CHN Elemental Analysis

The exact concentration of immobilized EDTA to the HNTs was assessed by CHN elemental analysis and it is determined to be 1.83 wt% of N, which is indicative of 9.56 wt% of EDTA loaded in HNTs.

8.3.2 Characterization of Iron Oxide Nanorods inside Halloysite Lumen

To entrap iron and subsequent formation of iron oxide nanostructures within the lumen, EDTA-HNTs were mixed with FeCl_3 solution in a round bottom flask and then evacuated using a vacuum pump. Once the suspension was slightly fizzed, the air basically has been removed from the lumen of the tubules and concomitantly filled with FeCl_3 solution by pulling and breaking vacuum, resulting in the formation of iron-EDTA complex. After

proper washing and drying, iron oxide was synthesized inside the lumen of HNTs by the decomposition of iron-EDTA complex (Scheme 8.2).



Scheme 8.2: Schematic illustration of halloysite lumen modification with EDTA to entrap iron (III) via the formation of iron-EDTA complex followed by the decomposition to produce iron oxide nanorods within the lumen and subsequently achieved α -Fe₂O₃/HNTs nanocomposites.

8.3.2.1 TEM and EDS Analysis

TEM image of iron oxide nanorods within the open ended lumen along the clay tubules is shown in Figure 8.5A. Iron oxide nanorods have diameter of ~ 15 nm and several micrometer of length, since the growth of the nanorods entirely depend on the length and inner diameter of the clay nanotubes. The low contrast of TEM images may be because of the immobilization of the iron oxide nanorods inside the inner surfaces (lumen) of the tubes. The compositional analysis by energy dispersive X-ray spectroscopy (EDS) of iron oxide/HNTs NCs ensures the presence of iron as the signals from iron are clearly evident in the spectrum along with three main constituents of pristine HNTs (Figure 8.5B).

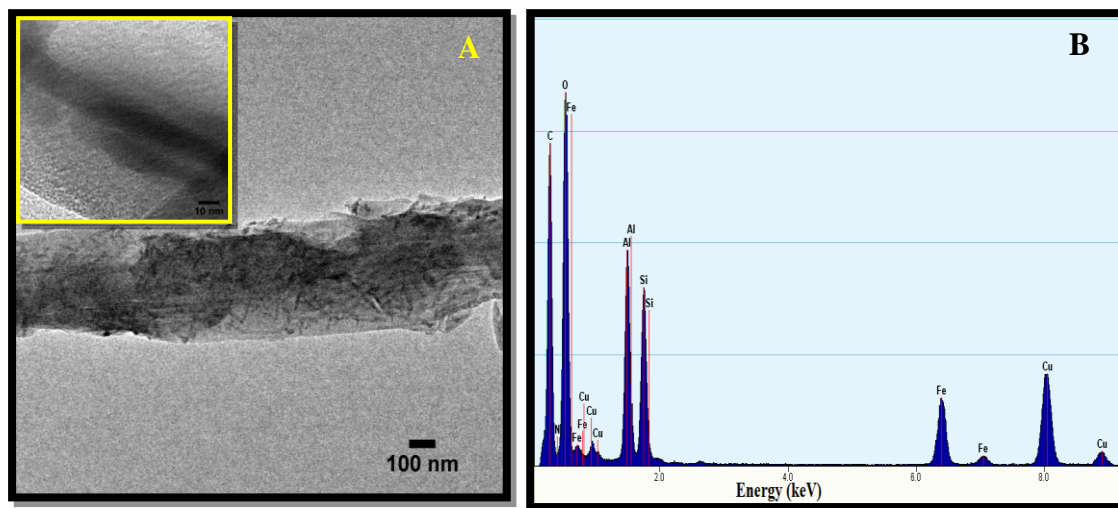


Figure 8.5: (A) TEM images of Fe_2O_3 nanorods within the lumen of the clay tubule and (B) EDS elemental analysis of immobilized Fe_2O_3 nanorods inside the tubes.

8.3.2.2 STEM-EDS Elemental Mapping Analysis

To directly visualize the formation of iron oxide nanorods, scanning transmission electron microscopy-energy dispersive spectroscopy (STEM-EDS) elemental mapping was performed on iron oxide/HNTs NCs. STEM images of a cylindrical shaped clay nanotube with an open ended lumen and after filled with iron oxide nanorods are presented in Figure 8.6A & B respectively. The elemental maps shown in Figure 8.6C-F, demonstrate the distribution of the constituent elements present in the NCs. Each element is represented by a specific color. The elemental mapping of Al and Si demonstrate their homogeneous distribution throughout the body of the cylindrical shaped tubes whereas Fe is mainly localized in rod-like crystallites along the open ended lumen of the tube. It is also interesting to point out that even after sonication during sample preparation for TEM, iron oxide nanorods still firmly stuck into the lumen, implying HNTs protect them against surrounding environmental effects. It should be noted that the external surface of HNTs was not functionalized with EDTA and thus should not exhibit any affinity toward iron. However, there are few signals coming from iron over the outer surface of the tube.

It could be attributed to the presence of external siloxane surfaces and defects on the outer surfaces of HNTs, which help to adsorb minor quantities of iron during the adsorption process, which gives rise to the formation of iron oxide nanoparticles during heating, further demonstrating the presence of liner defects on the external surfaces of HNTs. Early study suggests that the vacancies on the layers formed due to the absence of Si (IV), may generate localized negative charges which attract positively charged Fe (III) ions and subsequently leads to the formation of iron oxide nanostructures along the defects of the tubular clay.³⁰

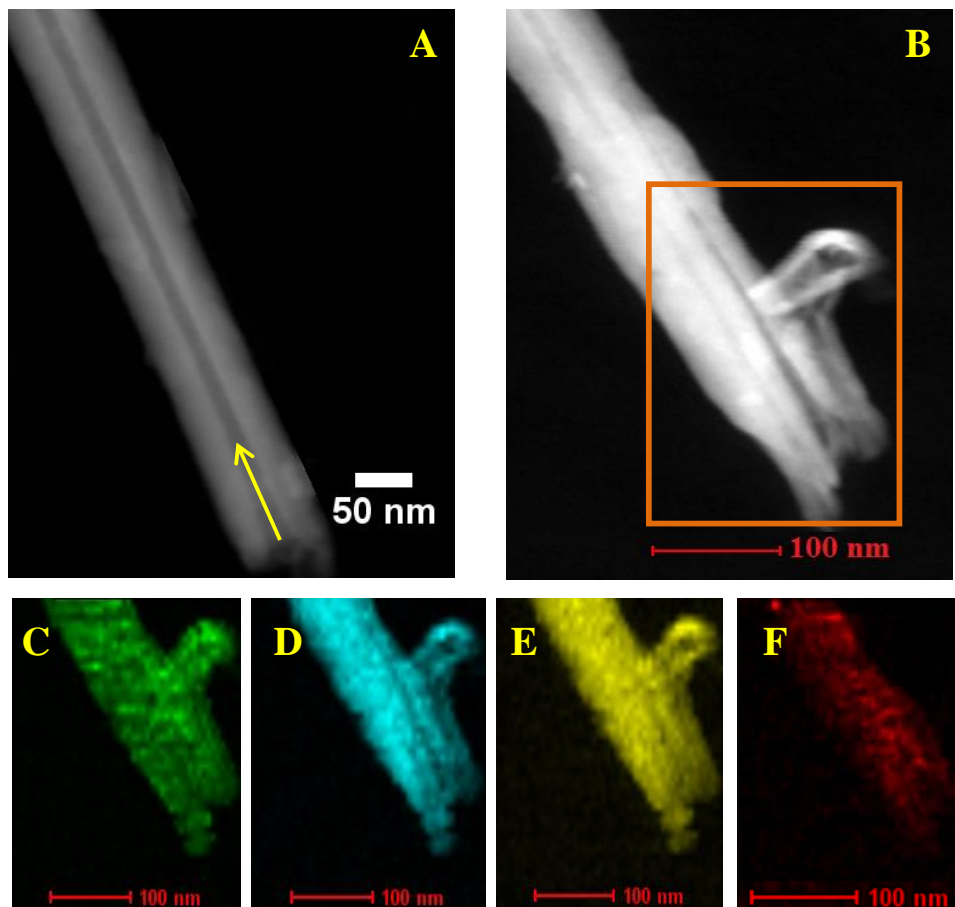


Figure 8.6: STEM images of a cylindrical shaped clay nanotube (A) before and (B) after loaded with iron oxide nanorods and corresponding elemental mapping of (C) Al, (D) Si, (E) O and (F) Fe respectively on a single nanotube.

8.3.2.3 XRD Study

The formation of iron oxides within the clay nanotubes due to the decomposition of iron-EDTA complex was evidenced from XRD analysis, which exhibits the presence of some newly emerged peaks corresponds to (012), (104), (110), (113), (024), (116) planes of α - Fe_2O_3 respectively (Figure 8.7A). Prussian blue test further ascertains the oxidation state of iron in the iron oxide/HNTs NCs. Upon addition of $\text{K}_4[\text{Fe}(\text{CN})_6]$ to the nanocomposite solution, the colour of the solution turns to blue due to the formation of $\text{KFe}^{\text{III}}[\text{Fe}^{\text{II}}(\text{CN})_6]$, which was not observed for $\text{K}_3[\text{Fe}(\text{CN})_6]$, demonstrating the presence of Fe (III) in the nanocomposite, see Figure 8.7B.

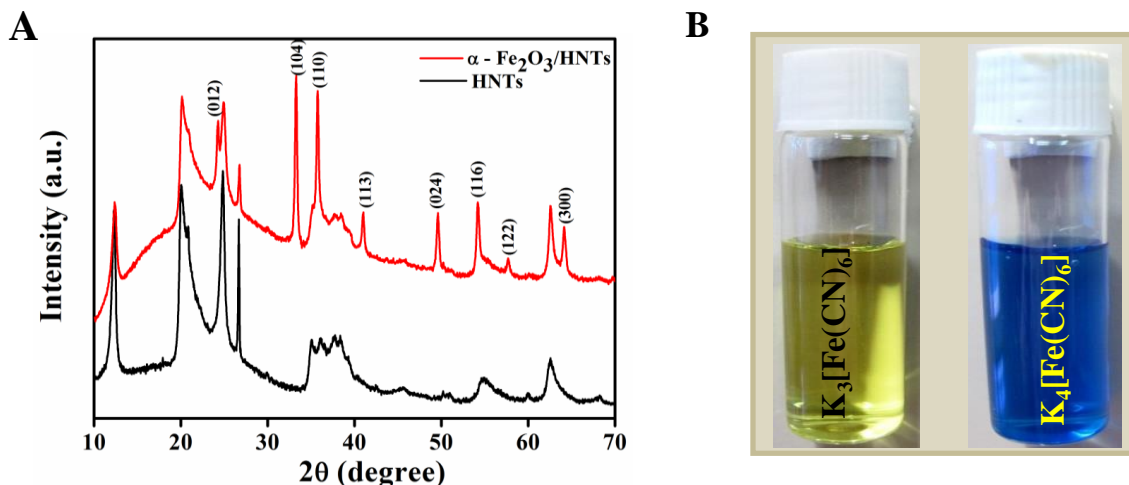


Figure 8.7: (A) XRD patterns of HNTs and α - $\text{Fe}_2\text{O}_3/\text{HNTs}$ nanocomposites. (B) Prussian blue test of iron oxide/HNTs NCs using $\text{K}_3[\text{Fe}(\text{CN})_6]$ and $\text{K}_4[\text{Fe}(\text{CN})_6]$, indicating the formation of Fe_2O_3 nanocomposites.

8.3.2.4 Zeta-potential Measurement

The zeta (ζ)-potential measurement was carried out after loaded with iron oxide nanorods inside the lumen of HNTs. The estimated ζ -potential for the α - $\text{Fe}_2\text{O}_3/\text{HNTs}$ NCs is found to be -36.3 mV in water.

8.3.2.5 BET Study

The specific surfaces of pristine HNTs and α -Fe₂O₃/HNTs NCs were measured by nitrogen adsorption/desorption at 77 K. The isotherms of the HNTs and nanocomposites are of type II with H3 hysteresis loops, according to IUPAC classification.^{31,32} All these isotherms indicate hysteresis, which are characteristic of mesoporous materials. The nitrogen adsorption/desorption isotherms of the clay samples are demonstrated in Figure 8.8 and their total specific surface areas (S) and pore diameter estimated using the BET method are summarized in Table 8.2.

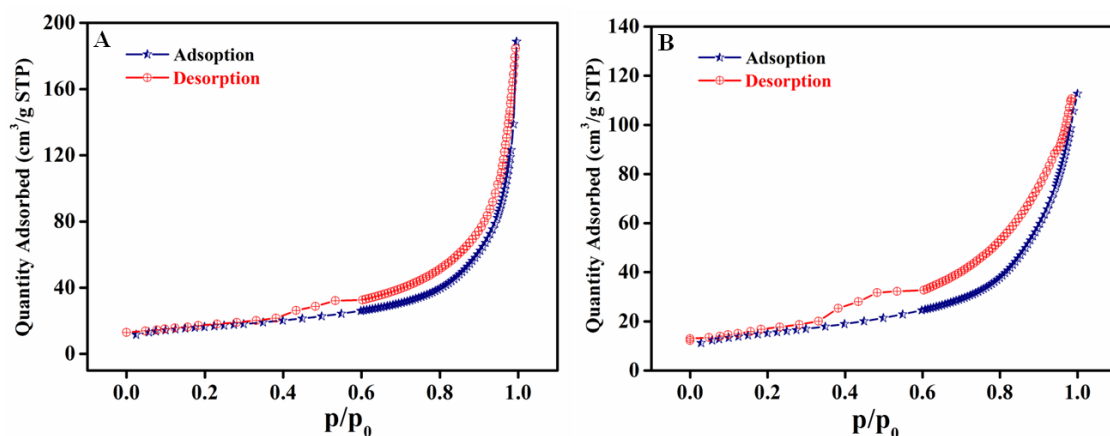


Figure 8.8: Nitrogen adsorption/desorption isotherms of (A) pristine halloysite and (B) α -Fe₂O₃/HNTs NCs at 77 K.

Table 8.2: BET specific surface areas (S) and average pore diameters of pristine halloysite and α -Fe₂O₃/HNTs NCs.

	S (m ² g ⁻¹)	BET average pore diameter (Å)
Pristine HNTs	56.76	193.4
α-Fe₂O₃/HNTs NCs	53.14	130.3

8.3.2.6 UV-Visible Diffuse Reflectance Analysis

UV-visible diffuse reflectance spectrum of α -Fe₂O₃/HNTs NCs also signifies the formation of α -Fe₂O₃ NCs it's owing to the presence of a band centered at 556 nm as shown in Figure 8.9. The spectrum consists of two peaks at 360 and 556 nm correspond to ${}^6A_1 \rightarrow {}^4E$ and $2({}^6A_1) \rightarrow 2({}^4T_1)$ ligand field transition of Fe (III) respectively.

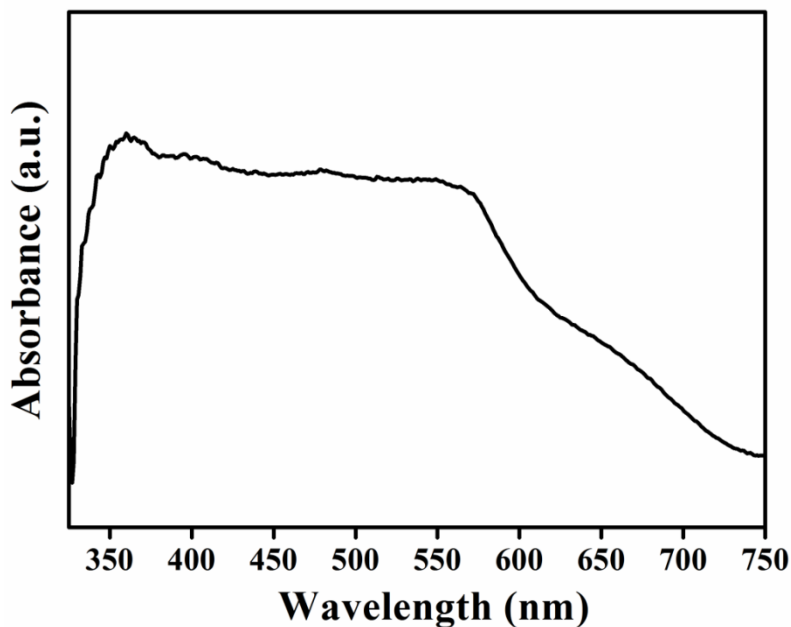


Figure 8.9: UV-visible diffuse reflectance spectrum of α -Fe₂O₃/HNTs nanocomposites, demonstrating two peaks at 360 and 556 nm.

8.3.2.7 VSM Study

Further vibrating sample magnetometer (VSM) measurements pointed out to the characteristic behavior of α -Fe₂O₃ with a Morin transition temperature (T_M) of 245K (Figure 8.10A). It is worth noting that the bulk hematite has the Morin transition from the low-temperature antiferromagnetic phase to a weakly ferromagnetic phase at 263 K,³³ which increases with the annealing temperature for the small-sized hematite and

decreases with decreasing particle size.^{34,35} Hence, the decrease in T_M may originate due to some lattice strain and defects in the oxide nanorods immobilized within the lumen of the halloysite clay. The field dependence magnetization of α - Fe_2O_3 at 100 and 300 K demonstrate the antiferromagnetic state of the nanorods at low temperature and weak ferromagnetic above T_M , as shown in Figure 8.10B & C. Room temperature saturation magnetization (M_S) is estimated to be 0.07 emu g^{-1} . However, no superparamagnetic state was observed for this material at this temperature, indicating the presence of larger crystallite size compare to the single domain size of hematite.³³

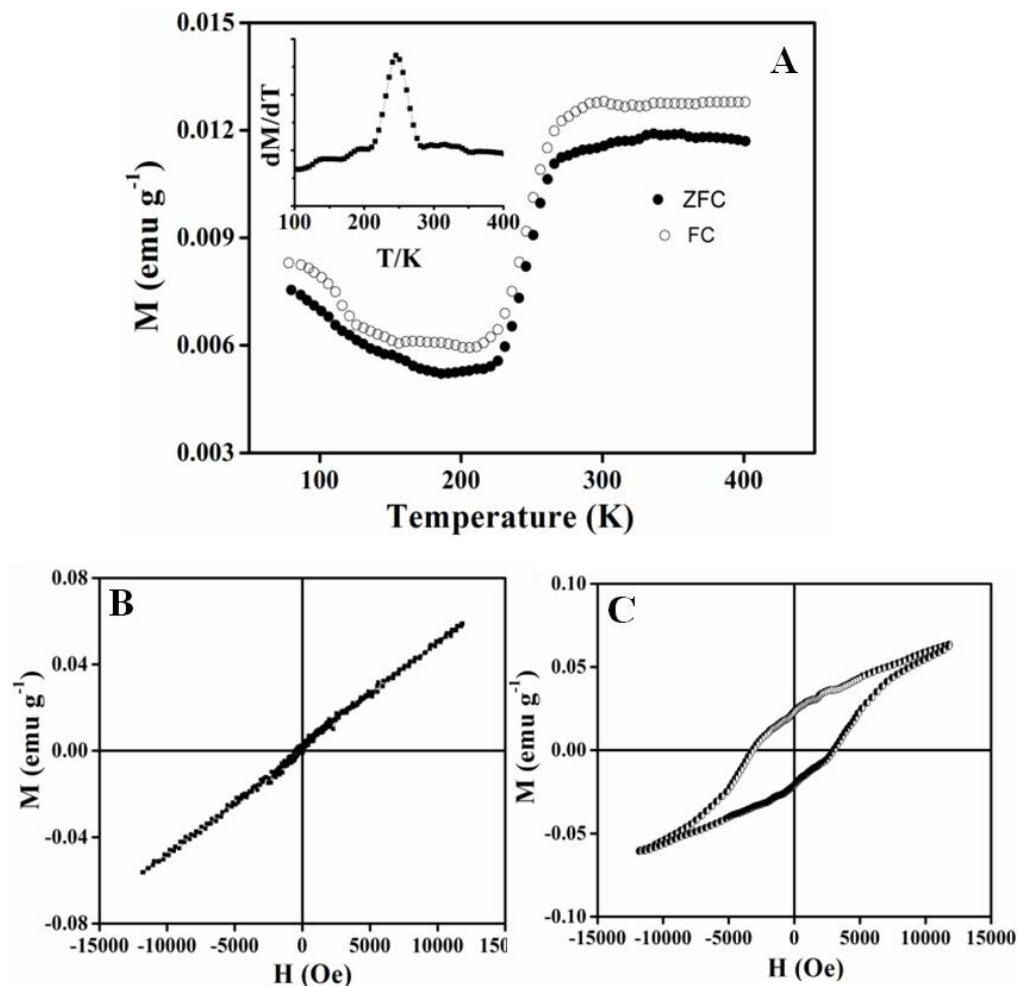


Figure 8.10: Magnetic measurements for α - $\text{Fe}_2\text{O}_3/\text{HNTs}$ NCs. (A) Temperature dependence of ZFC and FC magnetization at an applied field of 1000 Oe and corresponding differential ZFC curve (Inset). Field dependence of magnetization of α - $\text{Fe}_2\text{O}_3/\text{HNTs}$ NCs at (B) 100 K and (C) 300 K respectively.

8.3.2.8 ICP-OES Study

Based on the inductively coupled plasma optical emission spectrometry (ICP-OES), the concentration of the iron loaded with in the lumen of the clays was estimated to be ~2.45 wt% of halloysite clays.

Hence, this study points to the selective modification of halloysite lumen using a chelating ligand to direct the adsorption of iron and followed by *in situ* synthesis of α -Fe₂O₃nanorodsto study their visible light induced photocatalytic activity toward degradation of dye molecules.

8.3.3 Photocatalytic Activity of α -Fe₂O₃/HNTs NCs

8.3.3.1 Degradation of Organic Pollutants

To explore photocatalytic activity of α -Fe₂O₃/HNTs nanocomposites (NCs), the degradation of organic dyes was studied under UV, visible and direct sunlight irradiation at room temperature. For this degradation study, we have considered methylene blue (MB) and congo red (CR) as model pollutants. The UV-visible spectral changes for MB and CR aqueous solutions in the process of photo degradation under three different light sources were presented in Figure 8.11. With increasing irradiation time under sunlight, the characteristic absorbance of MB at $\lambda = 664$ nm gradually decreases, signifying the degradation of the dye as the time progresses (Figure 8.11A).^{36,37} This can also be visualized as the color of the MB solution changed from blue to light blue and finally to colorless with time, further attributes to the degradation of the dye molecule. Likewise, the distinctive absorbance of CR at $\lambda = 498$ nm was used to monitor the degradation of this dye molecule which demonstrate that red color of the solution turned into colorless upon irradiation of sunlight, as shown in Figure 8.11B.

It is important to note that once the dye solution reaches to adsorption–desorption equilibrium; it was then exposed to the irradiation source and studied the degradation

reaction. Based on the experimental results, the photodegradation activity of α - $\text{Fe}_2\text{O}_3/\text{HNTs}$ NCs was evaluated toward MB and CR under various light sources as shown in Figure 8.11C & D, which demonstrate that the dye degrades at a faster rate in presence of sunlight compared to the visible and UV light.

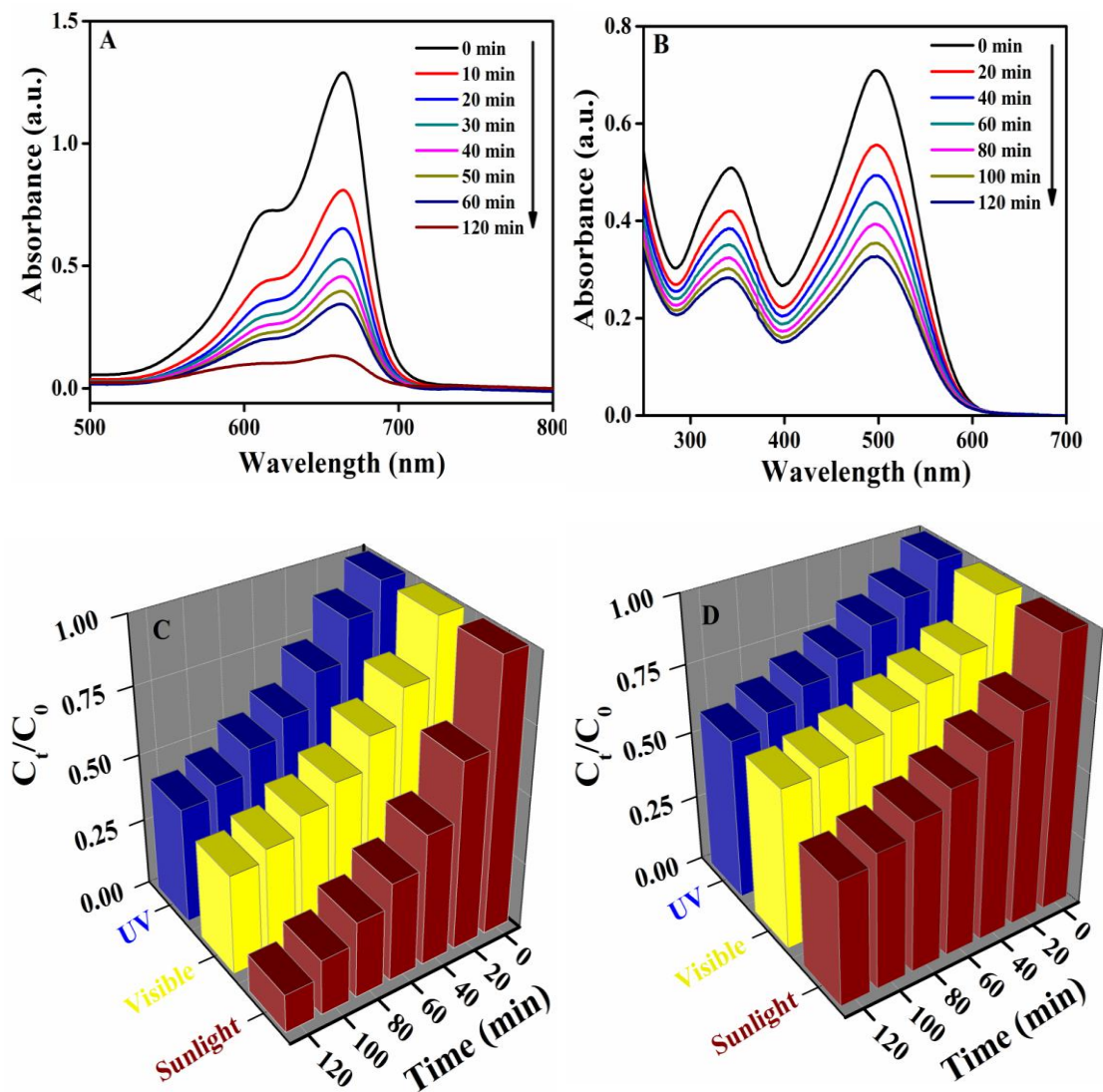


Figure 8.11: UV-Visible absorption spectra for the successive degradation of (A) MB and (B) CR under irradiation of sunlight in presence of α - $\text{Fe}_2\text{O}_3/\text{HNTs}$ NCs. Photocatalytic degradation of (C) MB and (D) CR under irradiation of UV, visible and sunlight respectively.

8.3.3.2 Kinetics of the Degradation Reaction

To elucidate the kinetics of the degradation process, the photodegradation rate of the α -Fe₂O₃/HNTs NCs towards MB was studied under different irradiation sources based on the pseudo-first-order kinetic model.

$$\ln(C_t/C_0) = -kt \quad (8.1)$$

where, C_0 is initial concentration of MB, C_t is the residual concentration of MB at each irradiation time t and k is the reaction rate constant. The photodegradation of MB proceeds through the pseudo-first-order kinetic model, as shown in Figure 8.12A. The reaction rate constant of the degradation reaction was estimated for UV, visible and solar irradiation and presented in Table 8.3. The results indicated that the degradation rate of MB under solar irradiation is much faster than that of the visible or UV irradiation and hence solar light leads to the faster degradation of the dye molecule since the sunlight has higher intensity. Additionally, we have verified the degradation reaction by carrying out the experiment with pristine HNTs, further demonstrating that they don't possess any catalytic efficacy for the degradation of dyes, as shown in Figure 8.12B.

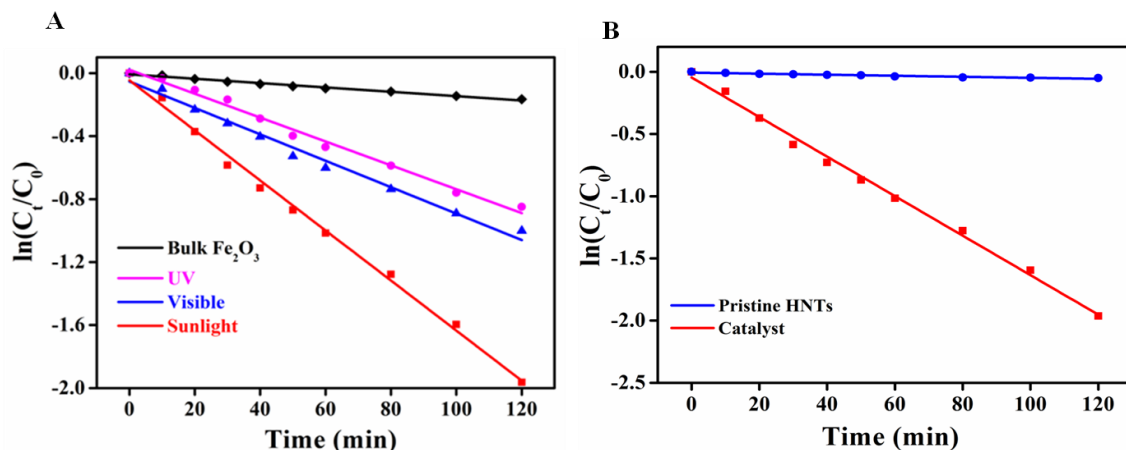


Figure 8.12: (A) Rate of degradation of MB using α -Fe₂O₃/HNTs NCs under three different light sources and with bulk Fe₂O₃ under sunlight respectively. (B) Degradation of MB under the illumination of sunlight using pristine HNTs and α -Fe₂O₃/HNTs nanocomposites respectively.

Table 8.3: Summary of the degradation percentage of MB after 2 h and corresponding rate constants under different irradiation sources using α -Fe₂O₃/HNTs NCs based on the pseudo-first-order kinetic model.

Catalyst	Irradiation source	First-order rate constant (k, min ⁻¹)	Degradation (%)
α -Fe ₂ O ₃ /HNTs	Sunlight	0.0159	88
	Visible light	0.0084	66
	UV light	0.0076	58

8.3.3.3 Recyclability of α -Fe₂O₃/HNTs NCs

To establish the recyclability of α -Fe₂O₃/HNTs NCs, they have been used repeatedly for this degradation process owing to their stability (Figure 8.13A) and easy recovery from the reaction solution through simple filtration, which further demonstrates an added advantage for the efficient separation and recycling of the photocatalyst (Figure 8.13B).

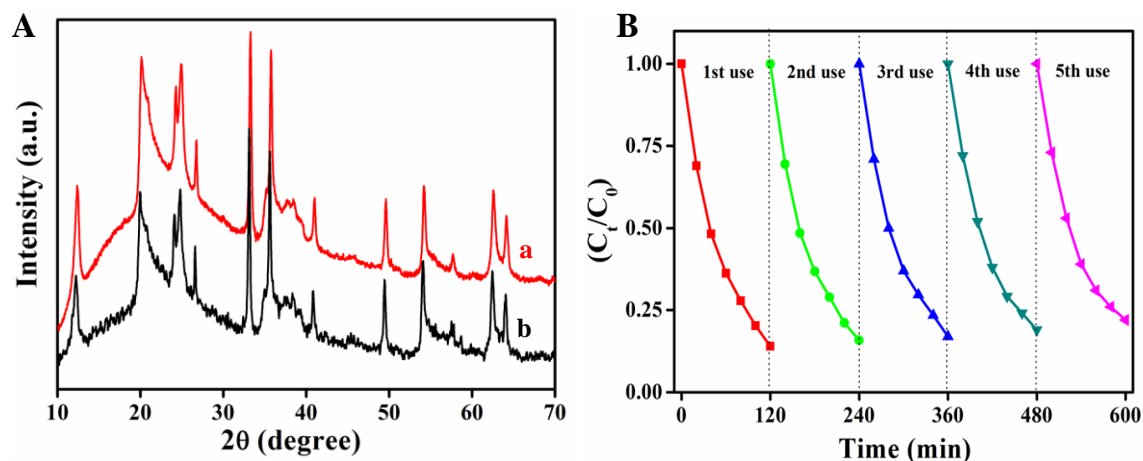


Figure 8.13: XRD patterns of α -Fe₂O₃/HNTs nanocomposites (a) before and (b) after the end of the photodegradation reaction, demonstrating no change in their diffraction pattern. (B) Multi-cycle degradation efficacy of α -Fe₂O₃/HNTs NCs toward MB under sunlight irradiation.

8.3.3.4 Degradation Mechanism

Keeping all the experimental condition the same, control experiment has also been performed taking bulk Fe_2O_3 , which shows lower efficacy compared to the synthesized rod shaped $\alpha\text{-Fe}_2\text{O}_3/\text{HNTs}$ NCs. The enhanced photocatalytic activity of the NCs may be account for the channelized electron transport in the 1D nanorods and also lowers the possibility of electron-hole recombination.³⁸ This may also be ascribed to the increase in the surface area induced by Fe_2O_3 nanorods, which helps to increase the reaction sites for photocatalysis since the specific surface area of a catalyst can give rise to the unsaturated surface coordination sites.³⁹⁻⁴¹

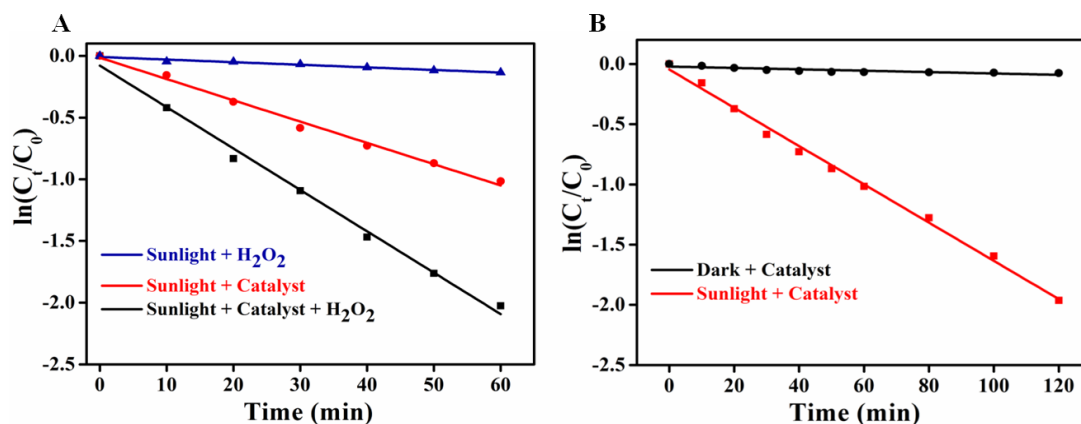


Figure 8.14 (A) Comparison of degradation rates of MB under sunlight illumination in presence of catalyst and/or H_2O_2 to demonstrate that the degradation of MB dye molecules proceeds through photocatalytic pathway. (B) Comparison of degradation rates of MB in dark and under sunlight illumination in presence of catalyst.

The photoactivities of $\text{Fe}_2\text{O}_3/\text{HNTs}$ NCs remarkably increased upon the addition of H_2O_2 in presence of sunlight. It has been found that the rate of photodegradation of MB is significantly increased upon the addition of both catalyst and H_2O_2 compared to the degradation rate of the reaction performed with only catalyst under same experimental condition (Figure 8.14A). Since the degradation reaction was influenced by the addition of H_2O_2 , we therefore presume that the degradation of dye molecules proceed through

photocatalytic pathway via the formation of reactive oxygen species due to the irradiation of light. To gain insight into the photocatalytic activity of α -Fe₂O₃/HNTs NCs, we have carried out the degradation study under dark, indicating no degradation of MB, as shown in Figure 8.14B.

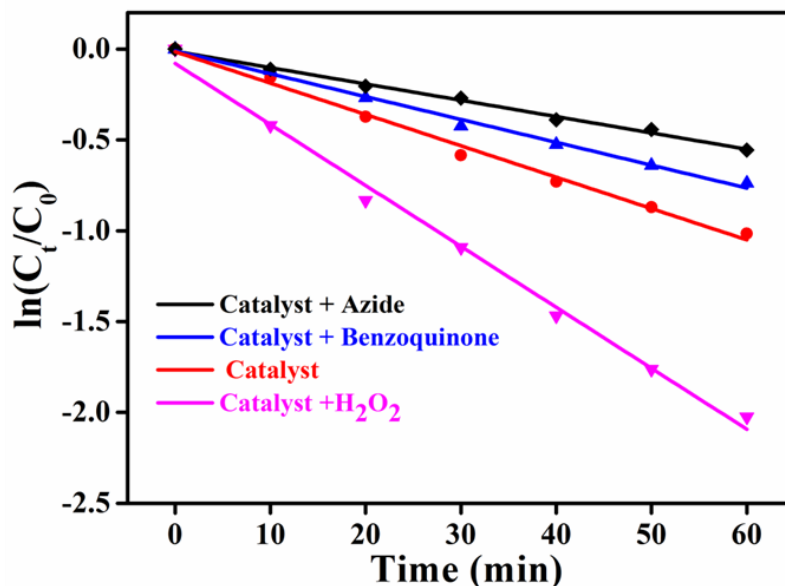


Figure 8.15: Comparison of degradation rates of MB under sunlight illumination in presence of catalyst and/or H₂O₂, sodium azide and 1,4-benzoquinone respectively to demonstrate that the degradation of MB proceeds through the photocatalytic pathway via the formation of reactive oxygen species.

It is again interesting for us to investigate the formation of oxidative intermediate species under photocatalytic conditions and their role in the dye degradation process using appropriate quenchers which will scavenge the generated reactive oxygen species in the reaction medium. To demonstrate the formation of oxidative intermediate species during photocatalysis, the degradation reaction was carried out with the use of sodium azide, a quencher of singlet oxygen (¹O₂) and hydroxyl radicals ([•]OH), and 1,4-benzoquinone which is a quencher of superoxide radicals (O₂^{•-}). It is evident from Figure 8.15 that the photodegradation of MB is suppressed considerably in the presence of azide and 1,4- benzoquinone, which further authenticates that the reaction takes place via the

formation of reactive oxygen species possibly due to the interaction of photoexcited conduction band electrons with molecular oxygen at the surface of the nanocomposites. Therefore, this study is the first demonstration of the modification of halloysite lumen using a chelating ligand EDTA, which in turn directs the immobilization of iron and subsequently produced iron oxide nanorods within the lumen of clay that exhibit enhanced photocatalytic efficacy for the degradation of such harmful organic dye molecules under direct sunlight and hold promise to the practical application of waste water treatment.

8.4 Conclusions

In conclusion, we have demonstrated the selective modification of halloysite lumen using a chelating ligand disodium salt of ethylenediaminetetraacetic acid and authenticated by FTIR and solid-state NMR spectroscopy, indicating the binding of EDTA exclusively to the alumina site. The selective modification of the clay lumen essentially produces an inorganic micelle-like architecture that facilitates the loading of iron and the successive formation of rod-shaped nanoscale iron oxides inside the lumen of the tubular clays, demonstrating a new direction in the frontier area of nanoconfined reactions. In consequence, exploiting the inner lumen of halloysite clays as nanoconfined reactors, we have successfully synthesized a nanocomposite having α -Fe₂O₃ core with halloysite shell. The as-prepared α -Fe₂O₃/HNTs NCs exhibit enhanced photocatalytic activity for the degradation of dyes in presence of solar light in associated to the UV or visible light. Therefore, halloysite clays may be utilized as an efficient template for complex molecular arrays because of their tunable physicochemical properties which allow encapsulating the guest molecules as well as studying chemical reactions; and they may also be attractive in medical research because of their biocompatible nature. Thus, the selective modification of lumen or outer surfaces of the clay under mild conditions for the design of novel inorganic-organic hybrid nanocomposites may open up a broader application in the field of catalysis, environments and even in drug delivery.

8.5 References

1. Hu, J.; Chen, M.; Fanga, X.; Wu, L. Fabrication and Application of Inorganic Hollow Spheres. *Chem. Soc. Rev.* **2011**, *40*, 5472–5491.
2. Wang, J.; Loh, K. P.; Zhong, Y.; Lin, M.; Ding, J.; Foo, Y. Bifunctional FePt Core-Shell and Hollow Spheres: Sonochemical Preparation and Self-assembly. *Chem. Mater.* **2007**, *19*, 2566–2572.
3. Martin, J.; Manzano, C. V.; Calero, O. C.; González, M. M. High Aspect Ratio and Highly Ordered 15-nm Porous Alumina Templates. *ACS Appl. Mater. Interfaces* **2013**, *5*, 72–79.
4. Botos, A.; Biskupek, J.; Chamberlain, T. W.; Rance, G. A.; Stoppiello, C. T.; Sloan, J.; Liu, Z.; Suenaga, K.; Kaiser, U.; Khlobystov, A. N. Carbon Nanotubes as Electrically Active Nanoreactors for Multi-step Inorganic Synthesis: Sequential Transformations of Molecules to Nanoclusters and Nanoclusters to Nanoribbons. *J. Am. Chem. Soc.* **2016**, *138*, 8175–8183.
5. Liu, B.; Shioyama, H.; Akita, T.; Xu, Q. Metal-organic Framework as a Template for Porous Carbon Synthesis. *J. Am. Chem. Soc.* **2008**, *130*, 5390–5391.
6. Yang, H.; Kruger, P. E.; Telfer, S. G. Metal-organic Framework Nanocrystals as Sacrificial Templates for Hollow and Exceptionally Porous Titania and Composite Materials. *Inorg. Chem.* **2015**, *54*, 9483–9490.
7. Bégu, S.; Durand, R.; Lerner, D. A.; Charnay, C.; Tourné-Péteilh, C.; Devoisselle, J. M. Preparation and Characterization of Siliceous Material Using Liposomes as Template. *Chem. Commun.* **2003**, 640-641.
8. Braun, E.; Eichen, Y.; Sivan, U.; Ben-Yoseph, G. DNA-templated Assembly and Electrode Attachment of Aconducting Silver Wire. *Nature* **1998**, *391*, 775–778.
9. Pileni, M.-P. The Role of Soft Colloidal Templates in Controlling the Size and Shape of Inorganic Nanocrystals. *Nature Mater.* **2003**, *2*, 145-150.
10. Abdullayev, E.; Joshi, A.; Wei, W.; Zhao, Y.; Lvov, Y. Enlargement of Halloysite Clay Nanotube Lumen by Selective Etching of Aluminum Oxide. *ACS Nano* **2012**, *6*, 7216–7226.
11. Cavallaro, G.; Lazzara, G.; Milioto, S. Exploiting the Colloidal Stability and Solubilization Ability of Clay Nanotubes/Ionic Surfactant Hybrid Nanomaterials. *J. Phys. Chem. C* **2012**, *116*, 21932–21938.
12. Das, S.; Maity, A.; Pradhan, M.; Jana, S. Assessing Atmospheric CO₂ Entrapped in Clay Nanotubes Using residual Gas Analyzer. *Anal. Chem.* **2016**, *88*, 2205–2211.
13. Bates, T. F.; Hildebrand, F. A.; Swineford, A. Morphology and Structure of Endellite and Halloysite. *Am. Mineral.* **1950**, *35*, 463–484.
14. Lvov, Y. M.; Shchukin, D. G.; Möhwald, H.; Price, R. R. Halloysite Clay Nanotubes for Controlled Release of Protective Agents. *ACS Nano* **2008**, *2*, 814–820.
15. Das, S.; Jana, S. A Facile Approach to Fabricate Halloysite/Metal Nanocomposites with Preformed and *In Situ* Synthesized Metal Nanoparticles: a Comparative Study of their Enhanced Catalytic Activity. *Dalton Trans.* **2015**, *44*, 8906–8916.
16. Wang, R.; Jiang, G.; Ding, Y.; Wang, Y.; Sun, X.; Wang, X.; Chen, W. Photocatalytic Activity of Heterostructures Based on TiO₂ and Halloysite Nanotubes. *ACS Appl. Mater. Interfaces* **2011**, *3*, 4154–4158.

17. Abdullayev, E.; Price, R.; Shchukin, D.; Lvov, Y. Halloysite Tubes as Nanocontainers for Anticorrosion Coating with Benzotriazole. *ACS Appl. Mater. Interfaces* **2009**, *1*, 1437–1443.
18. Chao, C.; Liu, J.; Wang, J.; Zhang, Y.; Zhang, B.; Zhang, Y.; Xiang, X.; Chen, R. Surface Modification of Halloysite Nanotubes with Dopamine for Enzyme Immobilization. *ACS Appl. Mater. Interfaces* **2013**, *5*, 10559–10564.
19. Das, S.; Ghosh, C.; Jana, S. Moisture Induced Isotopic Carbon Dioxide Trapping from Ambient Air. *J. Mater. Chem. A* **2016**, *4*, 7632–7640.
20. Cavallaro, G.; Lazzara, G.; Milioto, S.; Sanzillo, V. Modified Halloysite Nanotubes: Nanoarchitectures for Enhancing the Capture of Oils from Vapor and Liquid Phases. *ACS Appl. Mater. Interfaces* **2014**, *6*, 606–612.
21. Lvov, Y.; Wang, W.; Zhang, L.; Fakhrullin, R. Halloysite Clay Nanotubes for Loading and Sustained Release of Functional Compounds. *Adv. Mater.* **2016**, *28*, 1227–1250.
22. Fan, L.; Zhang, J.; Wang, A. *In Situ* Generation of Sodium Alginate/Hydroxyapatite/Halloysite Nanotubes Nanocomposite Hydrogel Beads as Drug-Controlled Release Matrices. *J. Mater. Chem. B* **2013**, *1*, 6261–6270.
23. Massaro, M.; Riela, S.; Meo, P. L.; Noto, R.; Cavallaro, G.; Milioto, S.; Lazzara, G. Functionalized Halloysite Multivalent Glycocluster as a New Drug Delivery System. *J. Mater. Chem. B* **2014**, *2*, 7732–7738.
24. Shchukin, D. G.; Sukhorukov, G. B.; Price, R. R.; Lvov, Y. M. Halloysite Nanotubes as Biomimetic Nanoreactors. *Small* **2005**, *1*, 510–513.
25. Jana, S.; Chang, J. W.; Rioux, R. M. Synthesis and Modeling of Hollow Intermetallic Ni–Zn Nanoparticles Formed by the Kirkendall Effect. *Nano Lett.* **2013**, *13*, 3618–3625.
26. Khlobystov, A. N. Carbon Nanotubes: from Nano Test tube to Nano-Reactor. *ACS Nano* **2011**, *5*, 9306–9312.
27. Ryczkowski, J. EDTA Interaction with γ -alumina.²⁷Al NMR Studies. *React. Kinet. Catal. Lett.* **1995**, *56*, 241–246.
28. Yah, W. O.; Xu, H.; Soejima, H.; Ma, W.; Lvov, Y.; Takahara, A. Biomimetic Dopamine Derivative for Selective Polymer Modification of Halloysite Nanotube Lumen. *J. Am. Chem. Soc.* **2012**, *134*, 12134–12137.
29. Jana, S.; Das, S.; Ghosh, C.; Maity, A.; Pradhan, M. Halloysite Nanotubes Capturing Isotope Selective Atmospheric CO₂. *Sci. Rep.* **2015**, *5*, 8711.
30. Abdullayev, E.; Sakakibara, K.; Okamoto, Ken.; Wei, W.; Ariga, K.; Lvov, Y. Natural Tubule Clay Template Synthesis of Silver Nanorods for Antibacterial Composite Coating. *ACS Appl. Mater. Interfaces* **2011**, *3*, 4040–4046.
31. Gregg, S. J.; Sing, K. S. W.; *Adsorption, Surface Area and Porosity*, 2nd ed, Academic Press: London, **1982**.
32. Groen, J. C.; Peffer, L. A. A.; Perez-Ramirez, J. Pore Size Determination in Modified Micro- and Mesoporous Materials. Pitfalls and Limitations in Gas Adsorption Data Analysis. *Microporous Mesoporous Mater.* **2003**, *60*, 1–17.
33. Morin, F. Magnetic Susceptibility of α -Fe₂O₃ and α -Fe₂O₃ with Added Titanium. *J. Phys. Rev.* **1950**, *78*, 819.

34. Raming, T. P.; Winnubst, A. J. A.; van Kats, C. M.; Philipse, A. P. The Synthesis and Magnetic Properties of Nanosized Hematite (α -Fe₂O₃) Particles. *J. Colloid Interface Sci.* **2002**, *249*, 346–350.
35. Cao, M. H.; Liu, T. F.; Gao, S.; Sun, G. B.; Wu, X. L.; Hu, C. W.; Wang, Z. L. Single-Crystal Dendritic Micro-Pines of Magnetic α -Fe₂O₃: Large-Scale Synthesis, Formation Mechanism, and Properties. *Angew. Chem. Int. Ed.* **2005**, *44*, 4197–4201.
36. Zhang, R.; Wang, X.; Song, J. Si, Y.; Zhuang, X.; Yu, J.; Ding, B. *In Situ* Synthesis of Flexible Hierarchical TiO₂ Nanofibrous Membranes with Enhanced Photocatalytic Activity. *J. Mater. Chem. A* **2015**, *3*, 22136–22144.
37. Shanmugam, M.; Alsalmeh, A.; Alghamdi, A.; Jayavel, R. Enhanced Photocatalytic Performance of the Grapheme-V₂O₅ Nanocomposite in the Degradation of Methylene Blue Dye under Direct Sunlight. *ACS Appl. Mater. Interfaces* **2015**, *7*, 14905–14911.
38. Hochbaum, A. I.; Yang, P. Semiconductor Nanowires for Energy Conversion. *Chem. Rev.* **2010**, *110*, 527–546.
39. Zhang, L.; Wang, W.; Zhou, L.; Xu, H. Bi₂WO₆ Nano- and Microstructures: Shape Control and Associated Visible-Light-Driven Photocatalytic Activities. *Small* **2007**, *3*, 1618–1625.
40. Jana, S.; Praharaj, S.; Panigrahi, S.; Basu, S.; Pande, S.; Chang, C. -H. ; Pal, T. Light-Induced Hydrolysis of Nitriles by Photoproduced α -MnO₂ Nanorods on Polystyrene Beads. *Org. Lett.* **2007**, *9*, 2191–2193.
41. Zeng, S.; Tang, K.; Li, T.; Liang, Z.; Wang, D.; Wang, Y.; Qi, Y.; Zhou, W. Facile Route for the Fabrication of Porous Hematite Nanoflowers: its Synthesis, Growth Mechanism, Application in the Lithium Ion Battery, and Magnetic and Photocatalytic Properties. *J. Phys. Chem. C* **2008**, *112*, 4836–4843.

Conclusions and Future Scope of the Study

9.1 Conclusions

The overall research findings are summarized here. Three clay based solid adsorbents have been synthesized through the selective modification of the outer surfaces of the clay using several viable aminosilanes having varied amine densities and adsorption sites for CO₂ capture from ambient air under standard temperature and ambient pressure using both the mass spectrometry and spectroscopic techniques. Relative humidity basically regulates the atmospheric CO₂ adsorption. The adsorption kinetics describing CO₂ uptake rate has been studied to evaluate the efficacy of the adsorbents. We have also explored the underlying adsorption mechanism under dry and humid conditions. The efficiency and excellent stability of these adsorbents even after prolonged cyclic adsorption-desorption experiments are demonstrated by their repetitive use in oxidative environment.

The synthesis of monodispersed mesoporous silica nanoflowers with large surface area through a novel light-assisted hydrolysis route has been developed. The synthetic route provides uniform silica nanoparticles with precise control over their morphology and size along with good thermal and mechanical stability. Tuning the surface chemistry of the silica nanoflowers using several amines having primary and/or secondary amine sites, they have been exploited as solid adsorbent to study their CO₂ uptake capacity. Their long term durability and sustainability have also been accredited by their multi-cycle adsorption-desorption study.

Hybrid nanocomposites have been fabricated containing thiol or amine sites to explore them as cost-effective sorbents for the removal of toxic heavy metal ions from the aqueous solution. Adsorption kinetics of Hg(II) ions follow pseudo-second-order rate equation as compared to pseudo-first-order kinetic model. The adsorption isotherms were well fitted with the Langmuir isotherm model with high value of

correlation coefficient compared to Freundlich isotherm model. This study suggests monolayer adsorption of the mercury ions on the surface of functionalized clay nanomaterials. All the adsorbents demonstrate excellent adsorption capacity even at low concentration and have multi-cycle Hg(II) uptake capability.

HNTs/Ag and HNTs/Au NCs have been fabricated based on the two different synthetic approaches through the immobilization of preformed as well as direct *in situ* growth of the metal NPs over the surface modified HNTs, resulting in the formation of efficient and low-cost heterogeneous catalysts. Uniformly distributed Au and Ag NPs successfully have been prepared over the surface of HNTs in presence and absence of any coupling materials. Catalytic efficacy of these NCs was performed for the reduction of nitroaromatics. A detailed kinetic study demonstrated the higher catalytic efficiency of *in situ* synthesized HNTs/Ag NCs amongst the four NCs, probably due to the absence of any capping agent over the surface of NPs.

A light-assisted solution chemistry route was developed for the synthesis of nanoscale hierarchical flower-like MnO₂ over the surface of clay nanotubes. MnO₂ nanoflowers comprise of assemblies of many wrinkled and intersected nanosheets and the XRD pattern indicates the formation of monoclinic structure of layered δ -MnO₂. The photocatalytic activity of the HNTs/ δ -MnO₂ NCs has been investigated towards the degradation of organic dyes in presence of renewable and never-ending solar energy. The photocatalytic mechanism suggests the formation of reactive oxygen species that assist the degradation of dyes. The process should be fascinating because of the easy control over reaction conditions, possible scaling up, and recycling of the nanocomposites. There is also no need of any supplementary oxygen sources during the photodegradation of organic pollutants.

At the end of the thesis, the selective modifications of halloysite lumen using a chelating ligand have been demonstrated. The selective modification of the lumen produces an inorganic micelle-like architecture that helps the loading of iron and the successive formation of rod-shaped nanoscale iron oxides inside the lumen of the tubular clays. Nanocomposites having α -Fe₂O₃ core with halloysite shell have been successfully synthesized. The α -Fe₂O₃/HNTs NCs

exhibit enhanced photocatalytic activity for the degradation of dyes in presence of solar light compared to the UV or visible light.

9.2 Future Scope of the Study

- ❖ Large-scale synthesis of dandelion-like silica nanoflowers may be the prospective candidate in the field of environmental remediation, catalysis, drug delivery and hard templates for the substructure of other materials to form nanocomposites.

- ❖ The selective modification of the surfaces of clay materials or silica nanoflowers may be a future pathway to design novel inorganic-organic hybrid nanocomposites for the selective adsorption of contaminants, targeted drug delivery, biosensing and as a support for catalysts.

- ❖ The low cost nanocomposites may be the new alternative of the other expensive current state-of-the-art materials for the production of green energy and CO₂ reduction.

- ❖ Design and synthesis of various nanomaterials of metals and metal oxides with specific shapes, sizes and morphologies may be an added advantage and subsequently can be utilized as nanocatalysts for the development of sustainable and challenging routes in photocatalysis, CO₂ capture and conversion of adsorbed CO₂ to fine chemicals.
